AMPLITUDE AND PHASE VARIATIONS OF SURFACE WAVES IN A LATERALLY HETEROGENEOUS EARTH: RAY- AND BEAM-THEORETICAL APPROACH

by

KIYOSHI YOMOGIDA

B.S., University of Tokyo
(1980)

M.S., University of Tokyo
(1982)

Submitted to the Department of Earth,
Atmospheric, and Planetary Sciences
in Partial Fulfillment of the
Requirements of the Degree of

DOCTOR OF PHILOSOPHY

at the

October, 1985

Signature of Author: _____
Department of Earth, Atmospheric, and Planetary Sciences

Certified by: _____
Sean C. Solomon
Thesis Co-Supervisor

_____
Keiiti Aki
Thesis Co-Supervisor

Accepted by: _____
William F. Brace
Chairman, Department of Earth, Atmospheric and Planetary Sciences

AMPLITUDE AND PHASE VARIATIONS OF SURFACE WAVES IN A LATERALLY HETEROGENEOUS EARTH: RAY- AND BEAM-THEORETICAL APPROACH

by

KIYOSHI YOMOGIDA

Submitted to the Department of Earth,
Atmospheric, and Planetary Sciences
on October 25, 1985 in Partial Fulfillment of the
Requirements for the Degree of Doctor of Philosophy

ABSTRACT

Lateral heterogeneity of the Earth has begun to be mapped extensively by measurements of phase velocities of surface waves since the installation of global digital network. The methods used in such studies are, however, based on simple ray theory: observed phase delays are assumed to be integrations of slowness along the great circles connecting sources and receivers. On the other hand, wave theories for seismic body wave propagation in a laterally heterogeneous medium have advanced remarkably. Most of these theories are based on asymptotic ray theory. This study tries to combine these two different developing fields: to improve the resolving power of surface waves to the lateral heterogeneity of the Earth through an inverse method based more closely on full wave theory (asymptotic ray theory). We chose the Gaussian beam method and applied it to the surface wave problem. This study consists of three principal parts: (1) derivations of formulations, (2) forward modelling, and (3) inversions of phase and amplitude data for phase velocity, including a non-linear iterative method.

First, asymptotic ray theory is applied to surface waves in a medium where the lateral variations of structure are very smooth. In such a medium the formulation for points exactly on the ray has previously been given by others. Using ray-centered coordinates, we obtain parabolic equations for lateral variations while vertical structural variations at a given point are specified by eigenfunctions of normal mode theory as for the laterally homogeneous case. Following the paraxial ray approximations developed for acoustic or elastic body waves, the formulation at points not only on the ray but also in the neighborhood of the ray is successfully derived. Final results on wavefields close to a ray can be expressed by formulations similar to those for elastic body waves in two-dimensional laterally heterogeneous media. The transport equation is written in terms of geometrical-ray spreading, group velocity and an energy integral. For the horizontal components there are both principal and additional components to describe the curvature of rays along the surface, as in the case of elastic body waves. With complex parameters the solutions for the dynamic ray tracing system correspond to Gaussian beams: the amplitude distribution is

bell-shaped along the direction perpendicular to the ray and the solution is regular everywhere, even at caustics. Because of the similarity of the present formulations to the original ones, most of the characteristics of Gaussian beams for two dimensional elastic body waves are also applicable to the surface wave case. At each frequency the solution may be regarded as a set of eigenfunctions propagating over a two-dimensional surface according to the phase velocity mapping.

Special attention to the following points is necessary for surface wave synthesis: (1) the speed of the wavepacket along the ray is the local group velocity even though the ray path itself is determined by the phase velocity distribution in an isotropic or transversely isotropic medium; (2) surface waves travelling on a spherical Earth may be mapped into Cartesian coordinates (2-D) using the Mercator transformation including the effect of ellipticity; (3) the weighting factors of each Gaussian beam for a moment-tensor representation of an earthquake are equivalent to those of a far-field radiation pattern in a laterally homogeneous model. Synthetic seismograms of narrow bandwidth with several different center frequencies are compared with real bandpass-filtered data to delineate the anomalies of three dimensional structures.

The reliability of the above methods are checked by calculating synthetic seismograms from simple to fairly complicated structures. Although there are some ambiguities in the selection of parameters used to synthesize seismograms by the Gaussian beam method, physically appropriate values may be estimated, and the choice of these parameters is not critical to the results. Several forward tests on regionalized models with periods 20-40 s show that this waveform synthesis is sensitive to slight variations of laterally heterogeneous structure which conventional methods, using only phase information, cannot resolve. Results of tests for heterogeneous structure in the Pacific Ocean imply that this method may help to resolve weak and small-scale velocity anomalies such as the Hawaiian hot spot or details of lateral changes in seismic velocities near spreading ridges.

Finally, Reyleigh wave phase velocities at periods 30-80s in the Pacific Ocean are calculated by inverting phase and amplitude anomaly data using the paraxial ray approximation and the Gaussian beam method. The model is divided into 5°x5° blocks, and approximately 200 source-receiver pairs from 18 well-studied events around the Pacific Ocean are used. First, we calculate phase anomalies for the lithospheric age-dependent model. Next, conventional phase data inversions are conducted assuming great circle paths to reduce phase discrepancies to less than π. This procedure is essential for later inversions using amplitude data. We then determine the residuals of both amplitude and phase terms by calculating ray-synthetic seismograms. Using the Born approximation for a 2-D wave equation, a non-linear iterative inversion for phase velocities is performed with both residuals. Frechet derivatives for the inversion consist primarily of two wavefields: (1) the wavefield at the model point from the source, and (2) the Green's function from the model point to the receiver. These wavefields are also calculated by the paraxial ray approximation and Gaussian beam methods. In the inverse formulations, the simple use of the conventional Backus-Gilbert approach breaks down in the non-linear iterative case and an extra term is necessary to control the model perturbations in order to

minimize departures from the a priori model. The use of this term guarantees that we are able to obtain a fairly reliable phase velocity model even in the present non-linear problem. In most cases residual variances are significantly reduced after two or three iterations. Compared with the phase data inversions, this inverse scheme gives more reliable resolution and shows that some features obtained by phase data inversions are suspicious. The resulting model displays some interesting deviations from the lithospheric age-dependent model. For example, low velocity regions are correlated with the Hawaii, Samoa, French Polynesia and Gilbert Islands hot spots.

Thesis Co-Supervisor: Sean C. Solomon

Title: Professor of Geophysics

Thesis Co-Supervisor: Keiiti Aki

Title: W.M. Keck Professor of Geological Sciences,
University of Southern California
(Formerly, R.R. Shrock Professor of Earth and
Planetary Sciences, M.I.T.)

ACKNOWLEDGMENTS

I would like to express sincere thanks to my advisors, Sean Solomon and Kei Aki. Sean provided financial support and allowed me to study freely. Without his kindness and generosity, I could not have finished my work at this time. Also, he impressed upon me how hard an American professor works. Kei (I should call him 'Aki-sensei', instead) gave me many useful suggestions and comments at every stage of my research. But more importantly, he taught me how to form original ideas and attack pioneering fields with an optimistic point of view. This is my favorite 'American spirit'.

I have found that Ted Madden is a really clever person. Even though in many instances I could not understand his points, I have learned a lot from him. With him I enjoyed sharing ideas of how to defend both my thesis and soccer goal. I am also grateful to Carl Wunsch and Don Forsyth for their comments on my work. During his stay at MIT in the spring of 1984, Ivan Pšenčík gave me many ideas on Gaussian beams and showed me the 'hearts' of east European scientists. I hope that I did not just steal from their work but have made some real contributions. Special thanks are due to John Woodhouse who eventually navigated me to this present topic when I visited him at the time his epoch-making work was just coming out. "It is too late for you to study only phase. Next is amplitude!"

Dorothy Frank and Jan Nattier-Barbaro kindly typed this thesis even though they were fed up with lots of messy equations. They sometimes worked for me after official working hours! Sharon Feldstein's efficient work prevented me from being bothered by many routine official procedures. I also appreciate help from Janet Sahlstrom. I thank Maggie Yamasaki at Lamont-Doherty Geological Observatory for her kindness when I collected

seismograms there. Thanks are also due to Linda Meinke for providing me with an lithospheric age map of the oceans and a program to draw contour lines.

At MIT I learned a lot of geophysics and general sciences, but I also learned some more important things. Rafael Benites and Fico Pardo-Casas, two 'El Loco' Peruvians, helped me to see my deficiencies. Thank you, both, for your comfort, encouragement and friendship. I will continue my efforts to improve myself. Thanks are extended to their wives, Elena and Mariella, for their kindness. With Paul Huang, I spent many late nights (sometimes even early mornings) critisizing each other's work ('bullshit'), fighting for the computer terminal, and talking about both useful and useless topics. I miss you (and his wife Theresa) and I am afraid I may not come across such a friend again. Tianquing Cao and Paul Okubo showed me their great friendships from the opposite directions. I would like to give my special thanks to Roger 'Bucky' Buck and his family for my two Christmas stays at their home in Virginia which I really enjoyed. Bucky taught me to be an authentic gentleman. Rob Comer helped me considerably when I first arrived in Boston, even though he was too busy with his own thesis at that time. My previous office mates Eric Bergman and Roy Wilkens provided me with occasional fun in their houses and Fenway Park. Jean Sauber, Wafik Beydoun and Kaye Shedlock kindly read and corrected some parts of this thesis. I am grateful to the people with whom I was happy to play intramural soccer, softball and volleyball games. Best wishes to Scott Phillips, Lynn Hall, Bob Nowack, Mark Murray, Bob Grimm, Joao and Jose Rosa, Stuart Stephens, Yves Bernabe, Craig Jones, Mike Nelson, Steve Bratt, Dave Olgaard, John Nabelek, Ru-shan Wu, Barbara Sheffels, Miguel Herraiz, Greg Beroza, Justin Revanaugh, Jean Titillah and Emilio Farco, and

Ichiro Fukumori. Best regards to my 'second mother' Mrs. Hanna Konrad for her heartful hospitality in her house. Special wishes to Jimmy who kept my office clean and encouraged me.

My study at MIT is possible because of the considerable support from my mentors in Japan: Seiya Uyeda, Masanori Saito, Hitoshi Takeuchi and Takafumi Matsui. I hope they are satisfied with this thesis!

Finally, my best thanks are given to my parents who approved my 'reckless' plan to go away from them and to study in U.S. Without their moral support I might have quit. Studying aboard is the first and maybe the biggest adventure in my life, and I am glad now that I can present this thesis to them. Mom and Dad, I wish you will worry about me much less from now on.

This reseach was financially supported by NSF grant EAR-8408714, NASA contract NAS5-27339 and Schlumberger-Doll research funds.

To the memory of my grandmother

Table of Contents

Chapter 1. Introduction

In a recent review paper, Chapman and Orcutt [1985] defined three eras in the history of seismic body wave interpretation in a vertically heterogeneous Earth: (1) observations of travel time, (2) direct array measurements of the ray parameter, that is, travel time differences, and (3) synthesizing seismograms to match waveforms. From the fact that a historical review has come out on this subject, we judge that the active research for one-dimensional structure may have been completed. Our generation must go beyond it. Anisotropy and lateral heterogeneity are two major targets. Studies on these subjects are not merely of theoretical interest but aid in our understanding of complex source processes and regional or global plate dynamics [e.g., Aki, 1981; Woodhouse and Dziewonski, 1984; Tanimoto and Anderson, 1984].

If "history repeats itself", parallels may be drawn between the investigation of one-dimensional structure as summarized by Chapman and Orcutt [1985] and the history of studies on anisotropic and laterally heterogeneous structures. Work marking the first era of seismology in a laterally heterogeneous Earth has only recently been completed. In this work, data such as body wave travel times and surface wave phase velocities are interpreted in terms of ray theory. The accumulation of a large amount of digital data makes it practical to invert for detailed heterogeneous structures, a procedure sometimes referred to as "seismic tomography". Examples of this type of study are those by Nakanishi and Anderson [1983], Woodhouse and Dziewonski [1984], Dziewonski [1984], Clayton and Comer [1983] and Tanimoto and Anderson [1984]. Measurements of P wave travel time anomalies have been performed in many areas since the study in NORSAR by Aki et al. [1977]. Since no particular parameter is any longer constant

along the ray or has significant meaning in the estimation of velocity, the second era may not exist for laterally heterogeneous media. As exemplified by the work on model resolution by Tanimoto [1985], we are now waiting in the first two eras of research for better quality data and denser coverage of stations to improve on the models.

If we consider only lateral heterogeneities, the third era, based on the use of wave theory, is still at an early stage of development. Conventional numerical methods, such as the finite-difference [e.g., Boore, 1972] and finite-element methods [e.g., Lysmer and Drake, 1972], require prohibitively large computational times in order to study complex heterogeneous structures even with supercomputers. The perturbation methods described in Chapter 13 of Aki and Richards [1980] are powerful but limited in application. For this reason, studies using synthetic seismograms in laterally heterogeneous media are still rare.

Several powerful methods, based mainly on asymptotic ray theory, have been developed recently to calculate body wave seismograms for laterally heterogeneous media: for example, dynamic ray tracing [Červený et al., 1977], Gaussian beam method [Červený et al., 1982], Maslov method [Chapman and Drummond, 1982], phase front method [Haines, 1983], Kirchhoff integral method [e.g., Scott and Helmberger, 1983], and so on. These newly-developed methods may make it possible to study the laterally heterogeneous Earth using full waveform data: that is, not only phase but also amplitude information.

The first applications of synthetic seismograms to real data were not for body waves but for long-period surface waves [e.g., Ewing et al., 1957] because the propagation of the latter is essentially restricted in 2-D

space as compared to the 3-D nature of the former, and the simpler structural models can be used to synthesize longer period waves. Again, if "history repeats itself," the theories for laterally heterogeneous structures should be applied first to surface waves because of the greater simplicity. The goal of the present study is to develop methods for modeling surface waves in a laterally heterogeneous earth and to apply them to real data.

The approach during the first era of surface wave studies has basically been the same in the early stages [e.g., Dorman et al., 1960] as in the most recent [e.g., Woodhouse and Dziewonski, 1984]. Heterogeneity is assumed to be sufficiently smooth so that the earth can be approximated by a sum of piecewise homogeneous regions. These conventional techniques rely on precise measurements of the phase term of surface waves and are based on the assumption that waves propagate along great circles. For a detailed study of lateral heterogeneity, the phase velocity along each path must be measured very precisely (e.g., better than 1% for surface waves with period longer than 100 s). Therefore, for real data that suffer from noise or multipath interference and with the usual ambiguity of source terms, the resolving power of these techniques to reveal lateral heterogeneity is limited.

In the presence of lateral heterogeneity, packets of surface waves propagate along paths deviating from great circles, and focusing (or defocusing) and multipath interference are to be expected. The spatial distribution of amplitudes is thus severely distorted from that predicted for a laterally homogeneous model. As early as the 1950's, Evernden [1953, 1954] demonstrated that, owing to lateral heterogeneity in the structure, the propagation direction of Rayleigh waves may deviate markedly from the great-circle path. Capon [1970] and Bungum and Capon [1974] found strong evidence at the LASA and NORSAR arrays for the occurrence of significant

multipathing of Rayleigh waves through continental margins. McGarr [1969b] observed amplitude anomalies for Rayleigh waves of 20-s period crossing the Pacific Ocean for several events in the Tonga-Kermadec region (see examples in Figure 1.1). Such remarkable anomalies are not observed for events at slightly different azimuths, for example, those near the Solomon Islands. McGarr suggested that such observations are due to zones of anomalously low velocity, such as the Hawaiian Islands, a hypothesis we discuss later.

Even for surface waves with periods longer than 150 sec for which the effects of lateral heterogeneity have been considered to be small, peculiar amplitude anomalies are sometimes observed. For example, see the anomalous R_3/R_2 observations (e.g., large R_3 energy at station KMY) for the Akita-Oki earthquake on May 26, 1983 given by Lay and Kanamori [1985] (Figure 1.2). These data imply that we can no longer assume that the waves propagate along great circles. In fact, the travel time calculations by Schwartz and Lay [1985] for recent models such as those of Nakanishi and Anderson [1984] and Woodhouse and Dziewonski [1984] show that the travel times along actual raypaths are sometimes longer than those along great circles (Figure 1.3). If this is the case, this is against Fermat's principle (according to which the travel time along the actual ray path is extreme, in this case, minimum) on which most of the previous studies are based. Thus, the procedure of measuring velocity along great circles may not be justified. This is why we need to study surface waves based on wave theories in laterally heterogeneous media. Moreover, the amplitude of a propagating wave is determined essentially by the second spatial derivative of velocity, as will be shown below, whereas the phase term depends on the velocity along the ray even though ray paths are determined by the first spatial derivative of velocity. Therefore, to delineate laterally

heterogeneous structure, methods which incorporate waveforms are considered to be more powerful than those involving only phase terms.

The Earth appears to be strongly stratified vertically, while the horizontal variation in structure is much weaker and usually quite smooth. For such a medium, we may not need to treat the heterogeneity in all directions equally as in three-dimensional ray tracing. Instead, this study aims at using the concept of ray theory only for the lateral propagation of normal modes while the vertical structure, assuming lateral homogeneity in the zeroth order approximation, is to be described by the conventional normal mode theory for surface waves. This means that a ray corresponding to a mode characterized by an eigenfunction determined for the local vertical structure propagates horizontally like a two-dimensional ray of a body wave. This approach is, in fact, not a new one. For example, long-range, low-frequency acoustic waves propagating in the ocean have been discussed in terms of normal modes in the vertical direction and by ray theoretical approaches in the horizontal direction for nearly horizontally stratified media [e.g., Pierce, 1965; Weinberg and Burridge, 1974]. A good summary of this subject is found in Burridge and Weinberg [1976]. For seismic surface waves, several theoretical works [e.g., Kirpichnikova, 1969; Gjevik, 1973; Woodhouse, 1974; Babich et al., 1976; Hudson, 1981] and numerical calculations based on the standard ray theory for realistic Earth models [Sobel and von Seggern, 1978; Wong and Woodhouse, 1983; Lay and Kanamori, 1985] have been performed. However, the standard ray theory requires a two-point ray tracing between source and receiver. This requirement leads to large computation time and has discouraged wide application of this approach.

In this study, to circumvent this problem, we apply one of the

recently developed methods, the Gaussian beam approach [Červený et al., 1982], to the surface wave problem. The Gaussian beam approach is an extension of the paraxial ray approximation, which is based on the standard ray theory [Červený et al., 1977]. Tests and applications of the Gaussian beam method to seismology have been conducted by Nowack and Aki [1984a], Cormier and Spudich [1984], Müller [1984], and Madariaga and Papadimitriou [1984].

We first derive the Gaussian beam formulations for surface waves in a laterally slowly-varying medium in Chapter 2. These formulations are for one beam. Then, in Chapter 3 we obtain the expressions for synthetic seismograms by the summation of each Gaussian beam derived in Chapter 2. We point out differences in these expressions between surface waves and body waves obtained in previous studies. In Chapter 4, numerical testing of the methods developed in the previous chapters is conducted by forward modelling of Rayleigh waves for a heterogeneous Pacific Ocean structure. Finally, in Chapter 5, we attempt to reach our ultimate goal: inversion of both amplitude and phase data to obtain laterally heterogeneous structure using the above methods. Rayleigh wave phase velocities in the Pacific Ocean are inverted for comparison with the conventional pure path phase velocity method. The inverse formulations are non-linear following Tarantola [1984a,b]. The main conclusions and the implications for future studies are summarized in Chapter 6.

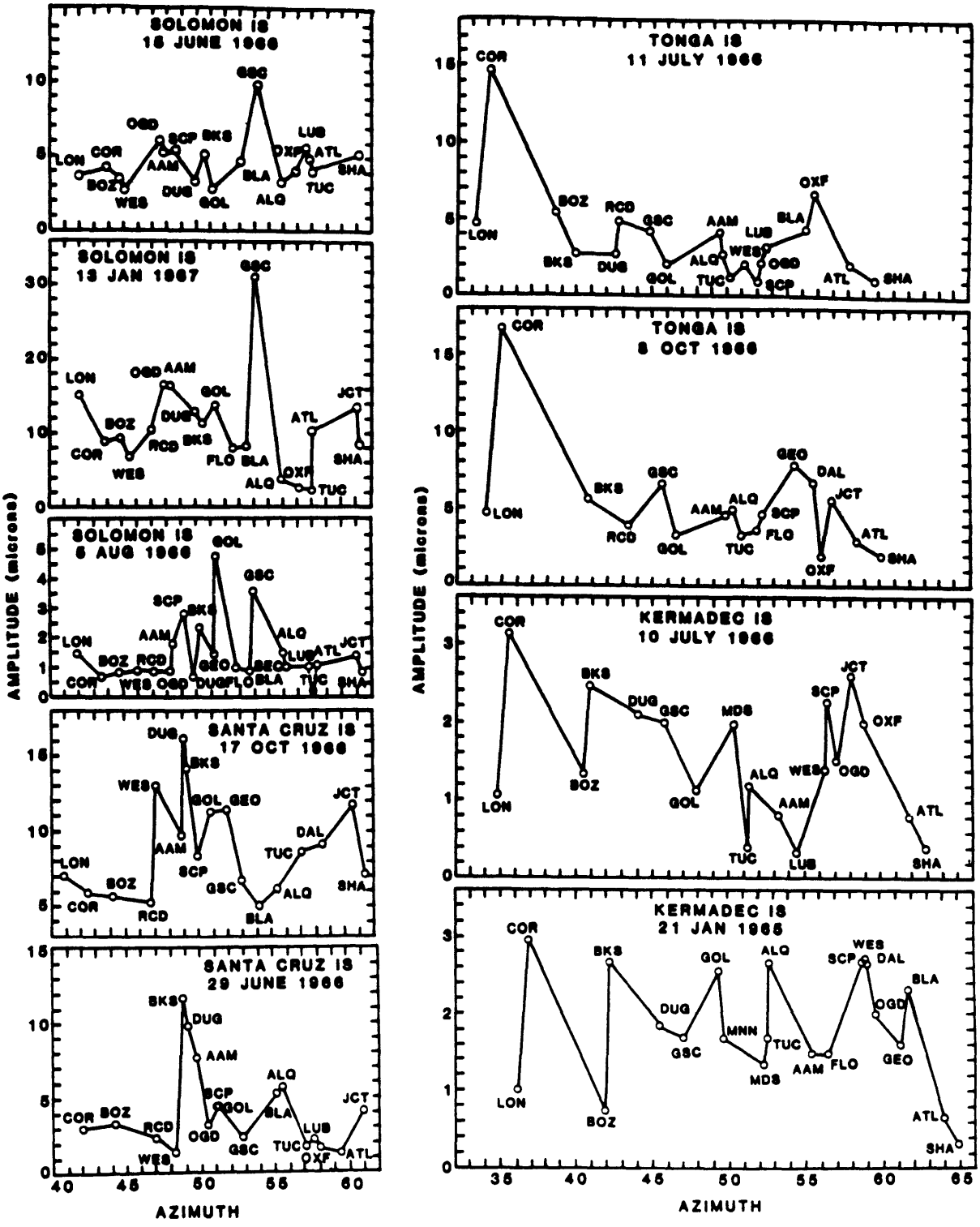

Figure 1.1. Observed amplitude variations of Rayleigh waves with periods of about 20 s at stations in North America for events in the Tonga-Kermadec trench. Note the large amplitude difference between Longmire (LON) and Corvallis (COR). Reproduced from McGarr [1969b].

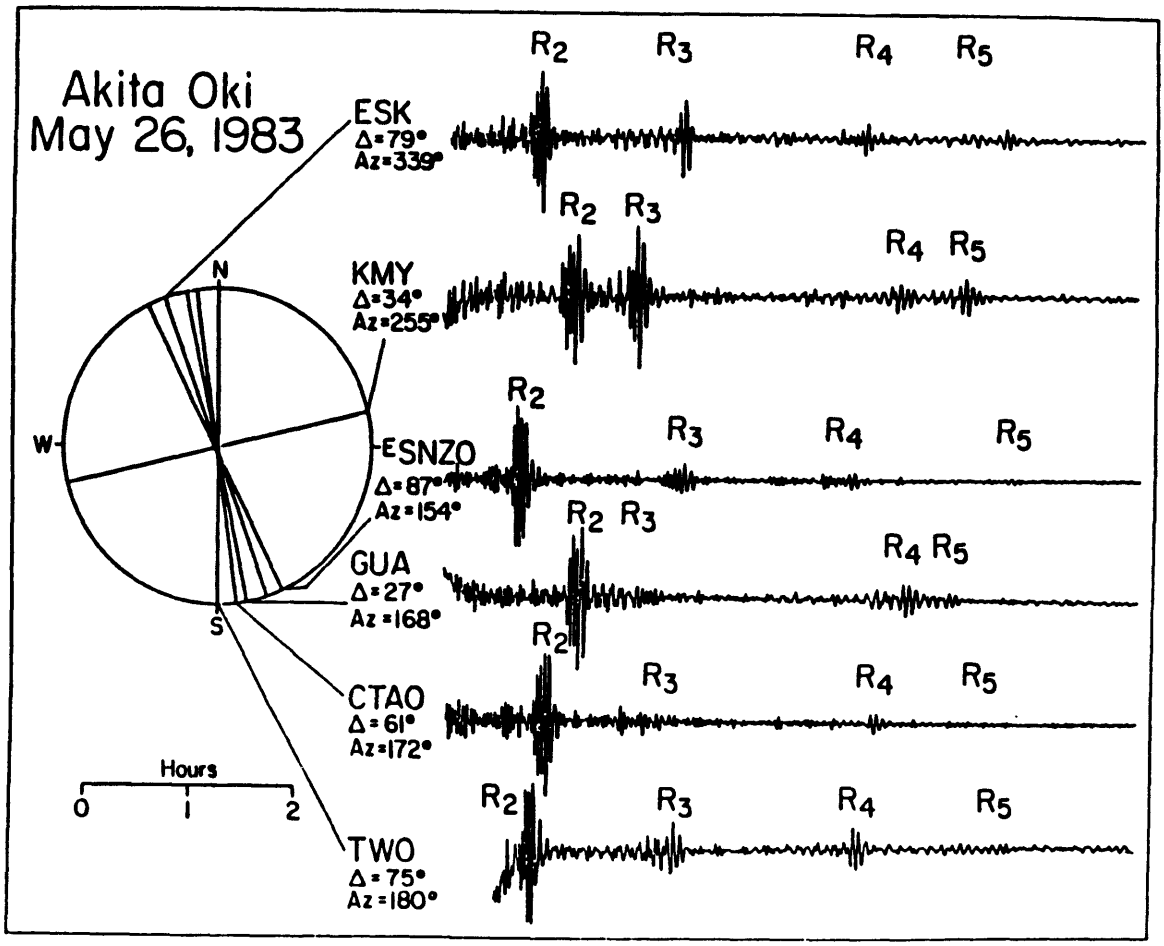

Figure 1.2. Anomalous R_3/R_2 observations at station KMY for the Akita-Oki earthquake. Reproduced from Lay and Kanamori [1985].

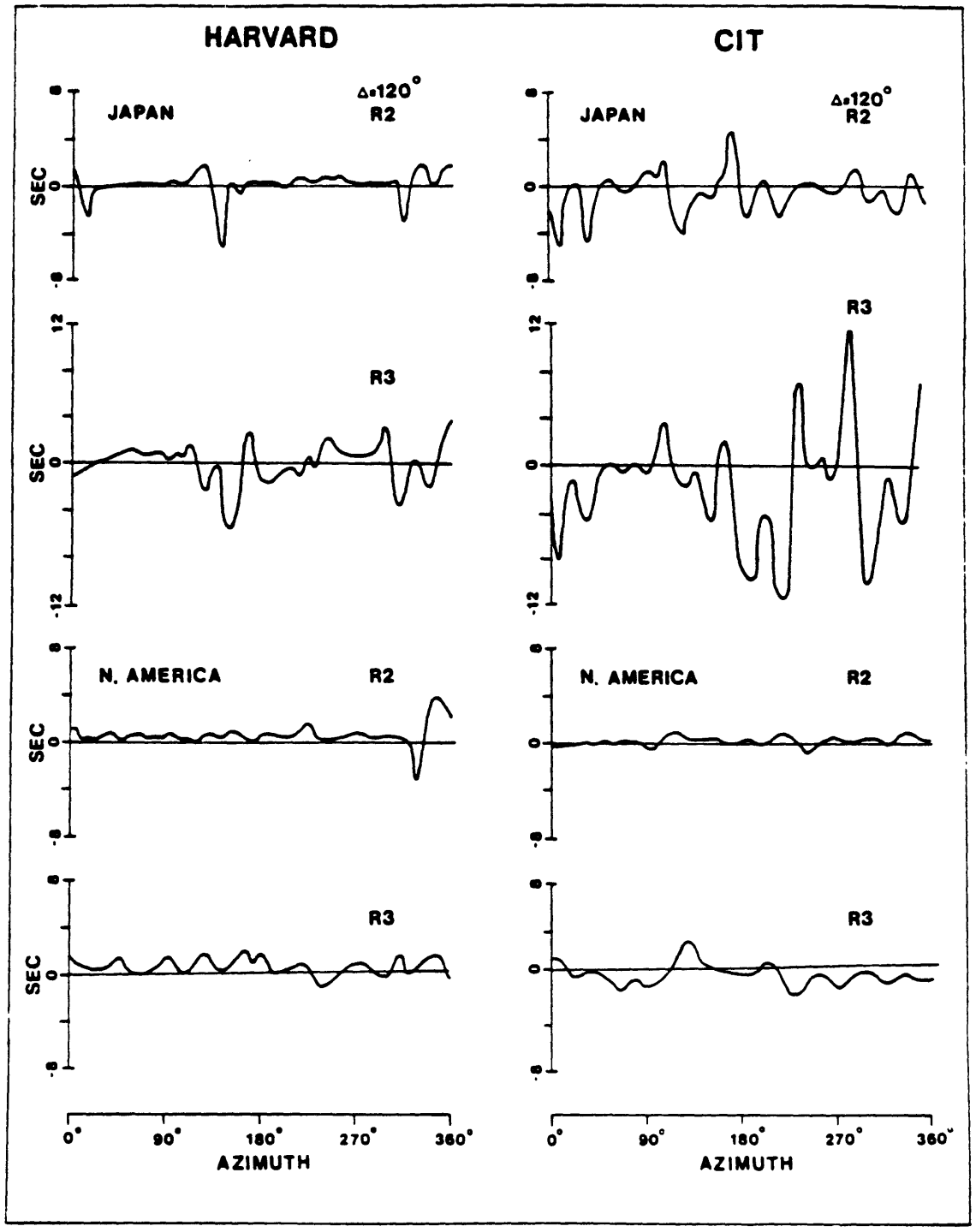

Figure 1.3. The difference in travel times between great circle and actual raypaths for 200s Rayleigh waves from sources in Japan and North America using recent models at Harvard [Woodhouse and Dziewonski, 1984] and CIT [Nakanishi and Anderson, 1984]. Reproduced from Schwartz and Lay [1985].

Chapter 2. Gaussian Beam Formulations for Surface Waves

In this chapter, we shall derive the Gaussian beam formulation of surface waves in a laterally-slowly varying medium. A flat and isotropic model with slight undulations of the free surface is assumed. Our procedure follows earlier papers on Gaussian beams such as that on seismic body waves by Červený and Pšenčík [1983]. The main difference in our method is that the variations of medium parameters in the vertical direction and in the horizontal directions are not treated equally. The vertical variations are assumed to be much more rapid than the horizontal ones, whose ratio is described by a small parameter $\varepsilon \ll 1$. The main features of the wavefield are followed by surface wave normal mode theory with an averaged vertical structure, and the lateral heterogeneity gives the modulation of such normal modes in a manner similar to two-dimensional ray theory. The final formulations are equivalent to the previous work of Woodhouse [1974], Babich et al. [1976], and Saastamoinen [1984]. However, our formulation gives a great advantage over those results because the wavefields can be evaluated not only on the ray but also in the neighborhood of the ray in the sense of the paraxial approximation. In this form, it can be naturally extended to the Gaussian beam method [Červený et al., 1982] based on the more complete wave theory. In the derivations of the formulation, we shall assume that parameters of the medium are continuous functions of depth, but the final results are also valid in layered media whose interfaces have gradual lateral variations.

In section 2.1, the elastodynamic equations are derived for laterally slowly-varying media. The horizontal variations in such media are much smoother than the vertical ones. We shall change the horizontal scales by

introducing one small parameter so that all of the variables are of the same order. In section 2.2, the trial form of the solution based on the asymptotic ray theory is inserted into the elastodynamic equations obtained in section 2.1. In the leading terms, the component perpendicular to the ray is decoupled from both that along the ray and the vertical component. This means that essentially there are two kinds of waves, Love and Rayleigh waves, as for laterally homogeneous media. In section 2.3, for each one of the above Love and Rayleigh waves, higher order equations are considered. Eventually, we obtain the parabolic equations which have been studied extensively in the literature on seismic body waves. Finally, in section 2.4, such parabolic equations are solved and we obtain two important equations: the dynamic ray-tracing equation and the transport equation. The final forms of the wavefields are then obtained. In section 2.5, we shall interpret the physical meaning of each term in the final formulation.

2.1 Elastodynamic Equations of Motion in Ray-Centered Coordinates

The elastodynamic equations of motion in a general orthogonal, curvilinear, right-handed coordinate system ξ_1, ξ_2 and ξ_3 with the corresponding scaling factors h_1, h_2 and h_3 are given in section 2.6 of Aki and Richards [1980]. Neglecting the body force term, the equation of motion may be expressed as

$$\rho \frac{\partial^2 \underset{\sim}{u}}{\partial t^2} = \frac{1}{h_1 h_2 h_3} \sum_{p=1}^{3} \sum_{q=1}^{3} \frac{\partial}{\partial \xi_q} (\tau_{pq} \underset{\sim}{n}_p h_1 h_2 h_3 / h_q) \tag{2.1}$$

where $\underset{\sim}{u}(\xi_1,\xi_2,\xi_3,t)$ are displacement vectors in the coordinate system ξ_i, ρ is density, t is time, τ_{pq} are stress-tensor components, and $\underset{\sim}{n}_p$ is the unit vector normal to the surface ξ_p = const. We consider only an isotropic medium, and the stress-strain relation is expressed in terms of two Lame constants λ and μ:

$$\tau_{pq} = \lambda \delta_{pq} \sum_{r=1}^{3} e_{rr} + 2\mu e_{pq} \qquad (2.2)$$

where δ_{pq} is the Kronecker delta and the strain components e_{pq} are expressed as

$$e_{pq} = \frac{1}{2}\left[\frac{h_p}{h_q}\frac{\partial}{\partial \xi_q}\left(\frac{u_p}{h_p}\right) + \frac{h_q}{h_p}\frac{\partial}{\partial \xi_p}\left(\frac{u_q}{h_q}\right)\right] + \frac{\delta_{pq}}{h_q}\sum_{r=1}^{3}\frac{u_r}{h_r}\frac{\partial h_p}{\partial \xi_r} . \qquad (2.3)$$

We consider a semi-infinite medium with axes $\xi_1 = x$, $\xi_2 = y$, and $\xi_3 = z$, in which the z-axis is directed downward (Fig. 2.1). In the remainder of this section, the medium is considered to be flat and to be described in Cartesian coordinates. The transformation between spherical and Cartesian coordinates is discussed in Yomogida and Aki [1985] and in Chapter 3.

As we mentioned in the Introduction, vertical structure is treated using normal mode theory, and we consider rays along the surface. For horizontal directions, we introduce ray-centered coordinates (s,n) in the following manner [Popov and Pšenčík, 1978]. The coordinate system (s,n) is connected with the ray as shown in Figure 2.2, where s represents the arclength along the ray, and n measures length perpendicular to the ray at the point s. On the ray, n is zero. We denote the unit vectors tangent and perpendicular to the ray as $\underset{\sim}{t}$ and $\underset{\sim}{n}$, respectively. The remaining coordinate is the same as the original one, $\underset{\sim}{z}$, which is directed vertically downwards (Fig. 2.1). Thus, we set $(\xi_1,\xi_2,\xi_3)=(s,n,z)$. In this study we assume a medium with weak lateral heterogeneity. We define

$$\eta_1 = S = \varepsilon s, \quad \eta_2 = N = \varepsilon n, \quad \eta_3 = z \quad \text{and} \quad T = \varepsilon t \qquad (2.4)$$

where ε is a small parameter. Since the energies propagate mainly along the rays (i.e., along the coordinate S), the time t should be measured with

the same scale as S. In this medium, elastic parameters and density have the following orders:

$$\frac{\partial \lambda}{\partial n_i} = 0(1), \quad \frac{\partial \mu}{\partial n_i} = 0(1) \text{ and } \frac{\partial \rho}{\partial n_i} = 0(1) \qquad i=1,2,3. \quad (2.5)$$

Also, the free surface, $z = \zeta(s,n)$ is allowed to have smooth undulations with the magnitude

$$\frac{\partial \zeta}{\partial n_i} = 0(1) \ . \qquad i=1,2 \qquad (2.6)$$

The medium approaches lateral homogeneity as $\varepsilon \to 0$ [e.g., Woodhouse, 1974; Babich et al., 1976]. The infinitesimal length element $\underset{\sim}{dr}$ is represented in the ray-centered coordinate system by

$$dr^2 = h^2 dS^2 + dN^2 + dz^2 \qquad (2.7)$$

where the scaling factor h is given by

$$h(s,n) = 1 + C^{-1}C_{,n}\, n = 1 + C^{-1}C_{,N}\, N \qquad (2.8)$$

and the phase velocity C and its first derivative $C_{,n} = \frac{\partial C}{\partial n}$ for the corresponding normal mode are evaluated on the ray (at n=0), because along the ray the phase front is propagating with the local phase velocity $[C(s,n)]_{n=0}$. Equation (2.7) shows that the scaling factors h_i for the coordinate system $(n_1,n_2,n_3) = (S, N, z)$ are

$$h_1 = h(s,n), \quad h_2 = h_3 = 1. \qquad (2.9)$$

Hereafter, we shall consider the wavefield horizontally close enough to the ray for the ray-centered coordinate system (s,n) to be regular [Červený et al., 1982].

Using this coordinate system (S,N,z,T), the elastodynamic equations (2.1)

may be written as

$$\varepsilon^2\rho\,\frac{\partial^2 u_S}{\partial T^2} = \frac{1}{h}\Big[\varepsilon\,\frac{\partial}{\partial S}\,\tau_{11} + \varepsilon\,\frac{\partial}{\partial N}(h\tau_{12}) + h\frac{\partial}{\partial z}\tau_{13}\Big] + \varepsilon\,\frac{\tau_{12}}{h}\,\frac{\partial h}{\partial N}\ ,$$

$$\varepsilon^2\rho\,\frac{\partial^2 u_n}{\partial T^2} = \frac{1}{h}\Big[\varepsilon\frac{\partial}{\partial S}\tau_{21} + \varepsilon\frac{\partial}{\partial N}(h\tau_{22}) + h\frac{\partial}{\partial z}\tau_{23}\Big] - \varepsilon\,\frac{\tau_{11}}{h}\,\frac{\partial h}{\partial N}\ , \tag{2.10}$$

$$\varepsilon^2\rho\,\frac{\partial^2 u_z}{\partial T^2} = \frac{1}{h}\Big[\varepsilon\,\frac{\partial}{\partial S}\,\tau_{31} + \varepsilon\,\frac{\partial}{\partial N}(h\tau_{32}) + h\,\frac{\partial}{\partial z}\,\tau_{33}\Big]$$

and the components of the stress tensor (2.2) are

$$\begin{aligned}
\tau_{11} &= \frac{\varepsilon}{h}(\lambda+2\mu)\Big[\frac{\partial u_S}{\partial S} + u_n\,\frac{\partial h}{\partial N}\Big] + \varepsilon\lambda\,\frac{\partial u_n}{\partial N} + \lambda\,\frac{\partial u_z}{\partial z}\ ,\\
\tau_{22} &= \frac{\varepsilon}{h}\,\lambda\Big[\frac{\partial u_S}{\partial S} + u_n\,\frac{\partial h}{\partial N}\Big] + \varepsilon(\lambda+2\mu)\,\frac{\partial u_n}{\partial N} + \lambda\,\frac{\partial u_z}{\partial z}\ ,\\
\tau_{33} &= \frac{\varepsilon}{h}\,\lambda\Big[\frac{\partial u_S}{\partial S} + u_n\,\frac{\partial h}{\partial N}\Big] + \varepsilon\lambda\,\frac{\partial u_n}{\partial N} + (\lambda+2\mu)\frac{\partial u_z}{\partial z}\ ,\\
\tau_{12} &= \tau_{21} = \varepsilon\mu\Big[\frac{\partial u_S}{\partial N} + h^{-1}\,\frac{\partial u_n}{\partial S} - h^{-1}\,\frac{\partial h}{\partial N}\,u_S\Big]\ ,\\
\tau_{23} &= \tau_{32} = \mu\Big[\frac{\partial u_n}{\partial z} + \varepsilon\,\frac{\partial u_z}{\partial N}\Big]\ ,\\
\tau_{31} &= \tau_{13} = \mu\Big[\varepsilon h^{-1}\,\frac{\partial u_z}{\partial S} + \frac{\partial u_S}{\partial z}\Big].
\end{aligned} \tag{2.11}$$

In order to simplify the above equations, we use commas before subscripts to represent the partial derivative with respect to the subscripted coordinate. For example, $u_{S,N} = \partial u_S/\partial N$, $u_{S,TT} = \partial^2 u_S/\partial T^2$, $\lambda_{,S} = \partial\lambda/\partial S$, and so on. Inserting (2.11) into (2.10), we get

$$\begin{aligned}
\varepsilon^2\rho\, u_{s,TT} &= \varepsilon^2 h^{-2}(\lambda+2\mu)\, u_{s,SS} + (\mu\, u_{s,z})_{,z} + \varepsilon h^{-1}\lambda\, u_{z,zS} + \varepsilon h^{-1}\lambda_{,S}\, u_{z,z} \\
&\quad + \varepsilon h^{-1}(\mu\, u_{z,S})_{,z} + \varepsilon^2 h^{-1}(\lambda+\mu)\, \overset{1}{u}_{n,SN} + \varepsilon^2 h^{-1}\overset{1}{[h^{-1}(\lambda+2\mu)]}_{,S}\, u_{s,S} \\
&\quad + \varepsilon^2 \mu\, u_{s,NN} + \varepsilon^2 \overset{1}{A}_{ns}\, u_{n,S} + \varepsilon^2 A_{sn}\, u_{s,N} + \varepsilon^2 A_{nn}\, u_{n,N} \\
&\quad + \varepsilon^2 B_s\, u_s + \varepsilon^2 B_n\, u_n \,, \\
\varepsilon^2\rho\, u_{n,TT} &= \varepsilon^2 h^{-2}\mu\, u_{n,SS} + (\mu\, u_{n,z})_{,z} + \varepsilon\lambda\, u_{z,zN} + \varepsilon(\mu\, u_{z,N})_{,z} \\
&\quad + \varepsilon^2 h^{-1}(\lambda+\mu)\, u_{s,SN} + \varepsilon^2 h^{-1}(h^{-1}\mu)_{,S}\, u_{n,S} + \varepsilon^2(\lambda+2\mu)\, u_{n,NN} \\
&\quad + \varepsilon \overset{2}{A}_{zz}\, u_{z,z} + \varepsilon^2 A^2_{ss}\, u_{s,S} + \varepsilon^2 A^2_{sn}\, u_{s,N} + \varepsilon^2 A^2_{nn}\, u_{n,N} \\
&\quad + \varepsilon^2 B^2_n\, u_n + \varepsilon^2 B^2_s\, u_s \,, \qquad (2.12) \\
\varepsilon^2\rho\, u_{z,TT} &= \varepsilon^2 h^{-2}\mu\, u_{z,SS} + [(\lambda+2\mu)u_{z,z}]_{,z} + \varepsilon h^{-1}(\lambda+\mu)\, u_{s,zS} \\
&\quad + \varepsilon h^{-1}\lambda_{,z}\, u_{s,S} + \varepsilon\mu\, u_{n,zN} + \varepsilon(\lambda\, u_{n,N})_{,z} + \varepsilon h^{-1}\mu_{,S}\, u_{s,z} \\
&\quad + \varepsilon^2\mu\, u_{z,NN} + \varepsilon^2 h^{-1}(h^{-1}\mu)_{,S}\, u_{z,S} + \varepsilon A^3_{nz}\, u_{n,z} \\
&\quad + \varepsilon^2 A^3_{zn}\, u_{z,N} + \varepsilon B^3_n\, u_n
\end{aligned}$$

where

$$\begin{aligned}
\overset{1}{A}_{ns} &= h^{-2}(\lambda+2\mu)h_{,N} + h^{-1}\mu_{,S} + h^{-1}\mu h_{,N} \,, \\
\overset{1}{A}_{sn} &= h^{-1}(\mu h)_{,N} \,, \\
\overset{1}{A}_{nn} &= h^{-1}\lambda_{,S} \,, \\
\overset{1}{B}_s &= -\, h^{-1}(\mu h_{,N})_{,N} - h^{-2}\mu h_{,N} \,, \\
\overset{1}{B}_n &= h^{-1}\overset{1}{[h^{-1}(\lambda+2\mu)h_{,N}]}_{,S} \,, \\
\overset{2}{A}_{zz} &= \lambda_{,N} \,, \\
A^2_{ss} &= h^{-1}\lambda_{,N} - h^{-2}(\lambda+3\mu)h_{,N} \,, \qquad (2.13) \\
\overset{2}{A}_{sn} &= h^{-1}\mu_{,S} \,, \\
\overset{2}{A}_{nn} &= h^{-1}[(\lambda+2\mu)h]_{,N} \,, \\
B^2_n &= h^{-1}(\lambda h_{,N})_{,N} - h^{-2}(\lambda+2\mu)(h_{,N})^2 \,, \\
\overset{2}{B}_s &= -\, h^{-1}(h^{-1}\mu h_{,N})_{,S} \,, \\
\overset{3}{A}_{nz} &= h^{-1}(\mu h)_{,N} + h^{-1}\lambda h_{,N} \,, \\
\overset{3}{A}_{zn} &= h^{-1}(\mu h)_{,N} \,, \\
\overset{3}{B}_n &= (h^{-1}\lambda h_{,N})_{,z} \,.
\end{aligned}$$

Equations (2.12) give the elastodynamic equations in ray-centered coordinates.

To consider surface waves (i.e., normal modes), we need boundary conditions in addition to the above equations. For $z \to \infty$, displacements must approach zero, that is, the radiation condition should be satisfied:

$$u_s, u_n, u_z \to 0 \qquad \text{as } z \to \infty \,. \tag{2.14}$$

Also, at the surface $z=\zeta$, any component of traction must vanish;

$$\tau_{i3} - \sum_{j=1}^{2} \tau_{ij} \frac{\partial \zeta}{\partial \xi_j} = 0 \quad (i=1,2,3) \qquad \text{at } z=\zeta. \tag{2.15}$$

Using the rescaled coordinate system (S, N, z) and (2.11), the above conditions may be expressed as

$$\mu[\varepsilon h^{-1} u_{z,S} + u_{s,z}] - \varepsilon \frac{\partial \zeta}{\partial S} [\varepsilon h^{-1}(\lambda+2\mu) u_{s,S} + \lambda u_{z,z}$$

$$+ \varepsilon\lambda u_{n,N} + \varepsilon D^1 u_n] - \varepsilon^2 \frac{\partial \zeta}{\partial N} \mu E^1 = 0 \,, \tag{2.16a}$$

$$\mu u_{n,z} + \varepsilon\mu u_{z,N} - \varepsilon^2 \mu \frac{\partial \zeta}{\partial S} E^2 - \varepsilon \frac{\partial \zeta}{\partial N} F^2 = 0 \,, \tag{2.16b}$$

$$\varepsilon h^{-1}\lambda u_{s,S} + (\lambda+2\mu) u_{z,z} - \varepsilon \frac{\partial \zeta}{\partial S} \mu[\varepsilon h^{-1} u_{z,S} + u_{s,z}] \tag{2.16c}$$

$$+ \varepsilon\lambda u_{n,N} + \varepsilon D^3 u_n - \varepsilon \frac{\partial \zeta}{\partial N} \mu E^3 = 0$$

where

$$D^1 = h^{-1}(\lambda+2\mu) h_{,N}, \quad E^1 = u_{s,N} + h^{-1} u_{n,S} - h^{-1} h_{,N} u_s \,,$$

$$E^2 = u_{s,N} + h^{-1} u_{n,S} + h^{-1} h_{,N} u_s \,,$$

$$F^2 = \varepsilon h^{-1}\lambda u_{s,S} + \varepsilon h^{-1}\lambda h_{,N} u_n + \varepsilon(\lambda+2\mu) u_{n,N} + \lambda u_{z,z} \,, \tag{2.17}$$

$$D^3 = h^{-1}\lambda h_{,N} \,,$$

$$E^3 = u_{n,z} + \varepsilon u_{z,N} \,.$$

Using the boundary conditions (2.14) and (2.16), we solve the equations (2.12) in a manner similar to the solution for a laterally homogeneous medium in the lowest order of ε.

2.2 Laterally Slowly-Varying Approximation For Elastodynamic Equations

For acoustic waves or body waves, it has been assumed that solutions of the elastodynamic equations are concentrated close to rays, or in other words, "the high-frequency elastic wavefield propagates mostly along rays" [e.g., Červený et al., 1982]. In this study we also seek approximate solutions for propagation along the ray in the direction of increasing s; however the solutions are expanded in powers of the parameter ε which has been introduced to describe the ratio of horizontal variation to vertical heterogeneity instead of the angular frequency ω for body waves [Červený and Pšenčík, 1983]. In the present study, the phase term cannot be expressed explicitly as a time-harmonic $e^{-i\omega t}$ as in the case of body waves or surface waves in a laterally homogeneous medium, because the phase velocity itself varies spatially. Thus, following Woodhouse [1974], we introduce the trial form (ansatz) of the solutions to equations (2.12) as nearly uniform harmonic wavetrains expanded into asymptotic series in powers of $\varepsilon^{1/2}$:

$$u_j(s,n,z,t) = e^{i\psi(s,t)} \sum_{k=0}^{\infty} \varepsilon^{k/2} \, U_j^k(S,N,z,T) \qquad j=s,n,z \qquad (2.18)$$

where $\psi(s,t)$ is the phase advance along the ray. We define wave number k and angular frequency as

$$k = \frac{\partial \psi}{\partial s} \quad \text{and} \quad \omega = -\frac{\partial \psi}{\partial t} \, . \qquad (2.19)$$

Ray-tracing based on these definitions is slightly different from that for non-dispersive waves [Yomogida and Aki, 1985]. We assume that k and ω are

slowly varying with respect to s and t:

$$k = k(S,T) = \omega(S,T)/C(S) \quad \text{and} \quad \omega = \omega(S,T) \tag{2.20}$$

where we assume that phase velocity does not vary with time.

To use the asymptotic ray theory developed above, the following conditions must be satisfied by analogy to the high-frequency approximation [Kravtsov and Orlov, 1980]:

$$k^{-1} << \ell, \qquad \ell = \frac{\lambda}{|\nabla_\perp \lambda|}, \frac{\mu}{|\nabla_\perp \mu|} \text{ or } \frac{\rho}{|\nabla_\perp \rho|} \tag{2.21}$$

and

$$\bar{L} << k\ell^2 \tag{2.22}$$

where ℓ is the characteristic scale length of heterogeneity, $\bar{L}$ is the distance from source to receiver, and $\nabla_\perp$ denotes the lateral gradient. These conditions mean that the lateral variation of a medium must be small within a wavelength and the receiver must be within the first Fresnel zone. For surface waves, this means that coupling among different modes can be neglected [e.g., Gregersen and Alsop, 1976]. For example, k is about 0.04 km^{-1} for 40-sec Rayleigh waves. In oceanic regions a typical value for ℓ may be over 1000 km and the raypath length $\bar{L}$ may not exceed 10,000 km. Thus, the conditions given in (2.21) and (2.22) are satisfied if we avoid paths crossing ocean-continent boundaries, where lateral variations of structure are much stronger.

Following Babich and Buldyrev [1972], the solutions concentrated close to a thin 'boundary layer' (the scale of one wavelength) along a ray have a scaling factor $N = O(\varepsilon^{1/2})$, which is similar to $n = O(\omega^{-1/2})$ of the high-frequency approximation for body waves [Červený and Pšenčík, 1983]. For consistency, the coordinate N should be replaced by

$$\nu = N/\sqrt{\varepsilon} \quad . \tag{2.23}$$

By inserting (2.18) into equations (2.12) with ν and neglecting all terms of order higher than $0(\varepsilon)$, we get the following equations. Hereafter, we use lower-case characters (s,n,t) for (S,N,T):

$$\begin{aligned}
&\left[\rho\omega^2 - h^{-2}(\lambda+2\mu)\omega^2 C^{-2} + \frac{\partial}{\partial z}\mu\frac{\partial}{\partial z}\right](U_s^0 + \varepsilon^{1/2}U_s^1 + \varepsilon U_s^2) \\
&\quad + i\omega C^{-1}h^{-1}\left[\lambda\frac{\partial}{\partial z} + \frac{\partial}{\partial z}\mu\right](U_z^0 + \varepsilon^{1/2}U_z^1 + \varepsilon U_z^2) \\
&\quad + \varepsilon^{1/2} i\omega C^{-1}h^{-1}(\lambda+\mu)(U_n^0{}_{,\nu} + \varepsilon^{1/2}\, U_n^1{}_{,\nu}) \qquad (2.24a) \\
&\quad + \varepsilon\{2i\omega\rho U_s^0{}_{,t} + i\rho\frac{\partial\omega}{\partial t}U_s^0 + ih^{-2}(\lambda+2\mu)C^{-1}\frac{\partial\omega}{\partial s}U_s^0 \\
&\quad + i\omega C^{-1}[2h^{-2}(\lambda+2\mu)U_s^0{}_{,s} - h^{-2}(\lambda+2\mu)C_{,s}C^{-1}U_s^0 + h^{-1}(h^{-1}(\lambda+2\mu))_{,s}U_s^0] \\
&\quad + h^{-1}(\lambda U_z^0{}_{,z})_{,s} + h^{-1}(\mu U_z^0{}_{,s})_{,z} + \mu U_s^0{}_{,\nu\nu} + i\omega C^{-1}A_{ns}{}^1U_n^0\} = 0,
\end{aligned}$$

$$\begin{aligned}
&\left[\rho\omega^2 - h^{-2}\mu\omega^2 C^{-2} + \frac{\partial}{\partial z}\mu\frac{\partial}{\partial z}\right](U_n^0 + \varepsilon^{1/2}U_n^1 + \varepsilon U_n^2) \\
&\quad + \varepsilon^{1/2}\{i\omega C^{-1}h^{-1}(\lambda+\mu)(U_s^0{}_{,\nu} + \varepsilon^{1/2}\, U_s^1{}_{,\nu}) \\
&\qquad + (\lambda\frac{\partial}{\partial z} + \frac{\partial}{\partial z}\mu)(U_z^0{}_{,\nu} + \varepsilon^{1/2}\, U_z^1{}_{,\nu})\} \\
&\quad + \varepsilon\{2i\omega\rho U_n^0{}_{,t} + i\rho\frac{\partial\omega}{\partial t}U_n^0 + ih^{-2}\mu C^{-1}\frac{\partial\omega}{\partial s}U_n^0 \\
&\qquad + i\omega C^{-1}[2h^{-2}\mu U_n^0{}_{,s} - h^{-2}\mu C_{,s}C^{-1}U_n^0 + h^{-1}(h^{-1}\mu)_{,s}U_n^0] \\
&\qquad + (\lambda+2\mu)U_n^0{}_{,\nu\nu} + i\omega C^{-1}A_{ss}{}^2U_s^0 + A_{zz}{}^2\, U_z^0{}_{,z}\} = 0 \ , \qquad (2.24b)
\end{aligned}$$

$$[\rho\omega^2 - h^{-2}\mu\omega^2C^{-2} + \frac{\partial}{\partial z}(\lambda+2\mu)\frac{\partial}{\partial z}](U_z^0 + \varepsilon^{1/2}U_z^1 + \varepsilon U_z^2)$$

$$+ i\omega C^{-1}h^{-1}[\mu\frac{\partial}{\partial z} + \frac{\partial}{\partial z}\lambda](U_s^0 + \varepsilon^{1/2}U_s^1 + \varepsilon U_s^2)$$

$$+ \varepsilon^{1/2}[\mu\frac{\partial}{\partial z} + \frac{\partial}{\partial z}\lambda](U_n^0{}_{,\nu} + \varepsilon^{1/2}U_n^1{}_{,\nu})$$

$$+ \varepsilon\{2i\omega\rho U_z^0{}_{,t} + i\rho\frac{\partial\omega}{\partial t}U_z^0 + ih^{-2}\mu C^{-1}\frac{\partial\omega}{\partial s}U_z^0$$

$$+ i\omega C^{-1}[2h^{-2}\mu U_z^0{}_{,s} - h^{-2}\mu\, C_{,s}C^{-1}U_z^0 + h^{-1}(h^{-1}\mu)_{,s}U_z^0]$$

$$+ \mu U_z^0{}_{,\nu\nu} + h^{-1}(\lambda U_s^0{}_{,s})_{,z} + h^{-1}(\mu U_s^0{}_{,z})_{,s} + A_{nz}{}^2\, U_n^0{}_{,z} + B_n{}^3U_n^0\}$$

$$= 0\ . \qquad (2.24c)$$

Equations (2.24) together with (2.18) and (2.23) describe solutions in asymptotic forms.

Similar expansions should be applied to the boundary conditions at the free surface (16). Taking the order only up to $0(\varepsilon)$, the results may be written as

$$\mu[i\omega C^{-1}h^{-1}(U_z^0 + \varepsilon^{1/2}U_z^1 + \varepsilon U_z^2) + (U_s^0{}_{,z} + \varepsilon^{1/2}\, U_s^1{}_{,z} + \varepsilon U_s^2{}_{,z})]$$

$$+ \varepsilon\{h^{-1}\mu U_z^0{}_{,s} - \frac{\partial\zeta}{\partial s}[i\omega C^{-1}h^{-1}(\lambda+2\mu)U_s^0 + \lambda U_z^0{}_{,z}]$$

$$- \frac{\partial\zeta}{\partial n}i\omega C^{-1}h^{-1}\mu U_n^0\} = 0\ , \qquad (2.25a)$$

$$\mu(U_n^0{}_{,z} + \varepsilon^{1/2}U_n^1{}_{,z} + \varepsilon U_n^2{}_{,z}) + \varepsilon^{1/2}\mu(U_z^0{}_{,\nu} + \varepsilon^{1/2}U_z^1{}_{,\nu})$$

$$- \varepsilon\{\frac{\partial\zeta}{\partial s}\mu i\omega C^{-1}h^{-1}\, U_n^0 + \frac{\partial\zeta}{\partial n}[\lambda i\omega C^{-1}h^{-1}U_s^0 + \lambda U_z^0{}_{,z}]\} = 0\ , \qquad (2.25b)$$

$$[i\omega C^{-1}h^{-1}\lambda(U_s^0 + \varepsilon^{1/2}U_s^1 + \varepsilon U_s^2) + (\lambda+2\mu)(U_z^0{}_{,z} + \varepsilon^{1/2}U_z^1{}_{,z} + \varepsilon U_z^2{}_{,z})]$$

$$+ \varepsilon^{1/2}\lambda(U_n^0{}_{,\nu} + \varepsilon^{1/2}U_n^1{}_{,\nu})$$

$$+ \varepsilon[h^{-1}\lambda U_s^0{}_{,s} - \frac{\partial\zeta}{\partial s}\mu\,(i\omega C^{-1}h^{-1}U_z^0 + U_s^0{}_{,z}) + h^{-1}h_{,n}\lambda U_n^0 - \frac{\partial\zeta}{\partial n}\mu U_n^0{}_{,z}]$$

$$= 0 \qquad (2.25c)$$

at $z = \zeta$.

Now the problem is to solve equations (2.24) under the boundary condition (2.25) and the radiation condition that $U_j \to 0$ (j=s, n, z) as $z \to \infty$.

2.3 Parabolic Equations for Surface Waves

We now discuss equations (2.24) with boundary conditions at the free surface (2.25) in order to get solutions concentrated close to rays which propagate with the local phase velocities of Love and Rayleigh waves. Then we obtain the parabolic equations which give the dynamic ray-tracing equations and transport equations. We shall find that the former are exactly the same as those for body waves or acoustic waves [Červený et al., 1977; Červený and Hron, 1980] and the latter are equivalent to those given by Babich et al. [1976] or Woodhouse [1974]. In equations (2.24), the terms of order unity are equivalent to the characteristic equations of Love waves (for U_n^0 in equation (2.24b)) and Rayleigh waves (for U_s^0 and U_z^0 in equations (2.24a) and (2.24c)) in a laterally homogeneous medium. Thus, under the assumption of this study (i.e., laterally slowly-varying media) there are two types of surface waves: Love and Rayleigh waves which are decoupled to the first order approximation. Each is discussed individually.

a) Love waves

The non-vanishing component of the displacement vector for Love waves is normal to the raypath along the surface in the zeroth-order approximation. The zeroth-order solution has neither the component tangent to the ray nor the vertical one. Thus, we shall consider the component U_n as a "principal component" [Červený and Pšenčík, 1983].

To obtain solutions we take the phase velocity C in equations (24) as

that for Love waves in the local vertical structure at (s,n) (hereafter referred to as a local Love wave). This means that component U_n must satisfy the characteristic equations of local Love waves (see section 7.2 of Aki and Richards, 1980):

$$[\rho\omega^2 - \mu\omega^2 C_L^{-2}(s,n) + \frac{\partial}{\partial z}\mu\frac{\partial}{\partial z}]\, U_n(s,n,z,t) = 0 \qquad (2.26)$$

where $C_L(s,n)$ is a local phase velocity. Under the above assumption we should take

$$C(s) = C_L(s,0). \qquad (2.27)$$

Then, $C_L(s,n)$ is written in a Taylor series expansion in n as

$$C_L(s,n) \simeq C(s) + C_{,n}(s)\, n + \frac{1}{2} C_{,nn}(s) n^2 \qquad (2.28)$$

where

$$C_{,n}(s) = \frac{\partial C_L(s,n)}{\partial n}\Big|_{n=0}, \quad C_{,nn}(s) = \frac{\partial^2 C_L(s,n)}{\partial n^2}\Big|_{n=0}$$

With (8), it is easily shown that

$$h^{-2} C^{-2}(s) \simeq C_L^{-2}(s,n) + C^{-3}(s)\, C_{,nn}(s) n^2$$

and (2.29)

$$h^{-1} C^{-1}(s) \simeq C_L^{-1}(s,n) + \frac{1}{2} C^{-2}(s)\, C_{,nn}(s) n^2.$$

Thus the leading term of order unity in (2.24b) may be written as:

$$[\rho\omega^2 - \mu\omega^2 h^{-2} C^{-2}(s) + \frac{\partial}{\partial z}\mu\frac{\partial}{\partial z}]U_n$$

$$\simeq [\rho\omega^2 - \mu\omega^2 C_L^{-2}(s,n) - \mu\omega^2 C^{-3}(s) C_{,nn}(s) n^2 + \frac{\partial}{\partial z}\mu\frac{\partial}{\partial z}]U_n$$

$$\simeq -\mu\omega^2 C^{-3}\, C_{,nn}\, n^2\, U_n \simeq -\varepsilon\, \mu\omega^2 C^{-3} C_{,nn}\, \nu^2\, U_n. \qquad (2.30)$$

In equation (2.30), the coordinate ν is used instead of n because, in the vicinity of the ray, ν is of order unity from the boundary layer assumption (2.23). The Taylor series expansion (2.28) in $n = \varepsilon^{1/2}\nu$ is in fact consistent with the expansion of each component by $\varepsilon^{1/2}$, as in (2.18).

As shown in equation (2.30), the first term of (2.24b) is not of order unity but of order ϵ.

The terms of order unity in equations (2.24a) and (2.24c) are in fact the characteristic equations for "local Rayleigh waves" except for the appearance of the Love wave velocity. Unless the phase velocity of Love waves is identical to that of Rayleigh waves, which is rarely the case, U_S^0 and U_Z^0 must vanish in order that these terms be zero:

$$U_S^0 = U_Z^0 = 0 \tag{2.31}$$

With (2.30), the terms of order $\epsilon^{1/2}$ in equations (2.24a) and (2.24c) are in fact written as

$$i\omega C_L^{-1}(\lambda+\mu)U_n^0{}_{,\nu} + [\rho\omega^2 - (\lambda+2\mu)\omega^2 C_L^{-2} + \frac{\partial}{\partial z}\mu\frac{\partial}{\partial z}]U_S^1 + i\omega C_L^{-1}[\lambda\frac{\partial}{\partial z} + \frac{\partial}{\partial z}\mu]U_Z^1 = 0 \tag{2.32a}$$

$$[\mu\frac{\partial}{\partial z} + \frac{\partial}{\partial z}\lambda]U_n^0{}_{,\nu} + [\rho\omega^2 - \mu\omega^2 C_L^{-2} + \frac{\partial}{\partial z}(\lambda+2\mu)\frac{\partial}{\partial z}]U_Z^1 + i\omega C_L^{-1}[\mu\frac{\partial}{\partial z} + \frac{\partial}{\partial z}\lambda]U_S^1 = 0 \tag{2.32b}$$

Differentiating U_n in (2.26) with respect to ν and substituting into (2.32a), we get

$$[\rho\omega^2 - (\lambda+2\mu)\omega^2 C_L^{-2} + \frac{\partial}{\partial z}\mu\frac{\partial}{\partial z}](U_n^0{}_{,\nu} + i\omega C_L^{-1}U_S^1) + [\lambda\frac{\partial}{\partial z} + \frac{\partial}{\partial z}\mu]U_Z^1 = 0. \tag{2.33a}$$

$$[\rho\omega^2 - \mu\omega^2 C_L^{-2} + \frac{\partial}{\partial z}(\lambda+2\mu)\frac{\partial}{\partial z}]U_Z^1 + [\mu\frac{\partial}{\partial z} + \frac{\partial}{\partial z}\lambda](U_n^0{}_{,\nu} + i\omega C_L^{-1}U_S^1) = 0. \tag{2.33b}$$

These are characteristic equations for local Rayleigh waves with Love wave phase velocity. Using the same argument which led to (31), and putting $C_L \sim C$,

$$U_Z^1 = 0 \quad \text{and} \quad U_n^0{}_{,\nu} + i\omega C^{-1}U_S^1 = 0, \tag{2.34}$$

that is,

$$U_S \simeq \epsilon^{1/2}\, i\omega^{-1}\, C\, U_n^0{}_{,\nu}.$$

U_s is the "additional component" in the terminology of Červený and Pšenčík [1983]; it is of higher order than the principal component U_n by $\varepsilon^{1/2}$ and related to the deviation of the real wavefield from the plane wave perpendicular to the ray path. It is reasonable that there is no U_z component under the above approximation because rays should propagate only horizontally.

Now let us return to the equation for the principal component U_n in (2.24b). The term of order $\varepsilon^{1/2}$ vanishes because of (2.31). Substituting (2.31) and (2.34) into (2.24b), the next term of order ε may be written as

$$2i\mu k U_n^0{}_{,s} + i\mu \frac{\partial k}{\partial s} U_n^0 + i\mu_{,s} k U_n^0 + \mu U_n^0{}_{,\nu\nu} - \mu\omega^2 C^{-3} C_{,nn} \nu^2 U_n^0$$

$$+ 2i\rho\omega U_n^0{}_{,t} + i\rho \frac{\partial \omega}{\partial t} U_n^0 = 0. \qquad (2.35)$$

This is the parabolic equation for the principal component U_n^0.

The boundary condition at the free surface $z=\zeta$ for local Love waves is (see section 7.2 of Aki and Richards (1980))

$$\mu \frac{\partial U_n}{\partial z} = 0. \qquad (2.36)$$

Thus, in equation (2.25b), the first term should disappear. From (2.31), and (2.34), the most dominant term is of order ε, which is

$$ik \frac{\partial \zeta}{\partial s} \mu U_n^0 = 0 \qquad \text{at } z=\zeta. \qquad (2.37)$$

This condition will be used later to obtain the transport equation for Love waves.

b) Rayleigh waves

The non-vanishing components of the displacement vector for Rayleigh

waves are tangent to the ray path along the surface and vertical to the surface in the zeroth order approximation. Thus, components U_s and U_z are to be the principal components and U_n the additional component. As in the case of Love waves, we take the phase velocity C in equations (2.24) to be the velocity of Rayleigh waves in the vicinity of the ray. That is, in the zeroth order approximation, the components U_s and U_z must satisfy the characteristic equations of local Rayleigh waves:

$$[\rho\omega^2 - (\lambda+2\mu)\omega^2 C_R^{-2} + \frac{\partial}{\partial z}\mu\frac{\partial}{\partial z}]U_s + i\omega C_R^{-1}[\lambda\frac{\partial}{\partial z} + \frac{\partial}{\partial z}\mu]U_z = 0 , \quad (2.38a)$$

$$[\rho\omega^2 - \mu\omega^2 C_R^{-2} + \frac{\partial}{\partial z}(\lambda+2\mu)\frac{\partial}{\partial z}]U_z + i\omega C_R^{-1}[\mu\frac{\partial}{\partial z} + \frac{\partial}{\partial z}\lambda]U_s = 0 \quad (2.38b)$$

where $C_R(s,n)$ is called a local phase velocity of Rayleigh waves. Using the analogy of Love waves, C(s) is related to $C_R(s,n)$ as in equations (2.27) and (2.28), replacing the subscript L with R.

Now, let us consider the terms of the zeroth order in equations (2.24a) and (2.24c). With (2.29) (C_R instead of C_L) they are reduced to

$$[\rho\omega^2 - (\lambda+2\mu)\omega^2 h^{-2} + \frac{\partial}{\partial z}\mu\frac{\partial}{\partial z}]U_s + i\omega h^{-1}C^{-1}[\lambda\frac{\partial}{\partial z} + \frac{\partial}{\partial z}\mu]U_z$$

$$\approx [\rho\omega^2 - (\lambda+2\mu)\omega^2\{C_R^{-2} + C^{-3}C_{,nn}n^2\} + \frac{\partial}{\partial z}\mu\frac{\partial}{\partial z}]U_s + i\omega\{C_R^{-1} + \frac{C^{-2}}{2}C_{,nn}n^2\}[\lambda\frac{\partial}{\partial z} + \frac{\partial}{\partial z}\mu]U_z$$

$$\approx -(\lambda+2\mu)\omega^2 C^{-3}C_{,nn}n^2 U_s + \frac{i\omega}{2}C^{-2}C_{,nn}n^2[\lambda\frac{\partial}{\partial z} + \frac{\partial}{\partial z}\mu]U_z$$

$$\approx \varepsilon\{-(\lambda+2\mu)\omega^2 C^{-3}C_{,nn}\nu^2 U_s + \frac{i\omega}{2}C^{-2}C_{,nn}\nu^2[\lambda\frac{\partial}{\partial z} + \frac{\partial}{\partial z}\mu]U_z\} \quad (2.39a)$$

and

$$\varepsilon\{-\mu\omega^2 C^{-3}C_{,nn}\nu^2 U_z + \frac{i\omega}{2}C^{-2}C_{,nn}\nu^2[\mu\frac{\partial}{\partial z} + \frac{\partial}{\partial z}\lambda]U_s\} \quad (2.39b)$$

Like equation (2.30) for Love waves, the above terms are of order ε rather

than order unity.

The terms of order unity in equation (2.24b) constitute the characteristic equation for "local Love waves", but with Rayleigh wave phase velocity. By similar arguments in the case of Love waves, U_n^0 must vanish:

$$U_n^0 = 0. \tag{2.40}$$

Then, the leading term of order $\varepsilon^{1/2}$ may be written as

$$i\omega C_R^{-1}(\lambda+\mu)U_S^0{}_{,\nu} + [\lambda \frac{\partial}{\partial z} + \frac{\partial}{\partial z}\mu]U_Z^0{}_{,\nu} + [\rho\omega^2 - \mu\omega^2 C_R^{-2} + \frac{\partial}{\partial z}\mu\frac{\partial}{\partial z}]U_n^1 = 0. \tag{2.41}$$

By differentiating (2.38a) with respect to ν, we obtain the following from (2.41):

$$[\rho\omega^2 - \mu\omega^2 C_R^{-2} + \frac{\partial}{\partial z}\mu\frac{\partial}{\partial z}][U_n^1 + i\omega^{-1}C_R U_S^0{}_{,\nu}] = 0. \tag{2.42}$$

The operator in (2.42) is that for the characteristic equation for Love waves, so putting $C_R \sim C$,

$$U_n^1 + i\omega^{-1}C_R U_S^0{}_{,\nu} = 0 ,$$

that is, (2.43)

$$U_n \simeq -\varepsilon^{1/2} i\omega^{-1} C U_S^0{}_{,\nu}.$$

Likewise, the terms of order $\varepsilon^{1/2}$ in both equations (2.24a) and (2.24c) vanish and the leading terms of order ε are now

$$\begin{aligned} &2i(\lambda+2\mu)kU_S^0{}_{,s} + i(\lambda+2\mu)\frac{\partial k}{\partial s}U_S^0 + i(\lambda+2\mu)_{,s}kU_S^0 + (\lambda+2\mu)U_S^0{}_{,\nu\nu} \\ &- (\lambda+2\mu)\omega^2 C^{-3}C_{,nn}\nu^2 U_S^0 + \frac{i\omega}{2}C^{-2}C_{,nn}\nu^2[\lambda\frac{\partial}{\partial z} + \frac{\partial}{\partial z}\mu]U_Z^0 \\ &+ (\lambda U_Z^0{}_{,z})_{,s} + (\mu U_Z^0{}_{,s})_{,z} + 2i\rho\omega U_S^0{}_{,t} + i\rho\frac{\partial\omega}{\partial t}U_S^0 = 0 , \end{aligned} \tag{2.44}$$

$$2i\mu k U_z^0{}_{,s} + i\mu \frac{\partial k}{\partial s} U_z^0 + i\mu_{,s} k U_z^0 + \mu U_z^0{}_{,\nu\nu} - \mu\omega^2 C^{-3} C_{,nn} \nu^2 U_z^0 +$$

$$+ \frac{i\omega}{2} C^{-2} C_{,nn} \nu^2 \left[\mu \frac{\partial}{\partial z} + \frac{\partial}{\partial z} \lambda\right] U_s^0 + (\mu U_s^0{}_{,z})_{,s} + (\lambda U_s^0{}_{,s})_{,z}$$

$$- iC\omega^{-1}\left[\mu \frac{\partial}{\partial z} + \frac{\partial}{\partial z} \lambda\right] U_s^0{}_{,\nu\nu} + 2i\rho\omega\, U_z^0{}_{,t} + i\rho \frac{\partial \omega}{\partial t} U_z^0 = 0.$$

Equation (2.43) shows that the additional component U_n is coupled to only one of the principal components U_s. The behavior of U_z is independent of U_n and is determined only from the local vertical structure along the ray and not from neighboring structure, within the accuracy of the above approximation.

Now let us find the boundary conditions at the free surface $z=\zeta$. For Rayleigh waves the boundary conditions are shown to be different from those in the laterally homogeneous medium while they are the same for Love waves (2.36). The boundary conditions at the surface for local Rayleigh waves are written (see section 7.2 of Aki and Richards, 1980):

$$i\omega C_R^{-1}(s,n) U_z + U_{s,z} = 0 ,$$

$$(\lambda+2\mu) U_{z,z} + \lambda i\omega C_R^{-1}(s,n) U_s = 0 \qquad (2.45)$$

with $C_R(s,n)$ the local phase velocity. Using (2.29), the terms of order unity in equations (2.25a) and (2.52c) are of order ε but not of order unity like the terms in (2.39). Then, the largest contribution comes from the terms $0(\varepsilon)$ in (2.25a) and (2.25c), which are

$$\mu \frac{i\omega}{2} C^{-2}C_{,nn}\nu^2 U_z^0 + \mu U_z^0{}_{,s} - \frac{\partial \zeta}{\partial s}\{(\lambda+2\mu) i\omega C^{-1} U_s^0 + \lambda U_z^0{}_{,z}\} = 0 ,$$

$$\lambda \frac{i\omega}{2} C^{-2}C_{,nn}\nu^2 U_s^0 - ik^{-1}\lambda U s^0{}_{,\nu} + \lambda U_s^0{}_{,s} - \frac{\partial \zeta}{\partial s}\mu(i\omega C^{-1} U_z^0 + U_s^0{}_{,z}) = 0 \tag{2.46}$$

2.4 Solutions of Parabolic Equations

For both Love and Rayleigh waves we obtained parabolic equations (2.35) and (2.44) with the boundary conditions (2.37) and (2.46). Although there are several differences between them and the parabolic equations for acoustic waves [Červený et al., 1982] or for elastic body waves [Červený and Pšenčík, 1983] (especially for Rayleigh waves, because of the coupling between components U_s and U_z), we solve them by similar procedures.

a) Love waves

Following Babich and Kirpichnikova [1974], we assume solutions of the form

$$U_n^0 = A(s,t)\ell_1(s,z) \exp[\frac{i}{2}\omega(s,t)\nu^2 M(s)] \tag{2.47}$$

where $\ell_1(s,z)$ is an eigenfunction of the local Love wave at a point (s,n=0) (same notation as in section 7.2 of Aki and Richards [1980]) which is normalized as $\ell_1=1$ on the surface, and A(s,t) and M(s) are complex-valued scalar functions. Note that we assume that M is not a function of t. Substituting (2.47) into (2.35) yields

$$i[2\mu k(A\ell_1)_{,s} + \mu \frac{\partial k}{\partial s} A\ell_1 + \mu_{,s} k A\ell_1 + \omega M\mu A\ell_1 + 2\omega\rho A_{,t}\ell_1 + \frac{\partial \omega}{\partial t}\rho A\ell_1] \tag{2.48}$$

$$- \nu^2 A\ell_1[\mu k(\omega M)_{,s} + \mu\omega^2 M^2 + \mu\omega^2 C^{-3}C_{,nn} + \rho\omega \frac{\partial \omega}{\partial t} M] = 0.$$

We multiply (2.48) by $A\ell_1$ and integrate with respect to z from the surface $\zeta(s)$ to ∞. For convenience, we define the following energy integrals (see section 7.3 of Aki and Richards [1980]),

$$I_1(s) = \frac{1}{2}\int_{\zeta(s)}^{\infty} \rho(s,z)\ell_1^2(s,z)dz ,$$
$$I_2(s) = \frac{1}{2}\int_{\zeta(s)}^{\infty} \mu(s,z)\ell_1^2(s,z)dz. \tag{2.49}$$

Using integration by parts, equation (2.48) may be written as

$$i\{\frac{\partial}{\partial s}(kA^2I_2) + \omega MA^2I_2 + \frac{\partial}{\partial t}(\omega A^2I_1) + \frac{1}{2}k\frac{\partial \zeta}{\partial s}\mu(A\ell_1)^2\Big|_{z=\zeta}\}$$
$$- \nu^2A^2[\omega kI_2(M_{,s} + CM^2 + C^{-2}C_{,nn}) + M(kI_2\frac{\partial \omega}{\partial s} + \omega I_1\frac{\partial \omega}{\partial t})] = 0. \tag{2.50}$$

From boundary condition (2.37), the term evaluated at $z=\zeta$ in (2.50) should vanish. Because the group velocity U is expressed by the energy integrals as

$$U = I_2/CI_1 \tag{2.51}$$

(see equation 7.70 in Aki and Richards [1980]), equation (2.50) may be written as

$$i\{\frac{\partial}{\partial t}(\omega A^2I_1) + \frac{\partial}{\partial s}(U\omega A^2I_1) + CU\omega MA^2I_1\}$$
$$- \nu^2A^2\omega I_1[k(M_{,s} + CM^2 + C^{-2}C_{,nn}) + M(\frac{\partial \omega}{\partial t} + U\frac{\partial \omega}{\partial s})] = 0. \tag{2.52}$$

Let us define the length of ray path as $ds=Udt$ (see Chapter 3). Since $(\partial s/\partial t)_\omega = -(\partial\omega/\partial t)_s/(\partial\omega/\partial s)_t$,

$$\frac{\partial \omega}{\partial t} + U \frac{\partial \omega}{\partial s} = 0. \tag{2.53}$$

Thus, for the left-hand side of (2.52) to be zero for any value of ν, it is clear that

$$\frac{\partial}{\partial t}(\omega A^2 I_1) + \frac{\partial}{\partial s}(U\omega A^2 I_1) + CU\omega MA^2 I_1 = 0 \tag{2.54}$$

and

$$M_{,s}(s) + C(s)M^2(s) + C^{-2}(s)\, C_{,nn}(s) = 0 \tag{2.55}$$

The above equations deal with only the lowest-order solution like U_n^k with k=0. In general, we might consider a solution with an infinite system for k>1. Babich and Kirpichnikova [1974] and Klimeš [1983] showed that general solutions of order k are represented by k-th order Hermite polynomials: these solutions are called Hermite-Gaussian beams. Here only the basic mode with k=0 will be discussed; higher modes are neglected.

Equation (2.55) is similar in form to the dynamic ray tracing equation for acoustic waves or elastic body waves. It has the form of a first order non-linear ordinary differential equation with respect to s of the Ricatti type and can be transformed into two linear differential equations. Let us introduce new complex functions q(s) and p(s):

$$M(s) \equiv \frac{1}{C(s)q(s)} \frac{dq(s)}{ds} \equiv \frac{p(s)}{q(s)}. \tag{2.56}$$

Then, equation (2.55) may be written as a system of two linear ordinary differential equations:

$$\begin{aligned} \frac{dq}{ds} &= C(s)p(s) , \\ \frac{dp}{ds} &= - C^{-2}(s)C_{,nn}(s)q(s). \end{aligned} \tag{2.57}$$

We may solve the differential equations (2.57) along the ray to get p and q at any point on the ray. The above procedures are followed to evaluate geometrical spreading in the conventional ray method [e.g., Červený et al., 1977; Popov and Pšenčík, 1978; Červený and Hron, 1980]. Using (2.54) and the fact that q does not depend on t, equation (2.56) may be written as

$$\frac{\partial}{\partial t}\left(A^2 q I_1\right) + \frac{\partial}{\partial s}\left(UA^2 q I_1\right) = 0. \tag{2.58}$$

Like the continuity equation of fluid mechanics, this equation means that

$$A^2 q I_1 U = \text{constant along rays} \equiv \Phi_L. \tag{2.59}$$

That is, the energy flow along the vertical column beneath the two-dimensional ray tube on the surface is constant because q(s) represents the horizontal geometrical spreading. The energy propagates along the ray not with the phase velocity but with the group velocity, and $I_1(s)$ denotes the vertical energy profile. Φ_L is a complex constant along the ray but may differ for different rays and is a function of the azimuth of the corresponding take-off angle.

By inserting equations (2.34) ($U_S^1 = i\omega^{-1} C U^0_{n,\nu} = - CM\nu U^0_n$), (2.47), (2.56) and (2.59) into (2.18) and transforming to the original coordinates (S → s, N → n, T → t) (note that M should be also rescaled because of the term ds in (2.56)), the final form for Love waves may be written as

$$\underset{\sim}{u}(s,n,z,t) = \frac{\Phi_L}{\sqrt{q(s)U(s)I_1(s)}} \left[\underset{\sim}{n} - \frac{np(s)C(s)}{q(s)} \underset{\sim}{t}\right] \ell_1(s,z) \cdot \exp i\left[\psi(s,t) + \frac{\omega}{2} \frac{p(s)}{q(s)} n^2\right] \tag{2.60}$$

with $\frac{\partial\psi}{\partial t} = -\omega$ and $\frac{\partial\psi}{\partial s} = k = \frac{\omega}{C}$. The function ℓ_1 is an eigenfunction on the rays for local Love waves in the same sense as for the laterally homogeneous medium. Note that there is no vertical component. When the variables p and q are real and on the ray (n=0), the results are equivalent to those in the ray method [Babich et al., 1976; Woodhouse, 1974].

b) Rayleigh waves

As in the case of Love waves, we assume solutions of the form

$$\begin{aligned} U_s^0 &= A(s,t)r_1(s,z)\exp\left(\tfrac{i}{2}\,\omega\nu^2 M(s)\right), \\ U_z^0 &= A(s,t)ir_2(s,z)\exp\left(\tfrac{i}{2}\,\omega\nu^2 M(s)\right). \end{aligned} \tag{2.61}$$

We put the imaginary unit i in U_z^0 because there is a $\pi/2$ phase difference between horizontal and vertical displacements for Rayleigh waves. The eigenfunctions r_1 and r_2 correspond to those in section 7.2 of Aki and Richards [1980], normalized so that $r_2=1$ on the surface. Substituting (2.61) into (2.44) gives

$$\begin{aligned} &i\{2(\lambda+2\mu)k(Ar_1)_{,s} + (\lambda+2\mu)\frac{\partial k}{\partial s}Ar_1 + (\lambda+2\mu)_{,s}kAr_1 + (\lambda+2\mu)\omega MAr_1 \\ &\quad + (\lambda Ar_{2,z})_{,s} + [\mu(Ar_2)_{,s}]_{,z} + 2\omega\rho A_{,t}r_1 + \frac{\partial\omega}{\partial t}\rho Ar_1\} \\ &\quad - \nu^2 A\{(\lambda+2\mu)r_1[k(\omega M)_{,s} + \omega^2M^2 + \omega^2C^{-3}C_{,nn}] \\ &\quad + \frac{1}{2}[(\omega M)_{,s} + \omega C^{-2}C_{,nn}][\lambda\frac{\partial}{\partial z} + \frac{\partial}{\partial z}\mu]r_2 + \omega\frac{\partial\omega}{\partial t}M\rho Ar_1\} = 0, \end{aligned} \tag{2.62a}$$

$$i\{2\mu k(Ar_2)_{,s} + \mu \frac{\partial k}{\partial s} Ar_2 + \mu_{,s} kAr_2 + \mu\omega MAr_2 - (\mu Ar_{1,z})_{,s}$$

$$- [\lambda(Ar_1)_{,s}]_{,z} - CMA[\mu \frac{\partial}{\partial z} + \frac{\partial}{\partial z} \lambda]r_1 + 2\omega\rho A_{,t} r_2 + \frac{\partial \omega}{\partial t} \rho Ar_2\}$$

$$- \nu^2 A\{\mu r_2[k(\omega M)_{,s} + \omega^2 M^2 + \omega^2 C^{-3} C_{,nn}]$$

$$- \frac{1}{2}[(\omega M)_{,s} + \omega C^{-2} C_{,nn} + 2\omega CM^2][\mu \frac{\partial}{\partial z} + \frac{\partial}{\partial z} \lambda]r_1 + \omega \frac{\partial \omega}{\partial t} M\rho Ar_2\} = 0. \tag{2.62b}$$

Then we multiply (62a) and (62b) by Ar_1 and Ar_2, respectively, integrate them with respect to z from ζ to ∞, and sum the two equations. Now we define the following energy integrals (see section 7.3 of Aki and Richards [1980]),

$$I_1(s) = \frac{1}{2} \int_\zeta^\infty \rho(r_1^2 + r_2^2)dz ,$$

$$I_2(s) = \frac{1}{2} \int_\zeta^\infty [(\lambda+2\mu)r_1^2 + \mu r_2^2]dz , \tag{2.63}$$

$$I_3(s) = \frac{1}{2} \int_\zeta^\infty (\lambda r_1 \frac{\partial r_2}{\partial z} - \mu r_2 \frac{\partial r_1}{\partial z})dz .$$

Using integration by parts and the radiation condition (2.14), we get

$$i\{\frac{\partial}{\partial s}[A^2(2kI_2 + I_3)] + CMA^2(2kI_2 + I_3) + 2 \frac{\partial}{\partial t}(\omega A^2 I_1)$$

$$- A^2[k((\lambda+2\mu)r_1^2 + \mu r_2^2) - (\lambda r_1 \frac{\partial r_2}{\partial z} - \mu r_2 \frac{\partial r_1}{\partial z})] \frac{\partial \zeta}{\partial s}\Big|_{z=\zeta}$$

$$+ CMA^2 \lambda r_1 r_2 \Big|_{z=\zeta} + A[\lambda(Ar_1)_{,s} r_2 - \mu r_1 (Ar_2)_{,s}]\Big|_{z=\zeta}\}$$

$$- \nu^2 A^2 \{\omega(2kI_2+I_3)(M_{,s} + CM^2 + C^{-2}C_{,nn}) \qquad (2.64)$$

$$+ \frac{\partial \omega}{\partial s} M(2kI_2+I_3) + 2\omega \frac{\partial \omega}{\partial t} MI_1$$

$$+ \frac{1}{2}[(\omega M)_{,s} + \omega C^{-2}C_{,nn} + 2\omega CM^2]\lambda r_1 r_2\Big|_{z=\zeta}$$

$$- \frac{1}{2}[(\omega M)_{,s} + \omega C^{-2}C_{,nn}]\mu r_1 r_2\Big|_{z=\zeta}\} \quad = \quad 0$$

Next we consider the boundary conditions at the free surface $z=\zeta$. Inserting (2.61) into the two equations of (2.46), multiplying by r_1 and r_2, respectively, and summing these two relations, we see that the terms evaluated at $z=\zeta$ in equation (2.64) vanish. Also, using the equation for group velocity (equation 7.76 in Aki and Richards [1980]),

$$U \quad = \quad (2kI_2+I_3)/2\omega I_1 \ , \qquad (2.65)$$

equation (2.64) becomes identical to equation (2.52) for Love waves. Thus, with definition (2.53), we get both the dynamic ray tracing equations (2.57) and the transport equation (2.59). We shall denote the constant in (2.59) by Φ_R in this case.

Finally, transforming back to the original coordinates, the vertical and horizontal components of Rayleigh wave displacement may be written as

$$\underset{\sim}{u}(s,n,z,t) \quad = \quad \frac{\Phi_R}{\sqrt{q(s)U(s)I_1(s)}}\left[r_1(s,z)\left(\underset{\sim}{t} + \frac{np(s)C(s)}{q(s)}\underset{\sim}{n}\right) + ir_2(s,z)\underset{\sim}{z}\right]$$

$$\cdot \exp i\left[\psi(s,t) + \frac{\omega}{2}\frac{p(s)}{q(s)}n^2\right] \qquad (2.66)$$

where r_1 and r_2 are eigenfunctions on the ray $(s,0)$ for local Rayleigh waves.

2.5 Properties of Gaussian Beams of Seismic Surface Waves

In this section we consider our results expressed in terms of displacement vectors (2.60) and (2.66) and discuss their physical meaning. Because the forms of the final results are similar to those for acoustic waves or elastic body waves [Červený et al., 1982; Červený and Pšenčík, 1983], the common features will be mentioned briefly and the differences between them will be emphasized.

a) Paraxial ray approximation

Before proceeding to the properties of Gaussian beams, let us start with a discussion of the formulations (2.60) and (2.66) with real variables q and p. At the point on the ray n=0, (2.60) and (2.66) are the same as in the standard ray formulation [e.g., Babich et al., 1976; Woodhouse, 1974]: The phase is delayed by the integral of the slowness of phase velocity along the ray, and the amplitude is proportional to $[q(s)U(s)I_1(s)]^{-1/2}$ where q (s) is the geometrical spreading, and the non-vanishing components are normal to the ray for Love waves and tangential to the ray and vertical for Rayleigh waves. In order to obtain the spreading q(s), dynamic ray-tracing equations (2.57) must be solved along the ray numerically. Equations (2.57) are mainly determined by the second spatial derivative, normal to the ray, of the phase velocity distribution. This is why the spreading, which is mainly related to the observed amplitude, is much more sensitive to the velocity structure than the phase term, which is determined only by the integrated effect of the phase velocity along the ray path.

Equations (2.60) and (2.66) give the solutions not only along the ray

but also in the neighborhood of the central ray at $n \neq 0$. In other words, we can evaluate the wave field at points through which the ray does not pass directly. It is necessary only for the ray to pass close enough to the observation point so that the paraxial ray approximation, which we employed to derive the formulations, is valid. Formulations (2.60) and (2.66) contain the factor $\exp(i\omega p n^2/2q)$, which is exactly the same as that for two-dimensional elastic body waves (e.g., see equations (2.52) and (2.53) in Červený and Pšenčík [1983]). The term $p/q = M$ represents the second derivatives of the travel-time field in the plane perpendicular to the ray and is accurate to order n^2; this term comes from the Taylor series expansion of the eikonal equation [Červený and Hron, 1980]. The quantity $K(s) = C(s)M(s) = C\ p/q$ describes the curvature of the wavefront at the point s on the ray (see Fig. 2.3). For example, if the curvature of the ray $K(s)$ is zero, the travel time or the phase delay of the wavefield on the line perpendicular to the ray is constant, irrespective of the distance n from the ray. Physically, this wavefield corresponds to a plane wave. For another extreme case, $K = \pm\infty$ or $q=0$, the phasefront is concentrated to a point, representing a line source at that point. That is a caustic where the ray method breaks down because of the amplitude factor $[q(s)U(s)I_1(s)]^{-1/2}$.

The directions of the horizontal components of the displacement vectors are

$$\underset{\sim}{n} - nK\underset{\sim}{t} \qquad \text{and} \qquad \underset{\sim}{t} + nK\underset{\sim}{n} \tag{2.67}$$

for Love and Rayleigh waves, respectively. Since K represents the curvature of the ray, the vectors (2.67) correspond approximately to the tangent and normal, respectively, to the phase front at the point (s,n) in

the ray-centered coordinates. The additional components give the corrections for the displacement vector tangent or perpendicular to the phase front (see Fig. 2.3). Thus, it is reasonable that there is no z component in the displacement vector of Love waves and the coupling is only between horizontal components for Rayleigh waves, because the phase front is restricted to the surface.

Since we are assuming a laterally slowly-varying medium, the displacement vectors with respect to the vertical coordinate correspond to local eigenfunctions of Love ($\ell_1(s,z)$) or Rayleigh ($r_1(s,z)$ and $r_2(s,z)$) waves. These are determined by the vertical structure at the point s on the ray, assuming a laterally homogeneous model. In the paraxial ray approximation, the eigenfunctions calculated at the point (s,0) on the ray can be used even if the wavefield is estimated in the vicinity of the ray (s,n) where $n \neq 0$. It is because of the above approximation that eigenfunctions have only higher order terms with respect to n.

In summary, with the obtained formulation we can treat the wavefield of surface waves using the local eigenfunctions determined by the local vertical structure propagating two-dimensionally over the surface with a given phase velocity distribution. Therefore, the phase velocity mapped on the surface plays the central role in determining the wavefield, which gives a great computational advantage over body wave studies in which the problem involves three-dimensional heterogeneity. The depth of a laterally anomalous structure can be inferred by phase velocity maps at different periods, because phase velocity at longer periods is affected by deeper structure while relatively short-period surface waves are determined by shallow structures. Even though our final goal is to obtain three-

dimensional Earth structure, ray-tracing or construction of the wavefield is essentially based on a two-dimensional problem.

The paraxial ray approximation overcomes one major difficulty in the calculation of the wavefield by the standard ray method, the need for the ray to hit the observation point exactly, but there are still several problems which may be encountered. First, there are points where the geometrical ray spreading q(s) vanishes, producing infinite amplitudes. This is not a problem with real data, however, because of the effect of finite wavelength. Also, there are regions where the rays never penetrate, such as a shadow zone, but where some contributions are observed. These singular regions can be eliminated by introducing a better approximation, closer to full wave theory. Second, the paraxial ray method is sensitive to velocity information only along one or more ray paths which directly connect the source and the receiver, but in reality the wavefield at the receiver is affected not only by such rays but partially by contributions from the wavefield over the whole region. These difficulties may be overcome by employing the Gaussian beam synthesis method proposed by Červený et al. [1982], which requires only a small modification to the paraxial ray approximation.

b) Gaussian beam method

So far, the discussion has been based on the assumption that the variables p and q are real. In the Gaussian beam method, the quantities p and q are considered to have complex values [Červený et al., 1982]. This is allowed because we have not employed any specifications or constraints on variables p and q in deriving the formulations (2.60) and (2.66) from the elastodynamic equations by using the parabolic equations. The following procedures for the surface wave problem are exactly the same as

those for two-dimensional elastic body waves [Červený and Pšenčík, 1983], so only a brief review will be given here.

Since the dynamic ray-tracing equations (2.57) are two ordinary first-order differential equations, any general solution is expressed as a linear combination of two independent solution pairs. Following the notation of Červený et al. [1982], the general solutions may be written as

$$\begin{aligned} q(s) &= \varepsilon q_1(s) + q_2(s) \\ p(s) &= \varepsilon p_1(s) + p_2(s) \end{aligned} \tag{2.68}$$

where q_i and p_i (i=1,2) are a pair of independent solutions. These solutions are real but the general solutions become complex with the choice of a complex-valued coefficient ε. The two independent solutions are specified by the two different initial conditions at $s = s_0$:

$$q_1(s_0) = 1, \quad p_1(s_0) = 0$$

and (2.69)

$$q_2(s_0) = 0, \quad p_2(s_0) = C^{-1}(s_0) \ .$$

The first solution pair (q_1,p_1) corresponds to a plane wave-like wavefield at $s=s_0$ because of zero curvature: $K(s_0) = C(s_0)p(s_0)/q(s_0) = 0$. The second solution pair (q_2,p_2) corresponds to line source-like wavefield at $s=s_0$ because of infinite curvature; $K(s_0) = \infty$. Using the solutions based on the WKBJ method [Chapman, 1978], Madariaga [1984] advocated another form for the first solution pair if the source is located in a heterogeneous region. However, numerical tests indicate that the question of which initial conditions give the appropriate seismograms may require further investigations [e.g., Beydoun and Ben-Menahem, 1984]. In the case of surface waves, the lateral heterogeneity at the source is fairly weak

compared to the seismic body wave problem, in which the vertical velocity change may be very large. Thus, for the purpose of the present study, the initial conditions given by Červený et al. [1982], that is, (69), are used.

The complex parameter ε is chosen to satisfy the following conditions:

(i) $q(s)\neq 0$, so that there is no singularity and the amplitude remains finite at the caustics.

(ii) $\mathrm{Im}(p/q)>0$, so that the solutions of the wavefield are concentrated near the ray. This guarantees the existence of a solution characterized as a beam.

Then the exponential factors in solutions (2.60) and (2.66) may be written

$$\exp\left[i\psi(s,t) + \frac{i\omega n^2}{2C(s)} K(s) - \frac{n^2}{L^2(s)}\right] \tag{2.70}$$

where

$$K(s) = C(s)\mathrm{Re}\left[\frac{p(s)}{q(s)}\right] \quad , \quad L(s) = \left\{\frac{\omega}{2} \mathrm{Im}\left[\frac{p(s)}{q(s)}\right]\right\}^{-1/2} \tag{2.71}$$

Because of the term $\exp\left[-\frac{n^2}{L^2(s)}\right]$ and condition (ii), the amplitude of the solution decreases exponentially with increasing distance n from the central ray. Since the shape of the exponential decay of the amplitude is Gaussian, solutions with a factor such as (2.70) are called Gaussian beams. K(s) corresponds to the curvature of the phase front of the beam at the central ray, and L(s) is the effective half beam width, which depends on frequency (Fig. 2.2).

Following Červený et al. [1982], the complex parameter ε is written as

$$\varepsilon = S_0 - \frac{i\omega}{2C(s_0)} L_M^2 = S_0 - iL_0^2 \tag{2.72}$$

In a homogeneous medium the quantities S_0 and L_M have the following physical meaning. The half beam width L(s) varies hyperbolically along the ray with a minimum at a certain point $s=s_M$. L_M represents the half beam width at the point $s=s_M$ for waves with $\omega = 2\pi$ Hz and s_1 is the distance between s_M and the reference point s_0. Červený et al. [1982] showed that the conditions to form Gaussian beams are satisfied if we choose $L_M \neq 0$. The frequency-independent parameter L_0, called "beamwidth parameter" in this study, is used later on in the text.

The precise choice of s_1 and L_M is controversial. Červený et al. [1982] suggested that beams have minimum width at $s=s_0$, that is,

$$s_1 = 0 \qquad \text{and} \qquad \varepsilon = -\frac{i\omega}{2C(s_0)} L_M^2 \tag{2.73}$$

They also recommended an optimal choice of L_M so that beams have a minimum value of the half beam-width L(s) at the receiver, for convenience of computation. This means

$$L_M = \left(\frac{2C(s_0)}{\omega}\right)^{1/2} \left| \frac{q_2(s)}{q_1(s)} \right| \tag{2.74}$$

where q_1 and q_2 are evaluated at the receiver. For detailed discussions on this matter, readers are referred to Červený et al. [1982] and Appendix 2 in Nowack and Aki [1984a].

With the complex coefficient ε, q(s) never becomes zero with $L_M \neq 0$ (for the above condition (i)) because the Wronskian of the two independent solutions, $q_1(s)p_2(s)-q_2(s)p_1(s)$, is constant ($= C^{-1}(s_0)$) and this means that $q_1(s)$ and $q_2(s)$ can never be zero simultaneously. Thus the Gaussian beam is said to be regular everywhere [Červený et al., 1982].

The horizontal components of (2.60) and (2.66), $\underset{\sim}{n} - \frac{np(s)C(s)}{q(s)} \underset{\sim}{t}$ and $\underset{\sim}{t} + \frac{np(s)C(s)}{q(s)} \underset{\sim}{n}$, now have the following physical meaning. With complex

variables p(s) and q(s), the real parts of the additional component and the principal component give the normal and the tangential directions to the phase front of the Gaussian beam at (s,n) for Love and Rayleigh waves, respectively. The imaginary part of the additional component represents the phase shift introduced by the finite width of the beam.

In summary, the final formulations of Love and Rayleigh waves in a laterally slowly-varying medium are given in equations (2.60) and (2.66). While the vertical profiles of wavefields are represented by the normal modes of surface waves in a laterally homogeneous medium, the horizontal ones are almost identical to the 2-dimensional seismic body wave formulations. The minor differences are the factors, (group velocity) x (energy integral), in the amplitude term. Thus, we can naturally extend the formulation of the paraxial ray approximation into the Gaussian beam as Červený and Pšenčík [1983] obtained the Gaussian beam formulation for seismic body waves.

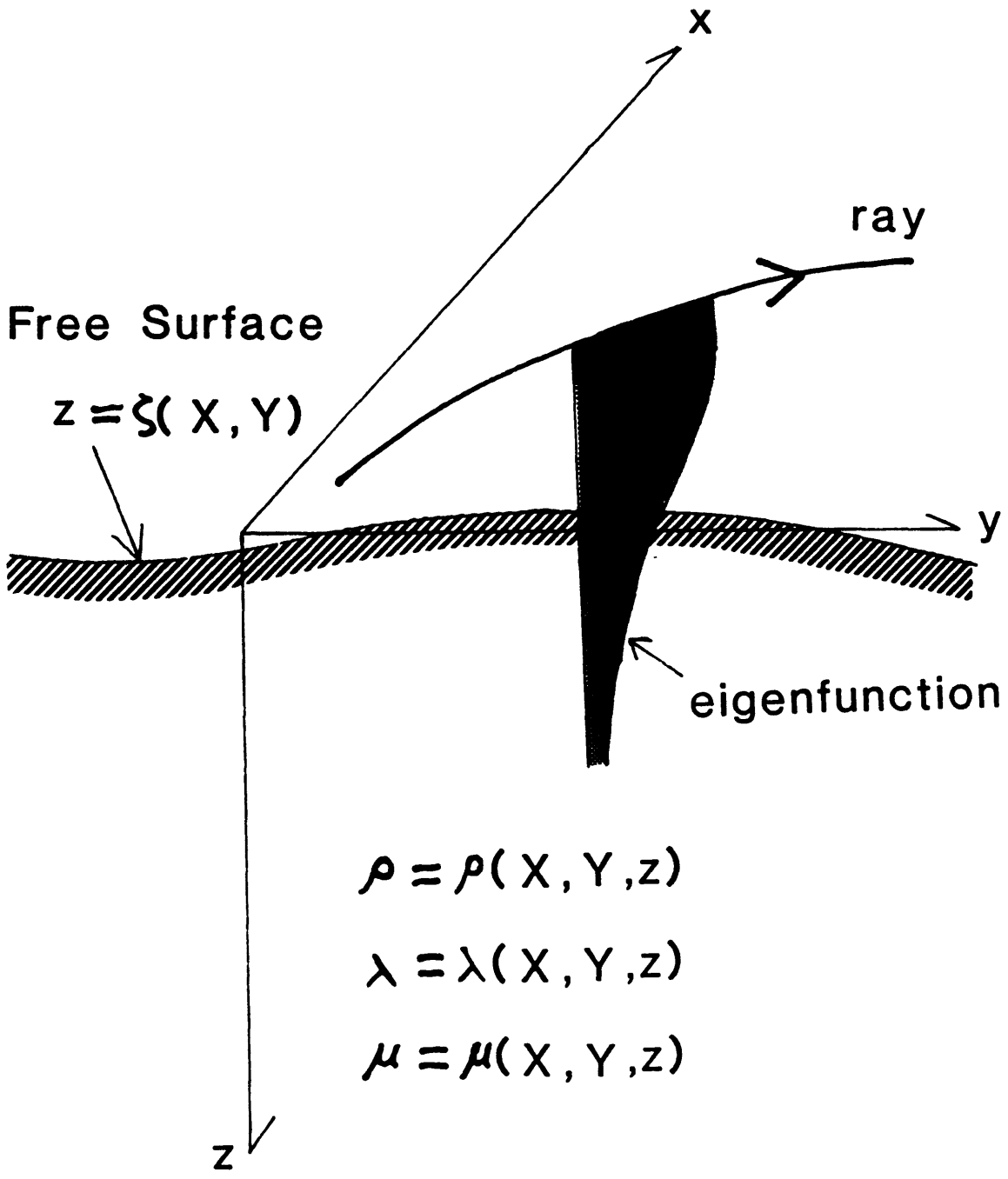

Figure 2.1 A laterally slowly-varying medium with a slightly irregular free surface in the coordinate system (x,y,z) and an eigenfunction of normal mode theory propagating along the ray. Elastic constants and density are weakly varying in the horizontal directions.

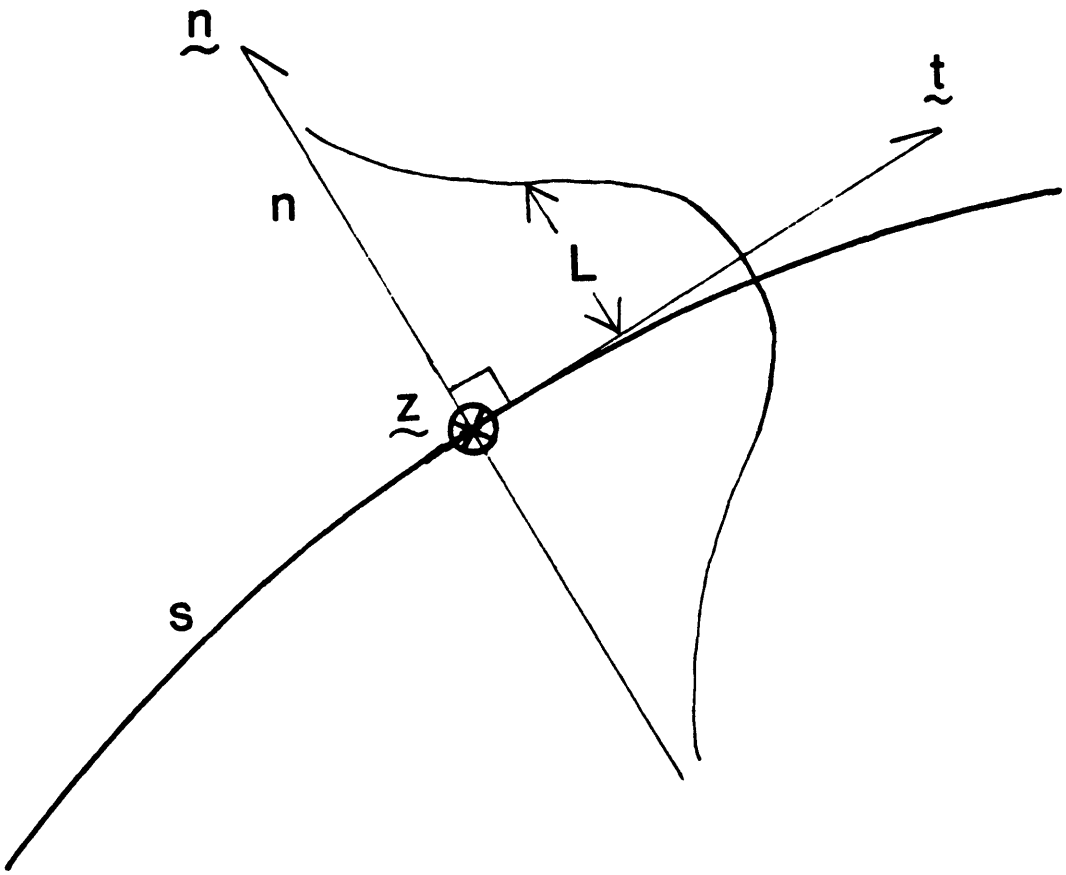

Figure 2.2 Ray-centered coordinates (s,n) and basic unit vectors $\underset{\sim}{t}$, $\underset{\sim}{n}$ and $\underset{\sim}{z}$. A Gaussian beam is shown with half beam-width L.

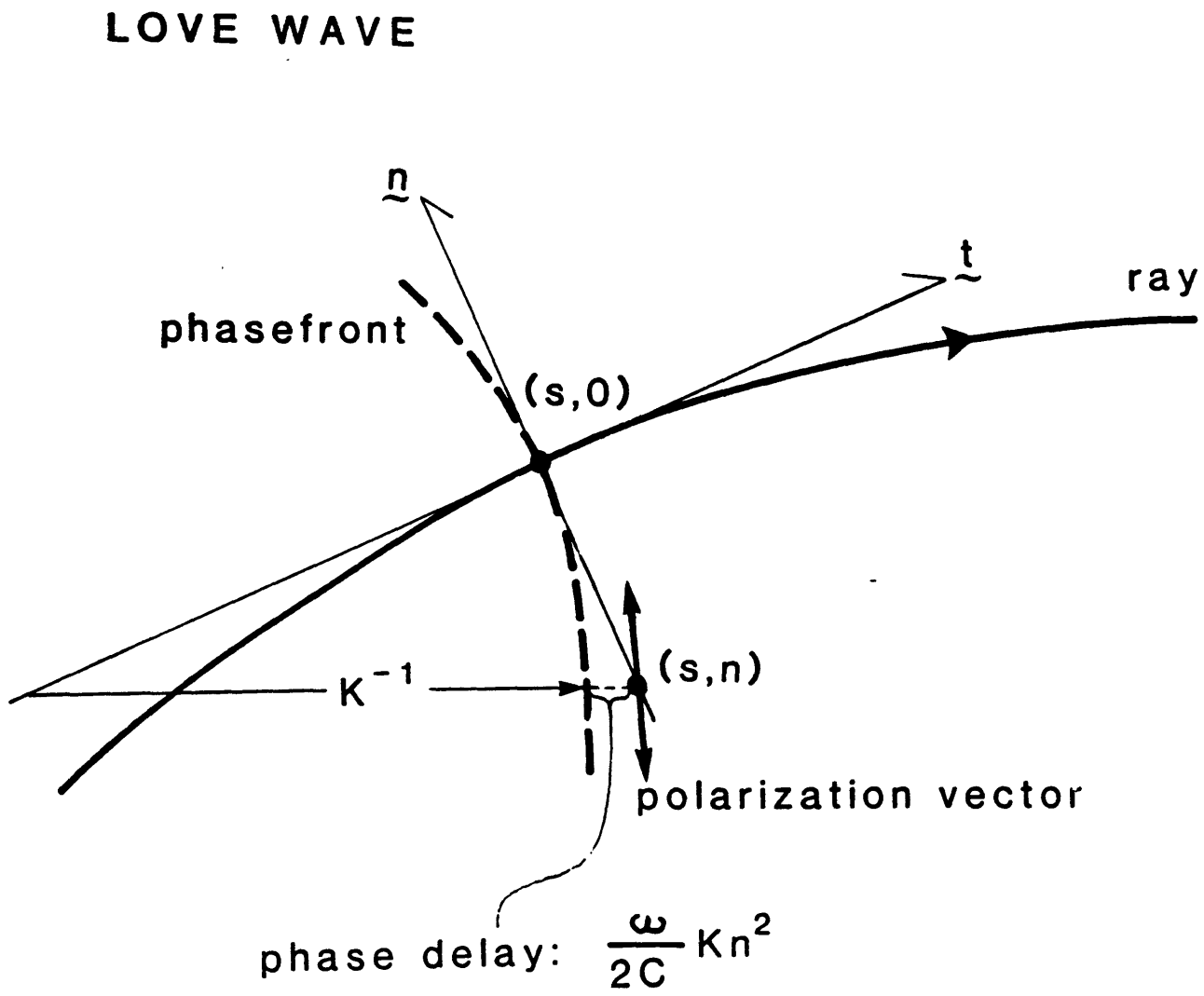

Figure 2.3. Polarization vector at the point (s,n) for Love waves. $\underset{\sim}{n}$ and $\underset{\sim}{t}$ are a principal component and an additional component, respectively. The phasefront passing through the point on the ray (s,0) is shown in the broken line whose curvature is given by $K = Cp/q$.

Chapter 3. Waveform Synthesis by the Gaussian Beam Method

In the previous chapter, we have obtained the Gaussian beam representations for surface waves in a laterally heterogeneous medium: equation (2.60) for Love waves and (2.66) for Rayleigh waves with complex variables p and q (2.68) in the dynamic ray-tracing equations. These are expressions for a single Gaussian beam. Following Červený et al. [1982], we are going to form synthetic seismograms by superposing many Gaussian beams for a given problem. In this chapter several steps which are required to obtain seismograms from many Gaussian beams will be discussed. These procedures have been already discussed in detail for acoustic or seismic body wave problems in the literature [e.g., Červený et al., 1982; Červený, 1983; Madariaga and Papadimitriou, 1984], so here we emphasize the modifications of these procedures for surface wave problems. These modifications include the ray-tracing equations (section 3.1), the effect of the sphericity of the Earth (section 3.2), the weighting factor for each Gaussian beam for realistic sources (section 3.3), and the appropriate time functions for seismograms (section 3.4).

3.1 Ray Tracing Equations for Dispersive Waves

For dispersive waves, such as surface waves, the ray tracing equations must be modified, compared to those for non-dispersive waves (body waves) because there are now two types of velocity: phase and group velocities. Thus, it may be wrong to specify the phase term of the trial form (ansatz) of the solution explicitly with time and space coordinates. Instead, we should specify the phase term in a form like equation (2.18), with the frequency and the wavenumber defined by equations (2.19):

$$\frac{\partial \psi}{\partial t}\,(\underset{\sim}{x},t) + \omega(\underset{\sim}{x},\frac{\partial \psi}{\partial \underset{\sim}{x}}) = 0 \qquad (3.1)$$

where $\omega(\underset{\sim}{x},\underset{\sim}{k})$ is angular frequency, which satisfies the local dispersion relation, and $\underset{\sim}{k}$ ($= \partial\psi/\partial\underset{\sim}{x}$) is wave number vector. This is analogous to the Hamilton-Jacobi equation in analytical mechanics. From classical mechanics [Landau and Lifshitz, 1976], we obtain the canonical equations which describe the ray tracing of surface waves. The results were given in Backus [1962] and Woodhouse [1974]. Wong and Woodhouse [1983] gave elaborate forms for the ray tracing of multi-orbit surface waves on a sphere. Here we derive compact ray tracing equations for dispersive surface waves on a flat Earth, and in the next section the effect of the sphericity of the Earth will be included.

The canonical equations for rays of general waves may be expressed as [Landau and Lifshitz, 1975]:

$$\frac{dx_i}{dt} = \frac{\partial\omega}{\partial k_i}(\underset{\sim}{x},\underset{\sim}{k}) \quad , \tag{3.2}$$

$$\frac{dk_i}{dt} = -\frac{\partial\omega}{\partial x_i}(\underset{\sim}{x},\underset{\sim}{k}) \qquad i=1,2 \tag{3.3}$$

under the constraint $d\omega/dt = 0$. This expression is valid for a general anisotropic and inhomogeneous medium and in the general coordinate system if x_i and k_i are canonical conjugate variables. We assume a transversely isotropic medium, where $\omega = \omega(\underset{\sim}{x},|\underset{\sim}{k}|)$. In this case Rayleigh and Love waves are decoupled, and the direction normal to the wave front is identical to that of energy propagation [Takeuchi and Saito, 1972]. That is, the direction of the slowness vector of the phase velocity is the same as that of the group velocity. In this case, formulations of Gaussian beams may be identical to an isotropic case. This assumption for surface waves in the real Earth may be approximately valid even though there appears to be weak horizontal anisotropy of surface waves [e.g., Forsyth, 1975, Tanimoto and Anderson, 1984].

Since $\partial\omega/\partial|\underset{\sim}{k}|$ is the group velocity U,

$$\frac{dx_i}{dt} = \frac{\partial\omega}{\partial|\underset{\sim}{k}|}\frac{\partial|\underset{\sim}{k}|}{\partial k_i} = \frac{\partial\omega}{\partial|\underset{\sim}{k}|}\frac{k_i}{|\underset{\sim}{k}|} = U\ C\ n_i \tag{3.4}$$

where $\underset{\sim}{n}$ is the slowness vector corresponding to the phase velocity C. ω is expressed as $|\underset{\sim}{k}|C(\underset{\sim}{x},|\underset{\sim}{k}|)$ in the transversely isotropic case. Since ω is constant along the ray, the equation of change of independent variables may be written as

$$\left(\frac{\partial|\underset{\sim}{k}|}{\partial x_i}\right)_{\omega,x_j} = -\left(\frac{\partial\omega}{\partial x_i}\right)_{|\underset{\sim}{k}|,x_j} \Big/ \left(\frac{\partial\omega}{\partial|\underset{\sim}{k}|}\right)_{x_i,x_j} \qquad j \neq i\ . \tag{3.5}$$

Therefore, the second ray tracing equation (19) may be written as

$$\frac{d(k_i/\omega)}{dt} = \frac{dn_i}{dt} = -\frac{1}{\omega}\left(\frac{\partial\omega}{\partial x_i}\right)_{|\underset{\sim}{k}|} = \frac{1}{\omega}\left(\frac{\partial|\underset{\sim}{k}|}{\partial x_i}\right)_{\omega}\left(\frac{\partial\omega}{\partial|\underset{\sim}{k}|}\right)_{x_i} = \frac{U}{\omega}\left(\frac{\partial|\underset{\sim}{k}|}{\partial x_i}\right)_{\omega}$$

$$= \frac{U}{\omega}\left[\frac{\partial}{\partial x_i}\left(\frac{\omega}{C}\right)\right]_{\omega} = U\left[\frac{\partial}{\partial x_i}\left(\frac{1}{C}\right)\right]_{\omega} = -\frac{U}{C^2}\frac{\partial C}{\partial x_i} \tag{3.6}$$

because $d\omega/dt=0$.

Thus, the ray tracing equations for dispersive waves are of the form

$$\frac{dx_i}{dt} = U\ C\ n_i\ , \tag{3.7}$$

$$\frac{dn_i}{dt} = -\frac{U}{C^2}\frac{\partial C}{\partial x_i}\ . \tag{3.8}$$

Defining the length of the ray path as $ds=Udt$ (i.e., the coordinate moving with the local group velocity), these equations may be expressed as

$$\frac{dx_i}{ds} = C\ n_i\ , \tag{3.9}$$

$$\frac{dn_i}{ds} = -\frac{1}{C^2}\frac{\partial C}{\partial x_i}\ . \tag{3.10}$$

These are the expressions in general coordinates. These ray tracing equations for Cartesian coordinates can be used for the spherical Earth after the coordinates and the velocity are transformed with the Mercator projection as shown later. We obtain explicit forms for the spherical Earth, following the notation and the transformation of section 13.1 of Aki and Richards [1980]. The above equations become

$$\frac{d\theta}{ds} = \frac{1}{R}\cos\zeta \ , \tag{3.11}$$

$$\frac{d\phi}{ds} = \frac{1}{R}\frac{\sin\zeta}{\sin\theta} \ , \tag{3.12}$$

$$\frac{d\zeta}{ds} = \frac{\sin\zeta}{R}\frac{1}{C}\frac{\partial C}{\partial\theta} - \frac{\cos\zeta}{R\cdot\sin\theta}\frac{1}{C}\frac{\partial C}{\partial\phi} - \frac{\sin\zeta\,\cot\theta}{R} \ . \tag{3.13}$$

where ζ now is the angle between the θ axis and the projection of the ray path into θ-ϕ plane (θ: colatitude, ϕ: longitude) with radius R. There is a discrepancy between these equations and those of Julian [1970] (shown by equation 13.9 in Aki and Richards [1980]): here ds=Udt while ds=Cdt in Julian [1970]. This is because the dispersive character of surface waves was neglected in Julian [1970]. It should be noticed that the group velocity appears in the formulation as the speed of propagation of the wave packets and can be included in the length increment along the ray, ds. Thus, for ray tracing we need only the phase velocity distribution. Also, it should be emphasized here that for a transversely isotropic medium the group velocity never appears in the frequency domain analysis except in the amplitude factor $U^{-1/2}$ in equation (2.60) or (2.66), because group velocity in the ray-tracing system related only to the travel time as shown above.

3.2 Mapping into Cartesian Coordinates from the Spherical Earth

For the real Earth, surface waves propagate not on a flat surface but on a slightly oblate spheroid. So far, we have developed the surface wave formulations for the flat Earth in a Cartesian coordinate system. We must now find a way to apply the above results to the case of a spherical Earth.

We shall introduce the Mercator projection proposed by Jobert and Jobert [1983] to transform the two-dimensional spherical coordinate system into a Cartesian coordinate system in which we can use the previous formulations. Jobert and Jobert [1983] employed the Mercator projection for the two-dimensional wave equation. However, for seismic surface wave problems an exact transformation does not exist.

The ray tracing equations in spherical coordinates are expressed as equations (3.11)-(3.13). If we use n_θ and n_ϕ given in (3.9) and (3.10) instead of the angle ζ, they may be rewritten as

$$\begin{aligned}
\frac{d\theta}{ds} &= \frac{C}{R} n_\theta \ , \\
\frac{d\phi}{ds} &= \frac{C}{R\sin\theta} n_\phi \ , \\
\frac{dn_\theta}{ds} &= \frac{C\cot\theta}{R} n_\phi^2 - \frac{1}{RC^2} \frac{\partial C}{\partial \theta} \ , \\
\frac{dn_\phi}{ds} &= - \frac{C\cot\theta}{R} n_\theta n_\phi - \frac{1}{RC^2\sin\theta} \frac{\partial C}{\partial \phi} \ .
\end{aligned} \tag{3.14}$$

Let us introduce the following new variable Θ:

$$\Theta \equiv \ln[\tan(\theta/2)] \qquad 0<\theta<\pi \tag{3.15}$$

with new phase and group velocities, V and $\overline{U}$

$$\begin{aligned}
V(\Theta,\phi) &\equiv C(\theta,\phi)/R\sin\theta \ , \\
\overline{U}(\Theta,\phi) &\equiv U(\theta,\phi)/R\sin\theta \ ,
\end{aligned} \tag{3.16}$$

Because this Mercator projection is a conformal mapping, the direction of the corresponding slowness vector $(\bar{n}_\theta, \bar{n}_\phi)$ in the θ-ϕ plane is preserved. Denoting the increment of ray as $ds' = \bar{V}dt = ds/R\sin\theta$, equations (3.14) may be written as

$$\begin{aligned}
\frac{d\theta}{ds'} &= V\,\bar{n}_\theta \,, \\
\frac{d\phi}{ds'} &= V\,\bar{n}_\phi \,, \\
\frac{d\bar{n}_\theta}{ds'} &= -\frac{1}{V^2}\frac{\partial V}{\partial \theta} \,, \\
\frac{d\bar{n}_\phi}{ds'} &= -\frac{1}{V^2}\frac{\partial V}{\partial \phi}
\end{aligned} \tag{3.17}$$

which means that we can treat equations in the coordinates θ-ϕ analogously to those in two-dimensional Cartesian coordinates. To include the effect of the ellipticity of the Earth, the transform may be modified slightly.

We briefly summarize here the formulation of the Mercator projection from spherical coordinates to Cartesian coordinates, modified by introducing the ellipticity of the Earth. For detailed discussions on conformal mappings such as the Mercator projection, readers may refer to books on mapping [e.g., Richardus and Adler, 1972].

Let us consider the ellipsoid, which is expressed in a Cartesian coordinate x, y, z (see Figure 3.1) by

$$\frac{x^2+y^2}{a^2} + \frac{z^2}{b^2} = 1 \tag{3.18}$$

where a is the equatorial radius, b is the polar radius, and a>b. P is a point on the ellipsoid. We define the distance from the center O as $\overline{OP} = r$, θ_c as the angle between the z-axis and $\overline{OP}$, called geocentric colatitude, and longitude ϕ as shown in Figure 3.1. By the relation between Cartesian and spherical coordinates (r,θ_c,ϕ), (3.18) gives the expression of $\overline{OP}$ as

$$r = \frac{ab}{\sqrt{a^2\cos^2\theta_c + b^2\sin^2\theta_c}} = \frac{b}{\sqrt{1-e^2\sin^2\theta_c}} \tag{3.19}$$

where $e = \sqrt{\frac{a^2-b^2}{a^2}}$ is the eccentricity. In geophysics, we usually use the geographic colatitude θ instead of the geocentric colatitude. θ is defined by the angle between the z-axis and the direction of PQ where Q is a point on the z-axis and $\overline{PQ}$ is the normal to the surface of the ellipsoid at point P (see Figure 3.1). We denote PQ by N; this quantity is the radius of curvature at P in the direction perpendicular to the meridian. On the plane y=0, from equation (3.18) and the geometry,

$$\frac{dz}{dx} = -\frac{b^2}{a^2}\frac{x}{z} = -\frac{b^2}{a^2}\tan\theta_c \ , \tag{3.20}$$

$$\frac{dz}{dx} = -\tan\theta$$

Therefore, the relation between θ_c and θ may be written

$$\cot\theta_c = \frac{b^2}{a^2}\cot\theta \ . \tag{3.21}$$

Also, it is easily obtained from Figure 3.1 that

$$r\sin\theta_c = N\sin\theta \tag{3.22}$$

Using (3.19), (3.21) and (3.22), $\overline{PQ}$ is expressed in terms of θ as

$$N = \frac{a^2}{\sqrt{a^2\sin^2\theta + b^2\cos^2\theta}} = \frac{a}{\sqrt{1-e^2\cos^2\theta}} \ . \tag{3.23}$$

Next, from (3.18)-(3.23) and, the radius of curvature M at P along the meridian is expressed as

$$M = \left|\frac{[1+(dz/dx)^2]^{3/2}}{d^2z/dx^2}\right| = \frac{a^2b^2}{(a^2\sin^2\theta+b^2\cos^2\theta)^{3/2}} = \frac{a(1-e^2)}{(1-e^2\cos^2\theta)^{3/2}} \tag{3.24}$$

Then, the elementary distance on the ellipsoid at P is given by

$$ds^2 = M^2 d\theta^2 + N^2 \sin^2\theta d\phi^2$$

$$= N^2 \sin^2\theta \left[\left(\frac{M d\theta}{N \sin\theta}\right)^2 + d\phi^2\right] \quad . \tag{3.25}$$

To transform into a Cartesian coordinate system, we may define the following new variable θ, where

$$d\theta = \frac{M}{N \sin\theta} d\theta = \frac{1-e^2}{(1-e^2\cos^2\theta)\sin\theta} d\theta \quad . \tag{3.26}$$

This formulation may be modified for integration as follows

$$d\theta = \frac{1-e^2\cos^2\theta-e^2\sin^2\theta}{(1-e^2\cos^2\theta)\sin\theta} d\theta$$

$$= \frac{d\theta}{\sin\theta} - \frac{e}{2} \frac{2e\sin\theta}{1-e^2\cos^2\theta} d\theta$$

$$= \frac{d\theta}{\sin\theta} - \frac{e}{2} \frac{e(1+e\cos\theta)\sin\theta+e(1-e\cos\theta)\sin\theta}{\left(\frac{1-e\cos\theta}{1+e\cos\theta}\right)(1+e\cos\theta)^2} \quad . \tag{3.27}$$

Integrating (3.27) and setting the constant of integration to be zero

$$\theta = \ln\left(\tan\frac{\theta}{2}\right) - \frac{e}{2} \ln\frac{1-e\cos\theta}{1+e\cos\theta}$$

$$= \ln\left\{\tan\frac{\theta}{2} \left(\frac{1+e\cos\theta}{1-e\cos\theta}\right)^{e/2}\right\} \quad . \tag{3.28}$$

Then, the elementary distance may be written from (3.25).

$$ds^2 = N^2 \sin^2\theta (d\theta^2+d\phi^2)$$

$$= \frac{a^2\sin^2\theta}{1-e^2\cos^2\theta} (d\theta^2+d\phi^2) \quad . \tag{3.29}$$

Thus, the system (θ,ϕ) is the two-dimensional Cartesian coordinate system. From the scaling factor in (3.29), the phase and group velocities in the ray-tracing equation may be transformed by

$$V(\theta,\phi) = \frac{\sqrt{1-e^2\cos^2\theta}}{a\sin\theta} C(\theta,\phi) \ , \quad U(\theta,\phi) = \frac{\sqrt{1-e^2\cos^2\theta}}{a\sin\theta} U(\theta,\phi) \ . \tag{3.30}$$

The formulations (3.28) and (3.30) are the Mercator projection for the ellipsoid.

Next, let us discuss the dynamic ray tracing equations (2.57). If variables are real, q corresponds to geometrical spreading along the ray. In spherical coordinates, the real variable q is

$$q = R\left[\left(\frac{\partial\theta}{\partial\zeta_0}\right)^2 + \sin^2\theta\left(\frac{\partial\phi}{\partial\zeta_0}\right)^2\right]^{1/2} \tag{3.31}$$

where ξ_0 is the azimuthal direction of the ray at the source. For the Mercator projection, the spreading $\bar{q}$ is related to that in spherical coordinates by

$$\bar{q} = \left[\left(\frac{\partial\theta}{\partial\zeta_0}\right)^2 + \left(\frac{\partial\phi}{\partial\zeta_0}\right)^2\right]^{1/2} = \left[\frac{1}{\sin^2\theta}\left(\frac{\partial\theta}{\partial\zeta_0}\right)^2 + \left(\frac{\partial\phi}{\partial\zeta_0}\right)^2\right]^{1/2} = q/R\sin\theta. \tag{3.32}$$

Similarly, for the Mercator projection p is related to that in the spherical coordinate, p, as $\bar{p} = p\, R\sin\theta$. Thus, the dynamic ray tracing equations (2.57) are expressed as

$$\begin{aligned} \frac{d\bar{q}}{ds'} &= V\,\bar{p} \ , \\ \frac{d\bar{p}}{ds'} &= -\,V^{-2}\,V_{,nn}\,\bar{q} \end{aligned} \tag{3.33}$$

where $V_{,nn}$ is the second derivative normal to the ray in θ-ϕ plane. That is, the dynamic ray tracing equations are also treated as in the two-dimensional Cartesian case in the Mercator projection. It should be noticed that the factor caused by the paraxial ray approximation, $\exp(\frac{i\omega}{2}\frac{p}{q}n^2)$, is invariant by this transformation.

For the complete formulation we must consider one more term in equation (16), $[q(s)U(s)I_1(s)]^{-1/2}$, which comes from the transport equation in ray theory. Unlike the ray tracing equations, this term is not invariant under transformation from spherical coordinates to Cartesian coordinates. Thus, we should use the variables q(s), U(s) and $I_1(s)$ directly in spherical coordinates. Since the energy integral $I_1(s)$ is related only to the vertical profile of the eigenfunctions and is normalized at the surface, there is no discrepancy between expressing it in spherical coordinates and under the Mercator mapping. The group velocity U under the Mercator mapping is easily transformed back into the spherical case by multiplying by Rsinθ as with the variable q (equation (3.32)). Thus, if we use all the variables under the Mercator mapping, the term $[q(s)U(s)I_1(s)]^{-1/2}$ in spherical coordinates should be expressed as $[q(s)U(s)I_1(s)]^{-1/2}(R\sin\theta)^{-1}$.

In summary, by means of the Mercator projection, the displacement components of surface waves on the spherical Earth may be rewritten from (2.60) or (2.66) as:

$$\underset{\sim}{u}(s,n,z,t) = \underset{\sim}{\Phi}_j \sqrt{\frac{q(s_0)U(s_0)I_1(s_0)}{q(s)U(s)I_1(s)}} \frac{\sin\theta_0}{\sin\theta_0} \underset{\sim}{r}(s,z) \exp\{i[\psi(s,t) + \frac{\omega}{2}\frac{p(s)}{q(s)} n^2]\} \tag{3.34}$$

where θ_0 and θ are the colatitudes of the points s_0 and s, respectively. $\underset{\sim}{r}(s,z) = \underset{\sim}{n}\ell_1(s,z)$ for Love waves and $r_1(s,z)\underset{\sim}{t}+ir_2(s,z)\underset{\sim}{z}$ for Rayleigh waves. $\underset{\sim}{\Phi}_j$ (j=L or R) is constant along the ray, now given at $s = s_0$.

Before concluding this section, we briefly mention another effect of the sphericity of the Earth. In the above discussions, at one specific point on the surface we have assumed that the eigenfunctions of normal modes and the wave expansions in the vicinity of the ray are based on the flat Earth model.

This means that the effect of curvature of the Earth is being neglected for small wave numbers. Under the laterally slowly-varying approximation, the irregularity of the surface is expressed as in (2.6), and this must be satisfied for the curvature of the surface of the Earth in the sense $\varepsilon<<1$. Since the wavelength of surface waves with period about 100 s is less than 500 km, the flat Earth approximation is considered to be valid for waves within this frequency range. When the period exceeds 300 s, the effect of the curvature of the surface should be carefully treated using expansions in ray-centered coordinates.

3.3 Superposition of Gaussian Beams

Since the elastodynamic equation is linear, synthetic seismograms may be constructed by superposition of Gaussian beams. We shall discuss the flat Earth model for simplicity, but it is easily extended to the spherical Earth model by the Mercator mapping as shown in the previous section.

Let us write the formulations of the basic Gaussian beam solution (3.34) for each Gaussian beam characterized by the ray parameter δ (e.g., the distance from some reference point on the initial wavefront for plane waves (Fig. 3.2) or the initial take-off angle for line sources (Fig. 3.3)), setting the weighting factor Φ_L or Φ_R equal to unity as:

$$\underset{\sim}{U}^L_\delta(s,n,z,t) = \sqrt{\frac{q(s_0)U(s_0)I_1(s_0)}{q(s)U(s)I_1(s)}}\left(\underset{\sim}{n} - \frac{np(s)C(s)}{q(s)}\,\underset{\sim}{t}\right)\ell_1(s,z) \qquad (3.35)$$

$$\exp\left\{i\left[\psi(s,t) + \frac{\omega}{2}\frac{p(s)}{q(s)}\,n^2\right]\right\}$$

for Love waves and

$$\underset{\sim}{U}^R_\delta(\delta,n,z,t) = \sqrt{\frac{q(s_0)U(s_0)I_1(s_0)}{q(s)U(s)I_1(s)}}\left[r_1(s,z)\left(\underset{\sim}{t}+\frac{np(s)C(s)}{q(s)}\underset{\sim}{n}\right)\right.$$

$$\left. + ir_2(s,z)\underset{\sim}{z}\right]\exp\left\{i\left[\psi(s,t)+\frac{\omega}{2}\frac{p(s)}{q(s)}n^2\right]\right\} \qquad (3.36)$$

for Rayleigh waves. Using the weighting factor $\Phi_L(\delta)$ or $\Phi_R(\delta)$ evaluated at the reference point, $s=s_0$, the wavefield at an arbitrary point may be written

$$\underset{\sim}{u}^j(s,n,z,t) = \int_{\delta_0}^{\delta_1} \Phi_j(\delta)\underset{\sim}{U}^j_\delta(s,n,z,t)d\delta \qquad (3.37)$$

where j denotes Love (L) or Rayleigh (R) waves. δ_0 and δ_1 give the range of ray index parameter δ. The remaining part to be determined is the weight factor $\Phi_j(\delta)$. This is given in Červený [1982] for plane waves and in Popov [1982] and Červený et al. [1982] for an acoustic line source. The weight factor for a point force in a two-dimensional elastic medium is given in Appendix C of Nowack and Aki [1984a]. Here we shall obtain it for surface waves.

a) Plane waves

If the incident wave is a plane wave, the weighting factor $\Phi_j(\delta)$ is constant because of the independence of azimuth. The results are given in Červený [1982] for acoustic waves, and they can be applied to surface waves without any modification, so only a brief review is given here.

Let us consider surface waves which propagate in laterally homogeneous media. At the reference point $s=s_0$, the waves are assumed to behave like plane waves horizontally, and the ray parameter δ is chosen as shown in Figure 3.2. The wavefield at the point (s,n) may be written:

$$\underset{\sim}{u}^j(s,n,z,t) = \int_{-\infty}^{\infty} \Phi_j(\delta)\underset{\sim}{U}^j_\delta(s,n,z,t)\,d\delta \qquad (3.38)$$

$$= \underset{\sim}{r}(s,z)e^{i\psi}$$

where $\underset{\sim}{U}^j$ is independent of n in this laterally homogeneous case. Since the weighting factors are constant in terms of δ for plane waves, $\Phi_j(\delta)=\Phi_0$ and $\delta=n$, the integration of (3.38) may be written as

$$\underset{\sim}{u}^j = \Phi_0 \sqrt{\frac{q(s_0)U(s_0)I_1(s_0)}{q(s)U(s)I_1(s)}}\, \underset{\sim}{r}\, e^{i\psi} \int_{-\infty}^{\infty} \exp\left(\frac{i\omega}{2}\frac{p(s)}{q(s)}\, n^2\right)dn \qquad (3.39)$$

$$= \Phi_0\, \underset{\sim}{r}\, e^{i\psi} \left[\frac{2\pi q(s)}{-i\omega p(s)}\right]^{1/2}$$

because q, U and I_1 are constant and $\frac{\omega}{2}\frac{p(s)}{q(s)}$ has a positive imaginary part for Gaussian beams. This result is equal to the right-hand side of (3.38) with q and p constant, so the weighting factor Φ_0 is

$$\Phi_0 = \sqrt{\frac{\omega}{2\pi i}}\ \sqrt{\frac{p(s_0)}{q(s_0)}} \qquad (3.40)$$

Finally, for a laterally heterogeneous medium, the synthetic seismograms for surface waves at the point D are expressed as

$$\underset{\sim}{u}^j(D,z,t) = \sqrt{\frac{\omega}{2\pi i}}\ \sqrt{\frac{p(s_0)}{q(s_0)}}\ \int_{-\infty}^{\infty} \underset{\sim}{U}_{\delta}^{j}(s,n,z,t)d\delta \qquad (3.41)$$

$$\simeq \sqrt{\frac{\omega}{2\pi i}}\ \sqrt{\frac{p(s_0)}{q(s_0)}}\ \sum_{\delta}\ \underset{\sim}{U}_{\delta}^{j}(s,n,z,t)\Delta\delta$$

that is, the superposition of Gaussian beams which are evaluated at the receiver D for each beam. If we take the initial conditions given in (2.69), $p(s_0) = \varepsilon p_1(s_0) + p_2(s_0) = 1/C(s_0)$ and $q(s_0) = \varepsilon$, so

$$\underset{\sim}{u}^j(D,z,t) = \sqrt{\frac{\omega}{2\pi i}}\ \frac{1}{\sqrt{C(s_0)\varepsilon}}\ \sum_{\delta}\ \underset{\sim}{U}_{\delta}^{j}(s,n,z,t)\Delta\delta \qquad (3.42)$$

b) Point sources

We now consider a more important problem, that is, the formulation of Gaussian beams for surface waves excited by a point source in a vertically heterogeneous medium with an arbitrary configuration (i.e., general representation of earthquake mechanisms). To get an excitation term, we shall assume that the source is located in a laterally homogeneous medium; we shall presume that the results are valid for a weakly heterogeneous case. As discussed by Madariaga [1984], an excitation term in heterogeneous media has not clearly been identified yet, but for surface wave excitation the laterally homogeneous assumption is usually valid because any lateral heterogeneity is likely to be weak in most cases. Like the case of plane waves, the weighting factors $\Phi_j(\delta)$ are to be obtained by the formulation for the laterally homogeneous case. Here the problem for a point source is that $\Phi_j(\delta)$ may depend on the azimuth δ, while $\Phi_j(\delta)$ is constant for a plane wave source. This means that there is a radiation pattern for a general point source.

As in appendix C of Nowack and Aki [1984a], we show that the radiation pattern of a 2-D line source is exactly the same as that for a plane wave decomposition. The Gaussian beam, which is essentially a linear combination of a line source and a plane wave source, as shown in equation (2.68), should share the same radiation pattern as these two extreme cases. For example, if we assume the beam half-width $L \to \infty$, the Gaussian beam summation (3.37) becomes a plane wave decomposition, and a direct comparison between a Gaussian beam summation and a plane wave decomposition can be made. This concept has also been emphasized by Madariaga and Papadimitriou [1985], who showed that the radiation pattern of shear dislocation sources is the same as that given by Langston and Helmberger [1975]. Similar results can be

obtained to general sources for either Love or Rayleigh waves.

Let us consider a displacement vector of a single Love mode excited by a point force F_x at (0,0,h) directed in the x_1 (i.e., x) direction. It is expressed as

$$\begin{aligned}\underset{\sim}{u}(\underset{\sim}{x},\omega) &= \frac{\ell_1(h)\ell_1(z)F_x}{8CUI_1}\left[\underset{\sim}{I}_k^{1(1)} + \underset{\sim}{I}_k^{-1(1)}\right] \\ &= \frac{i\ell_1(h)\ell_1(z)F_x}{8CUI_1}\left[-\sin\delta H_0^{(1)}(kr)\hat{\underset{\sim}{\phi}} + \frac{1}{kr}H_1^{(1)}(kr)(\cos\delta\hat{\underset{\sim}{r}}+\sin\delta\hat{\underset{\sim}{\phi}})\right]\end{aligned} \tag{3.43}$$

that is,

$$\begin{aligned}u_j(\underset{\sim}{x},\omega) = \frac{i\ell_1(h)\ell_1(z)F_x}{8CUI_1}&\left[(\delta_{j1}-\gamma_j\gamma_1)H_0^{(1)}(kr)\right. \\ &\left. + \frac{1}{kr}(2\gamma_j\gamma_1-\delta_{j1})H_1^{(1)}(kr)\right] \qquad j=1,2\end{aligned} \tag{3.44}$$

where the azimuth δ, unit vectors $\hat{\underset{\sim}{\phi}}$ and $\hat{\underset{\sim}{r}}$ and the basic vector $\underset{\sim}{I}_k^{m(1)}(r,\delta)$ are the same as given in section 7.4 of Aki and Richards [1980]. $\gamma_j = x_j/r$ are the direction cosines. Here we have used the relations of Hankel functions $H_{-1}^{(1)}(kr) = -H_1^{(1)}(kr)$ and $dH_1^{(1)}(kr)/dr = kH_0^{(1)}(kr) - H_1^{(1)}(kr)/r$. Equation (3.43) or (3.44) is the expression for displacement in terms of cylindrical waves.

In order to express these terms as a superposition of plane waves, the following relation is used for integrating the Weyl integral (an expression for spherical waves) with respect to one direction:

$$\frac{i}{4}H_0^{(1)}(kr) = \frac{1}{4\pi}\int_{-\infty}^{\infty}\frac{\exp(ik_1x_1+ik_2x_2)}{-ik_1}\,dk_2 \tag{3.45}$$

where $k_1 = +\sqrt{\frac{\omega^2}{C^2} - k_2^2}$. Differentiating both sides of (3.45) with respect to x_1 and x_j (j=1 or 2), we get

$$ik^2 \{-\gamma_j\gamma_1 H_0^{(1)}(kr) + \frac{1}{kr}(2\gamma_j\gamma_1-\delta_{j1})H_1^{(1)}(kr)\}$$

$$= -\frac{i}{\pi}\int_{-\infty}^{\infty} k_j \exp(ik_1x_1+ik_2x_2)dk_1 \qquad (3.46)$$

by using the relations for Hankel functions given above. From (3.44), (3.45) and (3.46), the displacements for Love modes may be written

$$u_j = -\frac{i\ell_1(h)\ell_1(z)F_x}{8\pi CUI_1k^2}\int_{-\infty}^{\infty}[k_j - \frac{\delta_{j1}k^2}{k_1}]\exp(ik_1x_1+ik_2x_2)dk_2 \qquad (3.47)$$
$$j=1,2$$

Since in laterally homogeneous cases $k_1 = k\cos\delta$ and $k_2 = k\sin\delta$, the displacements u_1 and u_2 are expressed as follows:

$$u_1 \simeq \int_{-\pi/2}^{\pi/2} \frac{i\ell_1(h)\ell_1(z)F_x}{8\pi CUI_1}(\sin^2\delta)\exp\{ik(x_1\cos\delta+x_2\sin\delta)\}d\delta$$

$$u_2 \simeq \int_{-\pi/2}^{\pi/2} \frac{i\ell_1(h)\ell_1(z)F_x}{8\pi CUI_1}(-\sin\delta\cos\delta)\delta\exp\{ik(x_1\cos\delta+x_2\sin\delta)\}d\delta \qquad (3.48)$$

$$u_3 \simeq 0$$

Compared to (3.44), it is clear that the azimuthally dependent terms in (3.48) for plane waves are exactly the same as those for a far-field term ($\propto H_0^{(1)}(kr)$) of a cylindrical wave representation (3.44).

Let us go back to the Gaussian beam representation of the wavefield (3.35) and (3.37) for laterally homogeneous cases:

$$\underset{\sim}{u} = \int_{-\pi/2}^{\pi/2} \Phi_L(\delta)\sqrt{\frac{q(0)}{q(s)}}\,\hat{\underset{\sim}{\phi}}\,\ell_1(z)\exp(iks + \frac{i\omega}{2}\frac{p}{q}n^2)d\delta \qquad (3.49)$$

where $q(s) = s+\varepsilon = s+S_0 - i\frac{\omega}{2C}L_M^2$ and $p/q = 1/C(s+\varepsilon)$. In order to compare this to the plane-wave representation (52), we may put $L_M\to\infty$. Then

$$\underset{\sim}{u} = \int_{-\pi/2}^{\pi/2} \Phi_L(\delta)\hat{\underset{\sim}{\phi}}\,\ell_1(z)\exp\{ik(x_1\cos\delta+x_2\sin\delta)\}d\delta \qquad (3.50)$$

Thus, from (3.48) the weight function $\Phi_L(\delta)$ for a point force F_x directed along the x-axis at a depth h is given by

$$\Phi_L(\delta) = \frac{i\ell_1(h)F_x}{8\pi CUI_1}(-\sin\delta) \tag{3.51}$$

Similarly, the displacement vectors of Gaussian beams excited by any arbitrary point force $\underset{\sim}{F} = (F_x,F_y,F_z)$ located at r=0 and z=h may be written

$$\underset{\sim}{u} = \int_{-\pi/2}^{\pi/2} \frac{i\ell_1(h)(F_y\cos\delta - F_x\sin\delta)}{8\pi C(0)U(0)I_1(0)} \underset{\sim}{U}^L_\delta(s,n,z,t)d\delta \tag{3.52}$$

for Love waves and

$$\underset{\sim}{u} = \int_{-\pi/2}^{\pi/2} \frac{\{F_z r_2(h) + i(F_x\cos\delta + F_y\sin\delta)r_1(h)\}}{8\pi C(0)U(0)I_1(0)} \underset{\sim}{U}^R_\delta(s,n,z,t)d\delta \tag{3.53}$$

for Rayleigh waves. In the laterally heterogeneous medium, we approximate the integral with respect to δ by the summation of a finite number of Gaussian beams.

For realistic earthquake sources, it is more convenient to express the formulations using moment tensor notation M_{ij} (i,j = x,y,z) [e.g., Saito, 1967; Mendiguren, 1977]. Since the radiation pattern by a single force in terms of Gaussian beams is equivalent to that for cylindrical waves, the displacement vectors for a moment tensor expressed by Gaussian beams are similar to cylindrical waves (using the same notation as in section 7.5 of Aki and Richards [1980]):

$$\underset{\sim}{u} = \frac{i}{8\pi C(0)U(0)I_1(0)} \int_{-\pi/2}^{\pi/2} \{ ik(0)\ell_1(h) [M_{xx}\sin\delta\cos\delta + M_{xy}(\sin^2\delta-\cos^2\delta)$$

$$-M_{yy}\sin\delta\cos\delta] - \frac{\ell_2(h)}{\mu(h)} [M_{xz}\sin\delta - M_{yz}\cos\delta] \} \underset{\sim}{U}^L_\delta (s,n,z,t)\, d\delta$$

$$\simeq \frac{i}{8\pi C(0)U(0)I_1(0)} \sum_\delta \{ \} \sqrt{\frac{q(0)U(0)I_1(0)}{q(s)U(s)I_1(s)}} \left(\underset{\sim}{n} - \frac{np(s)C(s)}{q(s)} \underset{\sim}{t} \right)$$

$$\cdot\ell_1(s,z)\cdot\exp[i\psi(s,t) + i\frac{\omega}{2}\frac{p(s)}{q(s)} n^2] \Delta\delta \qquad (3.54)$$

for Love waves, where $\Delta\delta$ is the interval of take-off angle better each ray and { } is the same as the braces of the first equation, and

$$\underset{\sim}{u} = \frac{1}{8\pi C(0)U(0)I_1(0)} \int_{-\pi/2}^{\pi/2} \{ k(0)r_1(h) [M_{xx}\cos^2\delta + 2M_{xy}\sin\delta\cos\delta +$$

$$M_{yy}\sin^2\delta] + \frac{-k(0)\lambda(h)r_1(h)+r_4(h)}{\lambda(h)+2\mu(h)} M_{zz} + i\frac{r_3(h)}{\mu(h)} [M_{xz}\cos\delta + M_{yz}\sin\delta] \}$$

$$\cdot\underset{\sim}{U}^R_\delta (s,n,z,t)\, d\delta$$

$$\frac{1}{8\pi C(0)U(0)I_1(0)} \sum_\delta \{ \} \sqrt{\frac{q(0)U(0)I_1(0)}{q(s)U(s)I_1(s)}}$$

$$\cdot[r_1(s,z)(\underset{\sim}{t} + \frac{np(s)C(s)}{q(s)} \underset{\sim}{n}) + ir_2(s,z)\underset{\sim}{z}] \qquad (3.55)$$

$$\cdot\exp[i\psi(s,z) + i\frac{\omega}{2}\frac{p(s)}{q(s)} n^2] \Delta\delta$$

for Rayleigh waves, where { } is the same as the braces of the first equation. Equations (3.54) and (3.55) are the general representations for synthetic seismograms of surface waves by Gaussian beams for arbitrary source configurations in a laterally heterogeneous medium (under the assumption of laterally slowly-varying media).

3.4 Wave Packets of Gaussian Beams

The final question in the synthesis of waveforms by superposition of Gaussian beams is how to express the source time function. Červený [1983] proposed that the wave-packet approach is the most efficient way to compute body wave seismograms. The wavefield excited by a source is expressed by wave-packets propagating along the corresponding ray. The seismogram at the observation point is constructed by superposing these wave-packets in the sense of Gaussian beams. Červený [1983] demonstrated using of the Gabor wavelet [Červený et al., 1977] as a source time function for each beam:

$$f(t) = \exp\{-(\frac{\omega_0 t}{\gamma})^2 - i\omega_0 t - i\phi_0\} \qquad (3.56)$$

where ω_0 is a center frequency, ϕ_0 is an initial phase and γ is a measure of the frequency bandwidth. Then the seismogram is expressed as

$$\underset{\sim}{u}(\underset{\sim}{x},t) = \sum_{i=0}^{N} \Phi(\delta_i)\underset{\sim}{g}(\underset{\sim}{x},t,\delta_i)\Delta\delta \qquad (3.57)$$

where $\underset{\sim}{g}(\underset{\sim}{x},t,\delta_i)$ is a wave packet. It is obtained as a convolution with the source time function (3.56) and the basic Gaussian beam representation (3.35) or (3.36) with an initial take-off angle δ_i. This formulation has been used by several authors [e.g., Červený, 1983; Nowack and Aki, 1984; Cormier and Spudich, 1984]. Madariaga and Papadimitriou [1984] used another kind of source time function (equation (10) in their paper)

originally proposed by Červený [1983]: a delta-function like wavepacket, following Chapman's [1978] WKBJ method but with complex Δt. They introduced this source time function in order to eliminate the singularity which appears in the basic Gaussian beam formulation in the time domain. Since seismic body waves are non-dispersive waves, that is, the velocity is constant for all frequencies, waves of all frequencies generated at the source should arrive simultaneously at the observation point. Therefore, if the source process is simple, the observed seismogram has an impulse-like shape. Since the Gaussian beam method is based in the frequency domain, synthesizing isolated impulse-like waveforms such as body waves necessitates the convolution of a wide range of frequencies into the time domain. Using either a Cerveny-type source time function (i.e., the Gabor wavelet) or a delta-function like wave packet, truncation phases in the synthetic seismograms are fairly prominent.

Now let us consider the appropriate source time functions for seismic surface waves. In contrast to body waves, surface waves are dispersive, so the observed seismograms usually show a long duration of wave trains in the time domain. For surface waves it should be noticed that the ray paths are varied for each frequency because the phase velocity distributions are generally different for each frequency. Thus, the discussions of synthetic and observed seismograms might be more appropriate in the frequency domain than in the time domain. However, for real data the amplitudes and phases in the frequency domain have large fluctuations because of contamination by noise. Instead, it may be more stable and reliable to pick real data with a small but finite range of frequencies. With such a small frequency range, the phase velocity distributions can be assumed to be the same, and we should perform ray tracing only once for the central frequency. Here we

shall use the Gabor wavelet (3.56) as a source time function. In the frequency domain the Gabor wavelet (3.56) may be written

$$F(\omega) = \frac{\gamma\sqrt{\pi}}{\omega_0} e^{-i\phi_0} \exp\{-[\frac{\gamma(\omega-\omega_0)}{2\omega_0}]^2\} \quad \omega>0 \tag{3.58}$$

The parameter γ dominates the range of sampling frequencies. To get a narrow range of frequencies, a large value of γ should be used. In order to compare the synthetic Gaussian beam seismograms with real data, the data are processed by a bandpass filter with the same characteristics as (3.58).

Since we study waves not of a single frequency but with a finite range of frequencies, there are several points to be noted. As we saw in the section on ray tracing equations for dispersive waves, the wavepacket propagates with the group velocity along the ray. On the other hand, the phase term is determined by the phase velocity. This situation is illustrated in Figure 3.4. Second, with the Gabor wavelet it may be possible to simulate the beating phenomena of surface waves due to multipath interference or side-refracted waves, because two frequency peaks close to each other produce the beating of waves. Finally, let us mention the results for different frequencies. If the frequencies are significantly different and the phase velocity mapping is no longer assumed to be the same, we may conduct ray-tracing and construct synthetic seismograms separately for each frequency band. As mentioned earlier, the variation in phase velocity mappings with frequency reflects the depths of anomalous regions. This kind of approach (i.e., making phase velocity mappings at several frequencies, specifying the depths of anomalies, and constructing three-dimensional structures) has already been employed for long-period surface waves [e.g., Nataf et al., 1984]. In practice, it is fairly difficult and time-consuming to make several phase velocity mappings. However, such phase velocity

mappings have a great advantage over strict three-dimensional modelling because they are essentially two-dimensional problems. In this study, we shall consider only a small number of frequencies. Studies utilizing many different frequencies and directed at the investigation of three-dimensional structures will be performed in future work.

To synthesize surface wave seismograms in a narrow frequency region, it remains to state the final formulations. Except for the fact that we must distinguish the group delay of the wave packet from the phase delay, the formulation is exactly the same as those for body waves. The wavepacket at the observation point for each Gaussian beam with the source time function given by (3.56) is expressed as

$$\underset{\sim}{g}(\underset{\sim}{x},t,\delta) = \left(\left|\frac{q(0)}{q(s)}\right|\frac{U(0)I_1(0)}{U(s)I_1(s)}\right)^{1/2}\underset{\sim}{r}\ \exp\left\{-\left(\frac{\omega_0 t_g}{\gamma}\right)^2 - \omega^* n^2 B - \left(\frac{\omega_0 n^2 B}{\gamma}\right)^2\right\}$$

$$\cdot \cos\left(\omega^* t_p + \phi_0 - \arg\left(\frac{q(0)}{q(s)}\right)^{1/2}\right), \qquad (3.59)$$

where $t_p = t - \int_0^s \frac{ds}{C} - \frac{n^2 K}{2}$, $t_g = t - \int_0^s \frac{ds}{U} - \frac{n^2 K}{2}$, $\omega^* = \omega_0\left(1 - \frac{2\omega_0 n^2 B}{\gamma 2}\right)$ and $B = \omega_0^{-1} L^{-2}$ (for details, see Červený, 1983). Multiplying by the weighting factors, (3.40), or those given in (3.54) or (3.55), the seismograms at the receiver are obtained by superposing a number of Gaussian beams of the form of equation (3.54).

Let us summarize how to construct synthetic seismograms of surface waves by the Gaussian beam approach. First, we must specify the model structure. Following Červený et al. [1982], the model is divided into a mesh. The phase velocities at the specific frequency are specified at mesh points, and using bicubic spline interpolation functions we may obtain

smooth values not only of phase velocity but also of the first and second spatial derivatives at any point. This is important because the second derivative of phase velocity dominates the results of dynamic ray tracing, that is, the values of p and q. In these formulations, the derivatives of group velocity at that frequency are not required, and simple linear interpolation may be sufficient. Next, we conduct ray tracings from the source using kinematic ray tracing equations (3.9) and (3.10) and we solve the dynamic ray tracing equations (2.54) to calculate the complex variables p and q. The interval of take-off angles should be small enough to sample the laterally heterogeneous structure by a finite number of rays. Then, the points on the rays which give perpendicular projections to the station are identified so that we obtain p, q, C, U, I_1 and ψ in ray-centered coordinates (s,n) for each Gaussian beam. Finally, we sum weighted Gaussian beams at points along the ray by equation (3.57) (see Figure 3.2 or 3.3).

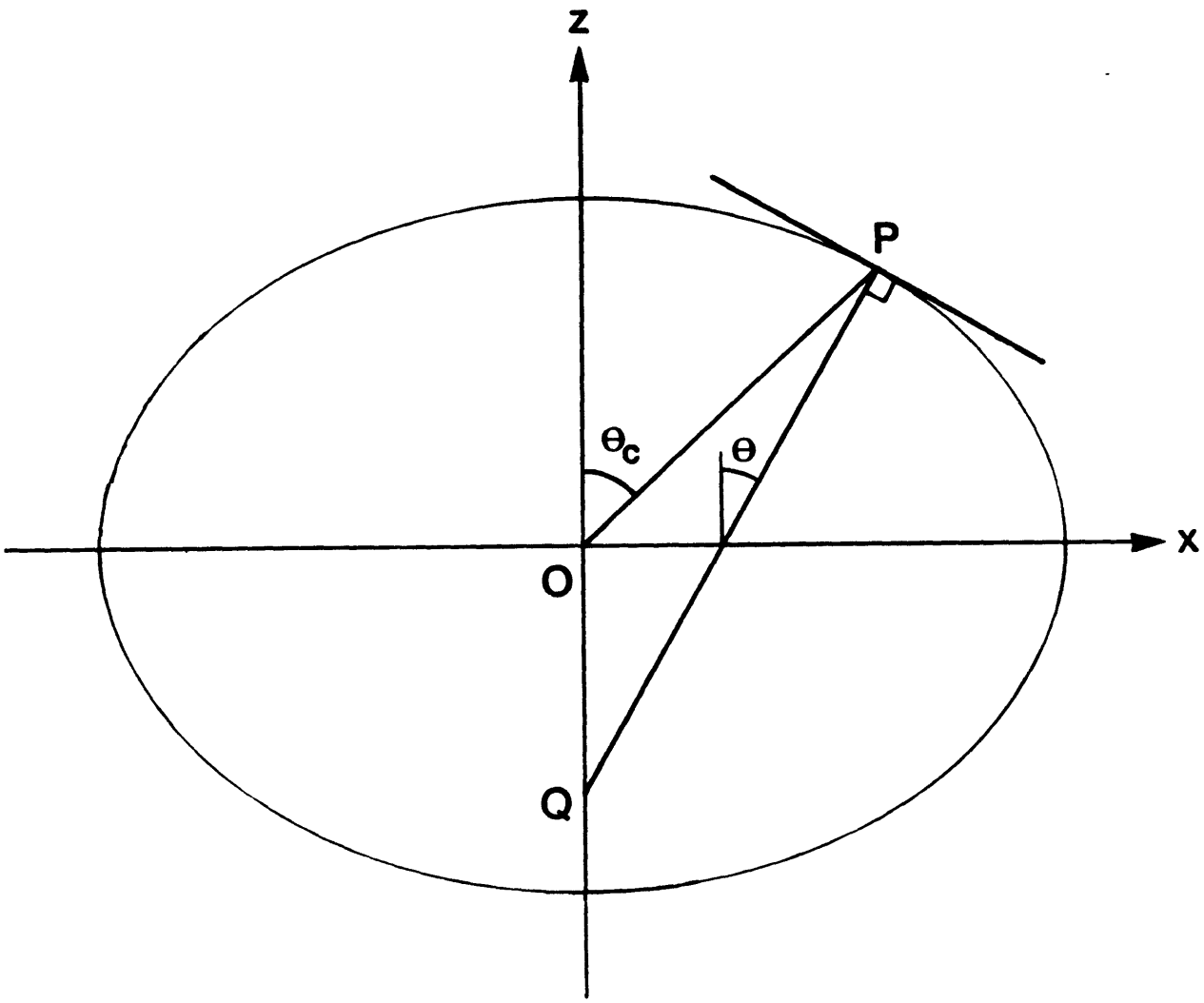

Figure 3.1. A cross section of the ellipsoidal Earth through a meridian, showing geocentric colatitude θ_c and geographic colatitude, θ.

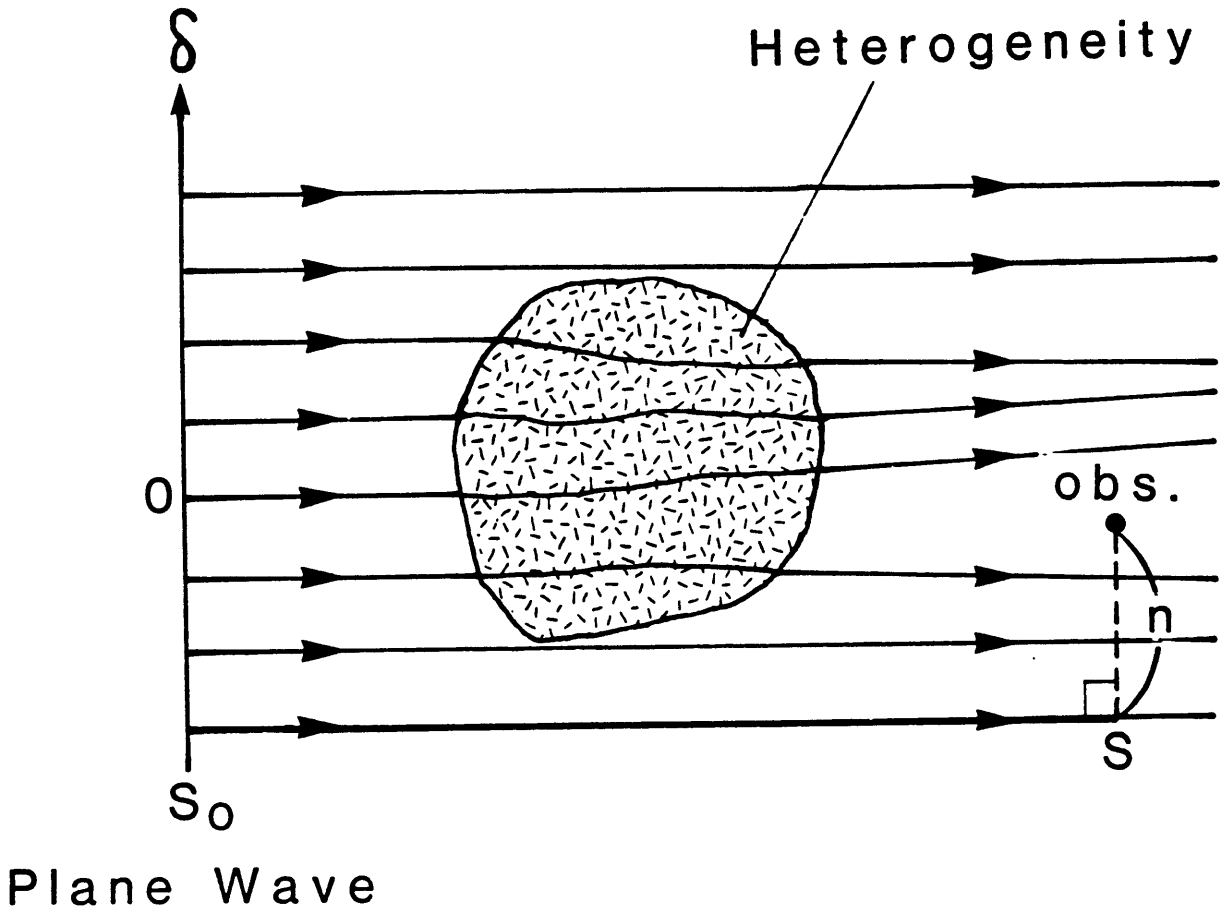

Figure 3.2. Ray centered coordinates (s,n) and ray index parameter, δ, for a plane wave source at $s=s_0$.

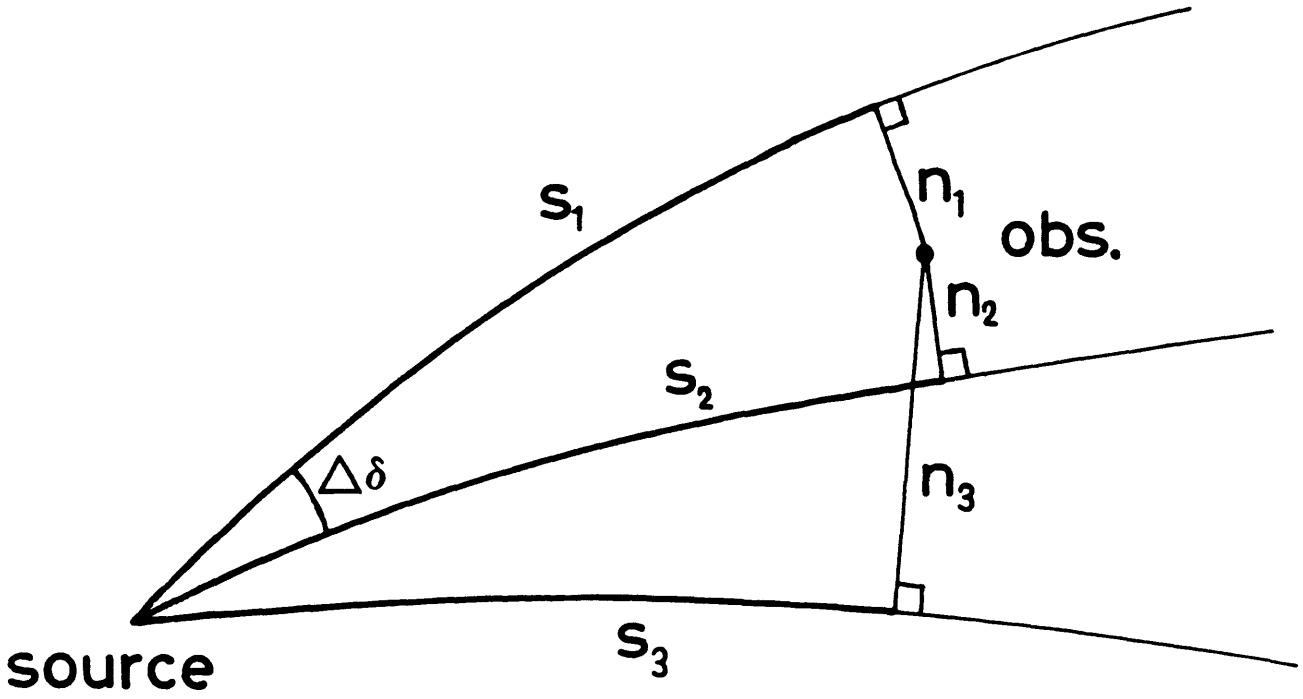

$$u(obs.) = \sum_i \Delta\delta \cdot u_i(s_i, n_i, t)$$

Figure 3.3. The points along rays where each Gaussian beam is constructed in order to produce seismograms at the station for the point source problem.

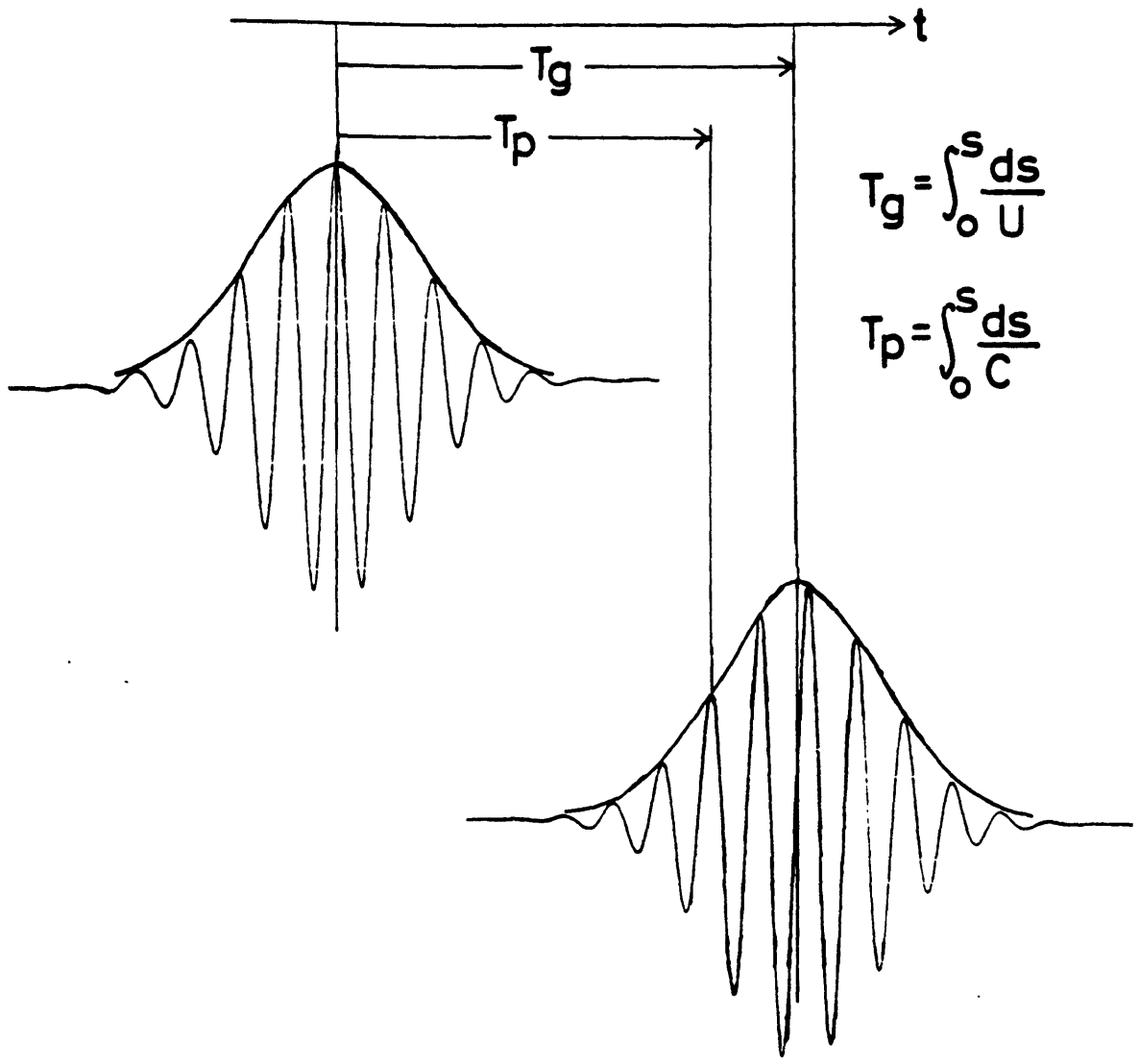

Gabor Wavelet (large $\gamma > 10$)

$$e^{-\left\{\frac{\omega_o}{\gamma}(t-T_g)\right\}^2} \cos\{\omega_o(t-T_p)+\phi_o\}$$

$$\frac{\gamma\sqrt{\pi}}{\omega_o} e^{-\left\{\frac{\gamma(\omega-\omega_o)}{2\omega_o}\right\}^2}$$

Figure 3.4. Propagation of the Gabor wavelet for dispersive waves. T_p and T_g are phase and group delays, respectively.

Chapter 4. Forward Modelling and Tests of the Synthetic Waveforms

In this chapter we show several numerical examples applying the method described in the previous chapter. Numerical tests concerning the validity and precision of the Gaussian beam method have been conducted for seismic body waves [e.g., Červený and Klimeš, 1984; Nowack and Aki, 1984a; Beydoun and Ben-Menahem, 1985]. In the Gaussian beam method there are several free parameters: for example, the range of take-off angles of the rays, the interval of take-off angles $\Delta\delta$, and the beamwidth parameter L_0. We must assign these parameters carefully in order to produce reliable and accurate results. Nowack and Aki [1984a] have checked these parameters extensively for body waves, especially the sensitivity of the choice of the parameter L_0. Their results show that the beamwidth parameter L_0 for plane wave sources should be comparable or smaller than the optimal value, $|q_2/q_1|$ evaluated at the receiver [Červený et al., 1982]. The initial beam width for line sources, on the other hand, should be comparable or larger than the optimal value to get stable results. While for seismic body waves the Gabor wavelet with a small value for γ (~4) has been used, a larger value of γ (>10) is used in this study for surface waves. In all of the examples of this study, only vertical components of Rayleigh waves are considered. Anelastic attenuation along the ray path is excluded, so that attention is paid mainly to the effect of lateral heterogeneity in velocity.

4.1 Homogeneous and Non-dispersive Model

We begin by showing ray tracing of surface waves and generation of synthetic seismograms in a laterally homogeneous spherical Earth model. A source is located at 50°N, 0°E and there is a station at a distance of 90° lying on the equator at 0°N, 90°E (Figure 4.1). Both the phase and group

velocities are set at 4.0 km/s, that is, dispersion is neglected for simplicity. The position of the minimum waist of beams, S_0, in equation (2.72) is set to zero, and the beamwidth parameter L_0 is a free parameter. The ray paths in Figure 4.1(a) are calculated by using a path-increment, ds, equal to 0.5°. In this example the initial phase and the radiation pattern of the source term are assumed to be constant with azimuth.

Because we are using the Mercator projection, the velocity field is heterogeneous in the direction of a meridian even when the model is laterally homogeneous. This example appears to be a fairly simple case, but it gives a pathological test of the Gaussian beam method. For this case, the wavefield at the source is that of a line source while it is a plane wave at the receiver. Since the wavefield is essentially expressed by a linear combination of line-source and plane-wave like equations (2.68) and (2.69), this example gives an extreme case: one set of fundamental solutions (i.e., q_2 and p_2 in (2.69)) at the source is changed to the other set (i.e., q_1 and p_1 in (2.69)) after propagation. This means that the results are expected to be quite critical to the choice of parameter ε, the beamwidth parameter L_0 in (2.72). For example, the optimal beamwidth parameter $L_0 = |q_2/q_1|^{1/2}$ evaluated at the receiver [Červený et al., 1982] should be infinite in this case because $q_1 = 0$ at the receiver even though q_1 may have a finite value in the numerical calculations (~0.01, compared to $q_2 = 1.0$ in our calculation). Nowack and Aki [1984a] discussed the choice of ε in synthesizing seismograms in the region of a caustic by the Gaussian beam method (see Example E, especially Figure 10, in their paper). In their case $q_2 = 0$ at the receiver, while $q_1 = 0$ in our "q_1-caustic" case. Nowack and Aki [1984a] showed that with large L_0 the obtained seismogram has a spurious truncation phase. Thus, we must check the choice

of ε carefully in this example. Although the proper value of ε is fairly well-constrained in this case as shown below, in general cases the value of ε is not so critical because wavefields are usually expressed by a combination of line source and plane wave source.

Figures 4.1b-f show Gaussian beam seismograms (right side) and the contribution of each beam to the seismogram for different assumed values of the beamwidth parameter L_0. Table 4.1 lists the maximum amplitude of the seismograms for different beamwidth parameters. Since we are using the Mercator projection, the unit of length is the radian in the longitudinal direction and also corrsponds to the length of a meridian between 0° and 45°N in the latitudinal direction. The exact solution is known in this case because of lateral homogeneity of the model:

$$\begin{aligned} u &= \frac{i}{4} H_0^{(1)}\left(\frac{\omega r}{C}\right) e^{-i\omega t} \\ &\simeq \frac{1}{4}\sqrt{\frac{2C}{\pi\omega r}}\, e^{i\omega r/C + i\pi/4 - i\omega t} \end{aligned} \tag{4.1}$$

Thus, the amplitude for $C = 4$ km/s, $\omega = 2\pi/40$ sec^{-1} and $r = 6378$ km is 1.260×10^{-2}, with a $\pi/4$ phase delay from the peak of the wavepacket. For any choice of beamwidth parameter L_0, the synthetic seismograms generated with large γ (=20) shown in these figures do not appear to be affected by computational or truncation errors, and spurious truncation phases are not apparent. With larger beamwidth parameter (e.g., $L_0 = 10$), there are some contributions from the beams away from the receiver, but most of them cancel out because of the phase differences from the adjacent beams. The effect of the finite aperture of rays is not obvious for seismograms with large γ because both ends of the wave packets gradually decay, thus, the truncation of the beams from each side does not clearly appear. For L_0 larger than 0.5, the amplitudes of the synthetic seismograms are close to

the exact value with an accuracy better than 1% (Table 4.1). For smaller L_0, beams are planar and wider, which may be the real property of the wavefield in this case. However, the truncation of ray aperture makes the amplitude of the seismogram at the receiver smaller than the exact value. If the aperture of rays is wider, the results are valid even with smaller L_0, so we must select a large aperture of rays. In any case the phase delay of the seismograms is correct: about $\pi/4$ from the peak of wavepacket.

In summary, the obtained seismogram is sufficiently precise if we select the beamwidth parameter L_0 to have a value close to the optimal one (~5.0) averaged over the group of rays. For large L_0, we must be careful of small truncation phases, even though this is not as obvious as in the case of elastic body waves with small γ. For small L_0, the phase is precise but the synthetic amplitude may be smaller than the real amplitude, depending on the ray aperture.

4.2 Latitude Dependence and Polar Phase Shift

In this example, the model is the same as the previous one: a homogeneous, non-dispersive and spherical Earth. The difference is that in this case the source is at the equator (0°N, 0°E) and there are receivers at a distance of 90° at different latitudes (0°~60°N,90°E) as shown in Figure 4.2a. γ is 15, but the other parameters for ray tracing are same as in the previous case. This example checks the validity of the Mercator projection.

All of the receivers are at the same distance as in the previous example, and the wavefields at the receivers are planar. Thus, the choice of the beamwidth parameter L_0 must be considered carefully. Figures 4.2b-e show seismograms at each station for different beamwidth parameters L_0. If

L_0 is larger than 0.5, all of the seismograms are similar to the exact solution with an amplitude of 0.0126 and a phase shift of -/4. For small L_0, the beamwidths at receivers are wider and the wavefield is like a plane wave, so the restricted ray aperture reduces the amplitudes of seismograms as in the previous example (see station A in Figure 4.2b). If the ray aperture is larger, we can still obtain good results at all receivers even with a smaller value of L_0. On the other hand, with L_0 close to the optimal value (~10), beamwidths at the receivers are so narrow that only a few of the closest beams contribute to the results and we cannot obtain a stable solution with the interval of take-off angle assumed here (2°). We can avoid this problem by shooting a denser packet of rays. In Figures 4.2f and g, contributions of beams with L_0 = 10 at receiver G are shown for different intervals of the take-off angle, $\Delta\delta$: 2° and 0.5°. For large $\Delta\delta$ (2°) only two beams contribute to the result and they give a wrong amplitude. For small $\Delta\delta$ (0.5°) there are contributions from a larger number of beams and the amplitude of the seismogram is accurate. Since the wavefield at the receiver is planar, the optimal beamwidth parameter $L_0 = |q_2/q_1|^{1/2}$ is large and the beamwidth at the receiver is very small; the contribution from only two or three of the closest beams are important. This causes an unstable solution because the results depend on a small change in the choice of take-off angles of individual beams. The Gaussian beam method employs a summation of a finite number of beams to approximate an integral of continuous functions of beams (3.41). A rule of thumb is that more than about five beams are needed to yield an accurate result. Thus, in this case (i.e., plane wave q_1 caustics) we should use a smaller value of L_0 so that the beams are wider at the receiver. Then we can get a stable solution. Thus, as in the previous example, a careful choice of L_0,

$\Delta\delta$ or ray aperture will yield synthetic seismograms that are reasonably accurate for stations at any latitude.

Before proceeding to other tests, we wish to mention another feature of the Gaussian beam method. Figure 4.2 shows a seismogram at a distance of 270° along the equator compared to one at 90°, station G, for the same model and with the same parameters (L_0 = 1.0). The amplitudes at the two distances should be similar because we do not include attenuation; as shown in the figure, the amplitudes are equal to an accuracy better than 1%. However, it should be noted that the phase of the seismogram at a distance of 270° is advanced by $\pi/2$ with respect to that at a distance of 90°. This is the well known "polar phase shift" of Brune et al. [1961]. The Gaussian beam method (with S_0 = 0) includes a $\pi/2$ phase shift when the trace of q (= $-iL_0q_1 + q_2$) crosses the real axis of the complex q plane (i.e., when rays pass through q_2-caustics, q_2 = 0). This phase shift is tracked in the Maslov method by Chapman and Drummond [1982] as the "KMAH index" in which passages over caustics are counted. An advantage of the Gaussian beam method with dynamic ray tracing is that there is no need for tracking and counting as long as p and q are computed continuously.

4.3 Regionalized Model for the Pacific Ocean

Next, let us consider more concrete models. The survey area for this preliminary study is the Pacific Ocean, an area whose gross structure has been studied in detail using surface waves with period 10-100 s. We can specify a fairly good initial model for the phase velocity mapping on the basis of several studies [e.g., Knopoff et al., 1970; Leeds, 1975; Forsyth, 1975; 1977; Mitchell and Yu, 1980]. As may be illustrated by two examples, there is a clear difference in the complexity of structures between continental and oceanic regions: Tréhu et al. [1981] succeeded in

retrieving the source mechanisms of earthquakes on the Mid-Atlantic Ridge by a moment-tensor inversion of Rayleigh waves of period 30-60 s with a simple regionalized phase velocity map of the Atlantic Ocean. Romanowicz [1982] showed, however, that with the same moment-tensor inversion a fairly detailed phase velocity map was required to obtain reliable focal mechanism solutions of continental earthquakes such as those in the Tibetan plateau. Thus, for the study of an oceanic region we are likely to need only a simple initial model of phase velocities for surface waves with periods greater than 20 s.

There is one serious problem in the application of the above method for surface waves: there are large lateral phase velocity gradients or rapid structural changes at ocean-continent boundaries. The Gaussian beam method is based on the assumption that the high-frequency approximation is valid everywhere. In other words, the scale of lateral heterogeneities should be much greater than the wavelength of the radiated waves [Kravtsov and Orlov, 1980]. Such an approximation may not hold in the vicinity of ocean-continent boundaries, however, where the scale of lateral heterogeneity in structure is small compared with the wavelength of the surface waves under consideration (about 60~400 km for surface waves with period between 20 and 100 s). Our method is based on the assumption that each normal mode is isolated and that there is no energy conversion from one normal mode to another [Yomogida, 1985]. However, mode-mode conversions do occur at sharp structural transitions such as ocean-continent boundaries [e.g., Boore, 1970; Bullitt and Toksöz, 1985]. There are several observations of mode-mode conversions of surface waves with periods of 20-100 s propagating across the continental margins [e.g., McGarr, 1969a, Gregersen and Alsop, 1976]. In particular, if waves are

obliquely incident on the boundary, the distortion of the wavefield is far more complicated than expected from ray theory. This phenomenon may be simulated by introducing reflection and transmission coefficients for the surface waves. Here, we are going to avoid this difficulty by choosing stations near a coastline and satisfying the criterion that rays cross ocean-continent boundaries at nearly normal incidence.

We also need reliable source parameters (focal mechanisms) of earthquakes in real data cases, as expressed by equation (3.54) or (3.55). Because we are going to use the waveform to investigate lateral structure, initial phases or seismic moment tensors must be known fairly accurately. However, if we avoid stations along paths with azimuths at the source within ~10° of nodal directions for surface wave radiation patterns the effect of uncertainty in the focal mechanism on calculated seismograms is not critical to our discussion. This is because the initial phases and magnitudes of radiated amplitudes in the directions of the stations are then smoothly varying function of azimuth.

We calculated synthetic seismograms of surface waves at coastal stations for the Pacific Ocean sources using the Gaussian beam method and starting with the regionalized model of Forsyth [1975, 1977] for Rayleigh waves. Although Forsyth inverted his data by dividing the Pacific Ocean into several discrete regions with oceanic lithosphere in different age ranges, we allow the phase velocity to change gradually and continuously as a function of lithospheric age (Figure 4.3). Even though it is an extrapolation of the previously obtained models, there is a strong heterogeneity (low velocity) in the vicinity of spreading ridges such as the East Pacific Rise or the Galapagos spreading center in this model. The ages of oceanic lithosphere are taken from Sclater et al. [1981]. The

phase velocities in the continents followed from Forsyth [1975]. The phase velocities are specified at 5°x5° grid points except near ridges, where the grid is 2.5°x2.5°.

Figure 4.4 shows ray tracing results (40 s) for an event on August 7, 1972, in the Tonga region (16.7°S, 172.1°E, M_S=6.0, thrust fault with nearly N-S strike). The length of the ray-path increment ds is 0.5°, and the interval of initial take-off angles, $\Delta\delta$, is 2°. There are no peculiar distortions of ray paths, and this model does not predict any strong amplitude anomalies at the stations near the western coast of the Americas. This contrasts sharply with the results of Patton [1980], who performed ray tracing for Rayleigh waves of the same period (40 s) for a regionalized model of the Eurasian continent with an event in the Pamir Mountains which showed large distortions of ray paths along some azimuths. The distortions in Rayleigh waves for paths across Eurasia are due to strong lateral heterogeneities such as the low-velocity region beneath the Tibetan plateau. For 40-s Rayleigh waves, the phase velocity across the Tibetan plateau is more than 15% lower than that associated with normal continental crust, while the maximum velocity difference in the Pacific Ocean (i.e., between the youngest and the oldest lithosphere) is only 5% with the resolution of surface waves at this period. Also, because the low-velocity region near the ridges is fairly narrow compared with the Tibetan Plateau and variations in phase velocity vary smoothly with age, rays are less distorted.

In Figures 4.4b,c and d, synthetic seismograms are shown at each of the five WWSSN stations in Figure 4.4a; alternative seismograms are depicted for several choices of L_0 and S_0. The dependence of the results on the beam parameters L_0 and S_0 is not strong, as long as we use a

beamwidth parameter L_0 close to an averaged optimal value for these laterally heterogeneous cases. For small L_0, the beams are wide at the receiver, and the waveforms are stable but have small amplitudes (e.g., at College in Figure 4.4b) because of the limitation of the range of take-off angles for ray shooting. Figure 4.5a exhibits the detailed ray configuration for the station, COL. Ray-tracing is performed with $\Delta\delta$ = 0.2°. Figures 4.5b-d represent contributions of all the beams to the final seismogram shown in the right of each figure. The effect of varying L_0 on the results, as discussed above, is clearly observed in these figures. Moreover, let us consider the effect of the location of S_0. As discussed in Červený et al. [1982], S_0 corresponds to the place where the beamwidth is a minimum for a homogeneous medium. Since stations must be located in the first Fresnel zone [Kravtsov and Orlov, 1980], Nowack and Aki [1984a] showed in example G of their paper that S_0 should be selected to make the beam the narrowest in the region where the scale length of heterogeneity is the shortest. This is because the heterogeneity must be smooth over the beam width for the paraxial approximation to be valid. For the present source-receiver pair, the main heterogeneity exists near coastlines and solutions may be more stable if we set S_0 to be about 1 or 1.5. If we set S_0 = 1.5, the maximum amplitude of the synthetic seismograms is not as dependent on the choice of L_0 as in the case with S_0 = 0 (Table 4.2). Thus, an appropriate choice of S_0 is also important to obtain stable results with the Gaussian beam method.

In an oceanic area, the largest lateral heterogeneity is expected to be contributed by a region of low velocity along oceanic ridges. In the Pacific Ocean such areas correspond to the East Pacific Rise and the Galapagos spreading center. If the source is located in these regions, the

wavefield may be strongly distorted, similar to the case for the event in the Pamir Mountains given by Patton [1980]. Figure 4.6 shows the results of ray tracing and construction of synthetic seismograms at several stations for a hypothetical event just south of the Galapagos spreading center. Compared to the previous example, the rays are severely distorted and large amplitude fluctuations are predicted to be present. The rays passing through ocean-continent boundaries (e.g., west coast of North America) show large deviations from a great circle path because of large variations in phase velocity across these boundaries, as shown in examples by Sobel and von Seggern [1978]. However, as noted above, the applicability of the present method to regions of rapid change in phase velocity is questionable. Therefore, we should avoid the use of a station like Matsushiro (MAT). On the other hand, we may deal with the distortions of the rays occurring within oceanic regions, such as the rays passing through the Galapagos Spreading Center. Because there are fairly large low velocity regions (5% lower in phase velocity) along the ridge, rays encountering these low velocity regions are distorted, and focusing phenomena may be observed to the south of station GUA. Rays not penetrating these regions but passing parallel to them are almost straight. Another example of ray distortion is seen near the back-arc basin behind the Tonga-Kermadec trench (Lau Basin). Since the oceanic lithosphere near the trench is fairly old, the phase velocity is high. In contrast, the Lau Basin is now actively spreading [e.g., Weissel, 1977]. Phase velocities at periods near 40 s are expected to be fairly low, similar to regions near oceanic ridges. Therefore, rays passing through this region are disturbed. Synthetic seismograms at several WWSSN stations with different beam parameters (Figures 4.6b and c) show that the results are not particularly

dependent on these parameters. Compared to the previous example, there are large differences in amplitude. At GUA the amplitude is nearly twice as large as that at RAB or HNR because of focusing. Small truncation phases are observed in some seismograms. These are caused by the finite interval of ray take-off angle and the limited range of ray aperture. This example implies that even in an oceanic area there is a possibility that large amplitude anomalies may be observed in some specific station-receiver pairs.

4.4 Sensitivity of Amplitude Anomalies: A Hot Spot Example

Since amplitude anomalies are determined essentially by the second spatial derivative of the phase velocity in the direction perpendicular to the rays (see equations 2.57), amplitude information is expected to be more sensitive to short-wavelength lateral heterogeneity than phase information. Here, we investigate such sensitivity problems with a simple model, based on the same regionalized model of the Pacific Ocean as in the previous example, but with the addition of a low velocity area around the Hawaiian hot spot [e.g., Morgan, 1971].

The low velocity anomaly is assumed to be circular and centered at the island of Hawaiia. Phase velocities within the anomaly are assumed to vary according to a two-dimensional Gaussian distribution with a half width of 5°. The maximum velocity difference from the surrounding region is taken to be variable (-0.05, -0.1 and -0.2 km/s) in order to check the sensitivity of the method. Using conventional techniques (only phase information) it is generally impossible to detect anomalies of such small spatial extent using surface waves and the present network of stations.

Figures 4.7, 4.8 and 4.9 show the results of ray tracing and synthetic seismograms at several stations for the above three models. Because of the

lower phase velocities around the Hawaiian Islands, rays passing through this region are curved toward the center of the low velocity area. Thus, rays are focused near Vancouver Island while rays are sparse near the stations Longmire and Corvallis. Since no stations are located near the great circle connecting the station and the heterogeneity, conventional phase velocity methods cannot resolve such a heterogeneity without extremely dense path coverages. Figure 4.10 shows the variation of Rayleigh wave amplitude predicted at Corvallis as a function of the maximum anomaly at the Hawaiian Islands. As the anomaly becomes larger, the amplitude decreases. Amplitudes at the stations Longmire and Corvallis are reduced by half for models including a low velocity region with a maximum phase velocity difference of -0.2 km/s or more, compared with a model without such a heterogeneity. On the other hand, the phase terms of the synthetic seismograms are nearly constant (differing by less than 1 s for 40-s surface waves) for these three models.

4.5 Large Amplitude Anomalies and Validity of the Method

Finally, we compare real data and synthetic seismograms. We attempt to synthesize seismograms from the earthquake of August 7, 1972, off the Tonga trench at the location used in the previous models. This earthquake is associated with the bending of the lithospheric slab, and the focal mechanism is considered to be quite simple on the basis of body wave analysis [Forsyth, 1982]. However, we found a large amplitude anomaly in Rayleigh waves at stations Longmire and Corvallis (see Figure 4.11). The amplitude of 20 s Rayleigh waves at Corvallis, which is located less than 2° from Longmire, is larger by a factor of four while the amplitudes are almost identical for 40 s Rayleigh waves. The nodes of the radiation pattern for Rayleigh waves are directed nearly north-south, and the data at

other stations show no significant amplitude anomalies. Therefore, the complexity of the source is likely to be a negligible contribution. This is similar to the observations by McGarr [1969b] (Fig. 1.1). Following McGarr [1969b], we presume that a low velocity area centered on the Hawaiian Islands is responsible and we attempt to reproduce the amplitude anomalies using Gaussian beams.

Waves of period 20 s show clear beating at Longmire (Fig. 4.11). Pilant and Knopoff [1964] suggested several reasons for the interference of dispersive wave trains. Among them, we test the possibility that trains "have travelled over paths of slightly different lengths", as they described. In the previous synthetic examples (Figures 4.7-4.9) for 40 s, large amplitude differences between the stations Longmire and Corvallis were not observed with phase velocity anomalies as large as -0.2 km/s in the Hawaiian Islands. For 20 s, we further reduced the velocity in this region and checked the amplitude variations at both stations. Figures 4.12a and b show the results of ray tracing and synthesizing seismograms at several stations for a model with a maximum phase velocity difference of -0.4 km/s. Since rays passing the anomalous regions are distorted in a complicated manner, amplitude anomalies must be treated carefully in these examples. We found that the synthetic seismograms exhibited a large difference in amplitude between Longmire and Corvallis, but in the opposite sense from the observed data.

The amplitude pattern of Figure 4.12 arises from a combination of focusing by the velocity anomaly in Hawaii and the effect of the low velocity area along the Juan de Fuca Ridge. Our velocity model (Figure 4.3) does allow a fairly large ambiguity in velocity in young oceanic lithosphere (ages less than 10 m.y.) because conventional pure-path

analysis cannot resolve such narrow regions. Thus, we also considered a model in which the area around the Juan de Fuca Ridge has a phase velocity equal to that of oceanic lithosphere 10 m.y. old. Figures 4.13a and b show the ray tracing and the synthetic seismograms for this case. Without strong velocity anomalies along the Juan de Fuca Ridge, rays are defocused around Longmire and the amplitude at Longmire is half that at Corvallis, more nearly consistent with the observations. Although this model is neither unique nor correct, this example clearly shows that a slight change of model can give a large variation in relative amplitudes and demonstrates the sensitivity of the present method.

Since these examples concern wavefields that are fairly disturbed, the validity of the present method might be suspect. Thus, it is important to check the above results. To do so, we employed reciprocal seismograms: exchanging the source and the receiver and comparing them to the original ones. The results of reciprocal ray tracing and seismogram synthesis for the model in Figure 4.13 at stations Longmire and Corvallis are shown in Figures 4.14 and 4.15, respectively. The amplitude of the reciprocal seismogram for Corvallis (Figure 4.15) is larger than that for Longmire (Figure 4.14) by a factor of two, similar to the seismograms in Figure 4.13. Therefore, we consider these results to be reliable with the present choice of beam parameters. The contributions from each beam in Figures 4.14 and 4.15 show that the final seismograms are determined mainly by direct waves and side-refracted waves produced by the low velocity areas. The large differences in amplitude between these two stations may be caused by interference between the above two wavetrains. If the phases of the two waves are matched, amplitudes are enlarged. On the other hand, the amplitude and energy are reduced if the phase difference between the two

wave trains is nearly an odd multiple of π.

So far we have concentrated on the effects of the phase velocity distribution. We now consider the importance of the group velocity distribution. We alter the model of Figure 4.13 by adding lower values of group velocities around the Hawaiian Islands as was done for phase velocities. We take the largest difference in group velocity from the surrounding area to be -0.4 km/s. Figures 4.16a and b show the results of ray tracing and seismogram synthesis. Because group velocity is not included in the formulations of ray tracing, the ray paths are exactly the same as those in Figure 4.13a. The amplitude factors $[U(s_0)/U(s)]^{1/2}$ in equation (3.34) are evaluated only at the source and the receiver, not along the path, so the group velocity is included in the results only as the propagation speed of the wave packets (see Figure 3.4). Comparing Figure 4.16b with Figure 4.13b, we see that the only difference is that the peak of the wave packet is slightly shifted by the low group velocity along the rays. However, the amplitudes and phases are almost identical. Thus, we conclude that the group velocity distribution is not as important as the phase velocity distribution in the synthesis of the final waveforms.

In summary, the methods developed in Chapters 2 and 3 are useful to synthesize surface wave seismograms in a laterally heterogeneous Earth. The main problem is the choice of beam parameters, especially the beam-width parameter L_0. However, in most cases we can get satisfactory results with an intuitively appropriate range of L_0, for example, by assuming the beamwidth at the receiver does not exceed the ray apertures. In the examples for the Pacific Ocean, the results indicate the good sensitivity of the present method to the details of lateral heterogeneity.

Table 4.1. Effect of initial beam-width L_0 on synthetic seismograms for the example of Figure 4.1

L_0	Max. Amp. ($x10^{-2}$)	Error (%)
0.1	0.4255	- 66.2
0.3	1.0187	- 19.2
0.5	1.2270	- 2.6
0.8	1.2669	+ 0.5
1.0	1.2651	+ 0.4
3.0	1.2601	- 0.0
5.0	1.2587	- 0.1
10.0	1.2568	- 0.3
exact	1.2604	———

Table 4.2. Effect of S_0 on seismograms for a laterally heterogeneous model (Figure 4.5).

L_0	Max. Amp. at COL ($x10^{-2}$)	
	$S_0 = 0$	$S_0 = 1.5$
1.0	0.966	1.519
2.0	1.608	1.678
5.0	1.910	1.697

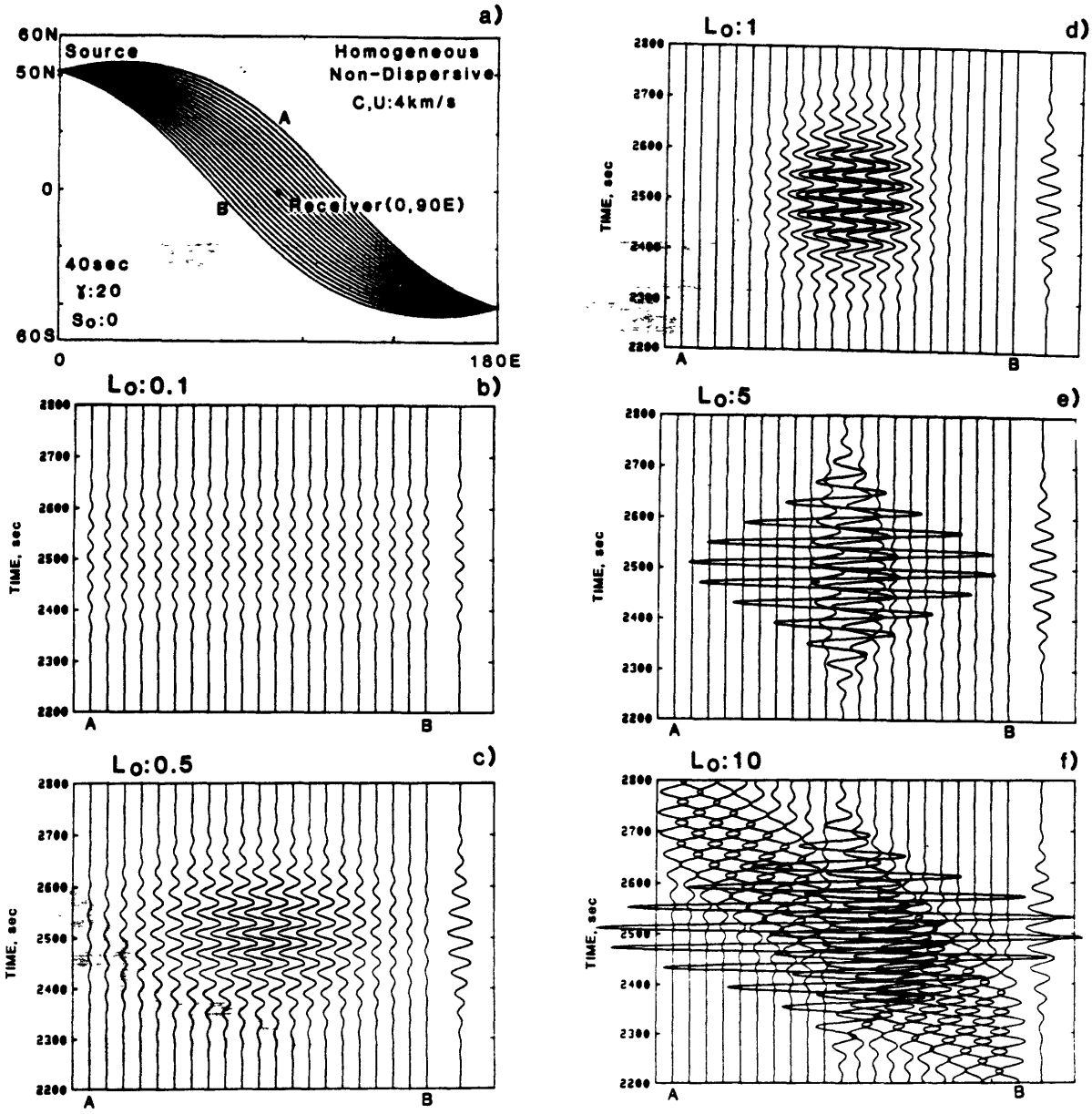

Figure 4.1. a) Ray tracing for a laterally homogeneous, non-dispersive, non-attenuating and spherical Earth model (C = U = 4 km/s). Source and receiver (o) are located at 50°N and 0°E and at 0°N and 90°E, respectively. The interval of initial take-off angles of rays, $\Delta\delta$, is 2°. b)-f) Contributions of each beam (A to B) to the synthetic seismogram (on the right-hand side) are shown for different initial beam half-widths, L_0 (0.1, 0.5, 5 and 10, respectively). The period is 40 s, γ is 20, and S_0 is 0 for all figures. Overall, the final results are not so sensitive to the choice of L_0.

Figure 4.2. a) Ray tracing for the same model as in Figure 4.1. Source is at 0°N and 0°E and receivers are located along 90°E and 60°N to 0° at latitude intervals of 10°. $\Delta\delta$ is 2°. b)-e) Synthetic seismograms at the seven stations for different assumed values of L_0 (0.1, 0.5, 1 and 5, respectively). The period is 40 s, γ is 15, and S_0 is 0 for all seismograms. The seismograms at various latitudes are almost similar and this shows the validity of the Mercator projection. f)-g) Effect of $\Delta\delta$ (2° and 0.5°, respectively) on synthetic seismograms when the beam widths are narrow in the vicinity of the receiver. S_0 is 0, and L_0 is 10. Contributions of each beam to the synthetic seismograms (right-hand side) are shown. The scales are the same for both two figures. h) Comparison of synthetic seismograms for stations at 0°N, 90°E and 0°N, 270°E. S_0 is 0, and L_0 is 1. Note the $\pi/2$ phase difference between the two seismograms.

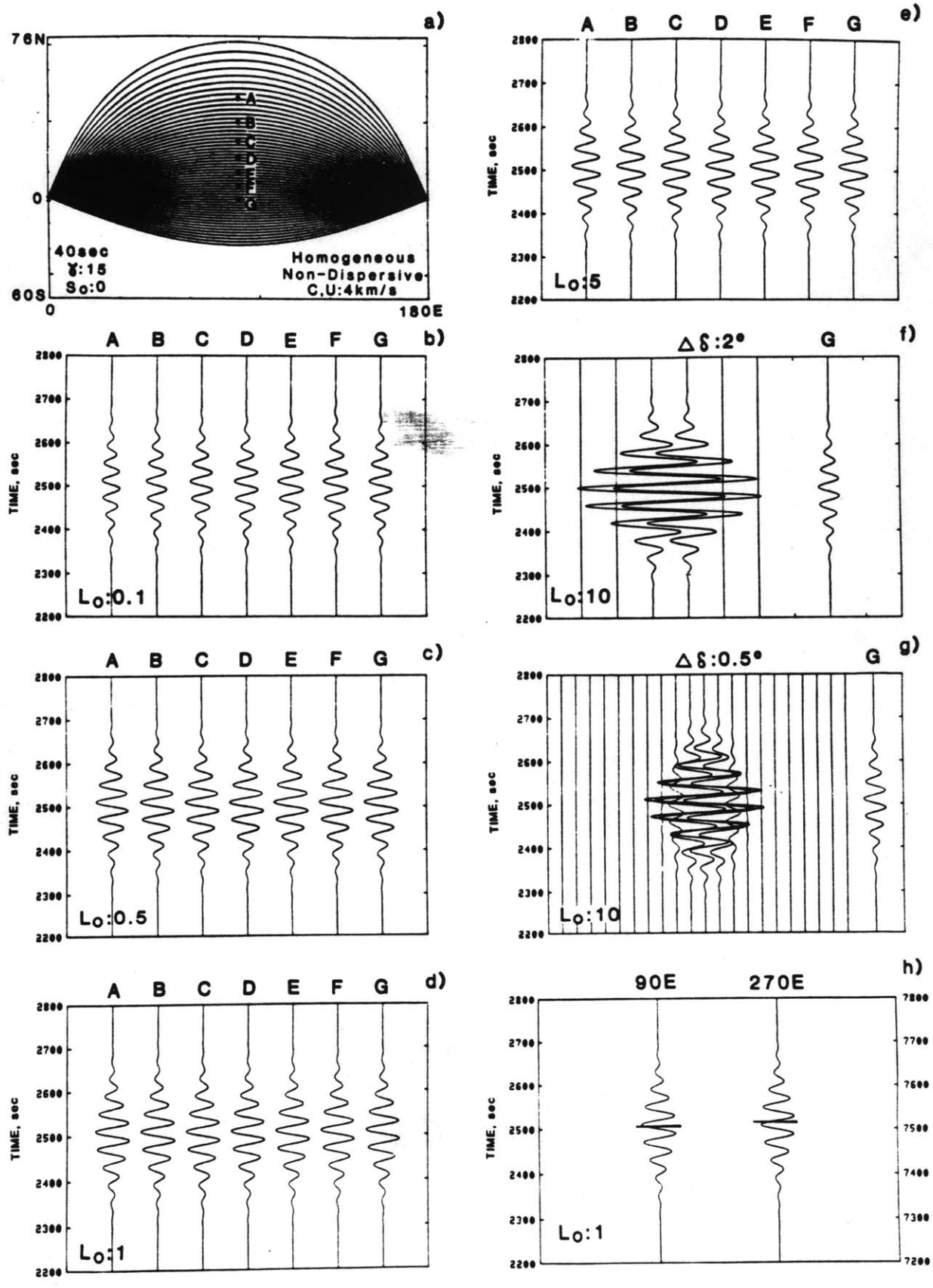
a)
76N
0
60S
0
180E
A
B
C
D
E
F
G
40sec
γ:15
So:0
Homogeneous
Non-Dispersive
C,U:4km/s
b)
A B C D E F G
TIME, sec
Lo:0.1
c)
A B C D E F G
Lo:0.5
d)
A B C D E F G
Lo:1
e)
A B C D E F G
Lo:5
f)
Δδ:2°
G
Lo:10
g)
Δδ:0.5°
G
Lo:10
h)
90E
270E
Lo:1

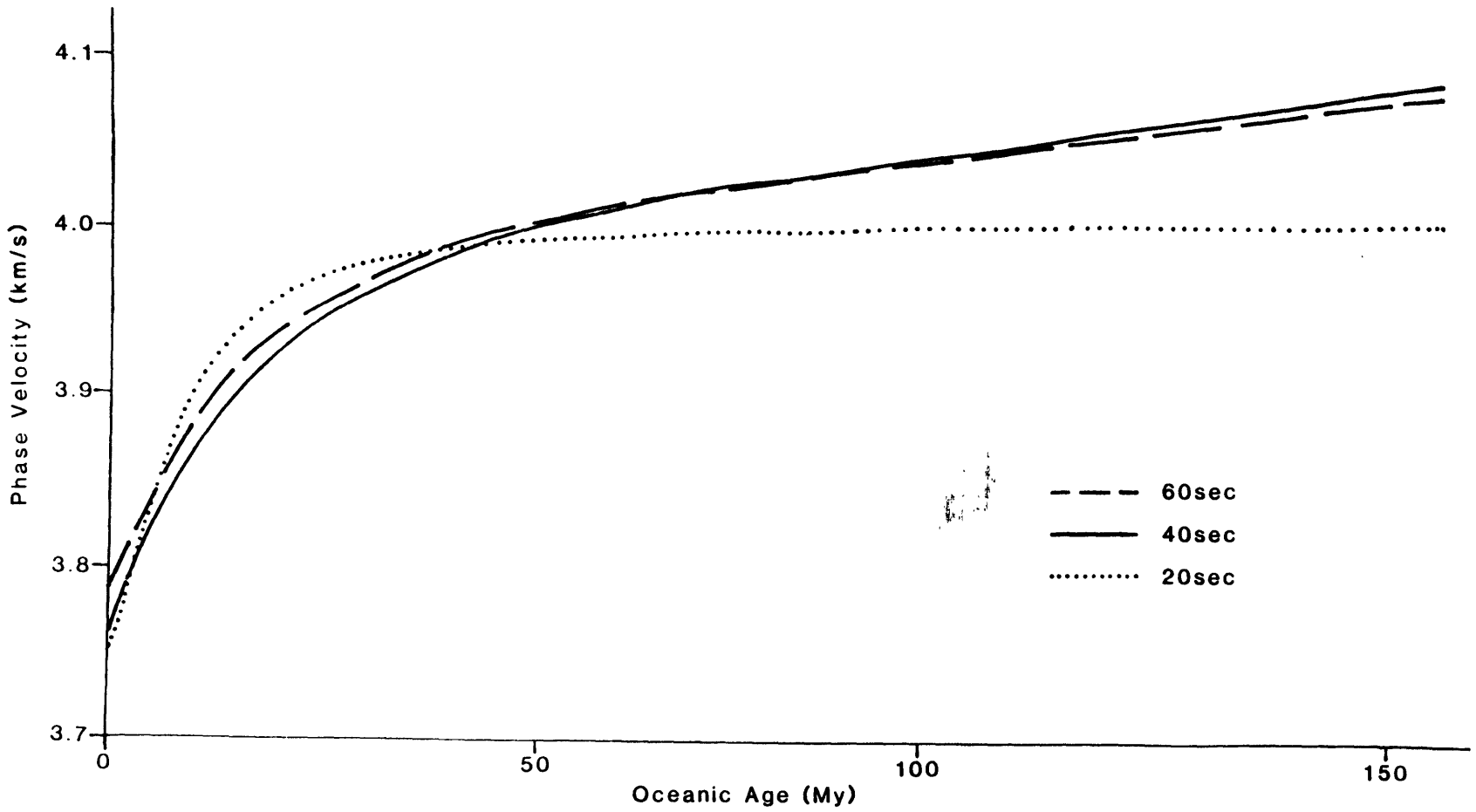

Figure 4.3. Phase velocity of Rayleigh waves versus age of oceanic lithosphere, from the data of Forsyth [1975, 1977]. The dotted, solid and broken lines are for periods of 20, 40 and 60 s, respectively. The large variations exist in the young oceans.

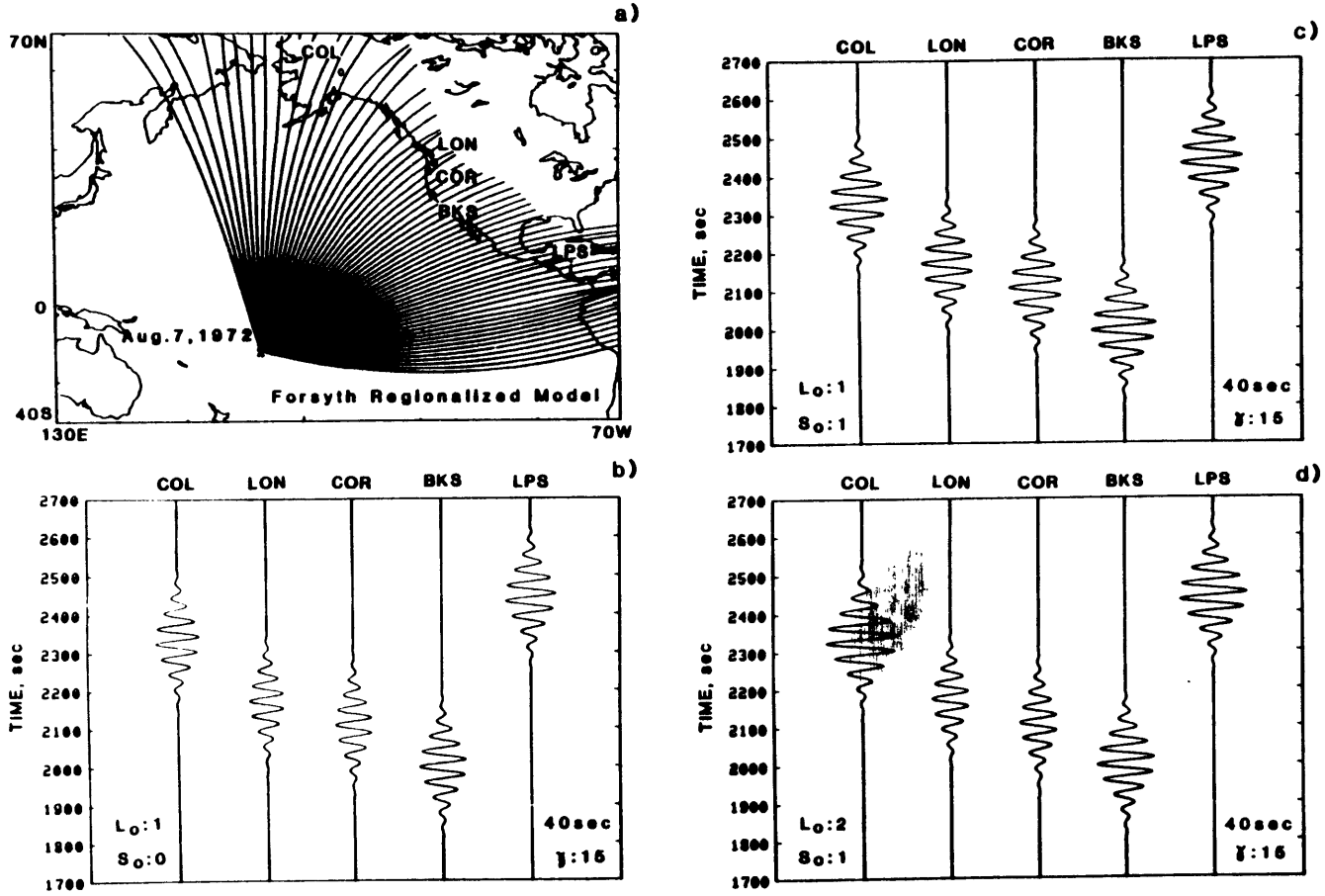

Figure 4.4. a) Ray tracing of 40-s Rayleigh waves for an event on August 7, 1972 off the Tonga trench (16.7°S, 172.1°W) with the model of Figure 4.3. $\Delta\delta$ is 2°. b)-d) Synthetic seismograms of the vertical component at stations College (COL), Longmire (LON), Corvallis (COR), Byerly (BKS) and La Palma (LPS) for different beam parameters: b) $S_0 = 0$, $L_0 = 1$, c) $S_0 = 1$, $L_0 = 1$ and d) $S_0 = 1$, $L_0 = 2$. We adopt $\gamma = 15$ and $\Delta\delta = 0.5°$ to produce these seismograms. The results are not sensitive to beam parameters, L_0 and S_0. This example does not predict large amplitude variations.

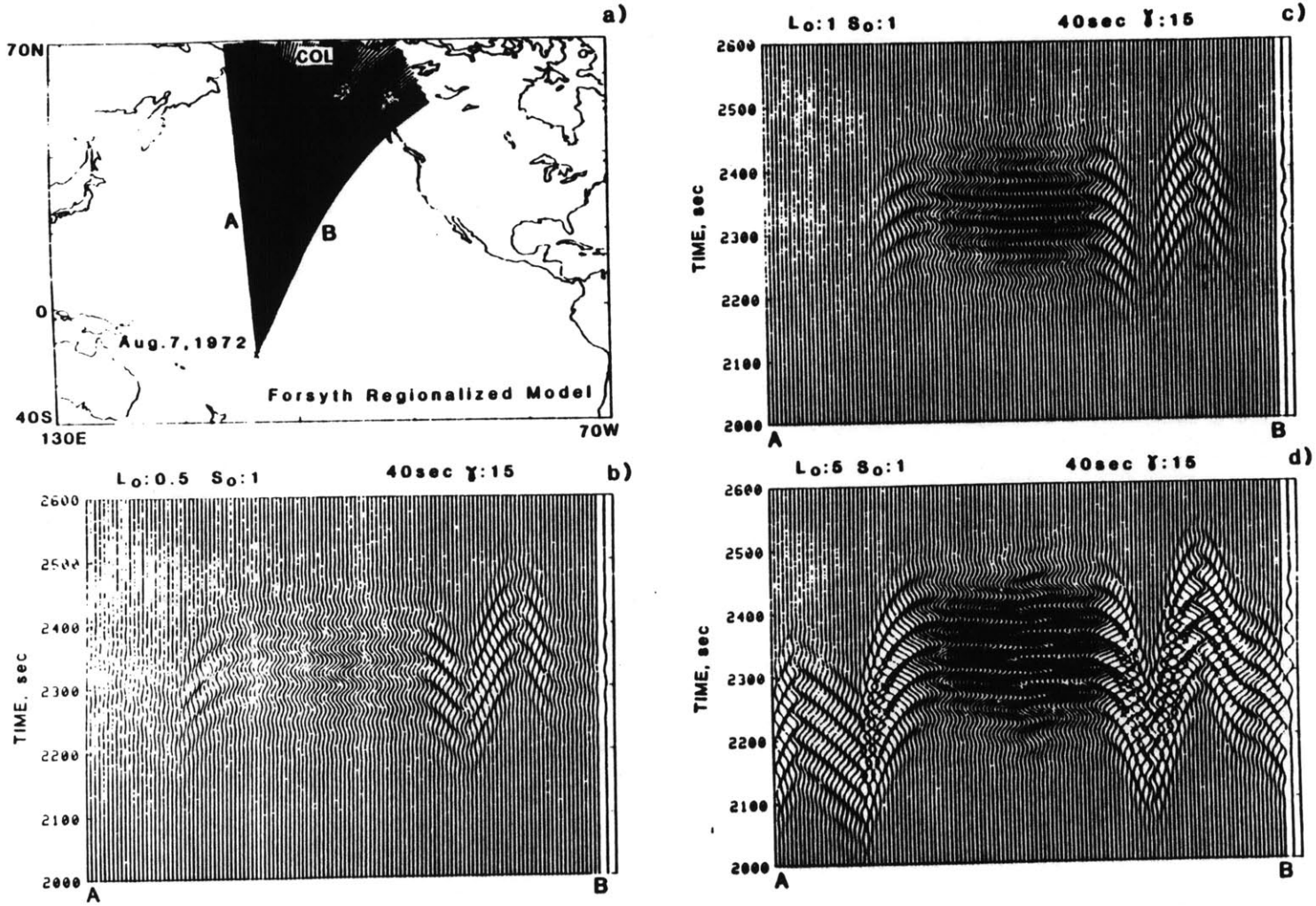

Figure 4.5. a) Detailed configurations of rays near the station College for the same event and model as in Figure 4.4. $\Delta\delta$ is 0.2°. b)-d) Contributions of each beam (A to B) to the synthetic seismograms at College (right-hand side of each figure) for different values of L_0 (0.5, 1 and 5, respectively). S_0 is 1.

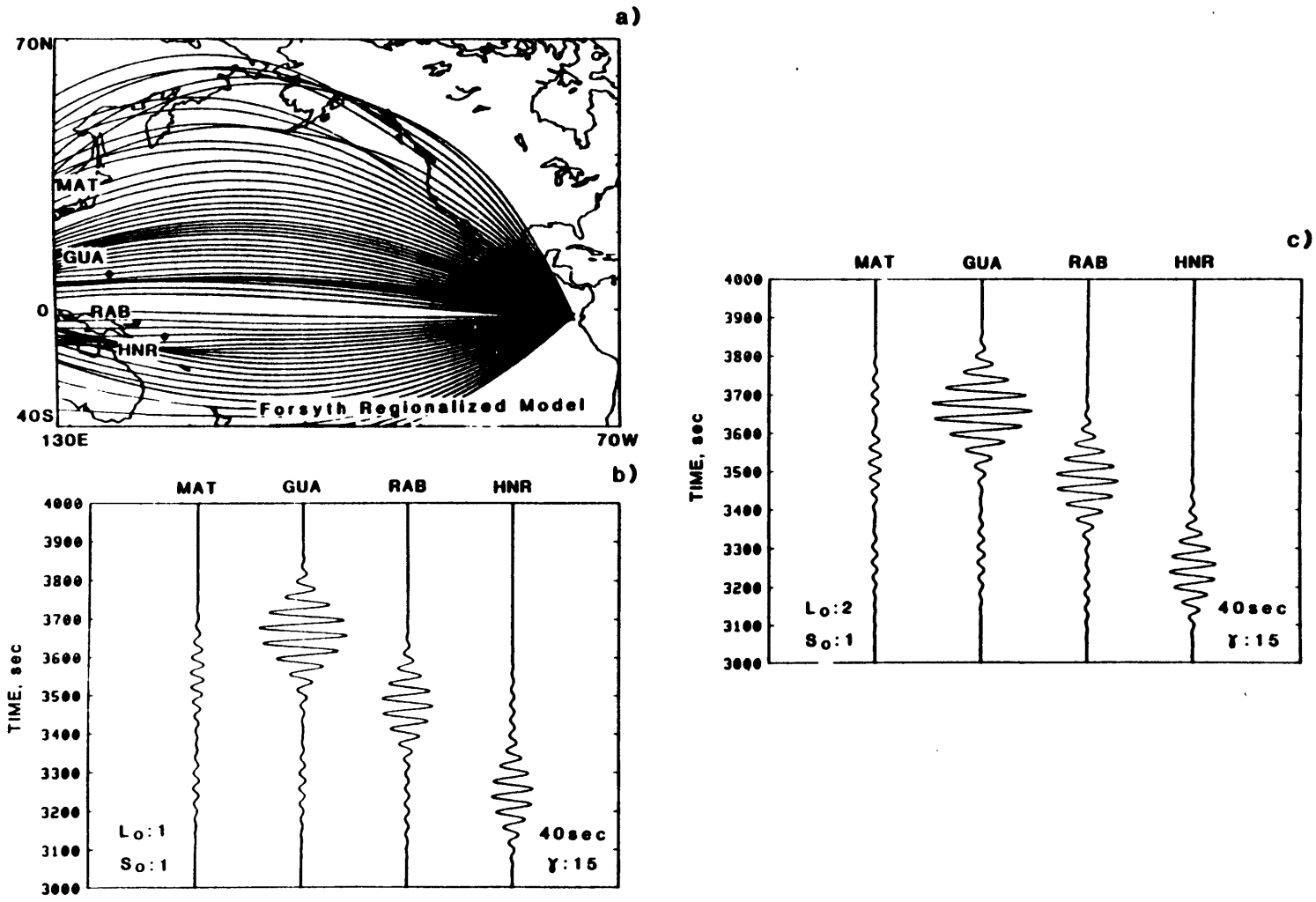

Figure 4.6 a) Ray tracing of 40-s Rayleigh waves for a hypothetical event off Ecuador for the model of Figure 4.3. $\Delta\delta$ is 2°. b)-c) Synthetic seismograms at stations Matsushiro (MAT), Guam (GUA), Rabaul (RAB) and Honiara (HNR) for different values of L_0 (1 and 2, respectively). S_0 is 1.0, and γ is 15. $\Delta\delta$ is 0.5° in these figures. The small precursors are caused by truncation errors. The large amplitude anomalies are expected because the rays pass in the young oceans.

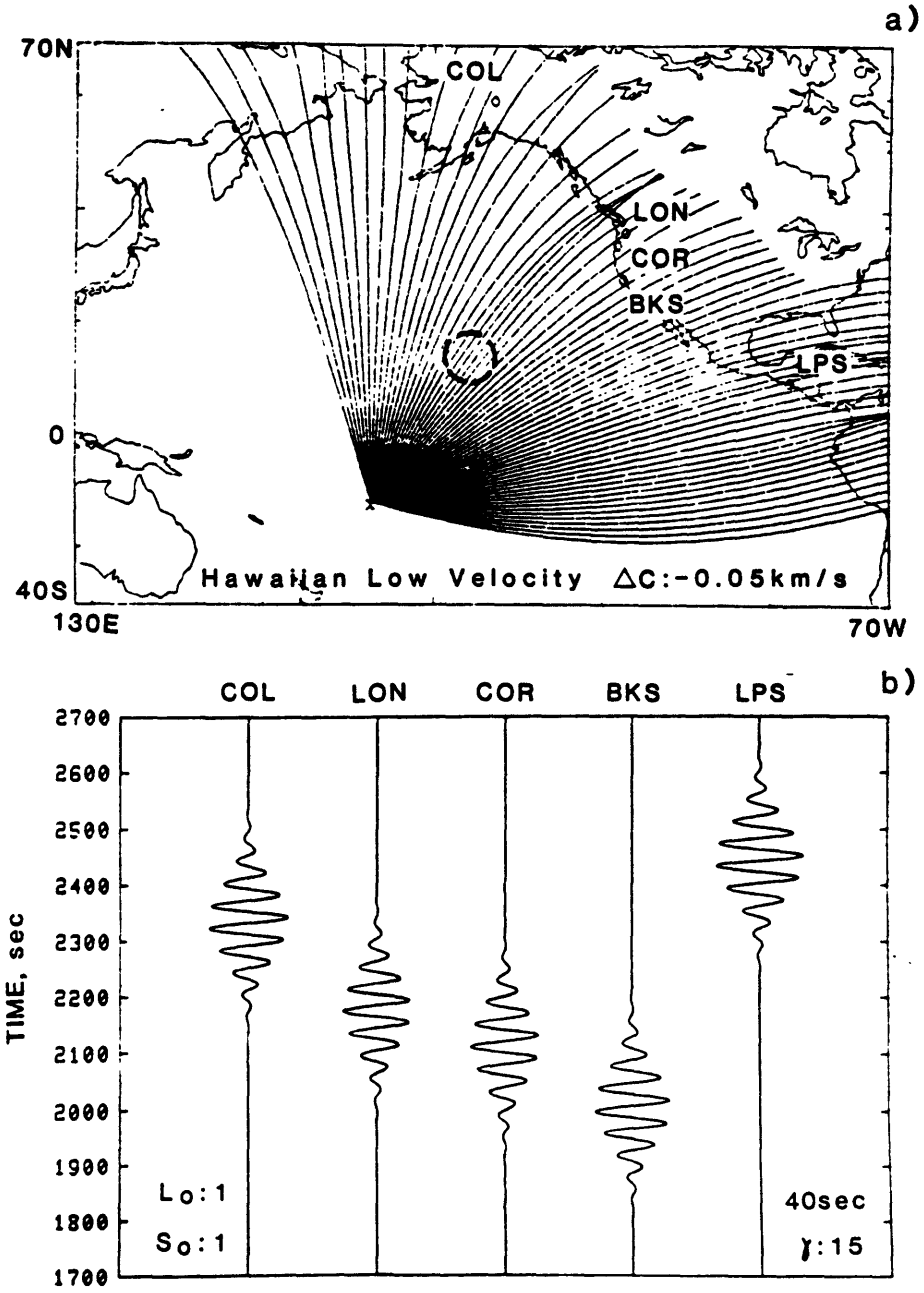

Figure 4.7. a) Ray tracing for the same period, event, ray parameters and model as those in Figure 4.4, except that there is a region of low phase velocity around the Hawaiian Islands (indicated by a broken circle). The anomalous velocity follows a Gaussian distribution with a half-width of 5°, and the maximum phase velocity difference from surrounding regions is -0.05 km/s. b) Synthetic seismogram at the five stations. S_0 is 1 and L_0 is 1. The amplitudes at LON and COR decrease relative to Figure 4.4.

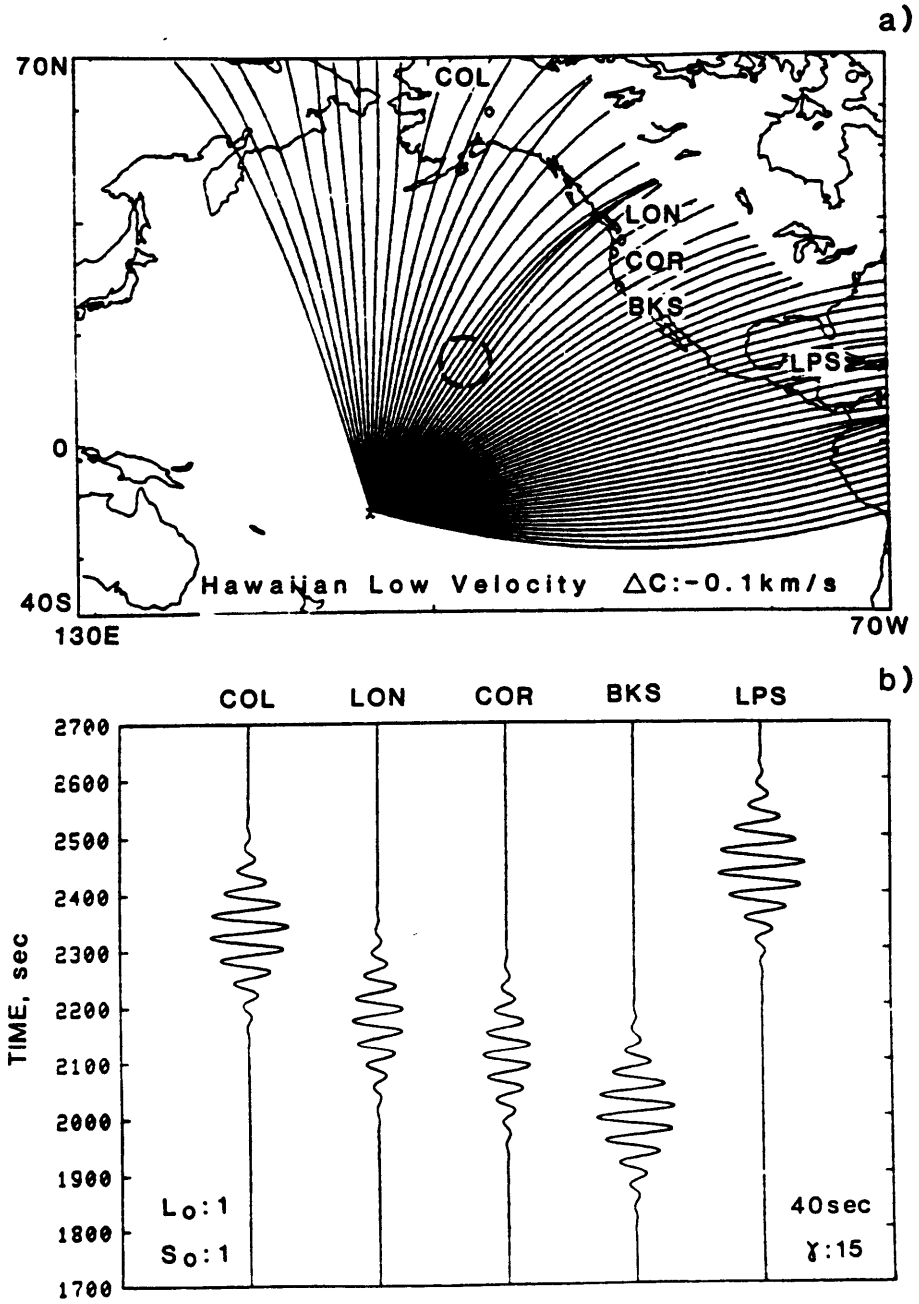

Figure 4.8. a)-b) Same as Figures 4.7 a)-b) except that the maximum phase velocity difference is -0.1 km/s in this model.

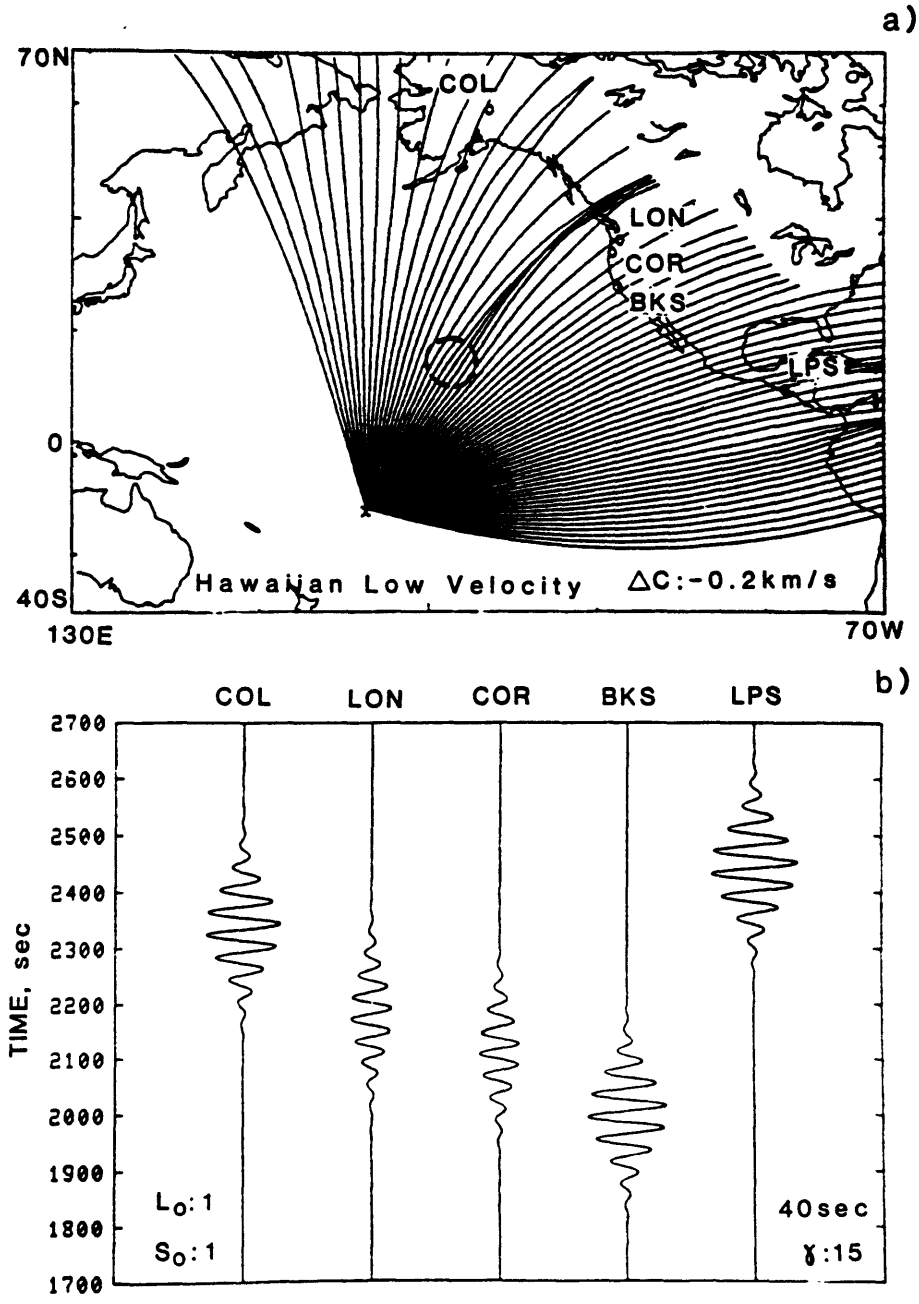

Figure 4.9. a)-b) Same as Figures 4.7 a)-b) except that the maximum phase velocity difference is -0.2 km/s in this model.

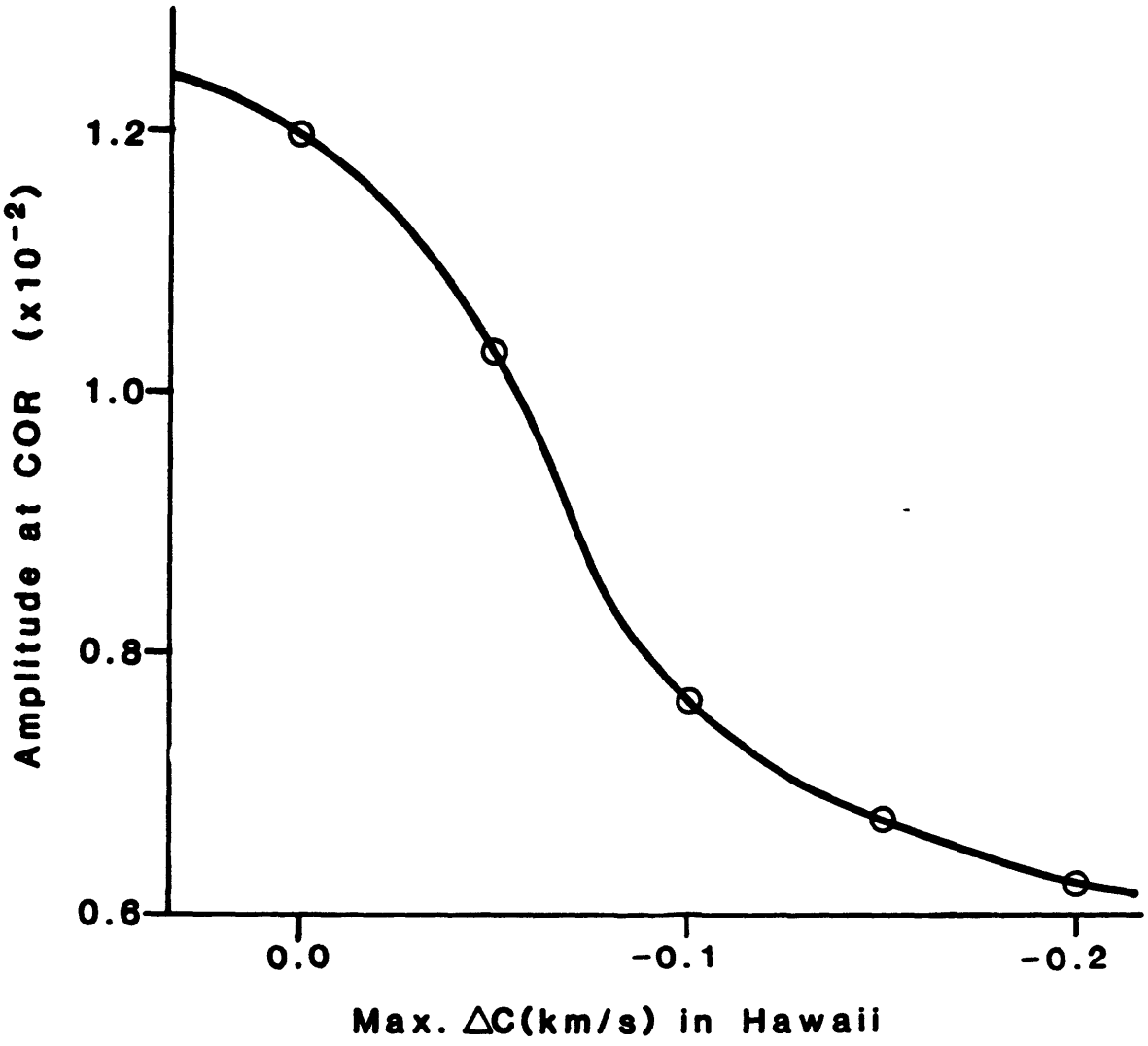

Figure 4.10. Amplitudes of synthetic seismograms at Corvallis for the models of Figures 4.7-4.9 (S_0 = 1, L_0 = 1) as a function of the maximum phase velocity anomaly in the region of the Hawaiian Islands. The amplitude decreases by half for a -0.2 km/s phase velocity change.

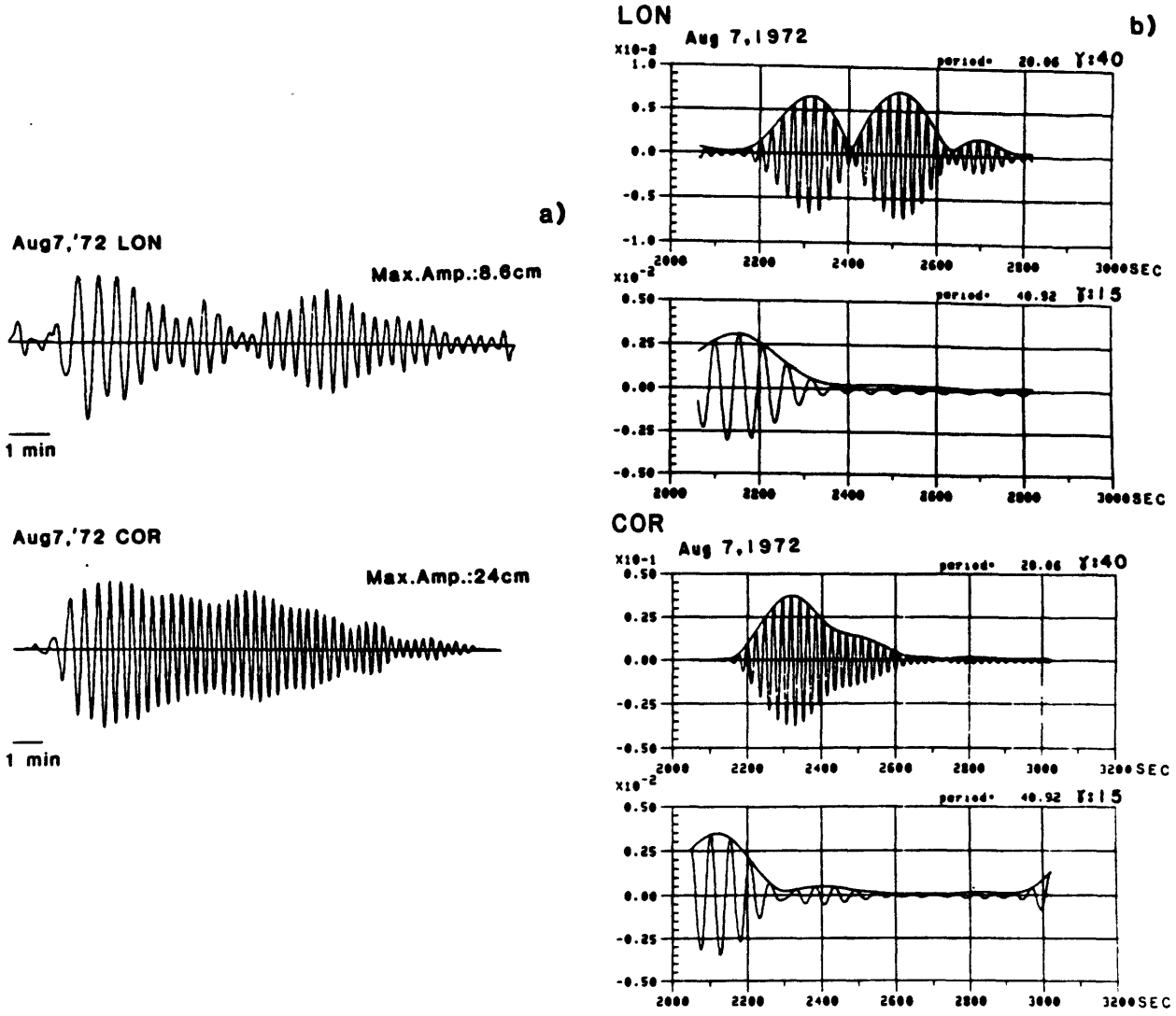

Figure 4.11. a) Observed vertical component Rayleigh wave seismograms at Longmire and Corvallis for an event on August 7, 1972 off the Tonga trench. b) Gaussian bandpass-filtered seismograms at these stations with center periods of 20 s (γ = 40) and 40 s (γ = 15). These seismograms include instrumental response corrections. Note the beating and the small amplitude of the seismogram at LON at 20 s.

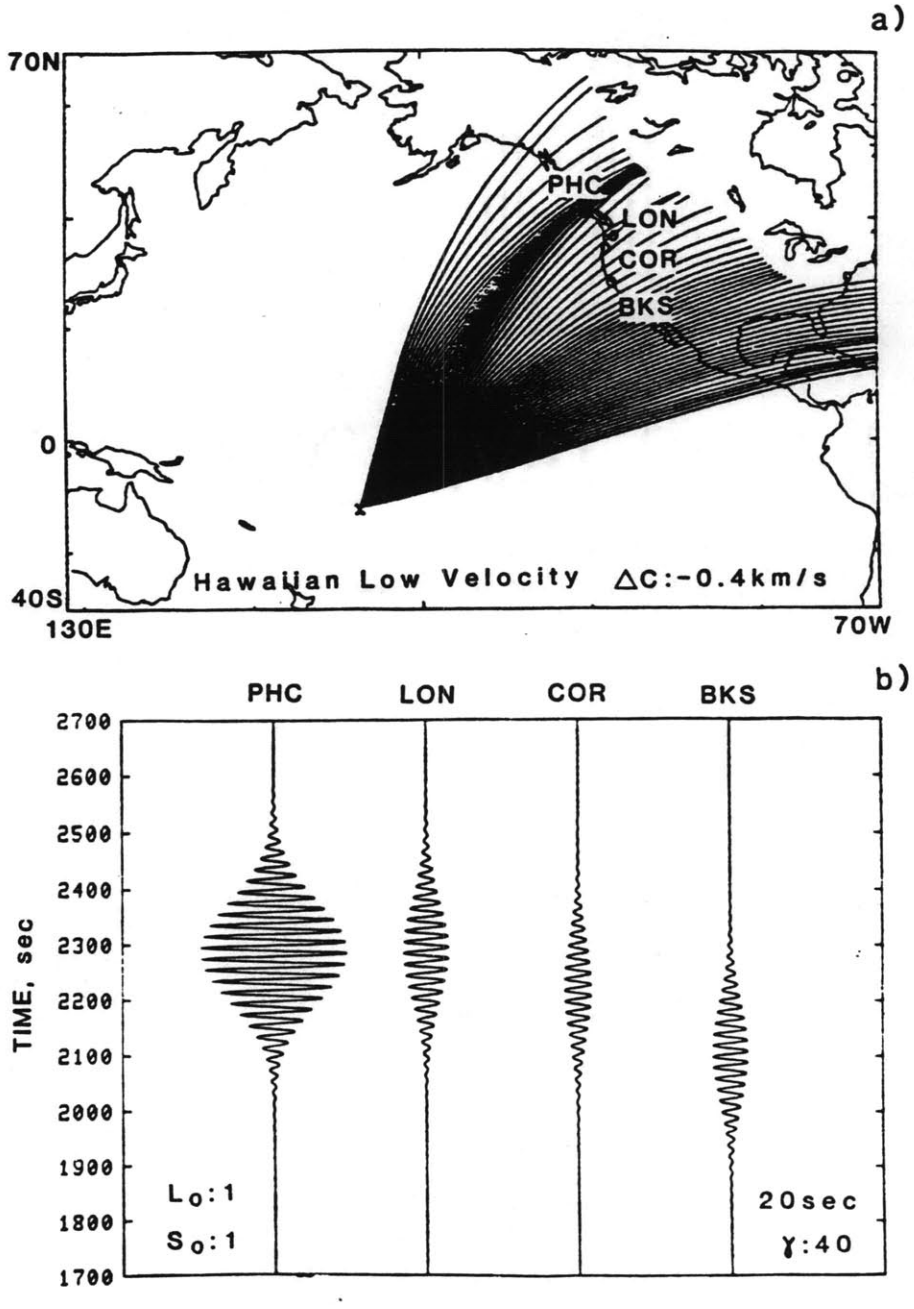

Figure 4.12. a) Ray tracing of 20-s Rayleigh waves for an event on August 7, 1972 off the Tonga trench with the model of Figure 4.3, adding a low velocity region with a maximum phase velocity difference of -0.4 km/s centered on the Hawaiian Islands. $\Delta\delta$ is 1°. b) Synthetic seismograms at stations of Port Hardy (PHC), Longmire (LON), Corvallis (COR) and Byerly (BKS). S_0 is 1, L_0 is 1, and γ is 40. $\Delta\delta$ is 0.5°.

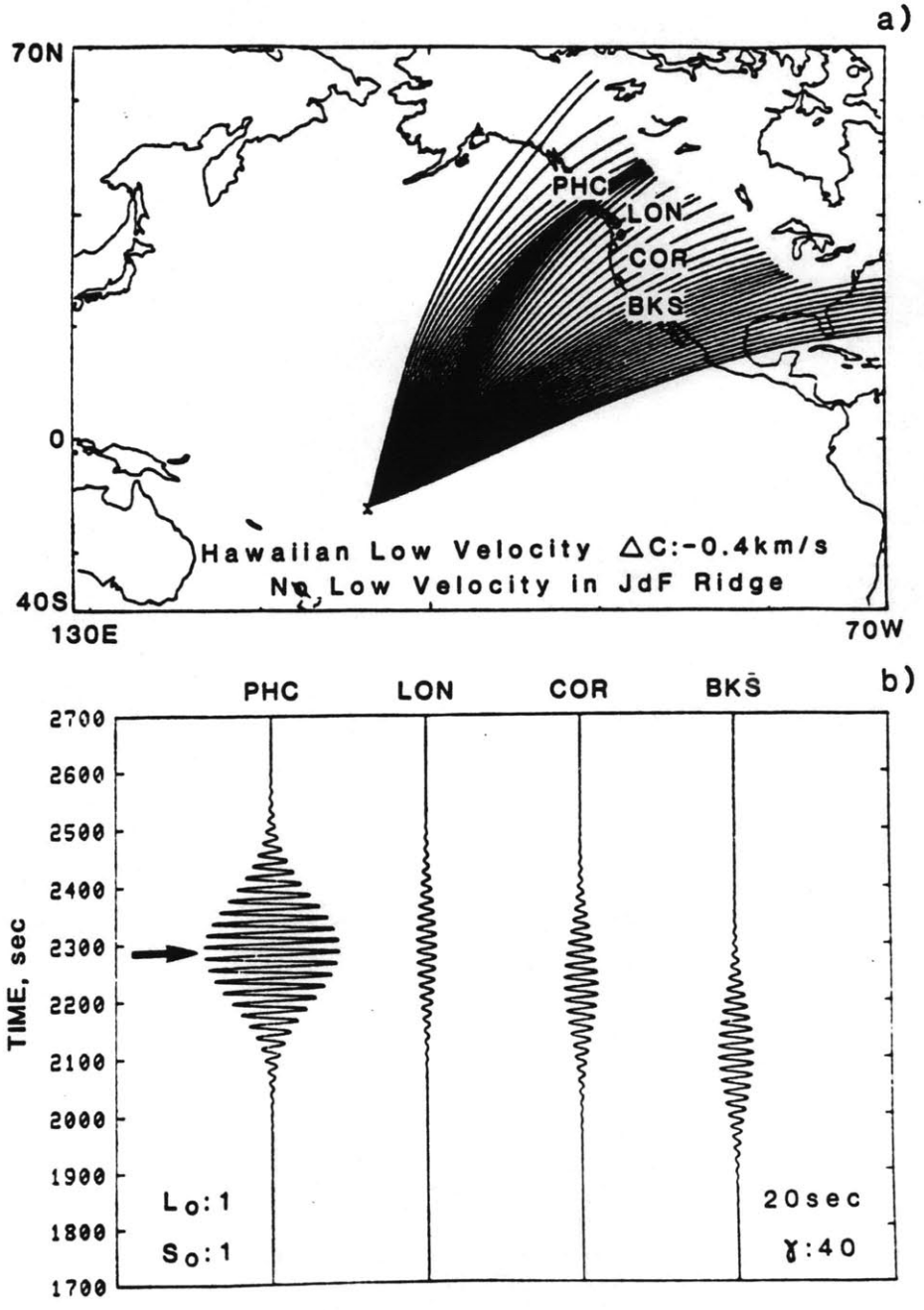

Figure 4.13. Same as Figures 4.12 a)-b) except that the low velocity area along the Juan de Fuca Ridge is removed. The arrow in the seismogram at Port Hardy represents the arrival time of the peak of the wavepacket. The amplitude of COR is twice that of LON.

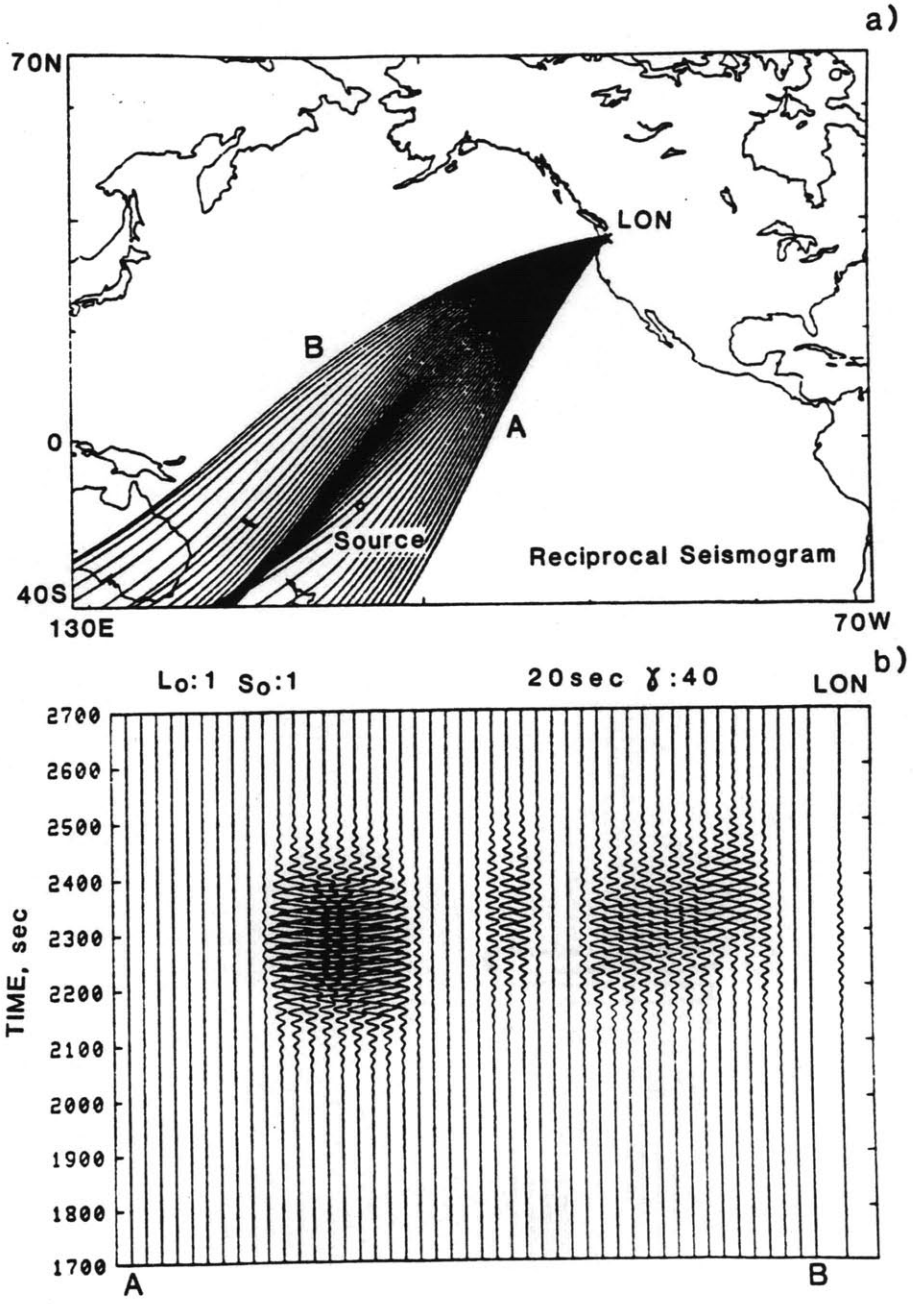

Figure 4.14. a) Ray tracing for the reciprocal seismogram at the station Longmire for the same model as in Figure 4.13. b) Reciprocal seismogram at the source from the radiation at Longmire. The contributions of each beam (A to B) and the synthetic seismogram (right-hand side) are shown. S_0 is 1.0 and L_0 is 1.0.

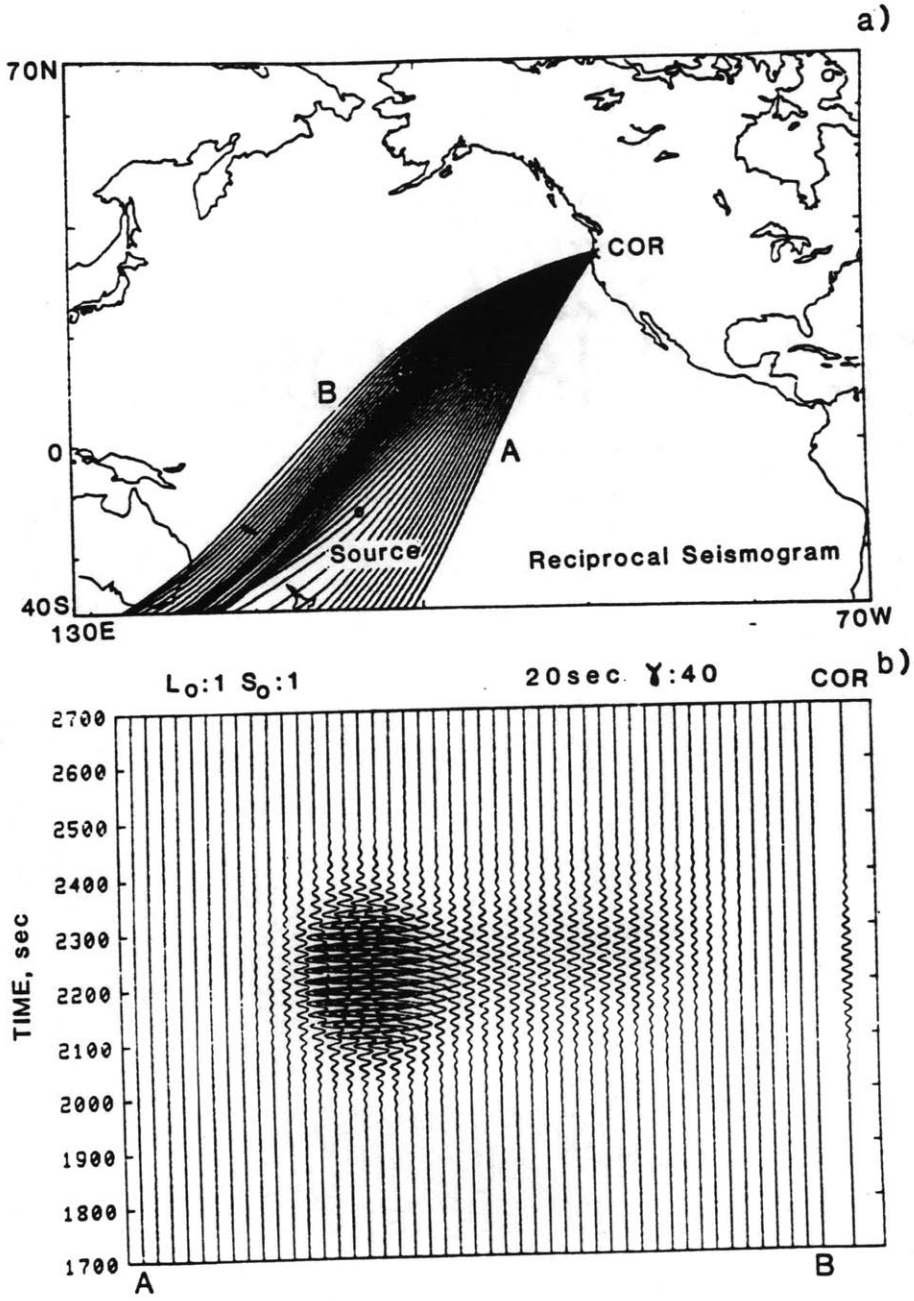

Figure 4.15. Same as Figures 4.14 a)-b) but for the reciprocal seismogram at the station Corvallis. The amplitude is twice that in Figure 4.14.

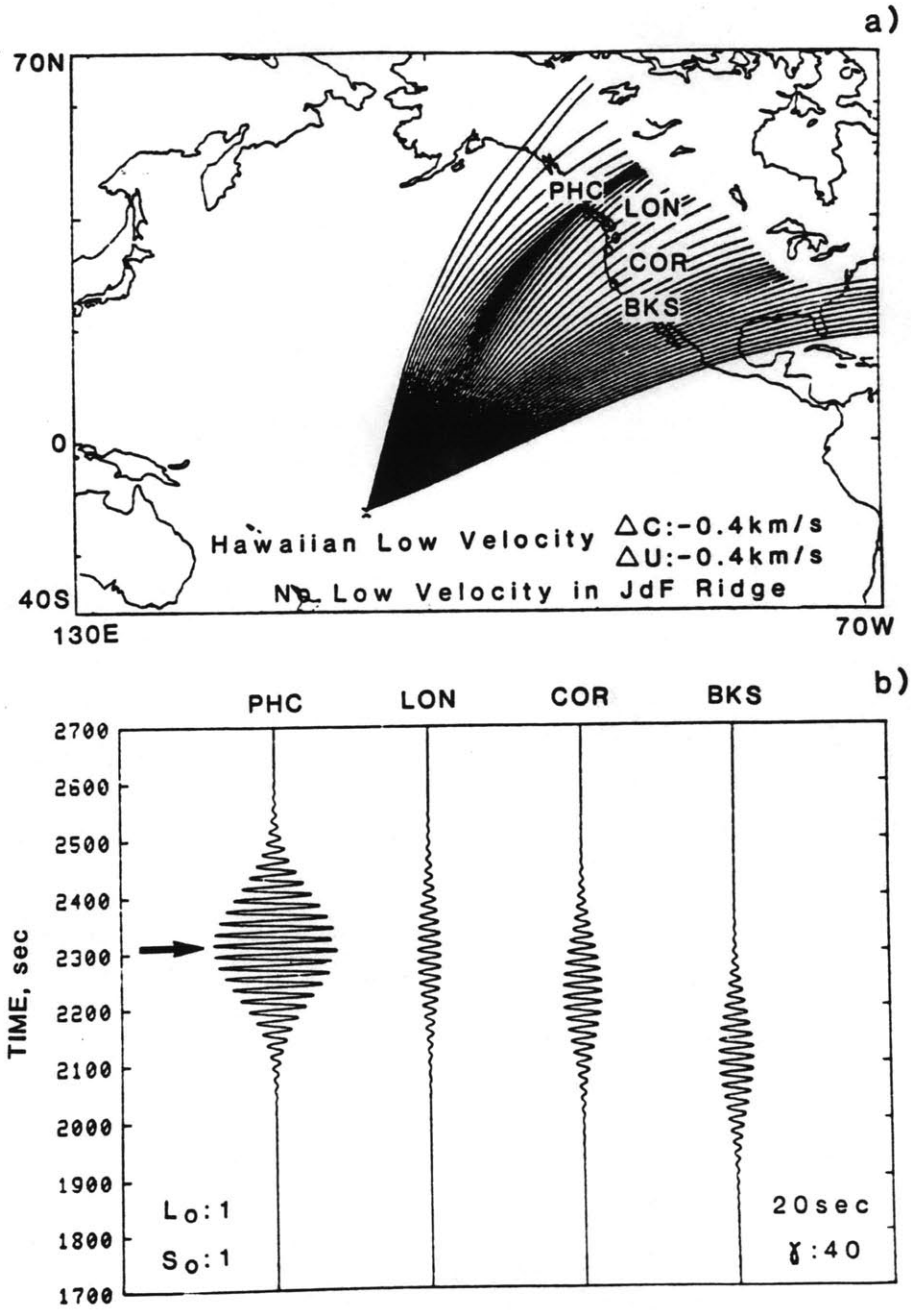

Figure 4.16. Ray tracing and synthetic seismograms as in Figure 4.13, except that in this model there is an anomaly at the Hawaiian Islands in group velocity as well as in phase velocity. The maximum anomaly in group velocity is -0.4 km/s. The arrow in the seismogram at Port Hardy represents the arrival time of the peak of the wavepacket. Both amplitudes and phases are almost identical to those in Figure 4.13.

Chapter 5. Inversions for Phase Velocity Anomalies in the Pacific Ocean Basin

So far, we have developed methods to synthesize surface waves in a laterally heterogeneous Earth and checked their stability and accuracy. Our results imply that these methods may resolve fine structure which cannot be detected by phase information alone. In this chapter we shall apply these methods to actual data. Specifically, we will invert both phase and amplitude information to recover two-dimensional anomalies in phase velocities. Since this study is one of the first attempts to invert amplitude anomalies to resolve lateral heterogeneity in a medium, including the literature of exploration geophysics (e.g., Thomson, 1983; Miller et al., 1985), the target area should be a relatively simple one. As described in Chapter 4, the Pacific Ocean is selected for this study. Unlike the linear and stable behavior of phase variations, amplitude anomalies in some cases can change extremely non-linearly or unstably as we observed in the previous chapters. Thus, we must start the procedures with a fairly reliable initial model. For this reason, the Pacific Ocean as viewed by surface waves with periods 30-100 s is an appropriate subject because of the fairly simple structure. We shall employ the method developed in the previous chapters to conduct the forward modelling essential for inversion. While this is itself fairly new, there is another new challenge in this chapter. Because of the non-linear behavior of amplitude information, we must employ a non-linear inversion scheme. Such schemes are fairly new to seismologists who so far have dealt with only linear inverse problems such as the milestone works by Backus and Gilbert [1967, 1968, 1970]. For non-linear inverse problems, direct inversions are usually impossible and iterative schemes are used in general. However, a simple-minded extension of the linear inverse scheme to

a non-linear case may not work. Recently, Tarantola and his colleagues have studied these topics extensively, and the subject of this thesis provides a good opportunity to apply their methods to a real problem. In non-linear inverse problems, the initial model has to be quite close to the true one, because of the presence of many local minima to which the solutions may converge. Both this local minimum problem and the notorious ill-posed nature (i.e., small eigenvalues) of linearized schemes [e.g., Koch, 1983] make the non-linear inversion difficult. Thus, in this study only one example of such applications is given, and we shall pay attention principally to the above methodological problems rather than to the geodynamical or tectonic implications of the results themselves.

In section 5.1, we shall develop the inverse formulations for the present problems. A form of the first Born approximation (i.e., weak scattering) for two-dimensional acoustic waves is adapted to the surface wave expressions. New aspects of this work are that the starting model is laterally heterogeneous and that we shall calculate the Frechet derivatives with the new methods developed in the previous chapters. In section 5.2, we shall describe the data processing used for the inversions. Since the phase differences between the initial model and the inverted model should be small, at first we perform conventional phase velocity inversions with only phase data in section 5.3. Finally, inversions of both amplitude and phase by the formulations developed in the previous sections are presented in section 5.4. The effects of damping factors and source ambiguities and error analysis are also discussed.

5.1 Inversion Formulation

We shall apply to surface wave problems the linerized iterative inverse scheme originally developed by Tarantola [1984a, 1984b] for acoustic wave propagation in a heterogeneous medium. Although Tarantola [1984a, 1984b] developed formulations for time-domain analysis, here a frequency-domain analysis will be given. This is because we shall concentrate on making 2-D maps of phase velocities at a single frequency rather than attempt to recover the complete three-dimensional structure of the Earth by using several frequencies simultaneously as in the study by Woodhouse and Dziewonski [1984]. This reduction to a 2-D problem reduces computational time enormously and makes the problem much simpler. Also, formulations in the frequency domain can skip several time-convolution procedures which are required in time domain analysis.

Although our problem is surface wave propagation in a laterally heterogeneous medium, for simplicity we employ for the sake of simplicity an "acoustic wave approximation", that is, the two-dimensional acoustic wave equation with a velocity equal to the surface wave phase velocity, in developing the inverse formulation instead of the original elastodynamic equations under the assumption of a laterally slowly-varying medium [Yomogida, 1985]. The two-dimensional acoustic wave equations whose velocity $v(\underset{\sim}{r})$ corresponds to the phase velocity of surface waves $c(\underset{\sim}{r})$ of a given frequency is

$$\left[-\frac{1}{c^2(\underset{\sim}{r})}\frac{\partial^2}{\partial t^2}+\nabla^2\right]w(\underset{\sim}{r},t) = f(\underset{\sim}{r},t) \qquad (5.1)$$

where ∇^2 is a two-dimensional Laplacian. In our case the Laplacian is expressed by Cartesian coordinates θ-ϕ according to the Mercator projection as shown in section 3.2 [Jobert and Jobert, 1983]. $w(\underset{\sim}{r},t)$ represents the

vertical component of Rayleigh waves and $f(\underset{\sim}{r},t)$ is a source term.

For a single frequency ω, the above equation may be expressed as

$$\left[\frac{\omega^2}{c(\underset{\sim}{r})^2} + \nabla^2 \right] w(\underset{\sim}{r},\omega) = f(\underset{\sim}{r},\omega) \tag{5.2}$$

Let us introduce the Green's function $G(\underset{\sim}{r},\omega;\underset{\sim}{r}')$ which satisfies

$$\left[\frac{\omega^2}{c(\underset{\sim}{r})^2} + \nabla^2 \right] G(\underset{\sim}{r},\omega;\underset{\sim}{r}') = - \delta(\underset{\sim}{r}-\underset{\sim}{r}') \ . \tag{5.3}$$

Then the solution may be expressed as

$$w(\underset{\sim}{r},\omega) = - \int_V d\underset{\sim}{r}' G(\underset{\sim}{r},\omega;\underset{\sim}{r}') f(\underset{\sim}{r}',\omega) \ . \tag{5.4}$$

Now let us perturb the velocity field $c(\underset{\sim}{r})$ into $c(\underset{\sim}{r}) + \delta c(\underset{\sim}{r})$, which introduces a small change in $w(\underset{\sim}{r},\omega;\underset{\sim}{r}_s)$ to $\underset{\sim}{w} + \delta \underset{\sim}{w}$, where $\underset{\sim}{r}_s$ is a location of the source. This corresponds to the Born approximation: the perturbed wavefields are assumed to be determined by the response of the medium only to the unperturbed wavefields. Then, equation (5.2) may be written as

$$\left[\frac{\omega^2}{(\underset{\sim}{c}+\delta \underset{\sim}{c})^2} + \nabla^2 \right] [\underset{\sim}{w}+\delta \underset{\sim}{w}] = \underset{\sim}{f} \tag{5.5}$$

Neglecting higher order terms, we obtain

$$\left[\frac{\omega^2}{c(\underset{\sim}{r})^2} + \nabla^2 \right] \delta w(\underset{\sim}{r},\omega;\underset{\sim}{r}_s) = \Delta f(\underset{\sim}{r},\omega;\underset{\sim}{r}_s) \tag{5.6}$$

where $\Delta f(\underset{\sim}{r},\omega;\underset{\sim}{r}_s)$ is the equivalent source term of the medium parameter perturbations:

$$\Delta f(\underset{\sim}{r},\omega;\underset{\sim}{r}_s) = \frac{2\omega^2}{c^3(\underset{\sim}{r})} \delta c(\underset{\sim}{r}) \ w(\underset{\sim}{r},\omega;\underset{\sim}{r}_s) \ . \tag{5.7}$$

Using the Green's function G and equation (5.4), the perturbation of the solution may be expressed as

$$\delta w(\underset{\sim}{r}_g,\omega;\underset{\sim}{r}_s) = -\int d\underset{\sim}{r}' G(\underset{\sim}{r}_g,\omega;\underset{\sim}{r}')\Delta f(\underset{\sim}{r}',\omega;\underset{\sim}{r}_s) \tag{5.8}$$

$$= \int d\underset{\sim}{r}' \{-\frac{2\omega^2}{c^3(\underset{\sim}{r}')} G(\underset{\sim}{r}_g,\omega;\underset{\sim}{r}') w(\underset{\sim}{r}',\omega;\underset{\sim}{r}_s)\}\delta c(\underset{\sim}{r}')$$

Thus, the term within braces of (5.8) corresponds to Fréchet derivatives:

$$F(\underset{\sim}{r}_g,\omega;\underset{\sim}{r}_s|\underset{\sim}{r}) \equiv \frac{\partial w(\underset{\sim}{r}_g,\omega;\underset{\sim}{r}_s)}{\partial c(\underset{\sim}{r})}$$

$$= -\frac{2\omega^2}{c^3(\underset{\sim}{r})} G(\underset{\sim}{r}_g,\omega;\underset{\sim}{r}) w(\underset{\sim}{r},\omega;\underset{\sim}{r}_s) \ . \tag{5.9}$$

The Gaussian beam expression for the Green's function of the acoustic wave equation (5.1) in a laterally heterogeneous medium is given in ray-centered coordinates (i.e., $\underset{\sim}{r} = (s,n)$ and $\underset{\sim}{r}' = (s',0)$) by

$$G(\underset{\sim}{r},\omega;\underset{\sim}{r}') = \frac{i}{4\pi} \sum_{\delta} \sqrt{\frac{c(s)q(s')}{c(s')q(s)}} \exp[i\psi(s,\omega;s') + \frac{i\omega}{2}\frac{p}{q}n^2]\Delta\delta \tag{5.10}$$

where ψ is a phase delay along the ray, $\psi = -\omega \int_{s'}^{s} \frac{d\zeta}{c(\zeta)}$ [Červený et al., 1981]. On the other hand, the vertical component of Rayleigh waves observed on the surface (z=0) and excited by the point source with a step time function, $M(\omega) = M_0/(-i\omega)$, is given by

$$w(\underset{\sim}{r},\omega;\underset{\sim}{r}') = \frac{1}{8\pi C(s')U(s')I_1(s')\omega} \sum_{\delta} \{\} M_0 \sqrt{\frac{U(s')I_1(s')q(s')}{U(s)I_1(s)q(s)}} \tag{5.11}$$

$$\exp[i\psi(s,\omega;s') + \frac{i\omega}{2}\frac{p}{q}n^2]\Delta\delta$$

where {} is a function of moment-tensor components, eigenfunctions of Rayleigh waves, elastic parameters at the source location, and a take-off angle of each ray given in equation (3.55). We have changed the sign from the original formulation so that upward motion is positive. These formulations imply that

$$w \cdot \frac{2c(s')U(s')I_1(s')\omega}{-i\{\}M_0} \sqrt{\frac{c(s')U(s')I_1(s')}{c(s)U(s)I_1(s)}} \qquad (5.12)$$

rather than w, obeys the two-dimensional acoustic wave equation. Our use of the acoustic equation in the formulation of the inverse solution means that the product $c(s)U(s)I_1(s)$ varies only weakly as compared with the amplitude variation caused by geometrical spreading and multipath interference. In our calculations, we shall evaluate the above product at a point near the receiver for each ray path.

Instead of the direct use of field variables and model parameters we employed in this study a procedure linearized for the logarithms of both field variables and model parameters. T.R. Madden [personal communication, 1985] has successfully applied this technique to electromagnetic problems. The use of logarithms of field variables and model parameters may be more natural and robust, especially in cases where the data contain signal-generated noise as in the present study (see section 11.5.5 of Aki and Richards [1980]) because this procedure corresponds to the normalization of both field variables and model parameters. In fact, the imaginary part of the logarithms of field variables constitutes the phase term, so that using only imaginary parts for linearized inversions corresponds to the simple travel time inversions which have been conventionally used in seismology. In this study we are going to use both real and imaginary parts.

Let us modify equation (5.8) into an inversion formulation for the logarithms of field variables and model parameters of the acoustic wave equation (5.2), similar to Rytov's method [Chernov, 1960]. Substituting $\phi \equiv \ln(w(\underset{\sim}{r},\omega))$ into (5.2), we obtain

$$\nabla^2\phi + (\underset{\sim}{\nabla}\phi)^2 + \frac{\omega^2}{c(\underset{\sim}{r})^2} = f\cdot\exp(-\phi) \tag{5.13}$$

Perturbing the variables and the velocity fields, (5.13) becomes

$$\nabla^2(\phi_0+\delta\phi) + (\underset{\sim}{\nabla}(\phi_0+\delta\phi))^2 + \frac{\omega^2}{(c(\underset{\sim}{r})+\delta c(\underset{\sim}{r}))^2} = f\cdot\exp(-\phi_0) \tag{5.14}$$

which gives for the first order perturbation equations:

$$\nabla^2(\delta\phi) + 2\underset{\sim}{\nabla}\phi_0\cdot\underset{\sim}{\nabla}(\delta\phi) = \frac{2\omega^2}{c(\underset{\sim}{r})^3}\,\delta c(\underset{\sim}{r}) \tag{5.15}$$

This equation can be linearized by substituting $\delta\phi \equiv \phi_1\exp(-\phi_0)$ and using the logarithms of model parameters $m(\underset{\sim}{r}) = \ln c(\underset{\sim}{r})$; i.e., $(\delta m=\delta c/c)$,

$$\nabla^2\phi_1 + \frac{\omega^2}{c(\underset{\sim}{r})^2}\phi_1 = \frac{2\omega^2}{c(\underset{\sim}{r})^3}\exp(\phi_0)\delta c(\underset{\sim}{r})$$

$$= \frac{2\omega^2}{c(\underset{\sim}{r})^2}\,w(\underset{\sim}{r},\omega;\underset{\sim}{r}_s)\delta m(\underset{\sim}{r}) \tag{5.16}$$

This is equivalent to equation (5.6). So with the Green's function for the original equation from (5.3), the solution may be written as

$$\delta\phi(\underset{\sim}{r}_g,\omega;\underset{\sim}{r}_s) = \int dr' \left\{\frac{-2\omega^2}{c^2(\underset{\sim}{r}')}G(\underset{\sim}{r}_g,\omega;\underset{\sim}{r}')\,\frac{w(\underset{\sim}{r}',\omega;\underset{\sim}{r}_s)}{w(\underset{\sim}{r}_g,\omega;\underset{\sim}{r}_s)}\right\}\delta m(\underset{\sim}{r}') \tag{5.17}$$

This corresponds to the Frechet derivatives for logarithms of field variables and model parameters. Comparing (5.17) to (5.8), we notice that the above Fréchet derivatives are just the derivatives for the field variables divided by $w(\underset{\sim}{r}_g,\omega;\underset{\sim}{r}_s)/c(\underset{\sim}{r}')$. Thus, in this case the magnitude derivatives are naturally normalized. Instead of (5.9), we shall use the following derivatives:

$$F(\underset{\sim}{r}_g,\omega;\underset{\sim}{r}_s|\underset{\sim}{r}) \equiv \frac{\partial\phi(\underset{\sim}{r}g,\omega;\underset{\sim}{r}s)}{\partial m(\underset{\sim}{r})} = \frac{c(\underset{\sim}{r})}{w(\underset{\sim}{r}_g,\omega;\underset{\sim}{r}_s)} \frac{\partial w(\underset{\sim}{r}_g,\omega;\underset{\sim}{r}_s)}{\partial c(\underset{\sim}{r})}$$

$$= -\frac{2\omega^2}{c^3(\underset{\sim}{r})} G(\underset{\sim}{r}_g,\omega;\underset{\sim}{r})w(\underset{\sim}{r},\omega;\underset{\sim}{r}_s)/w(\underset{\sim}{r}_g,\omega;\underset{\sim}{r}_s) \qquad (5.18)$$

and the field variables are now

$$\phi(\underset{\sim}{r}_g,\omega;\underset{\sim}{r}_s) = \ln[w(\underset{\sim}{r}_g,\omega;\underset{\sim}{r}_s)]$$

$$= \ln A(\underset{\sim}{r}_g,\omega;\underset{\sim}{r}_s) + i\psi(\underset{\sim}{r}_g,\omega;\underset{\sim}{r}_s) \qquad (5.19)$$

where A is an amplitude of a field variable (in this study, vertical component of Rayleigh wave) and ψ is a phase term. We are going to invert for $\delta m(\underset{\sim}{r}) = \delta c(\underset{\sim}{r})/c(\underset{\sim}{r})$ by using both $\delta(\ln A)$ and $\delta\psi$.

With the above derivatives we used the inversion formulation of Tarantola and Valette [1982], which they term "Total Inversion":

$$m_{k+1}(\underset{\sim}{r}) = m_k(\underset{\sim}{r}) + (I+C_mF_k+C_\phi^{-1}F_k)^{-1}$$

$$\{C_mF_k+C_\phi^{-1}[\phi_o(\underset{\sim}{r}_g,\omega;\underset{\sim}{r}_s)-\phi_k(\underset{\sim}{r}_g,\omega;\underset{\sim}{r}_s)]-(m_k(\underset{\sim}{r})-m_o(\underset{\sim}{r}))\} \qquad (5.20)$$

where $m_k(\underset{\sim}{r})$ is the logarithm of the velocity field at the k-th step, F_k is the Fréchet derivative with $m_k(\underset{\sim}{r})$ given by (5.17), C_m and C_ϕ are the covariance functions of data and models, $\phi_o(\underset{\sim}{r}_g,\omega;\underset{\sim}{r}_s)$ are the observations ($\ln A$ or ψ) for a particular source-receiver pair, $\phi_k(\underset{\sim}{r}_g,\omega;\underset{\sim}{r}_s)$ are the solutions of the forward problem for model $c_k(\underset{\sim}{r})$, I is the unit operator,

and the dagger (+) represents the adjoint operator, respectively. If we specify a model with a finite number of model parameters, equation (5.20) becomes a matrix formulation. The use of C_m and C_ϕ constitutes the introduction of damping factors; the solution philosophy is similar to that of Marquardt [1961] in that at each iteration a solution intermediate between a least-squares solution and a solution given by a steepest descent method is obtained in order to ensure a stable and rapid convergence of solutions. For detailed discussions on this subject, readers are referred to Tarantola and Valette [1982] and Tarantola [1984a,b].

In this study the following points must be carefully treated. In the present frequency domain analysis, there is essentially an ambiguity in the phase term: we cannot distinguish phases which differ from each other by multiples of 2π. As shown by Tarantola [1984a], in the inverse procedure (5.20) we compare the following two wavefields at the model point $\underset{\sim}{r}$: 1) the wavefield $w(\underset{\sim}{r},\omega;\underset{\sim}{r}_s)$ at the model point $\underset{\sim}{r}$ from the source $\underset{\sim}{r}_s$ and 2) the back propagation of the data residual $\delta w(\underset{\sim}{r}_g,\omega;\underset{\sim}{r}_s)$ from the receiver $\underset{\sim}{r}_g$ to the model point $\underset{\sim}{r}$ using the Green's function $G(\underset{\sim}{r}_g,\omega;\underset{\sim}{r})=G^*(\underset{\sim}{r},\omega;\underset{\sim}{r}_g)$. In the frequency domain analysis we unwrap the phase term for w or G to compare the phase differences between the above two wavefields and if the phase difference between the above two wavefields is larger than π, we set the Fréchet derivative F to be small. This is because the fundamental concept of ray or beam theory is that the energy is concentrated along rays and we can neglect the energy in the wavefield at a distance farther than half a wavelength (π-phase difference) from the ray (first Fresnel zone conditon (2.22)). For simplicity we multiply the Fréchet derivatives by the factor $\exp(-|\Delta\psi|)$, where $\Delta\psi$ is the phase difference of the above two wavefields, so that the magnitude of the derivative smoothly decreases

with distance from the actual rays. In the conventional travel time or pure-path type inversion, contributions to data come only from the model points along the ray. In the present method we incorporate some contributions from points not only along the ray but also in the neighborhood of the ray taking into account the finite wavelength [e.g., Woodhouse and Girnius, 1982]. This is more realistic and may give more stable results for our inversions.

We must also include the attenuation of surface waves to apply inversions to the real data. Here we assume that the attenuation factors are fixed. Before the inversions of phase velocities the data are corrected by the attenuation factors of the initial model (the age-dependent model in this study). After such corrections, we treat both synthetics and data as those in a lossless medium.

In summary, we must conduct three kinds of forward modelling in (5.18) at each iteration step: (1) $\phi_k = \ell n\,[w(\underset{\sim}{r}_g,\omega;\underset{\sim}{r}_s)]$, the synthetics to be compared with the data to obtain the data residuals for the k-th model, (2) $w(\underset{\sim}{r},\omega;\underset{\sim}{r}_s)$, which is a synthesis at a model point $\underset{\sim}{r}$ from a source at $\underset{\sim}{r}_s$, and (3) $G(\underset{\sim}{r}_g,\omega;\underset{\sim}{r})$, which is the Green's function from a medium point $\underset{\sim}{r}$ to a receiver at $\underset{\sim}{r}_g$. Synthetic seismograms are obtained by the Gaussian beam method, and results are checked by the paraxial ray approximation. Their generation consumes most of the computational time in the inversion.

Another difficulty arises from the calculation of the inverse matrix $(\underset{\approx}{I} + \underset{\approx}{C}_m\underset{\approx}{F}_k{}^{+}\underset{\approx}{C}_\phi{}^{-1}\underset{\approx}{F}_k)^{-1}$ in (5.20). The dimension of this matrix corresponds to the number of model parameters. In this study 567 model parameters are to be inverted. Calculataing the inverse of matrix of this size may require a fairly large computation time. Tarantola [1984a] suggested approximating the inverse by $\alpha\underset{\approx}{I}(0<\alpha<1)$, where $\underset{\approx}{I}$ is the identity matrix. However, such an

approximation is similar to the use of a large damping factor or a steepest descent method for non-linear inverse problems. That is, the results should be extremely stable but with a poor resolution and a slow convergence of iterations. This may eliminate the virtue of the good sensitivity of non-linear inverse problems. Thus, in this study we solve this symmetric inverse matrix $(\underset{\sim}{I}+\underset{\sim}{C}_m\underset{\sim}{F}_k{}^t\underset{\sim}{C}_\phi{}^{-1}\underset{\sim}{F}_k)^{-1}$ for 567 model parameters directly by the Cholesky decomposition [Lawson and Hanson, 1974] even though it involves some computation time. This problem on the shape of the inverse matrix (or damping factors) will be discussed further in examples below.

The choices of the data and model covariance operators are the same as those of Tarantola [1984a]:

$$C_\phi(\underset{\sim}{r}_g,\omega;\underset{\sim}{r}_s|\underset{\sim}{r}_g',\omega;\underset{\sim}{r}_s') = \sigma_{gs}^2\delta_{gg'}\delta_{ss'} \tag{5.21}$$

and

$$C_m(\underset{\sim}{r},\omega;\underset{\sim}{r}') = \frac{1}{(2\pi)^{1/2}}\frac{\sigma_m^2}{a}\exp[-\frac{1}{2}\frac{(\underset{\sim}{r}-\underset{\sim}{r}')^2}{a^2}] \tag{5.22}$$

where σ_{gs} represents the errors in the seismogram for the g-th receiver from the s-th source, and the errors among different seismograms are assumed to be uncorrelated. σ_m represents the a priori estimate of error in the model parameters, and a is the scale length within which the model is expected to be smooth.

The form of the model representation of the phase velocity field is one of the important factors for good inversion results. For describing lateral heterogeneity in surface wave phase velocities, regionalized or spherical harmonic models have been widely employed. Since the phase velocities at the periods in this study show a good correlation with lithospheric age [e.g., Forsyth, 1975], we employ a regionalized oceanic model as an initial model. We then invert the velocity perturbations to this initial model as in the

study by Nishimura and Forsyth [1985]. In order to avoid the bias in the modelling and to get an improved resolution, the Pacific Ocean is divided into 567 5°x5° meshes. This modelling might be too fine for the path coverage of the present study, but such problems are overcome by the introduction of smoothing by the Gaussian filter in the model covariance matrix (5.22). The representations (5.21) and (5.22) are specified under the assumption that errors follow a Gaussian distribution. While the errors in the data, σ_{gs}, can be estimated, the errors in the model parameters, σ_m, must be assumed a priori. We shall vary the values of σ_m and see how the resolution or the speed of convergence changes. The ratio of σ_m to σ_{gs} is directly related to the resolution and the speed of convergence of the solutions.

5.2 Data

We collected vertical component Rayleigh waves from WWSSN stations for 18 events which occurred along the margin of or within the Pacific Ocean basin. These events were selected by the criteria that the focal mechanisms are known from previous studies that the source process seems to be fairly simple. Source parameters used for the inversions are listed in Table 5.1. Since we use data on both amplitude and phase in the sense of the single-station method (e.g., section 11.2.5 of Aki and Richards [1980]), the accuracy of these source parameters may affect the final results of the structure significantly. These parameters were basically determined from the first motion polarities of P and S waves or from waveform analysis of body waves. The mechanisms were checked against the Rayleigh wave radiation pattern using the data collected in this study. Some of the mechanisms (e.g., April 8, 1973) in the references are inconsistent with the surface wave radiation patterns. In these cases, we corrected some parameters,

especially strike and depth, to fit the surface wave data. The observed amplitudes and phases are both strongly sensitive to source parameters for the case in which the azimuth of a path to a station is close to the nodal direction for surface wave radiation. We therefore eliminated data at stations within about 10° of the nodal azimuth in order to confine our study to fairly reliable initial phases and radiated amplitudes. Also, we used data only from propagation paths primarily within oceanic structure and paths with large segments within continents, or along island arcs, trenches or continental margins were avoided. (Such data were used nonetheless for the checks on focal mechanism.) In Table 5.2, as one example, we list the stations which were used for each event for the inversion of 40-s Rayleigh waves.

All the digitized seismograms were interpolated at an interval of 1 s [Wiggins, 1976]. Each digitized time series was then fast-Fourier-transformed and corrected for instrumental response. To reduce the effect of scattering by fine or complex lateral heterogeneities and of noise, the amplitude and phase spectra were smoothed by taking running averages over three adjacent points in the frequency domain. This procedure corresponds to filtering the data in the frequency domain with a box-car function $3\Delta f$ wide where Δf is the frequency interval of the data points in each spectrum. We then discarded portions of some spectra by inspection if the spectra were not smooth and appeared to suffer from severe multipath effects. In some spectra there are holes at certain frequencies because the combined effect of the focal depth and source mechanism [e.g., Tsai and Aki, 1970]. The parts of spectra near such holes were not used because they are too sensitive to the choice of source parameters. The fluctuations in the spectra at periods less than about 25 sec are large in most of the data and the excitation of

Rayleigh waves of periods longer than 100 sec are weak for earthquakes of the size used in this study. The range of periods for inversions was therefore between 30 and 80 sec. The number of data which were used to invert for phase velocities at each period is summarized in Table 5.3. In the appendix are given the data used for inversions and the radiation patterns of all earthquakes included.

The Earth model used to calculate excitation functions is model 8099 of Dorman et al. [1960] for all of the examples in this study. We adopted a point source approximation and the step time function approximation which is appropriate for the sizes of the earthquakes and the frequency range of this study. In the period range of the present study (i.e., 30-80 sec) it is sometimes difficult to resolve the phase ambiguities by 2π in the data. Since we used data whose propagation paths are almost purely oceanic, for most of the cases we could trace the phase cycles after path corrections with the simple homogeneous 8099 model (see one example of the data in Figure 5.1). If this procedure proved difficult, we discarded such a datum.

Figure 5.2 shows the path coverage of 40-s Rayleigh waves. The paths used for inversions at different periods are very similar. Even though some parts of the Pacific Ocean are not well covered (e.g., east of New Zealand), overall the number of rays scanning each model block is considered to be sufficient. Since amplitudes depend mainly on the spatial second-derivatives of phase velocity perpendicular to the paths, a good azimuthal coverage for each model block is important to achieve good resolution. From this point of view, the present azimuthal coverage of ray paths seems also to be sufficient. The resolution and the estimation of errors in the results will be discussed later.

5.3 Phase Data Inversions

As discussed before, phase differences between data and synthetics for the initial model must be quite small (less than π) to get reliable solutions from the inversion of both phases and amplitudes. With surface waves of the periods in the present study, such phase differences after path corrections with the initial regionalized model are sometimes large, even for an oceanic region (see Appendix). Therefore, in an effort to reduce these discrepancies, a conventional inversion of phase anomalies was attempted first. Also, this gives a good comparison of the present method with the conventional phase delay technique.

Model parameters for the initial regionalized model are summarized in Table 5.4 and shown in Figure 5.3. Lithospheric ages are from Sclater et al. [1981]. For the phase data inversions, phase perturbations are expressed as

$$\begin{aligned} \delta\phi_{sg} &= -\int_{\Gamma} \frac{\delta c(\underset{\sim}{r})}{c^2(\underset{\sim}{r})}\, d\Gamma \\ &\simeq \sum_i \left(-\frac{\Delta\Gamma_i}{c_i}\right)\frac{\delta c_i}{c} = \sum_i \left(-\frac{\Delta\Gamma_i}{c_i}\right)\delta(\ln c) \end{aligned} \tag{5.23}$$

where Γ is the great circle connecting a source (s) and a receiver (g). The summation of the second equation represents that over blocks through which the great circle passes, and $\Delta\Gamma_i$ is the path fraction through the i-th model block. Thus, the Fréchet derivative is $-\Delta\Gamma_i/c_i$, and because of the linearity of this method we need perform the inverse calculation (5.20) only once. We chose the smoothing scale a of model parameters in (5.22) to be 10° of arc. This value may be reasonable from the size of heterogeneity estimated in the next section.

The data variance σ^2_ϕ ($= \sigma^2_{gs}$) and model parameter variance σ_m^2 should be different for each datum and each model parameter. Data covariances are determined by the quality of data (i.e., signal-to-noise ratio) and the

uncertainty of the source parameters. For this example, we simply assumed that errors in the data are uncorrelated and are constant. The magnitudes of errors in surface wave phase delays over the period range of this study have been estimated by several workers [e.g., Forsyth, 1975; Patton, 1976]; overall the errors are around 5 sec, that is, $\pi/4$ for 40-sec Rayleigh waves. As shown in the appendix, some of the phase anomalies relative to the initial regionalized model are larger in magnitude than this value. In the later error analysis, we shall use a constant value of the covariance of the data, σ^2_ϕ, determined from the data residuals for the inversion solution.

Model covariances were estimated a priori. One way to estimate these values is to draw a trade-off curve in error-residual space with various values of model covariances and pick the optimal point closest to the origin [Backus and Gilbert, 1970]. Since this procedure takes considerable time if we do it for each point, we assumed instead a constant value of $\varepsilon^2 = \sigma_\phi{}^2/\sigma_m{}^2$ and find an appropriate value by changing ε^2 in the simple diagram of model norm versus residual norm instead of following the formal Backus-Gilbert procedure with calculation of resolution kernels [e.g., Tanimoto, 1984].

In Figures 5.4, results for velocity perturbations from the initial model, $\delta c/c$, are shown with various damping factors ε^2. Note that the contour interval is variable. A plot of relative residual (solution norm) versus model norm for various ε^2 at each period is shown in Figure 5.5. The smaller the damping factor, the better the resolution obtained, but because of the inconsistencies in the present data set many unstable features are observed in the solutions for such cases. Also, in such cases, computational errors may be severe. (At 40 sec the residual is slightly larger in the case of $\varepsilon^2 = 2 \times 10^6$ than in that with $\varepsilon^2 = 3 \times 10^6$). On the other hand, with a large damping factor the results show only the gross character of the

velocity perturbations. Because of the small values of both solution and model norms, the results with $\varepsilon^2 = 2\sim4 \times 10^6$ are judged to be the most appropriate. The adopted values of ε^2 are marked with circles in Figure 5.5.

Standard errors of residuals for both the initial model, σ_0, and the inversion solution, σ, are summarized in Table 5.5. Variance reductions, $(\sigma^2{}_0-\sigma^2)/\sigma^2{}_0$, for the present inversions are also given in this table. In the initial model, standard errors are larger at shorter periods, which implies that variations of phase velocities at shorter periods are more significant. After phase data inversions, standard errors are almost the same at each period. Patton [1980] summarized standard errors of phase data inversions in the present range of periods. Our standard errors are of similar magnitude to those of Patton for Eurasia but larger than those of Forsyth [1975] for the Nazca plate. Since areas in this study include the marginal seas in the western Pacific where velocities are fairly different from the neighboring subduction zones, our results may have a larger scatter of data residuals. Another possibility is an error of source parameters.

The inversion solutions for phase velocity variations at 30, 40, 60 and 80 s are shown in Figure 5.6. From these solutions, we see that the marginal seas in the western Pacific are slower than in the initial model while in the western and southern Pacific basin velocity is faster. This is reasonable because of systematic deviations obvious in the data, such as the Samoa event, of September 27, 1972 (see Appendix): stations to the east of the source show positive velocity anomalies while there are negative velocity anomalies at stations west of the source. Low velocity in the vicinity of the Hawaiian hot spot can also be detected. However, we need to check the reliability of such an anomaly.

To check which parts of the solution are reliable, we estimated uncertainties of the model parameters at each point. Since the present

procedure is a kind of damped least-square method, the standard error of the i-th model parameter, σ_i, is expressed by

$$\sigma^2{}_i = [\underset{\sim}{C}_m(\underset{\sim}{I}+\underset{\sim}{C}_m\underset{\sim}{F}^+\underset{\sim}{C}_\phi{}^{-1}\underset{\sim}{F})^{-1}]_{ii} \qquad (5.24)$$

where $[\underset{\sim}{C}_m(\underset{\sim}{I}+\underset{\sim}{C}_m\underset{\sim}{F}^+\underset{\sim}{C}_\phi{}^{-1}\underset{\sim}{F})^{-1}]_{ii}$ is the i-th diagonal component of $\underset{\sim}{C}_m(\underset{\sim}{I}+\underset{\sim}{C}_m\underset{\sim}{F}^+\underset{\sim}{C}_\phi{}^{-1}\underset{\sim}{F})^{-1}$ and F is the Fréchet derivative matrix given by (5.23). Data variances $\sigma_\phi{}^2$ at each period were calculated from data residuals and are given in Table 5.5. Figures 5.6 give the reslts at each period. With the uncertainties we can judge whether a specific anomaly in the results is reliable or not. Compared with Figure 5.4c, Figure 5.6b shows that most features obtained in the inversions are smaller than the size of the uncertainties. The low velocity in the marginal seas of the western Pacific is still clear by this measure and may be reliable. In the Pacific plate two low velocity areas are detected at each period: one is just southeast of the Hawaiian Islands and the other is east of Samoa. These are considered to be related to the upward flow of hot material beneath hot spots. The low velocity area southeast of the Hawaiian Islands provides fairly strong evidence for the hot spot hypothesis [Morgan, 1971]. Nishimura and Forsyth [1985] pointed out two low velocity areas in the Pacific Ocean using Love waves: one is around French Polynesia and the other is at the Gilbert Islands. Our results contain the latter anomaly. However, the former anomaly may be identified but is fairly obscure. There is a suggestion of a pattern of velocity variation aligned in the WNW-ESE direction, parallel to the motion of the Pacific plate. However, the number of collected raypaths in this direction is greater than that near the north-south direction (see Figure 5.1), so such a pattern may be the result of sampling bias in our inversion.

In Figure 5.7, we show the resulting laterally variable phase velocity

at each period from the phase data inversions, that is, the initial model (Figure 5.3) plus perturbations (Figure 5.6). Hereafter, we shall call this phase data model "model PP". Figure 5.8 shows an example of an improvement in the discrepancy of the phase data before and after inversion. This model PP is a starting model for amplitude-phase inversions with ray-tracing in the next section. We must, of course, check whether or not this model can predict the amplitude patterns in the data.

5.4 Amplitude-phase inversions

In the previous section, we assumed that the surface waves propagate along great circles. That is, phases are determined by the integration of slowness along great circles and amplitudes are calculated from simple geometrical spreading: amplitudes decay as $r^{-1/2}$, where r is a travel distance. Even in this simple example of the Pacific Ocean the obtained 'model PP' contains some amounts of lateral heterogeneity and we need to check the validity of the above assumptions. Hereafter, we shall investigate the phase and amplitude variations with model PP as a starting model.

At first, let us compare the results obtained via the above simple path corrections with more rigorous corrections; i.e., using phase and amplitude calculations for model PP by the paraxial ray approximation or the Gaussian beams method. Also, the attenuation factor, Q, is now varied as a function of ocean lithospheric age as shown in Table 5.4. Figure 5.9 shows one example of ray tracing (for an event on December 6, 1965 at 40 s period), and a comparison of the results of the simple path correction with those of the ray-traced correction is given in Figure 5.10. We notice that in some cases ray paths deviate significantly from great circles. In this example amplitudes and phases at the stations in South America (azimuth 120°-180°) are not very different from those predicted with the simple path corrections.

However, rays to stations in the southwestern Pacific are distorted in complicated patterns. In fact, some large anomalies in the data, especially in the amplitude data, are observed at such stations. In the comparison of phase residual plots in Figure 5.10, all the phases are slightly advanced in ray-traced paths (Figure 5.10 b) compared with great circle paths. Such a tendency is observed in most of the other data except for a few data at stations where ray paths are strongly distorted. This is reasonable because, according to Fermat's principle, travel times (i.e., phase delays) along the actual ray paths are extreme and usually minimum. This result is contrary to that of a similar travel time comparison for longer-period surface wave models by Schwartz and Lay [1985] as discussed in Chapter 1 (Figure 1.3). The above phase advance means that calculations in which propagations are assumed to be along great circles may give slightly higher phase velocity values.

Now we shall remark some methodological aspects of these calculations. As mentioned above, we evaluated amplitudes and phases by both the paraxial ray approximation and the Gaussian beam method. For the example of Figure 5.10, the paraxial ray approximation gave almost same values as those by the Gaussian beam method at the stations in South America. However, at some stations in the southwestern Pacific where rays are distorted complicatedly the paraxial ray approximation gave inaccurate results compared to the Gaussian beam method. Although the paraxial ray approximation requires less computational time and do not contains some ambiguous parameters such as beam parameters, we have to use this method with careful checks.

Before showing the results of inversions with phase and amplitude data, let us mention the statical character of the present data set briefly to check the applicability of the methods developed in the previous

chapters to the present problem. The basic assumption in our methods are use of asymptotic ray theory: the wavelength has to be shorter than the scale of heterogeneity (2.21) and the receiver must be within the first Fresnel zone (2.22). The unknown parameter here is the scale length of heterogeneity. In cases where the Born approximation is valid (weakly scattering media), Chernov [1960] gave the following formula for the normalized autocorrelation function of heterogeneity:

$$N(\underset{\sim}{r}) = \langle \mu(\underset{\sim}{r}')\mu(\underset{\sim}{r}'+\underset{\sim}{r})\rangle / \langle \mu^2 \rangle = e^{-|\underset{\sim}{r}|^2/a^2} \tag{5.25}$$

($\mu = -\delta v/v_0$ and $\langle\ \rangle$ represents the average over the whole medium):

$$\frac{\langle |\Delta\phi|^2 \rangle}{\langle |\Delta \ell nA|^2 \rangle} = \frac{D + \tan^{-1}D}{D - \tan^{-1}D} \tag{5.26}$$

where D is called the 'wave parameter' (the ratio of the size of the first Fresnel zone to the scale length of heterogeneity):

$$D = \frac{4L}{ka^2} \tag{5.27}$$

where L is the travel distance. The variable a, the correlation distance of heterogeneity, may correspond to the scale of the smoothness in the model covariance matrix (5.22). Thus, we can estimate the scale length of heterogeneity by the variance of the phase and amplitude data. In Table 5.6, we summarize variances of the present data set and estimated parameters from the above formulations. The phase and amplitude variances in this table are with respect to the path corrections calculated by the paraxial ray approximation and the Gaussian beam method for model PP and the adopted focal mechanism parameters described later. Even though these are not direct measures of the data but are values after phase data inversion, they may show the gross character of the present data.

In Table 5.6, variances of logarithms of amplitude are much smaller than those of phases, especially for shorter periods. The wave parameter D is equal to or less than 1. In contrast, in the teleseismic P wave measurements across the Montana LASA by Aki [1973] the standard deviations of phases are comparable to those of logarithms of amplitude and wave parameters in most cases as large as 2. This means that the medium in this study is less heterogeneous. The obtained correlation distances in our case are about 10 degrees irrespective of periods. This implies the validity of our previous choice of the smoothing scale length in the model covariance matrices (5.22) as 10 degrees. The values of wave parameters and correlation distances show that ray theory is applicable to the present data set even though for the longer periods there may be some risks in the first Fresnel zone assumption (2.22). More illustratively, we plot in Figure 5.11 the locations of the present data set in ka (wavenumber x correlation distance) versus kL (wavenumber x travel distance), following Figure 13.11 of Aki and Richards [1980]. This diagram shows clearly that the present problem is within the range of ray-theoretical approach. Because the data for 80 sec surface waves are near the border of the 'ray-theoretical approach' region, we feel that the validity of the ray-theoretical approach to much longer period surface waves is suspicious. For multi-orbit surface waves (e.g., R5 and R6) ray-tracing may be meaningless. One remedy to the use of a ray-theoretical approach in studies of longer period surface waves is to reduce the travel distances. In the case of sharp structural transitions such as an ocean-continent boundary, the present method may not be applied because the correlation distance, a, is much smaller than the present case.

Back to the original problem, let us invert the velocity structure using both amplitude and phase data with model PP as a initial model. With

amplitude and phase calculated from ray theoretical seismograms for model PP, systematic anomalies are detected for some events, especially in amplitude data. Figure 5.12a shows one peculiar example for an event on September 9, 1971. In this example, amplitude anomalies at the longer periods are systematically positive while those at the shorter periods become negative. These kinds of anomalies are considered to be due to inadequacy of the employed source parameters rather than to heterogeneity of the medium. Therefore, we changed some source parameters to eliminate such systematic anomalies. In particular, seismic moments which are important in evaluation of amplitude anomalies, were obtained from inversion of our data for each event. Other parameters were revised by trial-and-error searches, because the poor azimuthal coverages for most of the events prevented us from performing formal inversions. For example, for the event on September 9, 1971 shown in Figure 5.12a, the dip angle was reduced from 82° to 59°. The radiation patterns and phase data for the revised source parameters in this event are shown in Figure 5.12b. In Table 5.1, the corrected values are given in parentheses. With these corrections, amplitude anomalies are reduced in some case (up to 20% variance reductions in the logarithms of amplitude) but the phase anomalies do not change much. We shall not modify with source parameters further in this study. Detailed investigations on the effects of errors in source parameters to the final velocity inversion results are required in future works.

Since in the present problem the response to velocity perturbations is non-linear, the initial or 'a priori' model plays an important role, as emphasized by Tarantola [1984b]. We already know the gross features of lateral heterogeneity, such as the age-dependent model. Since this initial model is laterally heterogenous, analytical forms of Frechet derivatives

(5.18) do not exist and we have to calculate them numerically at each model point with ray-theoretical seismograms. Moreover, we have to recalculate Fréchet derivatives at each iteration. This process took most of the computational time (up to 80 % of the whole calculation). For each iteration the estimated computational time with the VAX 11/780 is about 18 hours for the present number of model parameters and data. Figures 5.13 shows some typical features of Fréchet derivatives calculated for model PP. Unlike derivatives (5.23) in ray theory, which are non-zero only along the ray paths, these derivatives have finite widths on both sides of ray paths. This is because we employed wave theory in the inversion formulation and included the effects of finite wavelength, while ray theory assumes infinitesimal wavelength. One important feature is that the regions of non-zero derivatives are narrower as the period is shorter (i.e., higher frequency) and closer to the case of ray theory. For the station-receiver pair in Figures 5.13 a) and b), derivatives are close to the forms for the laterally homogeneous case (e.g., see Figure 13.9 of Aki and Richards [1980] with an opposite sign and without side lobes), and the present size of model meshes may be sufficient, especially for the case of 80s. However, in the case of Figures 5.13 c) and d), erratic features may be noticed: there are some curious bumps oblique to the ray path. This may be due to the deficiency of our model specifications. In this case the ray path is oblique to the direction of model meshes and we cannot simulate the shape of the Frechet derivatives well with the present mesh specification. Especially in the case of shorter periods (i.e., shorter wavelength), we need much finer meshes to calculate derivatives accurately. The results of inversions at 30 sec, given below, do not appear to be as accurate as good as for other periods because of this modelling deficiency. Due to a limit on computation time, in this

study the adopted mesh size is effectively a lower limit.

Using these derivatives we inverted phase velocity perturbations with the formulation (5.20). Once again, a primary problem is the choice of data and model variances, σ_{gs}^2 and σ_m^2 in (5.21) and (5.22), similar to the case of phase velocity inversions in the previous section. At first, we simply assumed that variances (or weights in this case) of the data are constant and used the values given in Table 5.6. The ratio of variances of logarithm of amplitude to those of phase were thus different at different periods. The size of variances in the travel times are basically independent of period as shown in Table 5.5 and the phase variances, which are products of frequency and trave time variances, are larger at the shorter periods while amplitude variances are almost constant among different periods. Therefore, in this study we put more weight on amplitude data at shorter periods. The choice of model variances followed procedures similar to those we used in the phase data inversions in the previous section: with various damping factors, that is, ratios of data variances to model variances, we plotted model norm versus residual norm and found a point close to the origin. For example, in Figure 5.14 we show results of inversion with one iteration at 60 sec with three different damping factors. The effects of dampings are similar to the case of phase data inversions in the previous section: with a bigger damping factor, velocity perturbations are small and broad but the most reliable features are observed, while with a small damping factor detailed features emerge but these are erratic in some cases. The damping factor in this section is defined as a reference of variances of logarithms of amplitude: $\varepsilon^2 = \sigma_{\ln A}^2/\sigma_m^2$.

Figure 5.15 is a residual norm versus solution norm diagram at 60s period, similar to Figure 5.5. Note that the residuals in this figure do not

correspond to those for the inversion models but simply to the products of Fréchet derivatives and model perturbations because of the nonlinearity of the present problem. In this study we chose $\varepsilon^2 = 1.5 \times 10^4$. One remark is that we cannot compare this value to that for phase data inversions in the previous section because we used travel time (second) as a unit of data variance in the previous section while here the data variance is that of logarithms of amplitude, which is non-dimensional. Similarly, we chose values of damping factors to be 3.5×10^4, 2.0×10^4 and 3.5×10^3 for 30, 40 and 80 sec, respectively. Because we need to repeat the above procedure and Frechet derivatives are changed at each iteration step, it is quite difficult to predict an optimal size of damping only by the results of the first iteration. Observing the obtained final results, we feel that with the above damping factors the results at 60s were slightly overdamped and those of 80s were underdamped compared to the quality of data. Thus, in the following results we should not pay much attention to the magnitute of perturbations but only their pattern. Another way to estimate the optimal model variances is the use of statistical character of the data. Following the Chernov [1960]'s scattering theory, we can estimate the variance of model perturbations by the variances of phase and amplitude data (5.26). At each period, an estimated model variance is about 1.2 %, which is close to the choice of this study.

After the first iteration, we need to shoot rays, recalculate data residuals and evaluate Fréchet derivatives for each model parameter in the obtained perturbed model. The calculation of further perturbations was made using the formulation (5.20). From the second iteration we need one additional term in the right-hand side of (5.20), $m_k(\underset{\sim}{r}) - m_0(\underset{\sim}{r})$, which never appears in linearized inverse schemes. It may be worthwhile in our problem

to show the importance of this term.

Equation (5.20) is derived so that we are going to minimize the following quantities at the k-th iteration:

$$(\underset{\sim}{\phi} - \underset{\sim}{f}(\underset{\sim}{m}_k))^+ \underset{\approx}{C}_{\phi}^{-1} (\underset{\sim}{\phi} - \underset{\sim}{f}(\underset{\sim}{m}_k)) + (\underset{\sim}{m}_{k+1} - \underset{\sim}{m}_0)^+ \underset{\approx}{C}_m^{-1} (\underset{\sim}{m}_{k+1} - \underset{\sim}{m}_0) \quad (5.27)$$

where $\underset{\sim}{f}(\underset{\sim}{m}_k)$ is the data prediction of model $\underset{\sim}{m}_k$. $\underset{\sim}{f}$ is related to the Frechet derivative as $\underset{\approx}{F}_k = [\partial \underset{\sim}{f}/\partial \underset{\sim}{m}]\underset{\sim}{m}_k$. The first term is the L_2-norm of the data residuals weighted by the data covariance matrix $\underset{\approx}{C}_{\phi}$ and the second term is L_2-norm of the model perturbations from an 'a priori' model weighted by the model covariance matrix $\underset{\approx}{C}_m$. Thus, this expression is a natural extension of the Backus-Gilbert approach of linearizing to non-linear problems: to overcome the non-uniqueness in geophysical problems with combining the common sense to minimize the departure from the initial guess. However, if we use a formulation similar to the Backus-Gilbert approach in non-linear problems at each iteration step without the above term, we are in fact minimizing the quantity of

$$(\underset{\sim}{\phi} - \underset{\sim}{f}(\underset{\sim}{m}_k))^+ \underset{\approx}{C}_{\phi}^{-1} (\underset{\sim}{\phi} - \underset{\sim}{f}(\underset{\sim}{m}_k)) + (\underset{\sim}{m}_{k+1} - \underset{\sim}{m}_k)^+ \underset{\approx}{C}_m^{-1} (\underset{\sim}{m}_{k+1} - \underset{\sim}{m}_k) \quad (5.28)$$

at the k-th step [Tarantola, 1984b]. In this case the norm of model perturtions is measured from the model of the previous iteration, while we measure the departure from an 'a priori' or initial model in the former case. Thus, as iterations are repeated, models may behave freely from the 'a priori' model in the latter case. In Figure 5.16 we show the velocity perturbations obtained after the second iteration from the first iteration model at 60 sec a) with and b) without the additional term. The damping factor is the same as in the first iteration. The additional perturbations in Figure 5.16 b) have a pattern to the first iteration (i.e., Figure 5.14 c)

and they give smaller data residuals. However, there are some fine-scale troughs and peaks and if we overlapped these to the first iteration model, the total perturbations from the initial model become chaotic. This is because in this case we are inverting the velocity perturbations independently at each iteration. On the other hand, with the 'total inversion' of Tarantola and Valette [1982] the results are generally different. For some regions the second term is dominant over the first term (data residual parts) on the right-hand side of (5.20), and the second velocity perturbations have a pattern opposite to that of the first perturbations. This phenomenon can be observed well in the areas northeast of New Zealand where there are large-amplitude and fine-scale but probably erratic variations in the first iteration solution (Figure 5.14 c)). Such features are suppressed by the second iteration and the total perturbations become more reliable. If we use the 'total inversion' of Tarantola and Valette [1982], solutions never behave chaotically from an a priori model even in a non-linear problem. This scheme guarantees at least that the solution is the best one around the a priori model.

Because at each iteration the departure from the a priori model depends on the model covariance, it may be better to keep the model covariance (i.e., damping factor) constant to get a consistent result. In some cases a matrix whose inverse is used in the formulation (5.20) has small eigenvalues which give huge perturbations at several isolated model points. In order to obtain stable calculations, we add extra damping to the diagonal components corresponding to such points.

Figures 5.17 and 5.18 exhibit one example (at 40 s period) of iterative procedures in this study. Figure 5.17 shows velocity perturbations from the a priori model, that is, model PP, at each step while Figure 5.18 shows

perturbations from the model of the previous iteration. Note that in Figure 5.18 contour line intervals become generally smaller as the number of iterations increases. This implies that the magnitude of additional perturbations is reduced each time and the solutions seem to converge. As with Figure 5.16 at 60 s, in this example the small erratic perturbations are also suppressed in the process of iteration. Figure 5.17 shows a clear view of the process of solution convergence.

It may be difficult to decide the optimal choice of the number of iterations. In Table 5.7, we summarized the variance reductions at each iterative step compared with the initial model. This table also includes the standard errors for both logarithms of amplitude and phases. At every period, the principal variance reduction occurred at the first or second iteration and was minor thereafter. At 30 s period the variance became larger in the first iteration and the inversion seemed to have failed. However, after the second iteration, the variance started to be reduced normally. At 80 s period even the first iteration reduced the variance greatly. In general, the variance was reduced more at longer periods. Here we used a simple statistical estimation of the significance of variance reductions. We compared two variances, of the starting model and of the specific iteration, and checked whether there was a significant difference between these two values by the F-test. In this study the number of model parameters is difficult to be defined because we assumed the correlation among neighboring points in the model covariance matrix (5.22). From the correlation distance of 10 degrees in this study, we assumed that the independent model points were about one-quarter of the 567 total model points. Since the total data number (i.e., amplitude + phase) is about 400, here we set the degree of freedom at about 250. In this case, to reach a 95%

significance level, variance reduction should exceed about 20%; it should exceed about 30% for a 99% confidence level. In our example, after three iterations the variance reductions exceeded 95% confidence level and by the normal statistical measures we judged that about 3 or 4 iterations are sufficient.

Figure 5.19 shows the final results of amplitude-phase inversions at each period after five iterations. At the bottom of each figure is an estimate of uncertainty at each model point. In non-linear problems, there is no simple way to estimate uncertainties of model parameters. For these figures we simply use the formulation (5.24) for the estimation of uncertainty for linear problems. Because of non-linearity, it is possibile that some local minima are not included in the above linear estimation of uncertainties.

Because the contour intervals are the same for the velocity perturbation maps, it is easily seen that the magnitude of the perturbations are different for different periods. In particular, the results at 60 s period show modest and broad-scale perturbations while at 80 s period the perturbations are larger and contain many shorter wavelength features. As mentioned before, this result does not relate to a real frequency dependence of velocity perturbations but may be caused by the different choices of damping factors: the ratio of data covariances to model covariances. At a period of 60 s, the selected damping factor may be larger than the optimal value, resulting in reduced amplitudes and suppressed short wavelengths in the phase velocity perturbations. On the other hand, at a period of 80 s the selected damping factor may be too small, resulting in large and unrealistic perturbations. In fact, model uncertainties at 80 s are twice as large as those at 60 s. If we measure the size of the perturbations in units of the estimated

uncertainty, features in the solutions at both periods do not look as different as shown in Figure 5.20. The size of the damping factors at 30 and 40 s may be appropriate, and we obtained fairly reliable velocity anomalies of moderate size.

One important result may be obtained if we compare Figure 5.6 and Figure 5.20. Compared with the model uncertainties from the phase data inversions, the amplitude-phase inversions yield smaller uncertainty values. This means that the present inversions have better resolution. Since the uncertainty levels shown in Figure 5.19 may be smaller than the real uncertainties, however, this statement should be regarded with care. Aside from the local minimum problem, we nonetheless conclude that amplitude-phase iterative inversion gives more reliable results than conventional phase data inversion. It is remarkable that at 80 s period the amplitude-phase inversion gives velocity perturbations which reduce the perturbations obtained after the previous phase data inversion. In the central Pacific Ocean, from Hawaii to the east of New Zealand, there are east-west trending velocity anomalies in model PP, and the present inversion yields perturbations with opposite features. The actual phase velocity anomalies may not be as strong as the variations in model PP; the amplitude-phase inversion apparently corrected such errors in model PP. The present velocity anomalies patterns are surprisingly similar to those for Love waves obtained by Nishimura and Forsyth [1985]. Some low velocity areas correspond to hot spots, for example, the Gilbert Islands and French Polynesia. The Hawaiian hot spot does not appear in these results.

The final results of phase velocity inversion are summarized in Figure 5.21 at each period. At the top, we show the obtained phase velocity fields which we shall call 'model AP', and at the bottom we show the total

perturbations from the original age-dependent model, that is, the sum of perturbations from the phase data inversion and the amplitude-phase inversion. Overall, the following features are observed. The velocity of the marginal seas in the west Pacific Ocean is relatively low compared with the Pacific plate, even accounting for the young seafloors age. Low velocity areas are fairly well correlated to hot spot locations such as the Gilbert Islands, Samoa, French Polynesia, and the Hawaiian Islands. However some anomalous areas are not related to specific tectonic features: for example, a low velocity area off the coast of California and a high velocity area north of the Hawaiian Islands.

Figures 5.22 and 5.23 show some examples of improvements in the fit of data to model predictions before and after phase velocity inversions. Figure 5.22 shows ray paths and the fit of data to predictions with model AP at 40 s period for an event on December 6, 1965, which can be compared with the situation before inversion in Figure 5.10. Because the velocity perturbations are on the order of a few percent, ray paths vary only slightly. However, in this example the locations of caustics in the western Pacific were slightly shifted, which gave large amplitude differences at some stations such as Riverview and Port Morseby. In comparison with Figure 5.10 b) fairly significant improvements of the fit of amplitude and phase data are observed. Since the paths go through the fairly simple regions, phase and amplitude perturbations are small and correlated each other at the stations in South America. This agrees with the theory on weak heterogeneous media by Chernov [1960]. On the other hand, amplitude data at some stations in the southwest Pacific show the nonlinear response to model perturbations and behave independently compared with phase data.

We show four typical examples of improvements of fittings in Figure

5.23. In Figure 5.23 a) the scatter in the fit of amplitude data is generally reduced, but the phase data are not greatly improved. Figure 5.23 b) is one example in which the original anomalies were small and the final residuals are as well. Figure 5.23 c) shows a satisfactory result for both phase and amplitude anomalies. Figure 5.23 d) is an example in which the present inverse scheme did not work well. In this example there are still strong amplitude anomalies at several stations after inversion. In the last two examples there may be different causes for the amplitude anomalies. One possibility is large anomalies in the attenuation factor "Q" along the ray paths.

Even though there are some anomalies which could not be explained by the present inversions, most anomalies were reduced and the fit of data to model predictions was significantly improved. With the use of logarithms of amplitude instead of amplitude itself, as in this study, the response of amplitude data to velocity perturbations is not as unstable or useless as previously expected. Up to now, most seismologists have neglected amplitude information in studying velocity structures. This study suggests, however, that such data have the potential to improve the resolution of heterogeneity in the Earth, which is also independent of phase data.

Table 5.1. Source parameters of the earthquakes included in the Rayleigh wave inversions. Parameters in brackets are revised versions used for amplitude-phase inversions.

Date	Time	Latitude °N	Longitude °E	M_S	Depth[a] km	ϕ[b] deg	δ[b] deg	λ[b] deg	$M_0 \times 10^{25}$ dyn·cm	References[c]
August 18, 1964	0445:02	-26.37	-71.78	6.2	48	235	41	92	2.6	1
December 6, 1965	1134:49	18.87	-107.18	6.0	2	112	90	178	8.5 (7.2)	2
November 12, 1967	1036:54	-17.19	-171.98	6.0	42	215	63	120	1.6	3
January 21, 1970	1751:37	7.03	-104.24	6.8	4	332	41	106	9.5 (8.7)	4
March 19, 1970	2333:29	51.34	173.75	6.2	20	125(100)	52(60)	-112	9.0 (7.3)	5
April 4, 1971	1015:37	-56.25	-122.46	6.6	7	110	90	0	10. (9.7)	6
September 9, 1971	2301:07	44.34	150.85	5.9	15	220	82(59)	-100	1.8 (2.0)	5
July 23, 1972	1913:09	50.10	-129.30	6.4	3	140(145)	90	180	3.5 (3.9)	7
September 27, 1972	0901:44	-16.47	-172.16	6.0	6(11)	207	65	-43	2.0 (2.7)	3
April 8, 1973	1241:03	-15.81	167.24	6.4	20	137	57	92	5.8 (5.4)	1
April 26, 1973	2026:27	20.05	-155.16	5.9	41(46)	3(11)	101(106)	150	4.7 (4.3)	8
September 18, 1973	1332:52	-54.52	-132.62	6.4	4	113	90	0	3.0 (2.7)	6
July 3, 1974	2325:09	-29.37	-176.13	6.6	15(4)	180(200)	40(25)	-79	7.0 (3.4)	5
August 25, 1974	0118:40	32.18	142.37	5.6	7(11)	174(181)	37	-114	1.0 (1.2)	5
March 29, 1976	0539:36	3.96	-85.88	6.5	8(10)	199(205)	82	181	6.2 (5.5)	4
December 20, 1976	2033:08	48.84	-129.13	6.7	3	130	90	180	10.	7
February 5, 1977	0329:19	-66.49	-82.45	6.2	15(10)	4	43(42)	74	3.6 (2.4)	9
October 17, 1977	1726:40	-27.93	173.13	6.7	11	266	77	12	19. (23.)	9

[a] Centroid depth below seafloor

[b] Strike ϕ, dip δ and rake λ follow the definitions of Aki and Richards [1980].

[c] (1) Chinn and Isacks [1983]; (2) Sykes [1967]; (3) Chen and Forsyth [1978]; (4) Bergman and Solomon [1984]; (5) Forsyth [1982]; (6) Stewart and Okal [1983]; (7) this study, (8) J.L. Nabelek, personal communication [1985]; (9) Bergman [1984].

Table 5.2 Stations used for the inversions of 40-sec Rayleigh waves.

Source	WWSSN Stations
August 18, 1964	AFI BKS CTA GIE GUA KIP WEL
December 6, 1965	AFI GIE HNR NNA PEL PMG RAB RAR RIV SOM TAU WEL
November 12, 1967	ANT ARE BAG BKS BOG COL COR CTA DAV GSC HKC HNR LON LPB MAT NNA PEL RAR RIV SHK TAU UNM
January 21, 1970	ADE BHP GUA HNR MAN PEL PMG RAB RAR RIV SBA SHK WEL
March 19, 1970	AFI BKS GUA KIP LON RAR
April 4, 1971	ADE ARE BHP BKS COL COR LPB LPS WEL
September 9, 1971	AFI BKS GIE GUA HNR KIP RAB
July 23, 1972	AFI CTA DAV HNR PMG RAB RAR
September 27, 1972	ALQ ANT BKS COL COR CTA DAV GIE GSC HKC HNR JCT LON LPB LPS PMG RIV TUC
April 8, 1973	ANT ARE BAG BKS BOG GIE HKC LPB MAN MAT SHK WEL
April 26, 1973	ALQ ANP ANT ARE BAG COL COR CTA DAV GIE GSC HKC JCT LON MAT NNA RAB RAR RIV SBA SHK TUC
September 18, 1973	AFI ALQ ARE COL COR CTA GIE GSC LON LPB PMG RIV TUC WEL
July 3, 1974	ALQ ANT ARE BOG GUA LON LPB NNA QUI SHK
August 25, 1974	AFI BKS DAV GIE GUA HKC HNR KIP MAN NNA PMG RAR TUC WEL
March 29, 1976	CTA HNR RAR RIV SBA WEL
December 20, 1976	ADE GUA MAN PMG RIV
February 5, 1977	AFI BKS COL LPS NNA TUC WEL
October 17, 1977	ANP ARE HKC LON LPB LPS NNA SEO SHK

Table 5.3 The number of paths used for inversions at each period.

Period (sec)	Number of source-station paths
30	191
40	200
60	232
80	219

Table 5.4 Initial model for inversions

Region / Ocean age (m.y.)	Phase Velocity,[a] km/s — Period (sec)				Group Velocity,[a] km/s — Period (sec)				Q^b — Period (sec)			
	30	40	60	80	30	40	60	80	30	40	60	80
0	3.775	3.79	3.83	3.93	3.76	3.71	3.64	3.62	173	137	116	129
3	3.81	3.81	3.848	3.94	3.83	3.76	3.67	3.63	174	144	118	131
10	3.86	3.88	3.885	3.96	3.95	3.87	3.74	3.68	180	151	120	133
15	3.915	3.91	3.908	3.975	3.97	3.92	3.79	3.70	187	154	122	134
20	3.94	3.925	3.925	3.985	3.98	3.95	3.82	3.73	195	158	123	136
30	3.97	3.95	3.955	4.00	3.99	3.99	3.87	3.76	205	164	125	138
50	3.995	4.00	3.995	4.028	4.01	4.02	3.92	3.81	218	171	127	140
75	4.025	4.01	4.03	4.048	4.02	4.05	3.95	3.85	223	173	128	140
100	4.045	4.04	4.05	4.073	4.03	4.08	3.97	3.88	226	175	129	141
150	4.06	4.07	4.065	4.09	4.04	4.10	3.98	3.92	227	176	130	140
200	4.07	4.09	4.08	4.10	4.05	4.11	3.99	3.95	229	177	131	140
North America	3.78	3.81	3.88	3.96	3.23	3.44	3.70	3.70	220	170	126	138
South America	3.84	3.86	3.97	4.09	3.20	3.31	3.67	3.73	220	170	126	138
Island	3.84	3.85	3.90	3.98	3.21	3.38	3.60	3.69	220	170	126	138

a) mainly after Forsyth [1975, 1977]

b) after Ben-Menahen [1965] and Canas and Mitchell [1978, 1981]

Table 5.5 Standard errors, σ, before and after phase data inversions and variance reductions (VR).

Period (sec)		30	40	60	80
σ (sec)	initial	18.7	17.0	16.5	14.9
	inverted	13.8	12.3	13.1	12.9
VR (%)		45.5	47.6	36.5	24.8

Table 5.6 Data variances and related parameters

period (sec)	30	40	60	80
$\sigma_{\ell nA}$	0.577	0.503	0.490	0.472
σ_{ψ}	3.10	2.14	1.47	1.23
D	0.478	0.620	0.950	1.15
k $(km^{-1})^a$	0.0525	0.0394	0.0263	0.0194
a $(km)^b$	1260	1280	1270	1340

a) The adopted phase velocities are 3.99, 3.99, 3.99, 4.04 km/s for 30, 40, 60, 80 sec, respectively.

b) The travel distance, L, is chosen to be 10,000 km.

Table 5.7 Standard errors of log amplitudes and phases and variance reductions after each iteration step.

Period (sec)		$\sigma_{\ell nA}$	σ_{ψ}	total variance reduction (%)	95% confidence level
	initial	0.577	3.10	----	
	1st	0.595	2.41	-5.01	x
30 s	2nd	0.531	2.39	16.0	x
	3rd	0.515	2.36	21.0	o
	4th	0.516	2.28	20.9	o
	initial	0.503	2.14	----	
	1st	0.482	1.74	9.63	x
40 s	2nd	0.461	1.71	17.2	x
	3rd	0.444	1.67	22.9	o
	4th	0.437	1.63	25.3	o
	initial	0.490	1.47	----	
	1st	0.458	1.23	14.3	x
60 s	2nd	0.449	1.18	17.8	x
	3rd	0.432	1.16	23.6	o
	4th	0.422	1.16	27.0	o
	initial	0.472	1.23	----	
	1st	0.432	0.834	21.1	o
80 s	2nd	0.404	0.817	30.3	o
	3rd	0.399	0.796	32.3	o
	4th	0.385	0.810	36.3	o

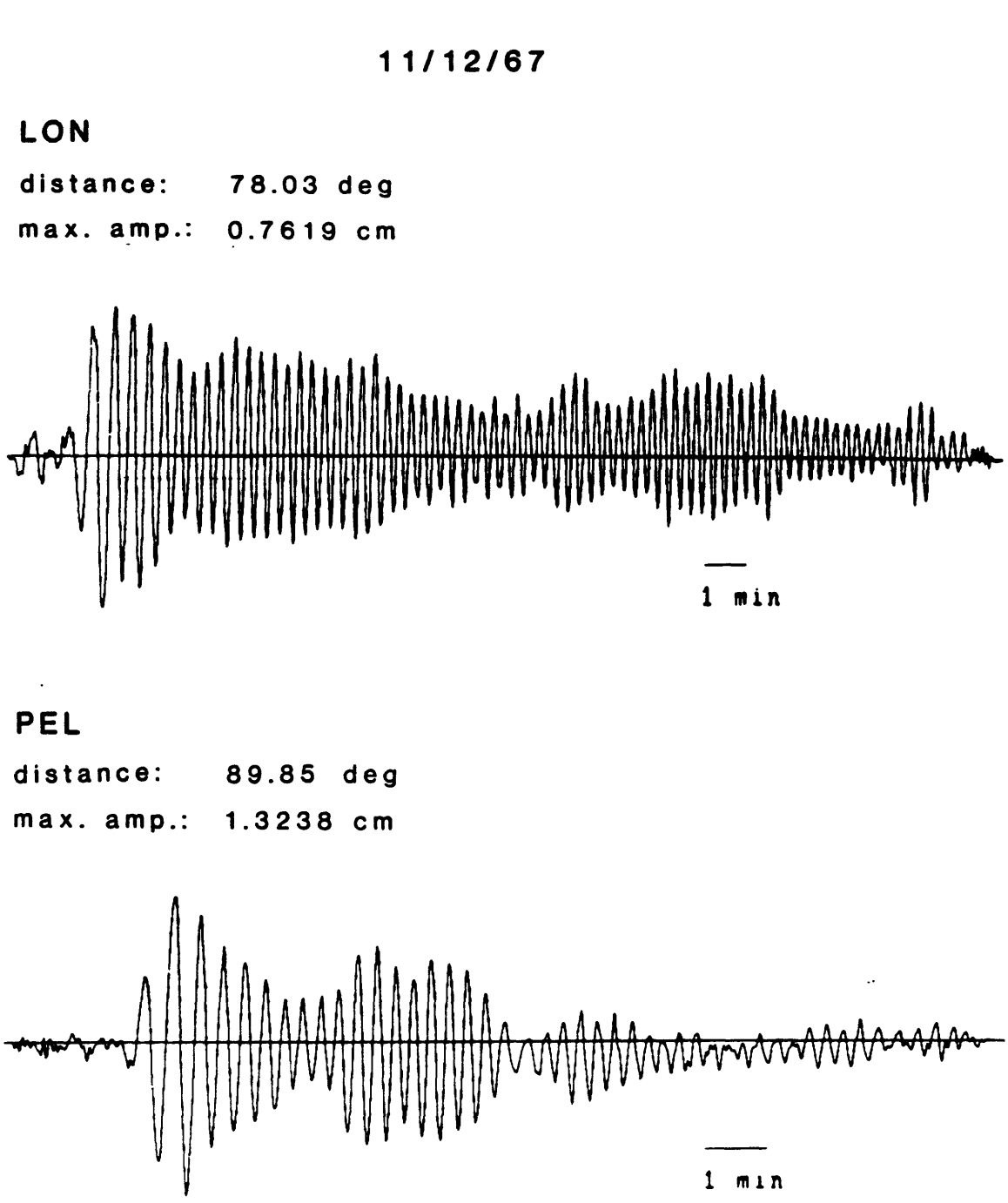

Figure 5.1. Two examples of seismograms for the event on November 12, 1967. a) Recorded vertical components. b) Spectra after corrections for instrumental response and propagation effects in the homogeneous model of 8099 [Dorman et al., 1960]. Amplitudes are normalized to a distance of 90° after removing the effects of attenuation. The spectrum at LON is smooth between 25 and 80 sec but that at PEL has an unstable hole around 60 sec (indicated by the arrow in the figure); this part was discarded in further study.

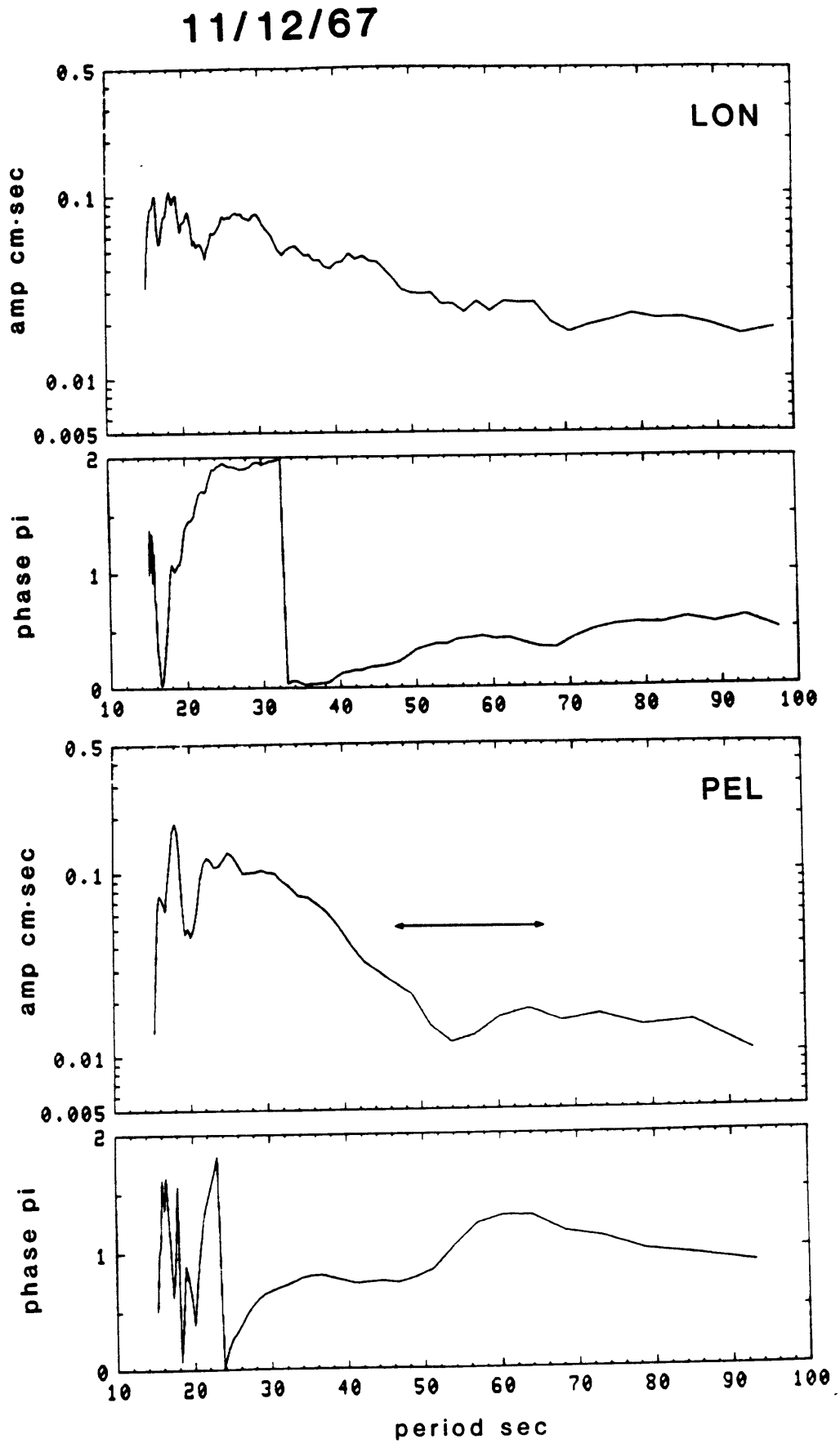
11/12/67
LON
amp cm·sec
0.5
0.1
0.01
0.005
phase pi
2
1
0
10
20
30
40
50
60
70
80
90
100
PEL
amp cm·sec
0.5
0.1
0.01
0.005
phase pi
2
1
0
10
20
30
40
50
60
70
80
90
100
period sec

Figure 5.1 b).

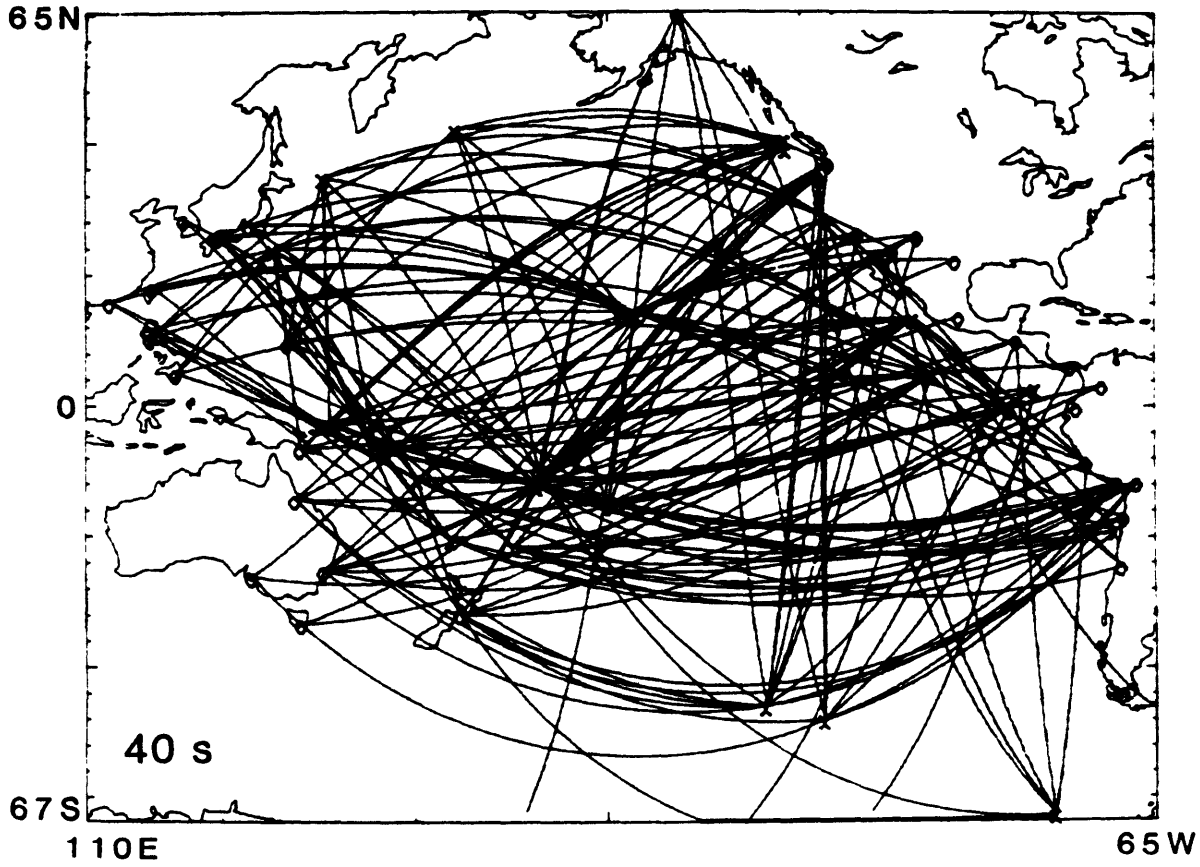

Figure 5.2. Path coverage at 40 sec (200 paths) in the Mercator projection.

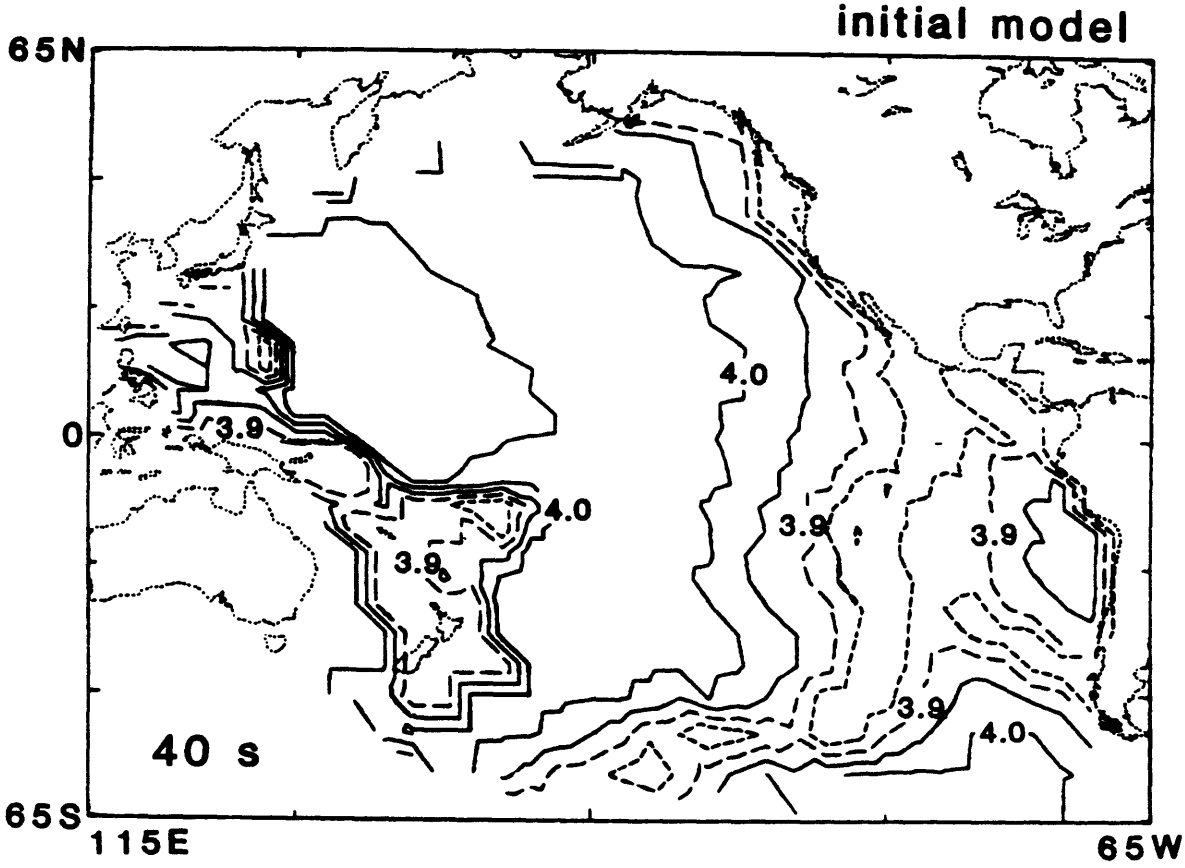

Figure 5.3. Initial (age-dependent) model of Rayleigh wave phase velocities at 40 sec. The contour interval is 0.05 km/s. The solid lines correspond to high velocity regions, the dashed lines to low velocity regions.

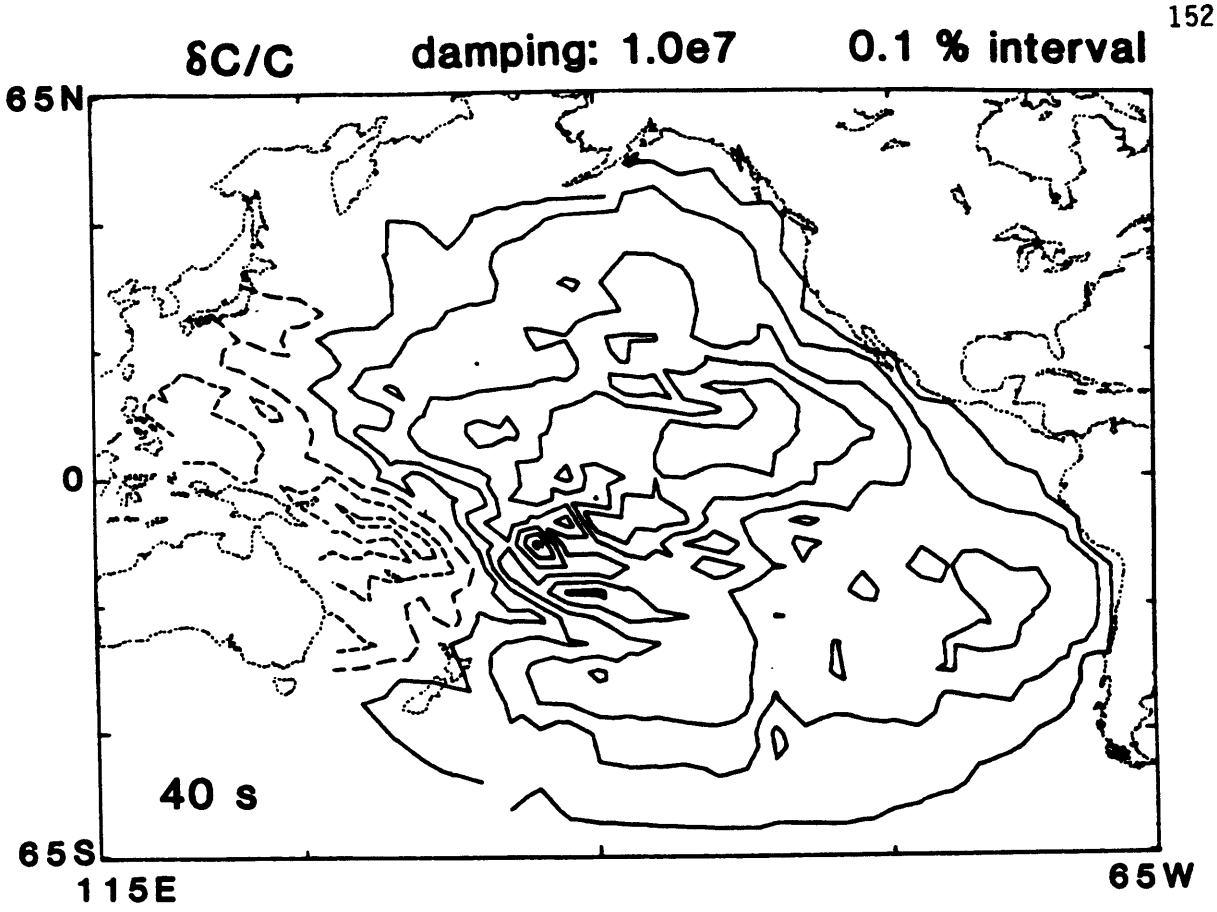

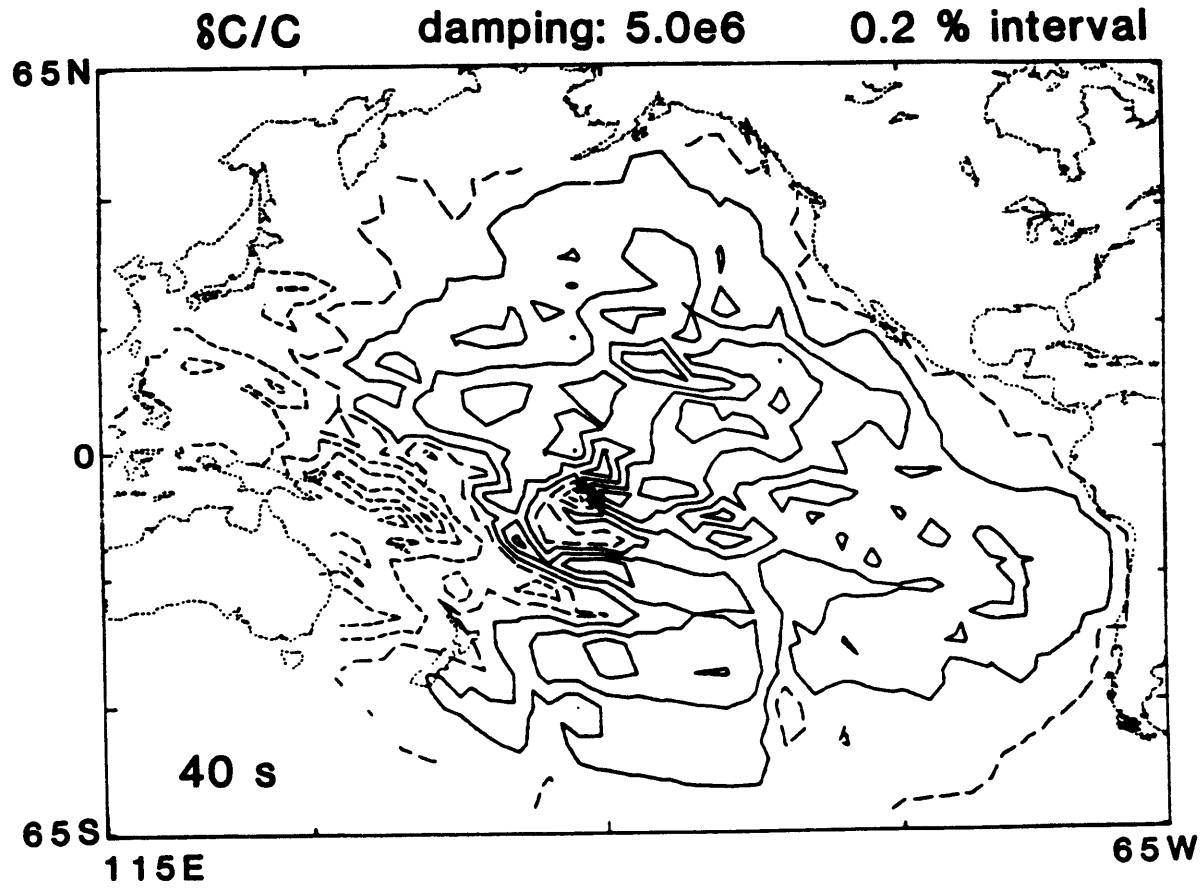

Figure 5.4. Phase velocity variation maps relative to the initial model at period 40 s with different damping factors ε^2: a) 10^7, b) 5×10^6, c) 3×10^6 and d) 2×10^6. The solid lines represent positive perturbations while the dashed lines are negative.

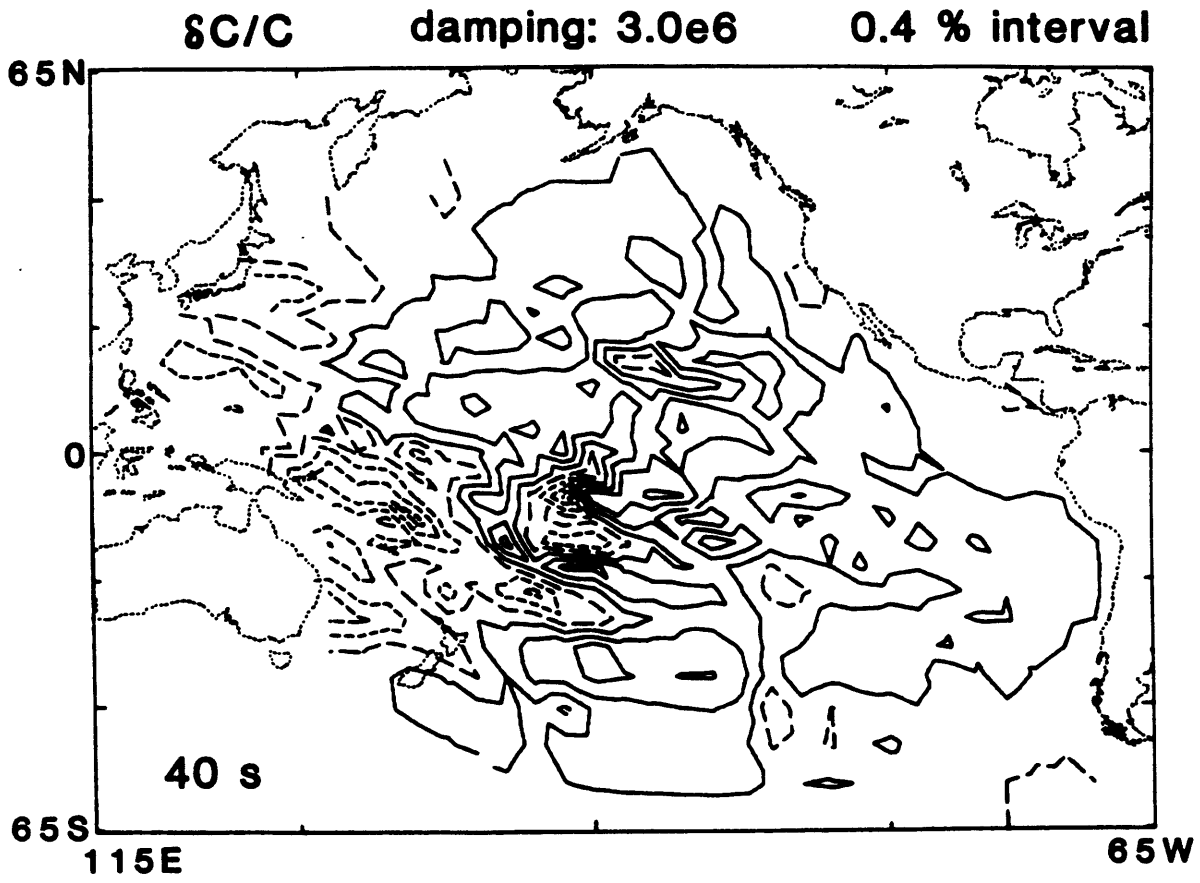

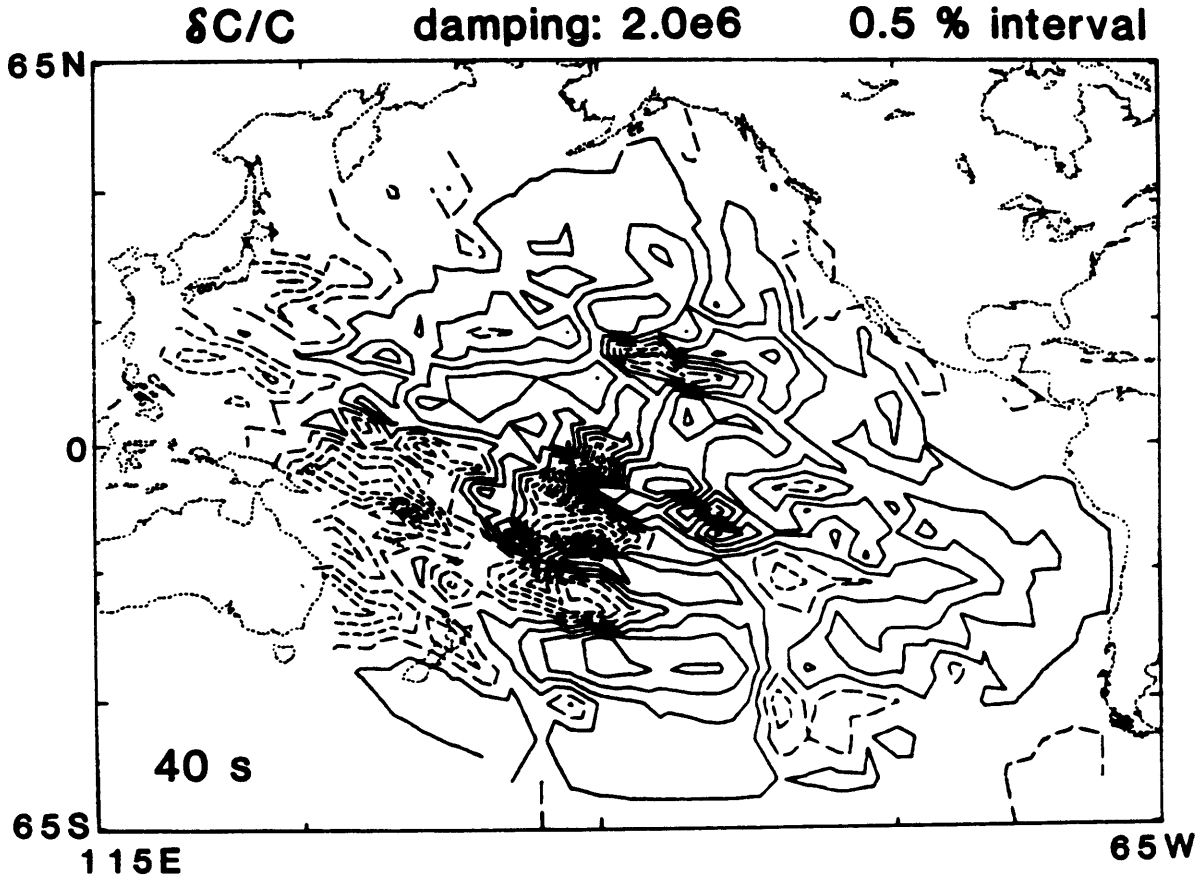

Figure 5.4 c) and d).

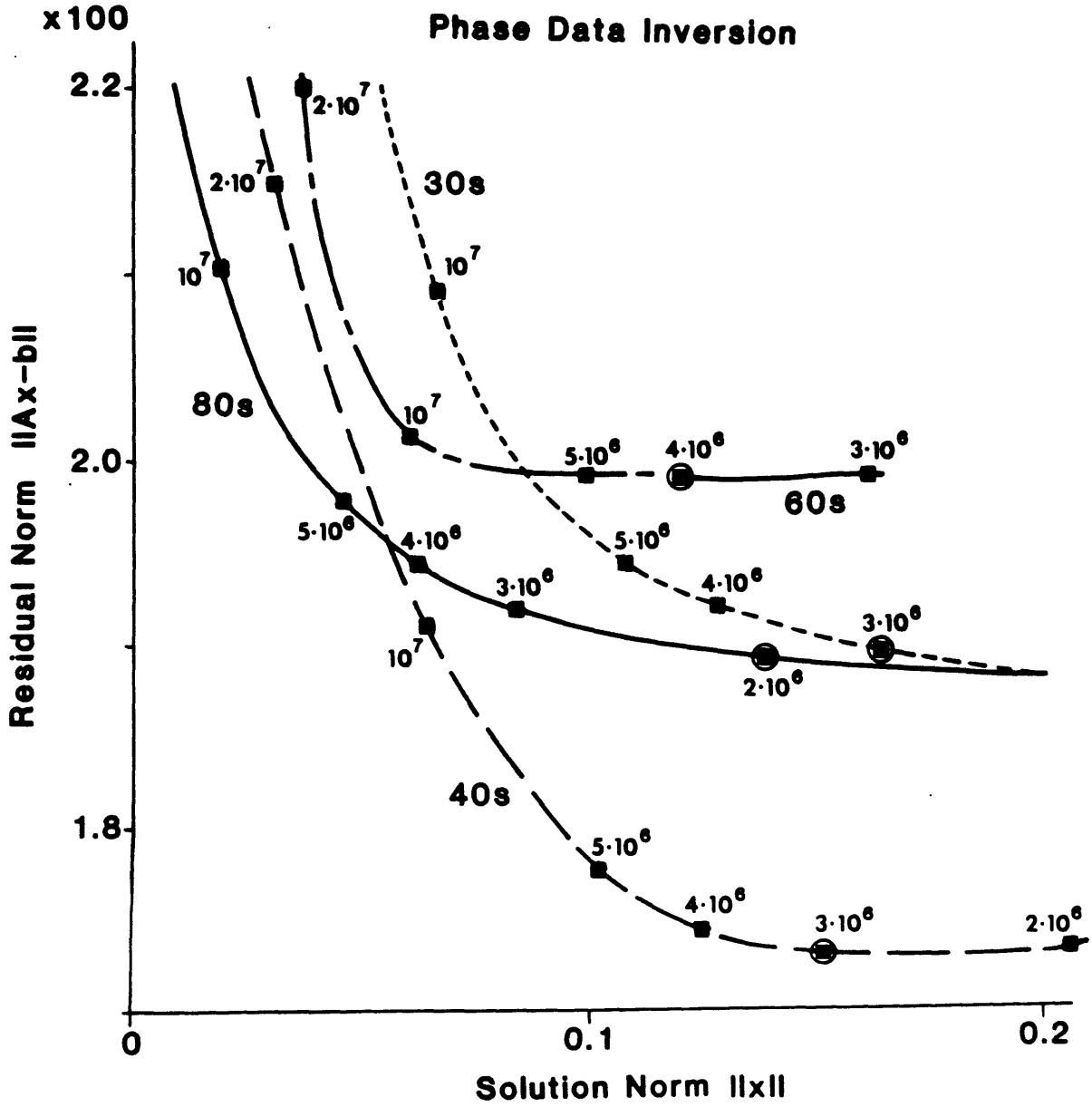

Figure 5.5. The residual norm versus the solution norm as a function of various damping factors ε^2 at each period. The adopted values of ε^2 at each period are circled.

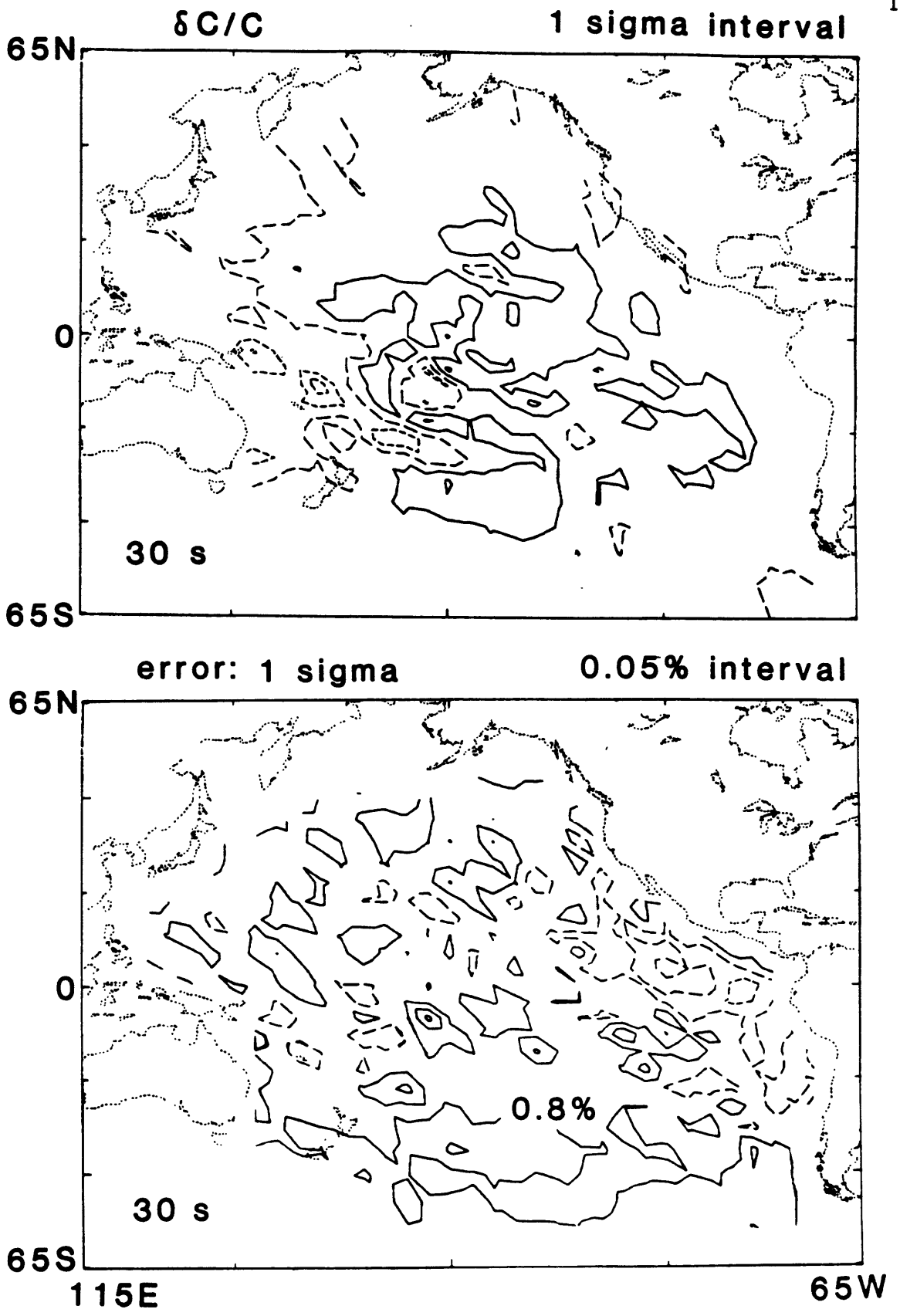

Figure 5.6. Phase velocity perturbations and estimated errors of model parameters at a) 30s, b) 40s, c) 60s and d) 80s. The contour interval of velocity perturbations is one sigma (0.6~0.9%) so that the reliability of the results can be judged easily.

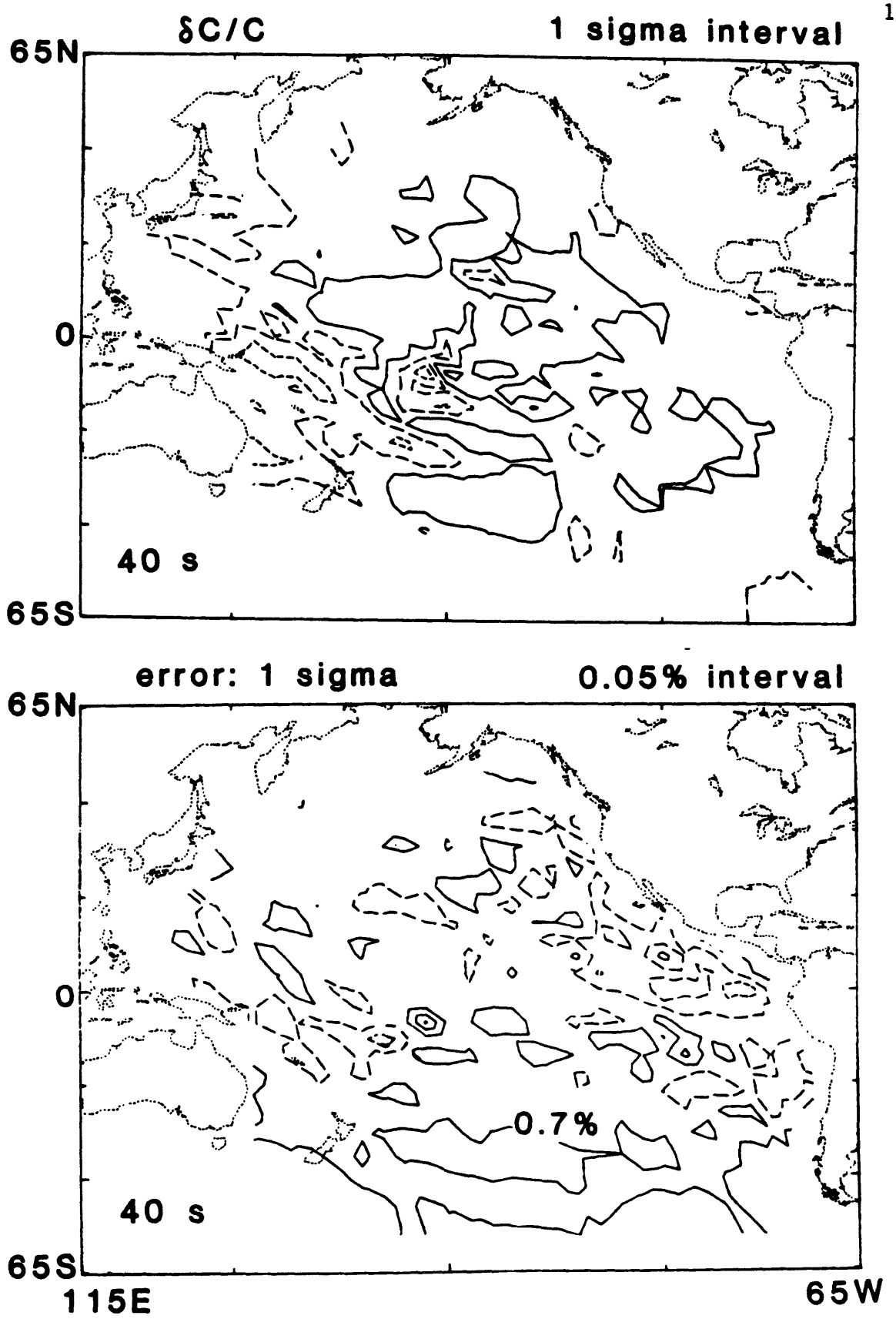
δC/C
1 sigma interval
65N
0
65S
40 s
error: 1 sigma
0.05% interval
65N
0
0.7%
40 s
65S
115E
65W

Figure 5.6 b).

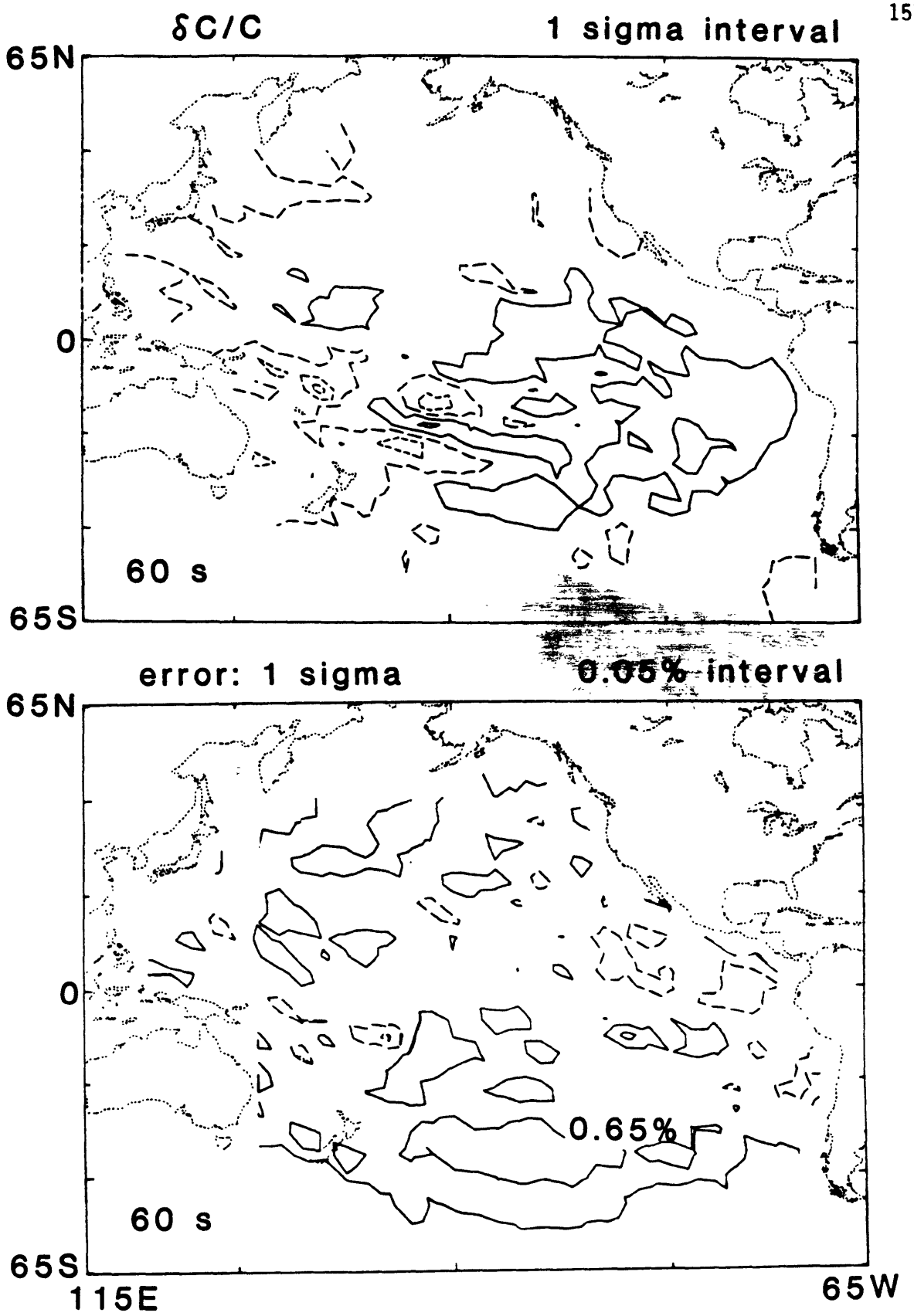
δC/C
1 sigma interval
65N
0
65S
60 s
error: 1 sigma
0.05% interval
65N
0
0.65%
60 s
65S
115E
65W

Figure 5.6 c).

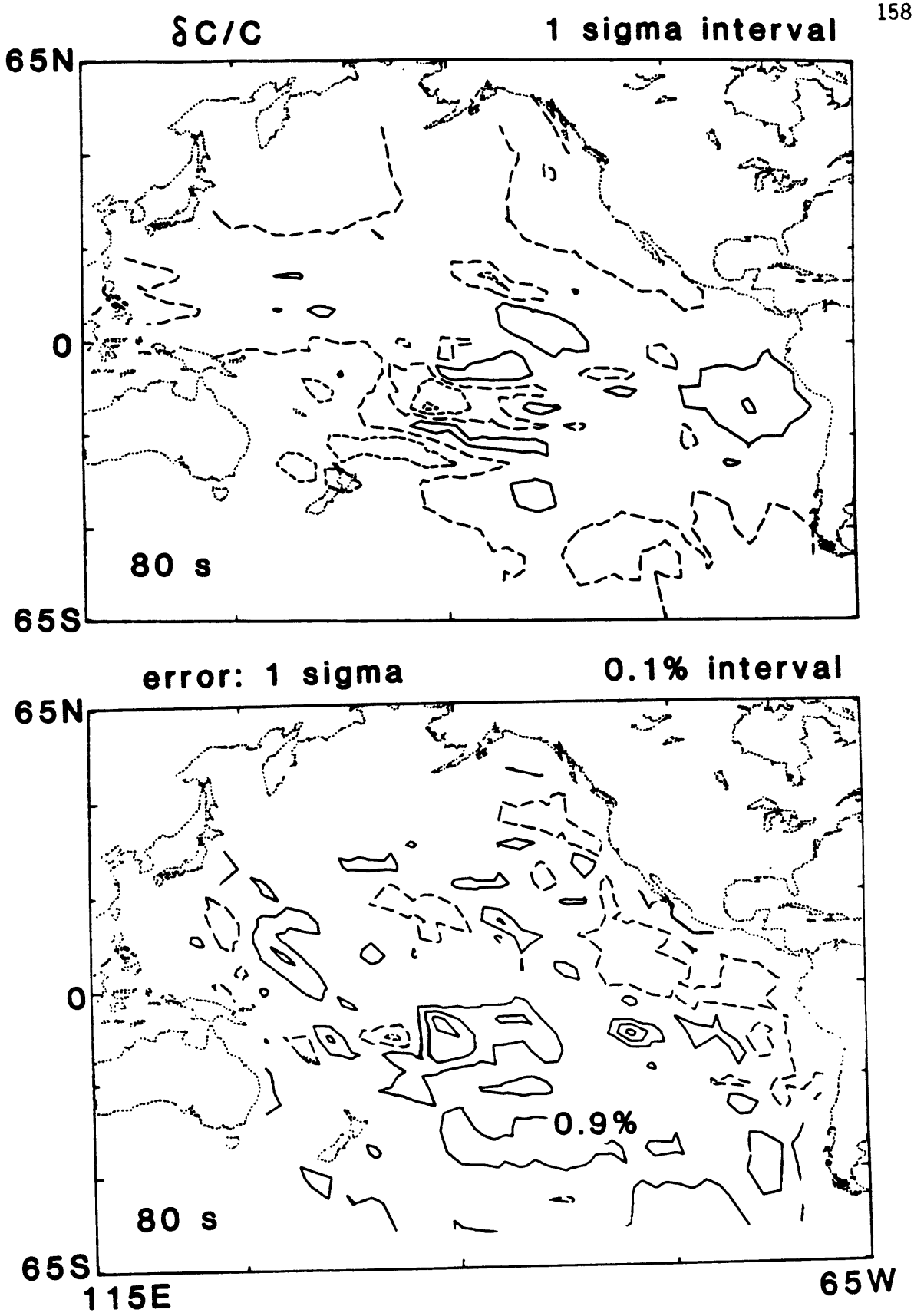
δC/C
1 sigma interval
65N
0
65S
80 s
error: 1 sigma
0.1% interval
65N
0
0.9%
80 s
65S
115E
65W

Figure 5.6 d).

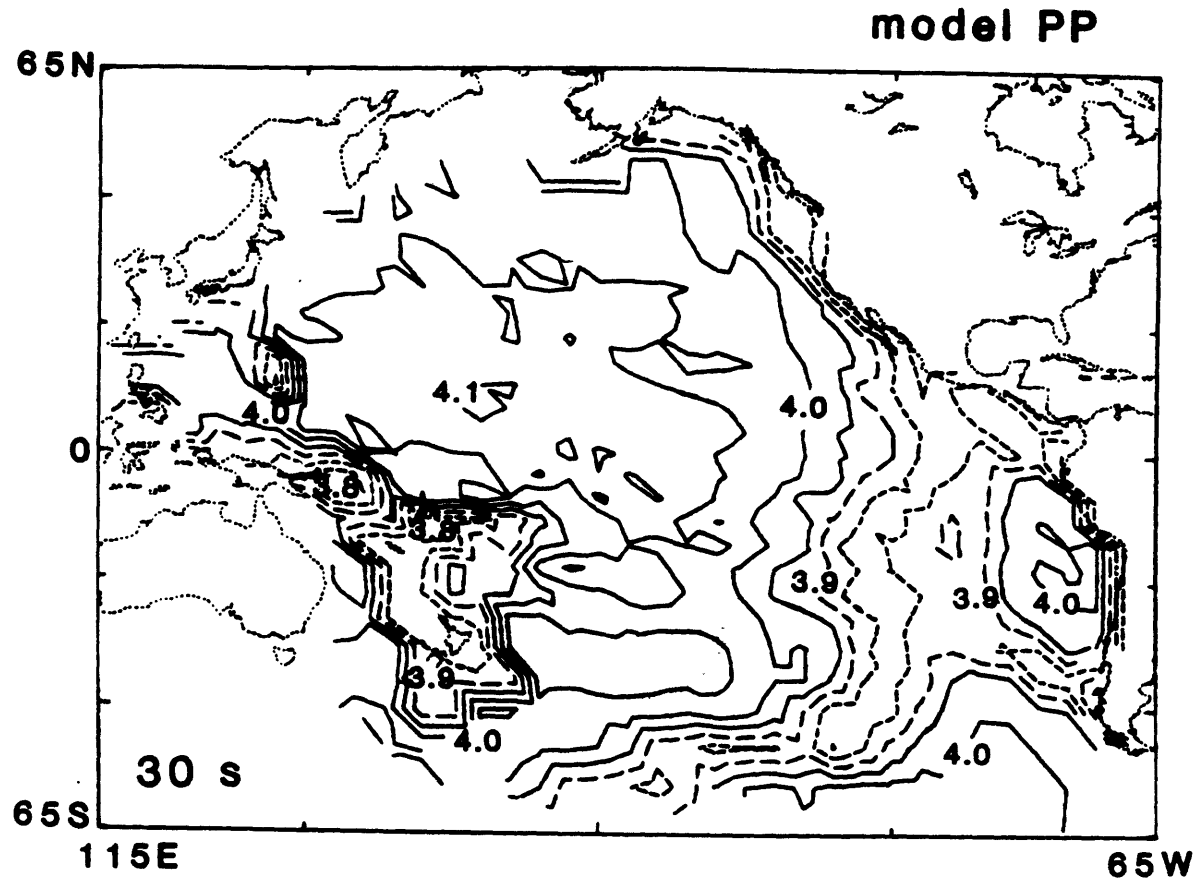

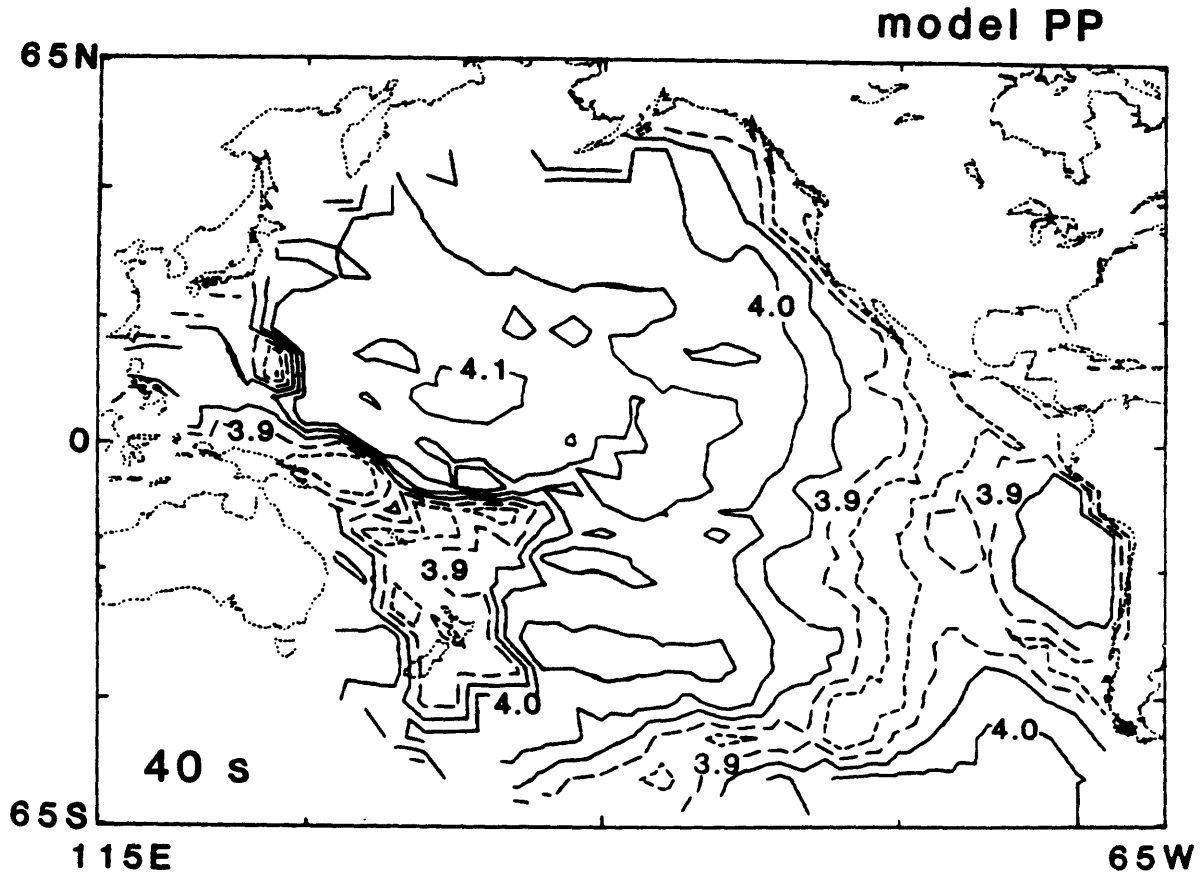

Figure 5.7. The results of phase data inversions, "model PP", at a) 30s, b) 40s, c) 60s, and d) 80s. The contour intervals are 0.05 km/s for 30and 40s, and 0.025 km/s for 60 and 80s.

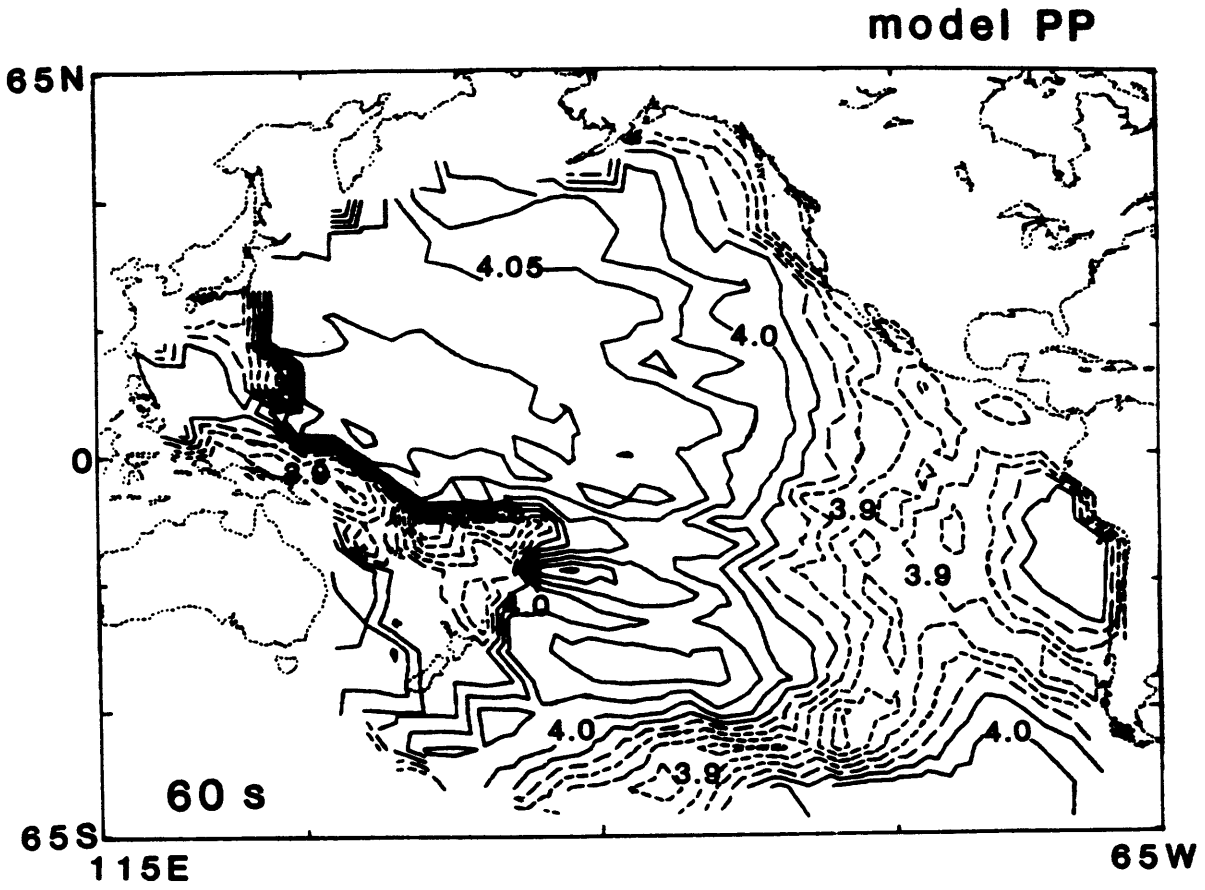

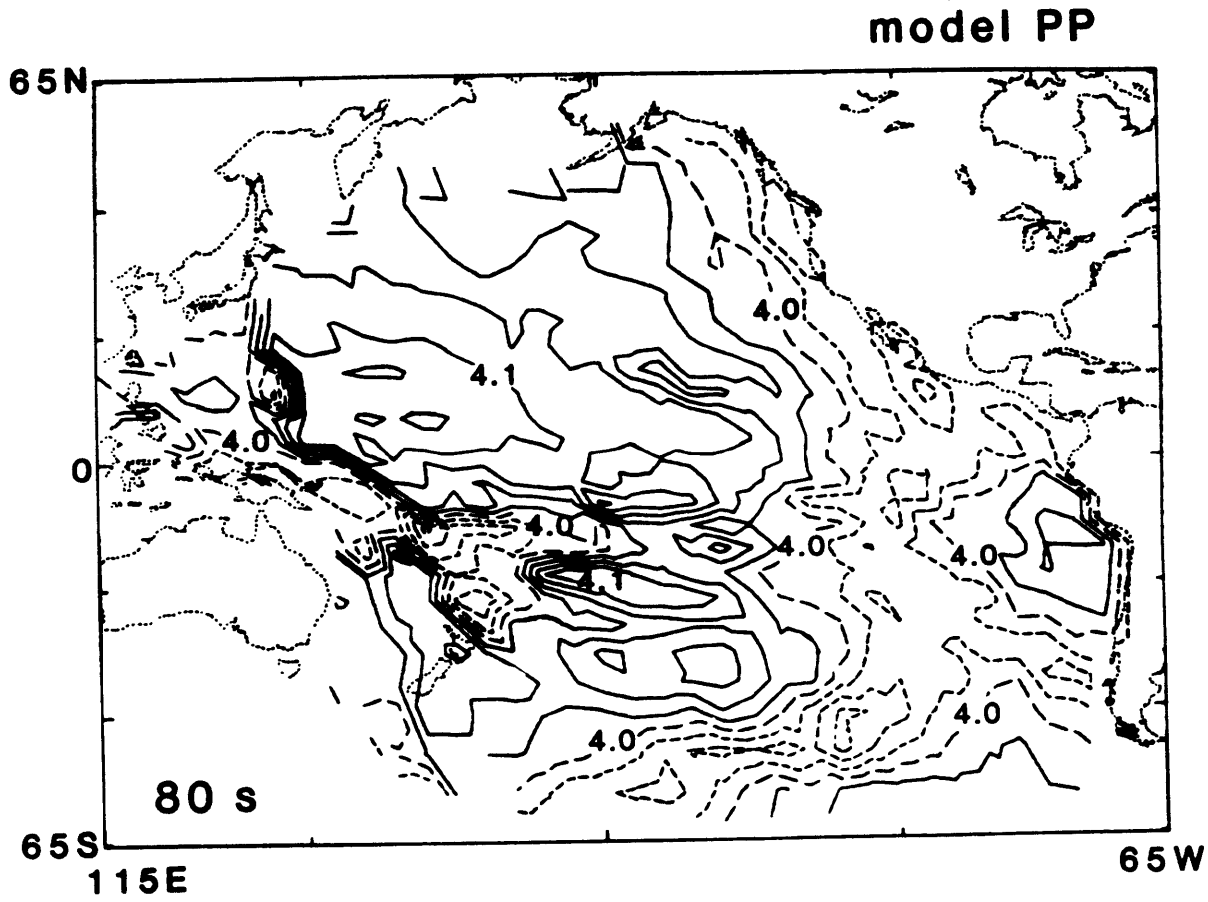

Figure 5.7 c) and d).

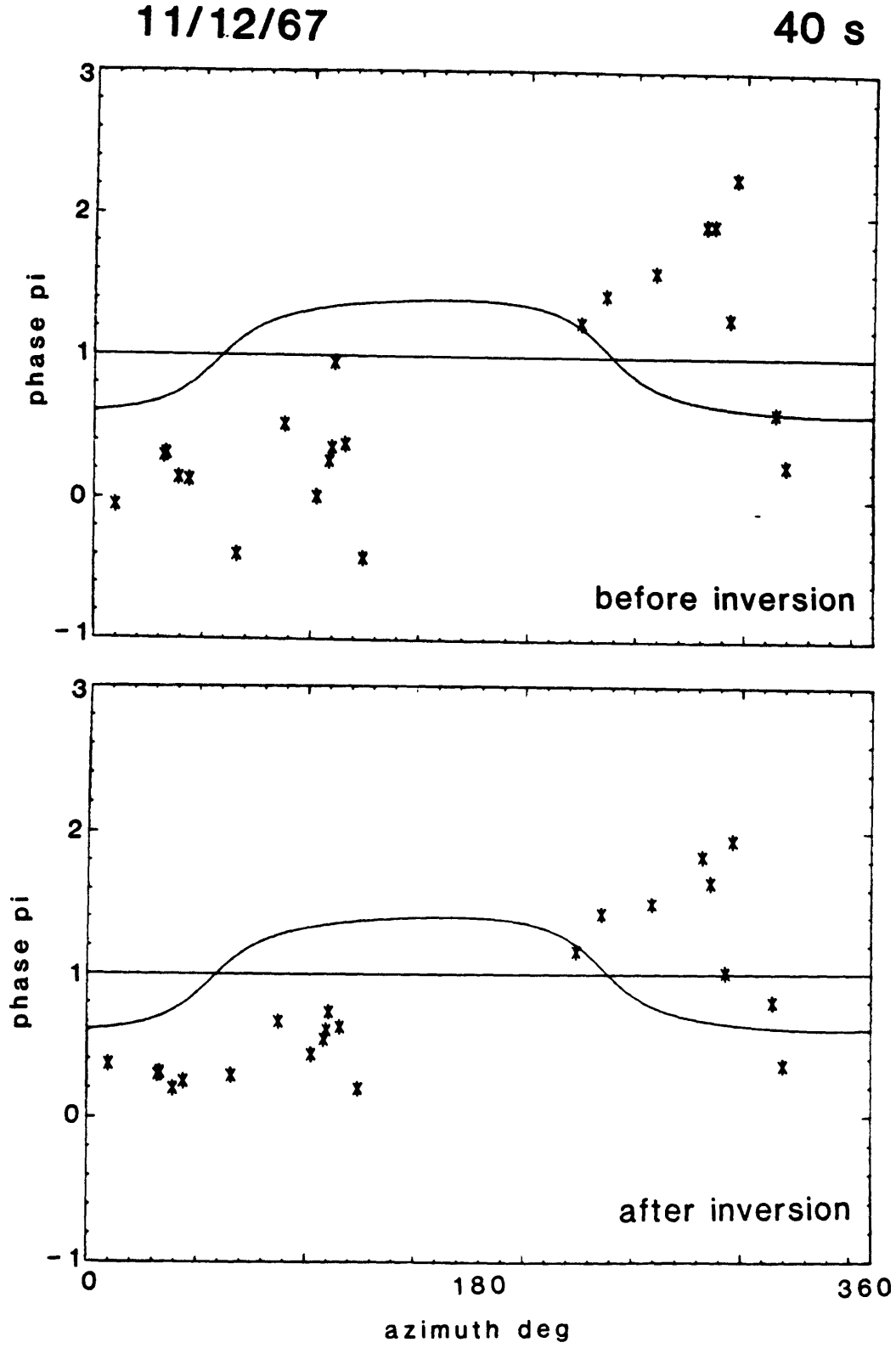

Figure 5.8. One example of the fit of phase data (a) before and (b) after phase data inversion (for the event of November 12, 1967).

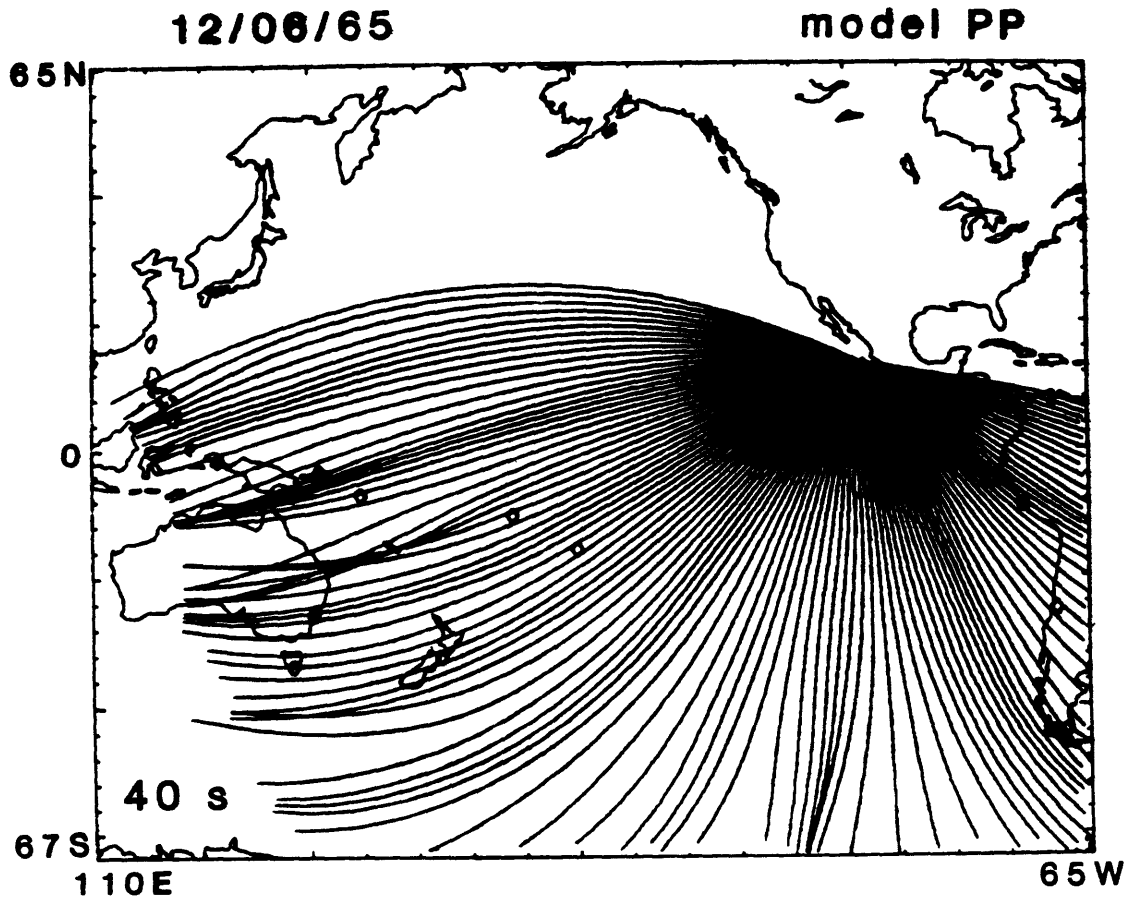

Figure 5.9. One example of ray-tracing with model PP for an event on December 6, 1965. Circles indicate station locations.

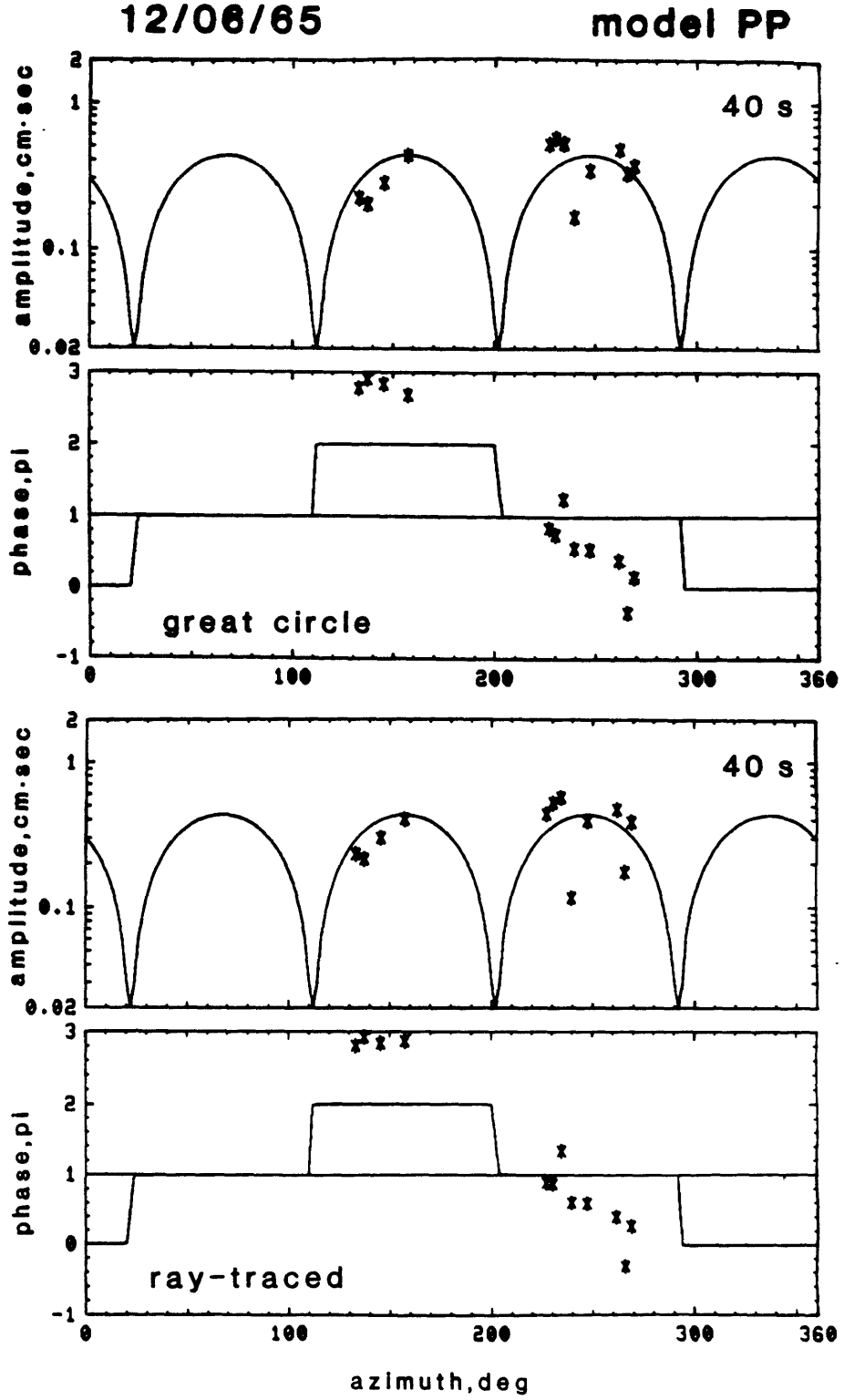

Figure 5.10. Amplitude and phase fit to model PP with different path corrections; a) Phases along great circles and amplitudes as $(\text{distance})^{-1/2}$ with constant Q model, and b) ray-traced path with age-dependent Q model.

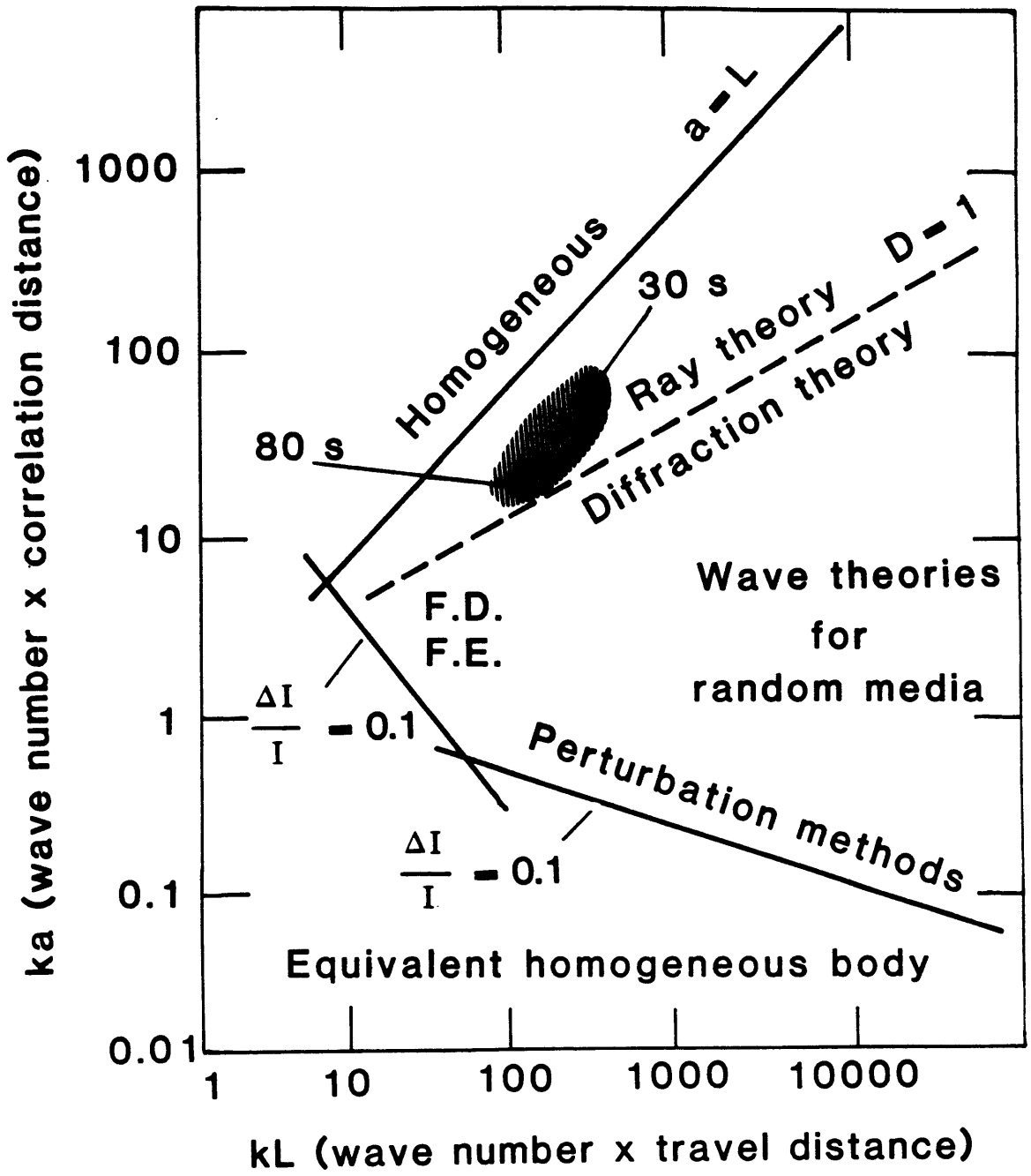

Figure 5.11. Classification of scattering problems and applicable methods in ka-kL diagram. Shaded areas indicate the location of surface waves in the present study. Reproduced from Figure 13.11 of Aki and Richards [1980].

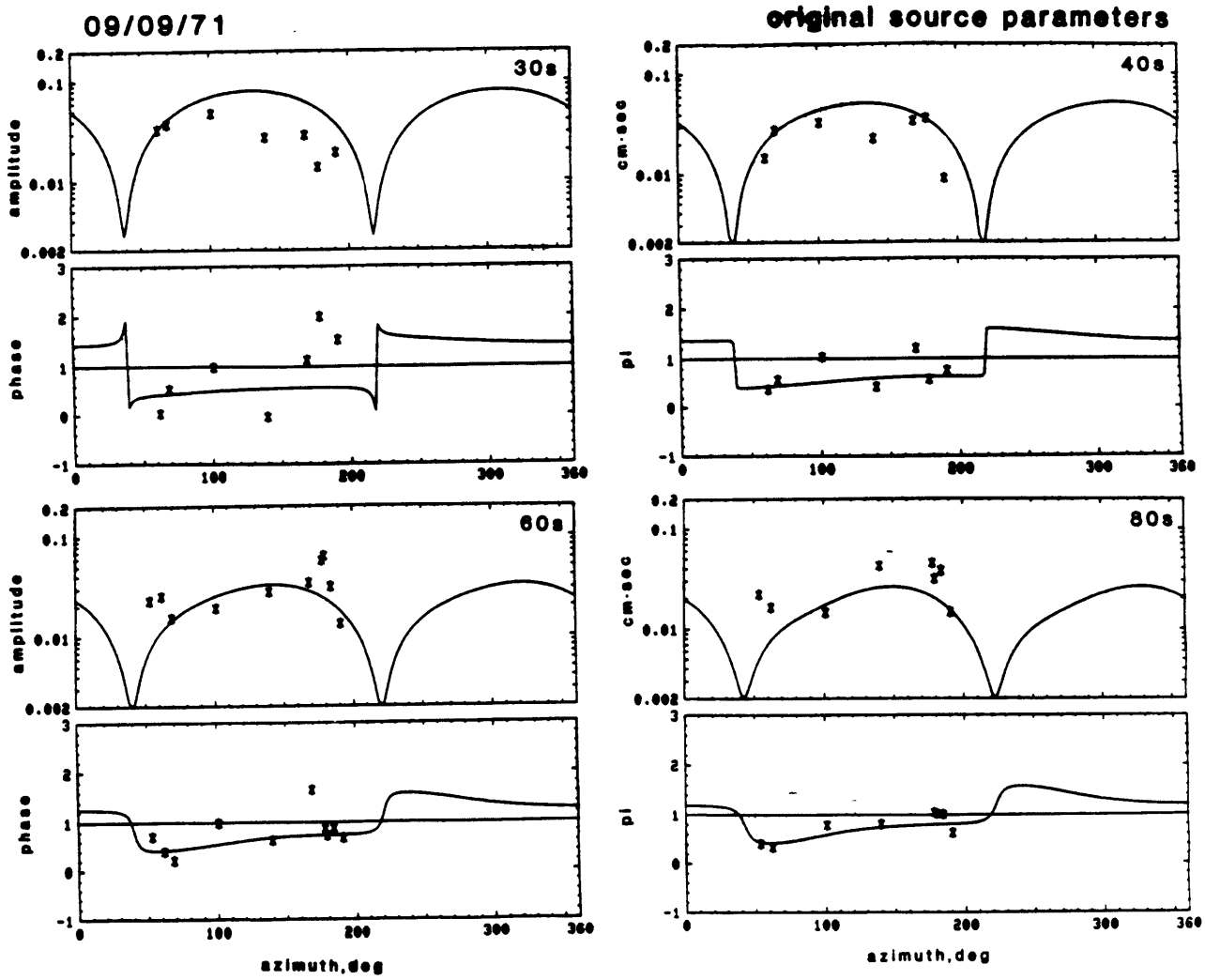

Figure 5.12. Amplitude and phase fit to model PP by ray-traced corrections with a) original focal mechanism and b) revised mechanism for an event on September 9, 1971.

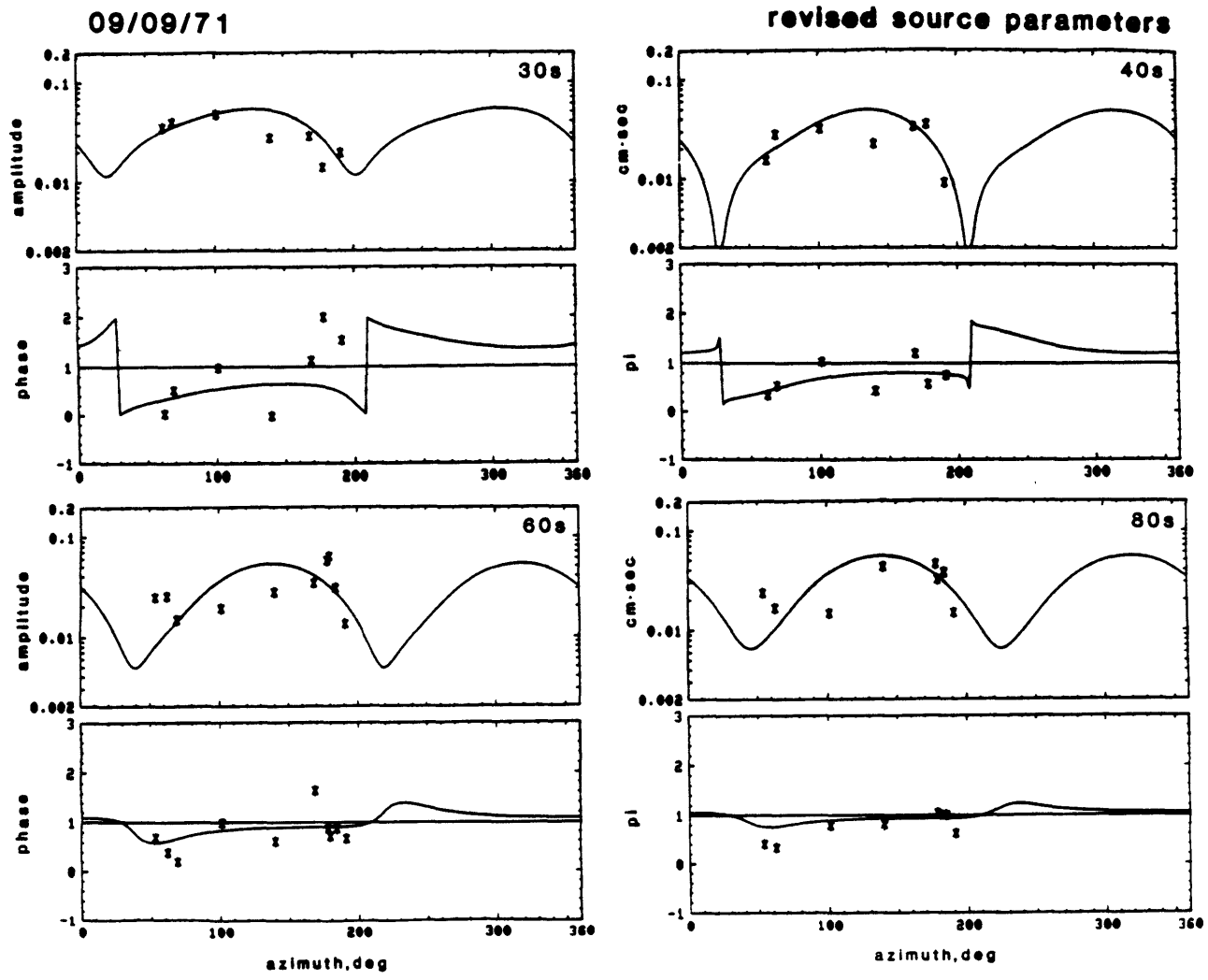
09/09/71
revised source parameters
30s
40s
60s
80s
amplitude
cm-sec
phase
pi
azimuth,deg

Figure 5.12 b).

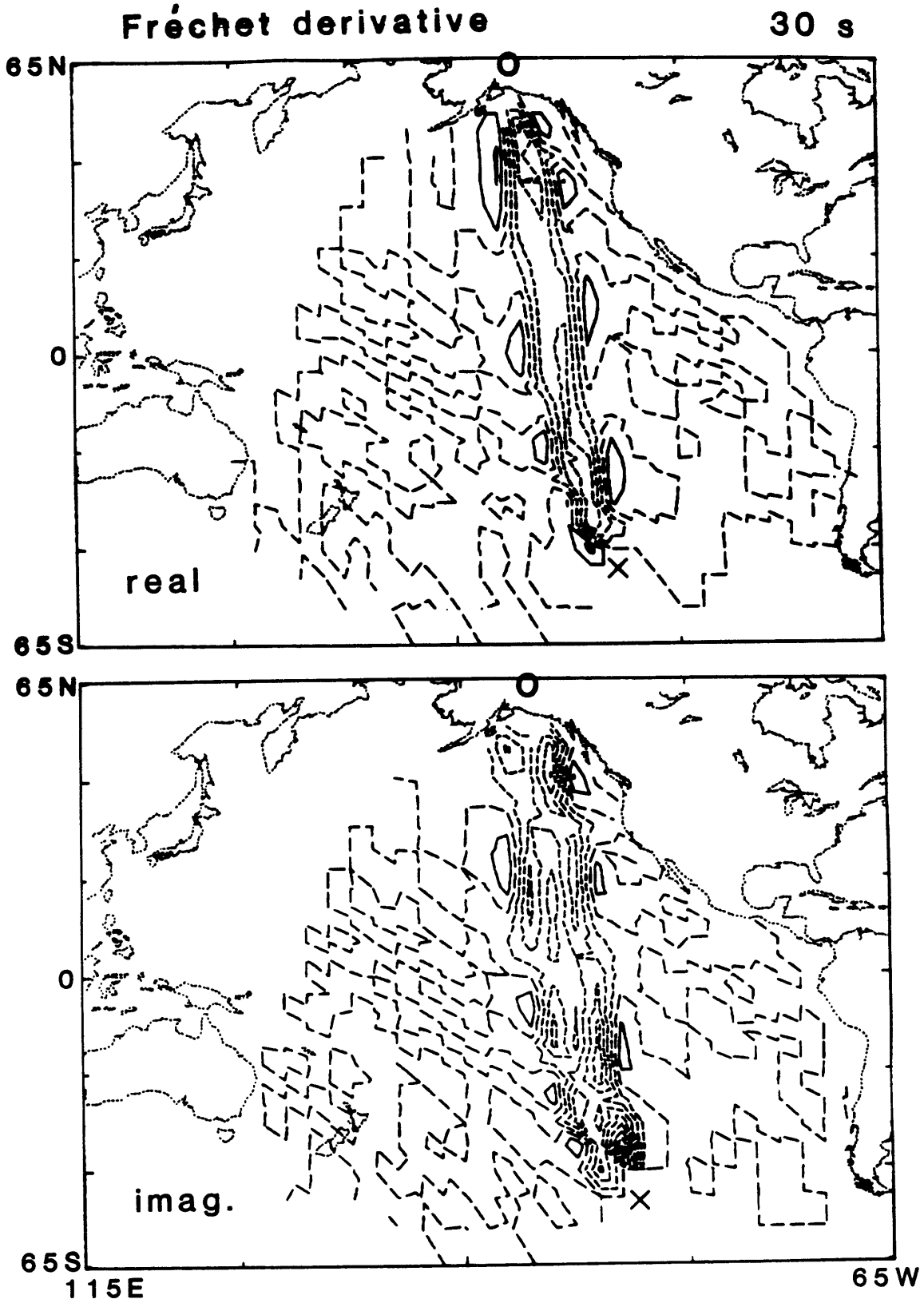

Figure 5.13. Real and imaginary parts of Frechet derivatives of inversions for some source-station pairs. Short-dashed lines are negative, long-dashed zero and solid positive. Crosses indicate source locations and circles denote stations. a) station COL and event of April 4, 1971 on Eltanin F.Z. at periods of 30 s and b) 80 s; c) station TUC and event of April 8, 1973 in the New Hebrides at periods of 30 s and d) 80 s.

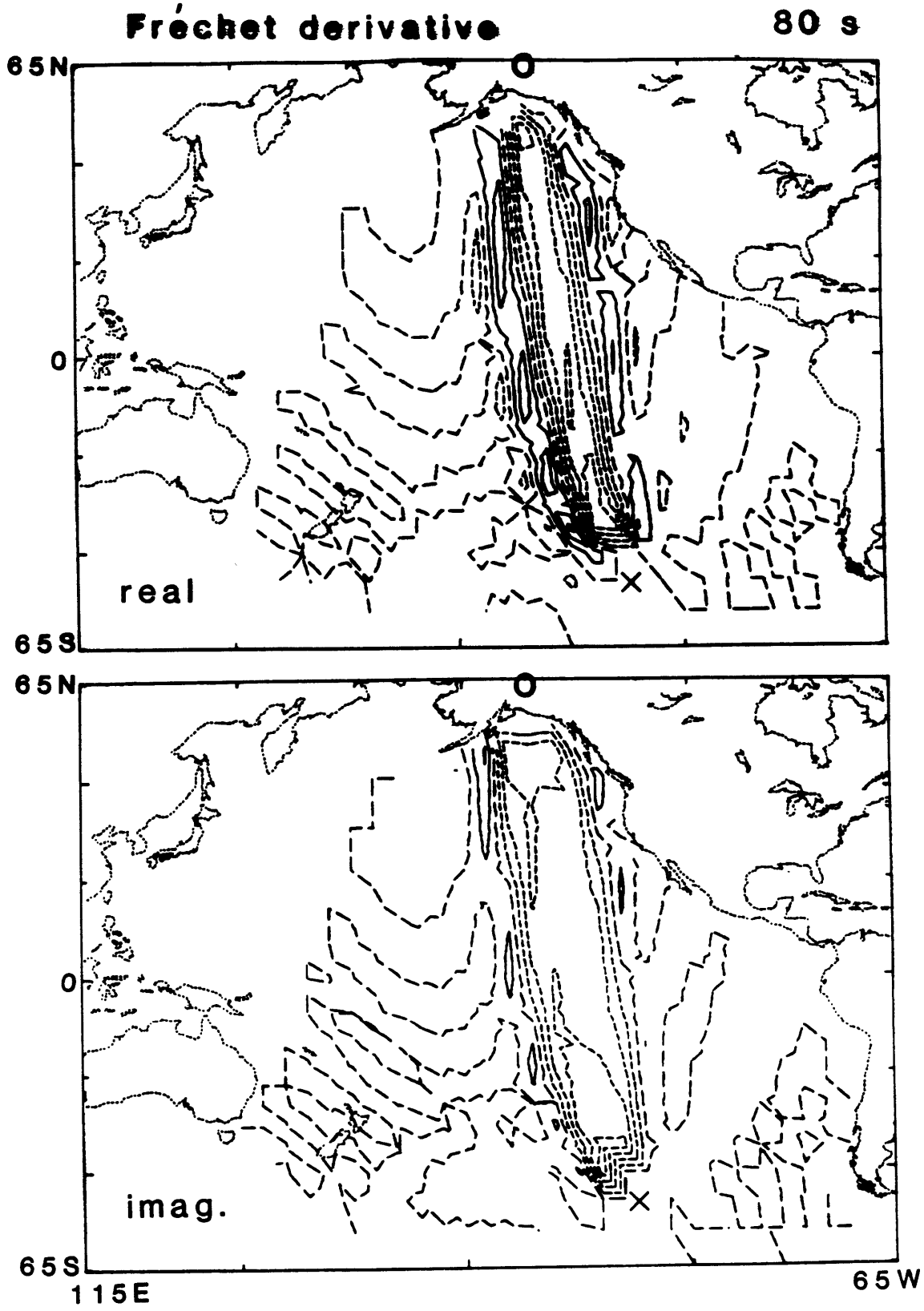

Figure 5.13 b).

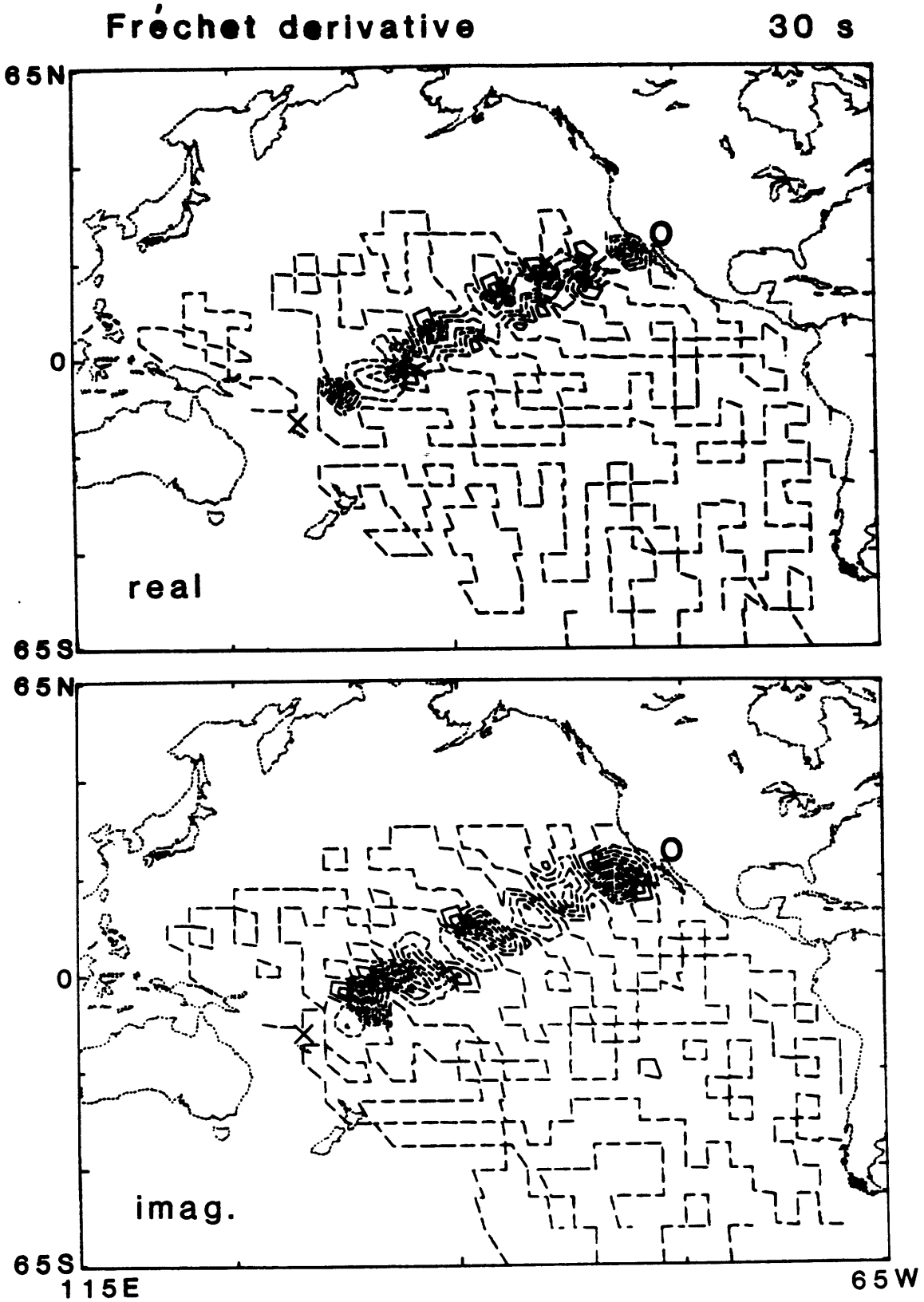

Figure 5.13 c).

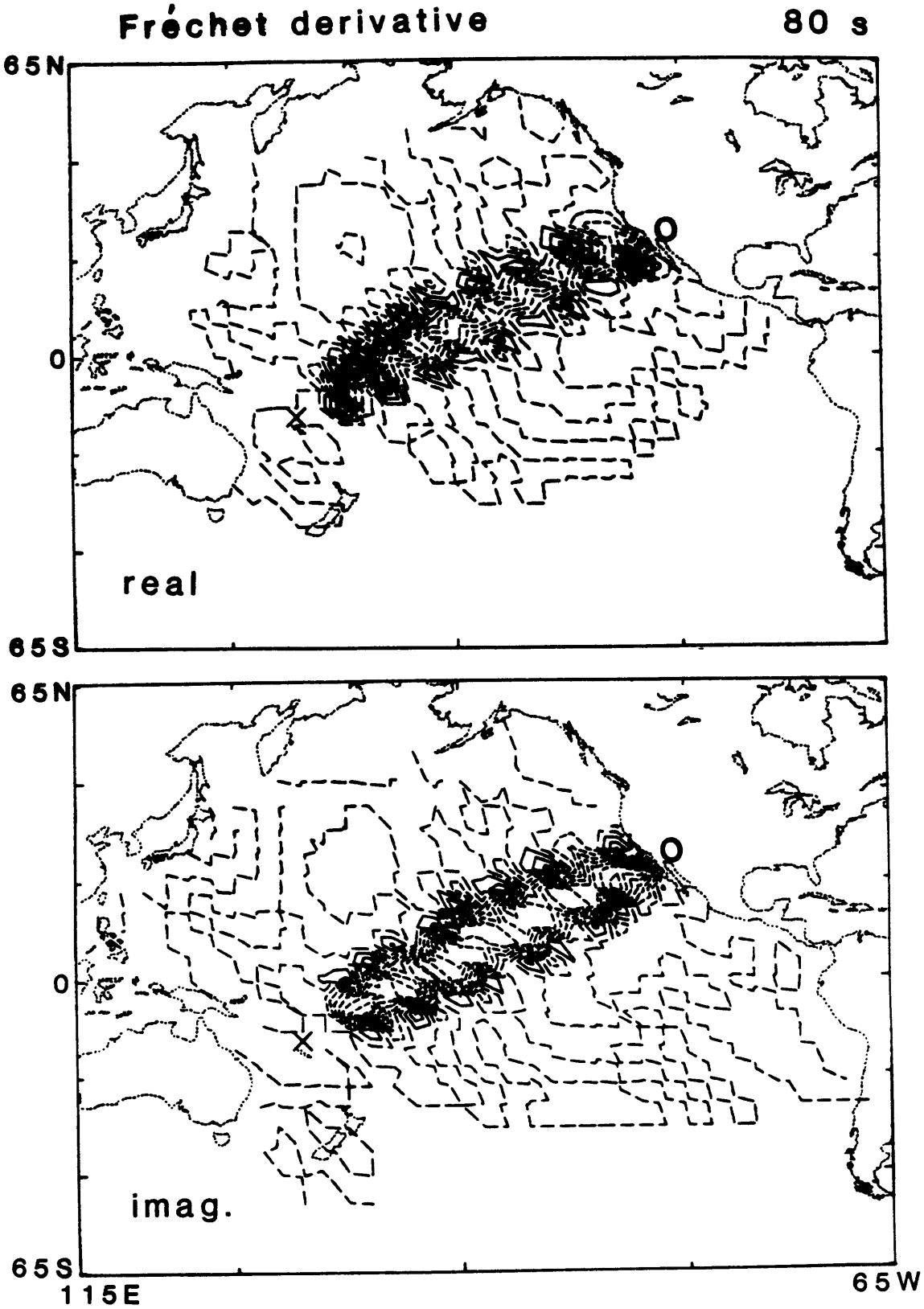

Figure 5.13 d).

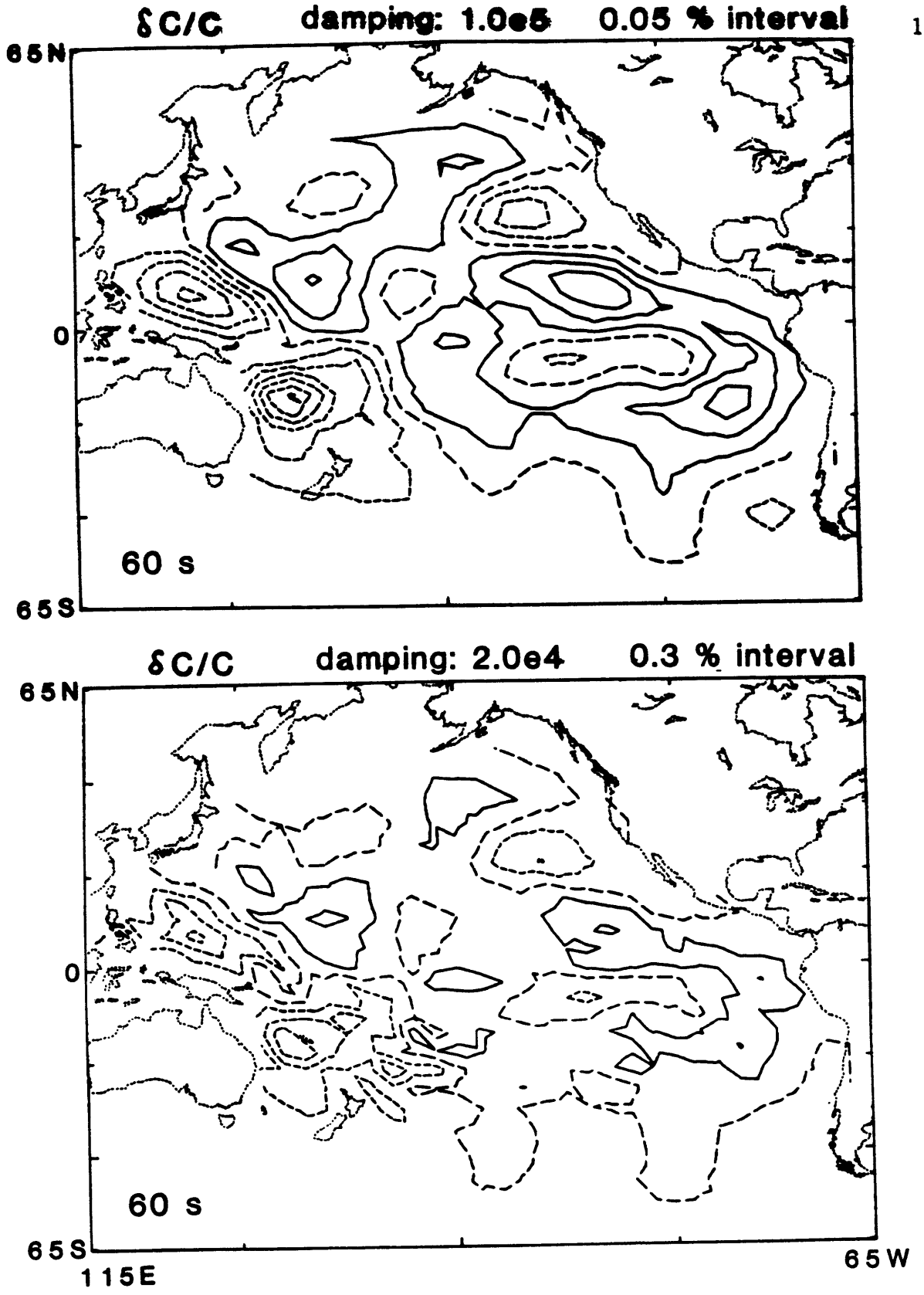

Figure 5.14. Phase velocity variation map over model PP at period 60 s in the first iteration of amplitude-phase inversions with different damping factors ε^2, a) 10^5, b) ? x 10^4 and c) 1.5 x 10^4. We adopted the case c).

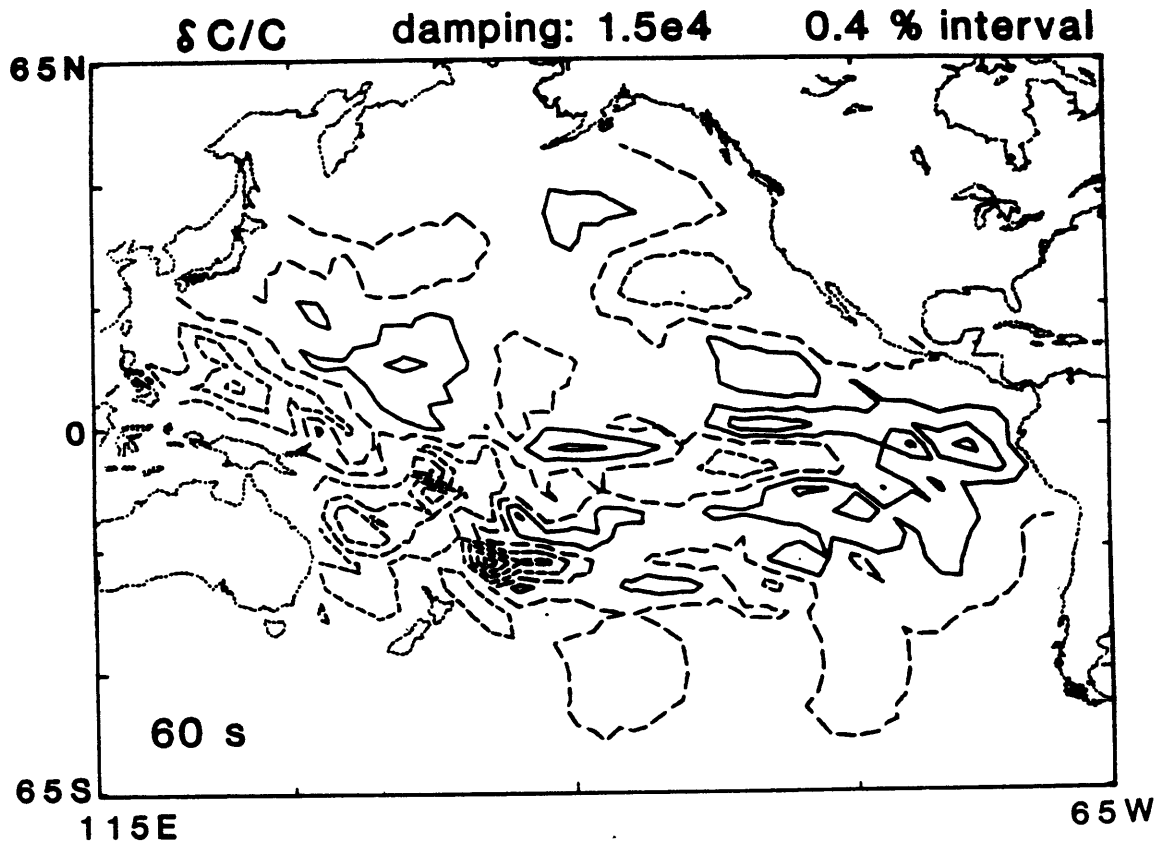

Figure 5.14 c).

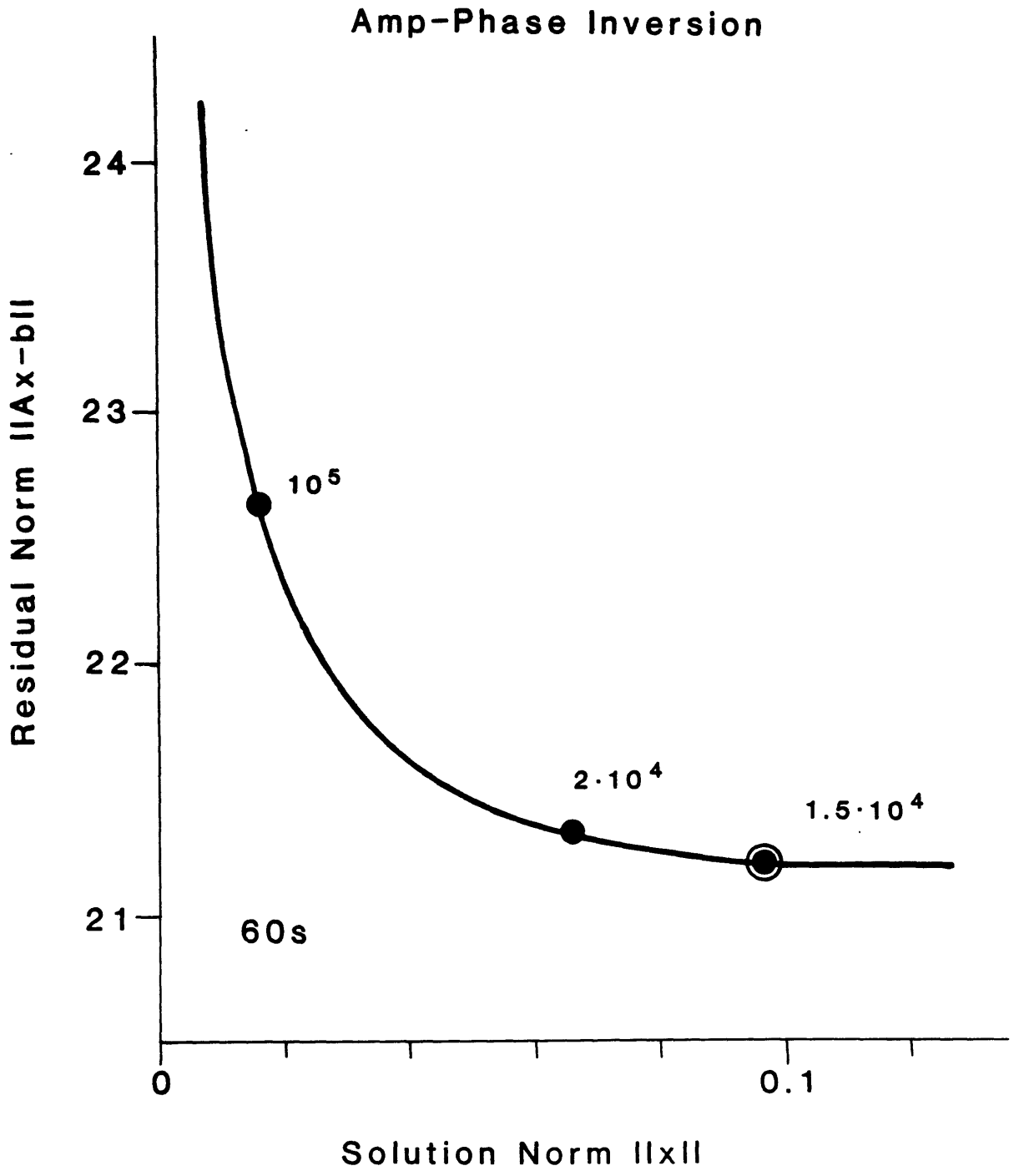

Figure 5.15. The residual norm versus the solution norm diagram as a function of various damping factors, ε^2, at a period of 60 s in the first iteration of amplitude-phase inversions. The adopted value was $\varepsilon^2 = 1.5 \times 10^4$.

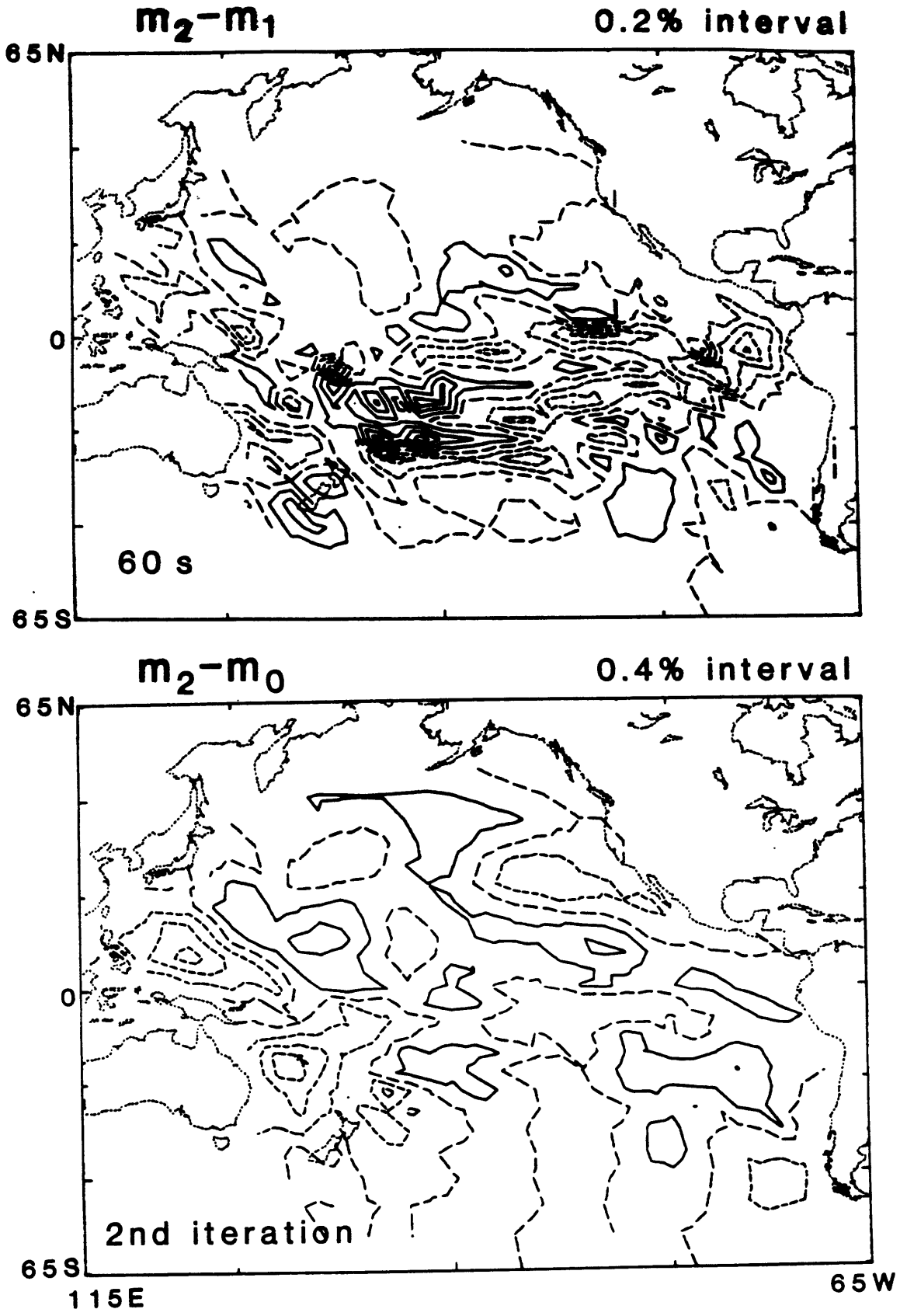

Figure 5.16. Phase velocity perturbations at the second iteration for 60 s a) with and b) without an additional term of Tarantola and Valette [1982]. In each figure the top shows perturbations from the first iteration model and the bottom shows those from the a priori model.

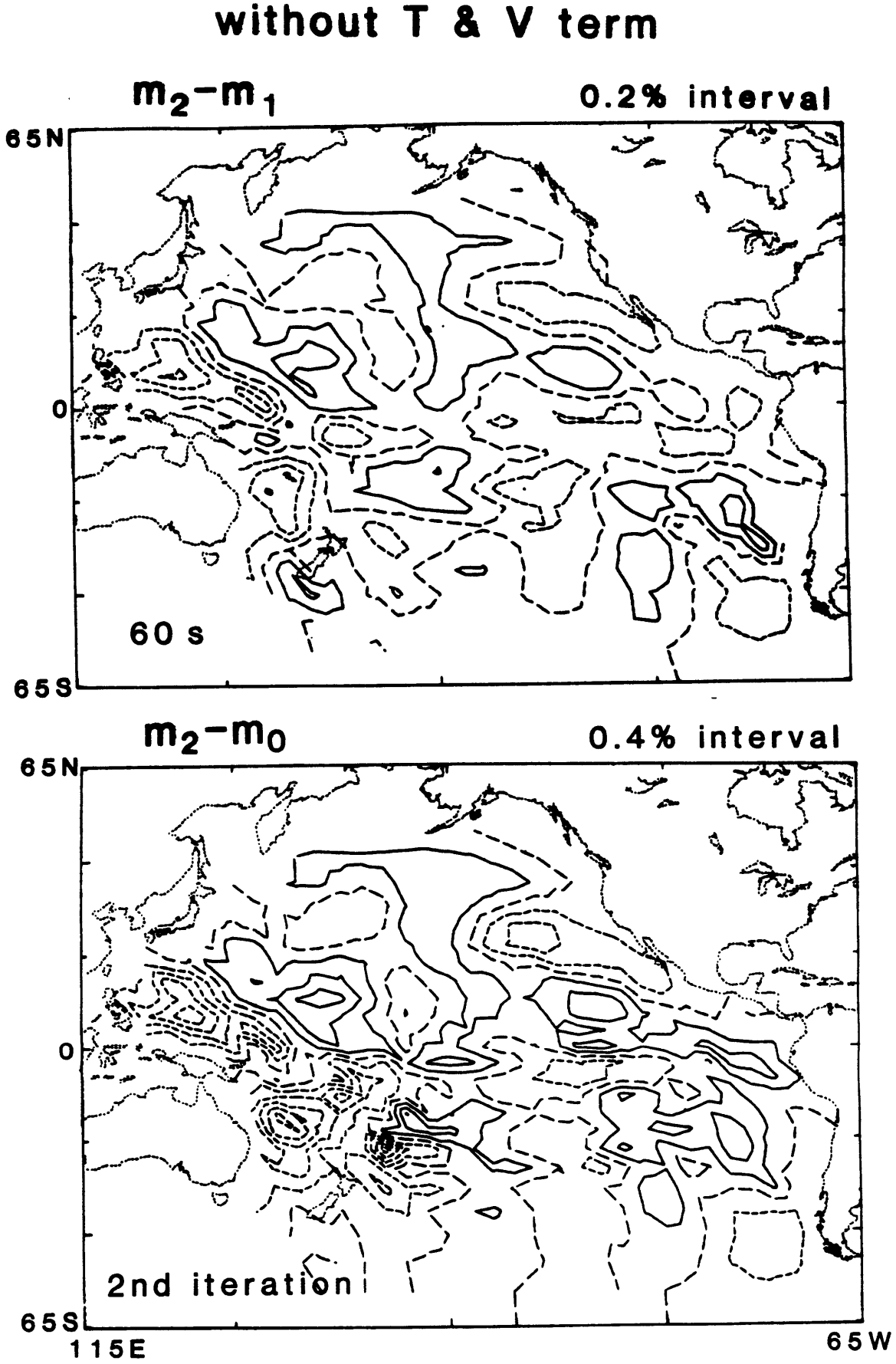
without T & V term
m_2-m_1
0.2% interval
65N
0
65S
60 s
m_2-m_0
0.4% interval
65N
0
65S
2nd iteration
115E
65W

Figure 5.16 b).

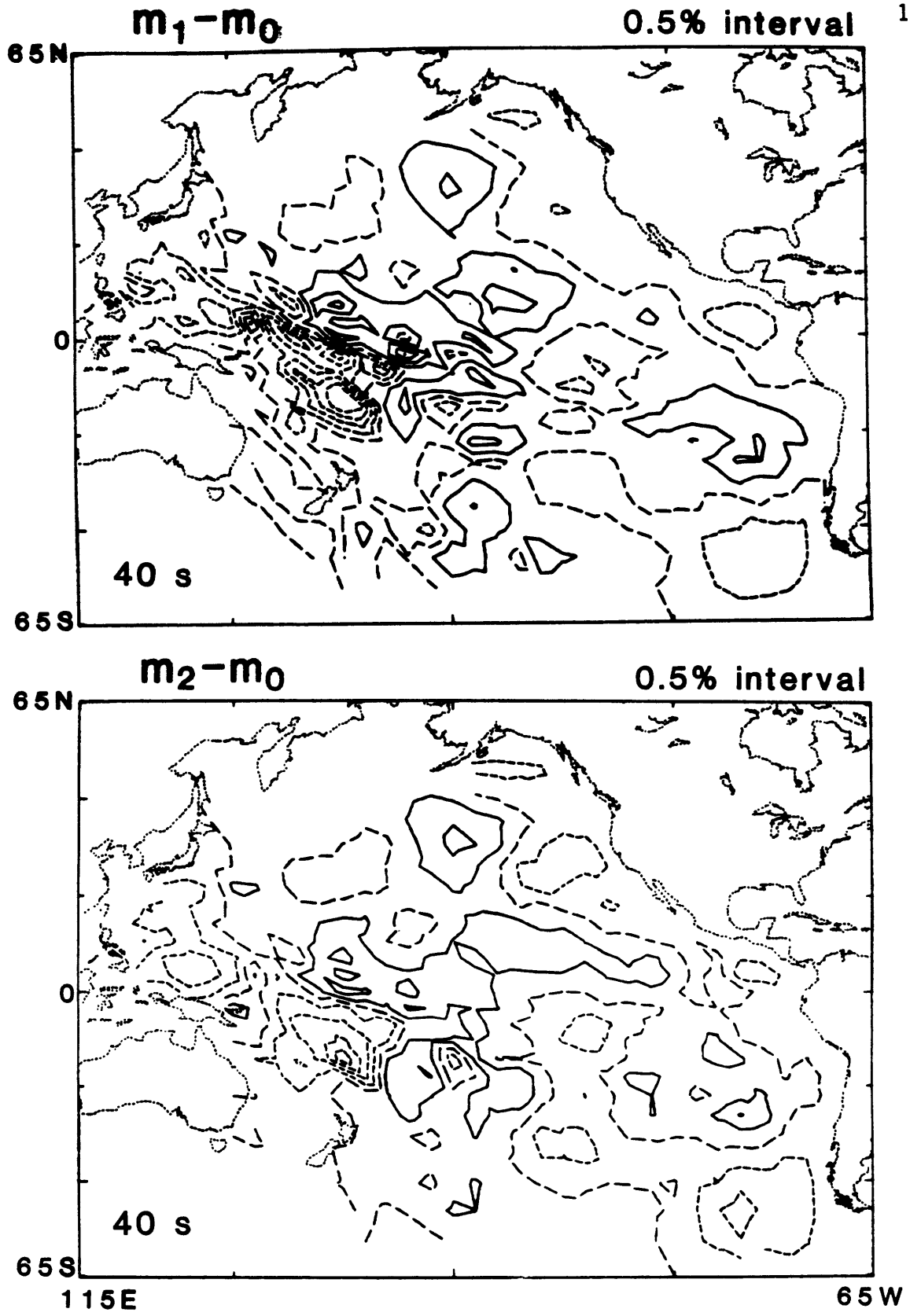

Figure 5.17. Total perturbations from the 'a priori' model at each iteration step at 40 s. a) First, b) second, c) third, d) fourth, and e) fifth iteration steps, respectively.

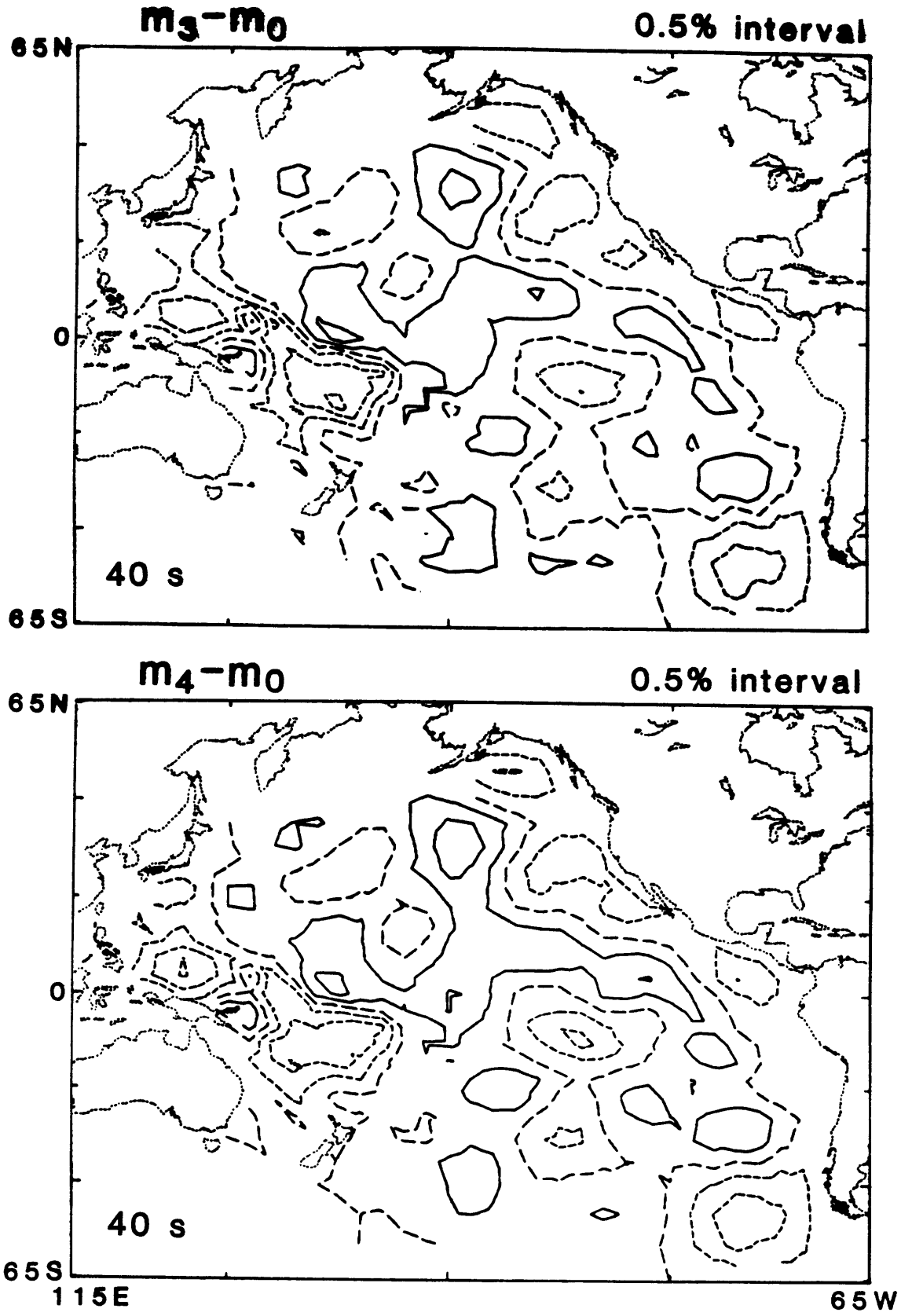

Figure 5.17 c) and d).

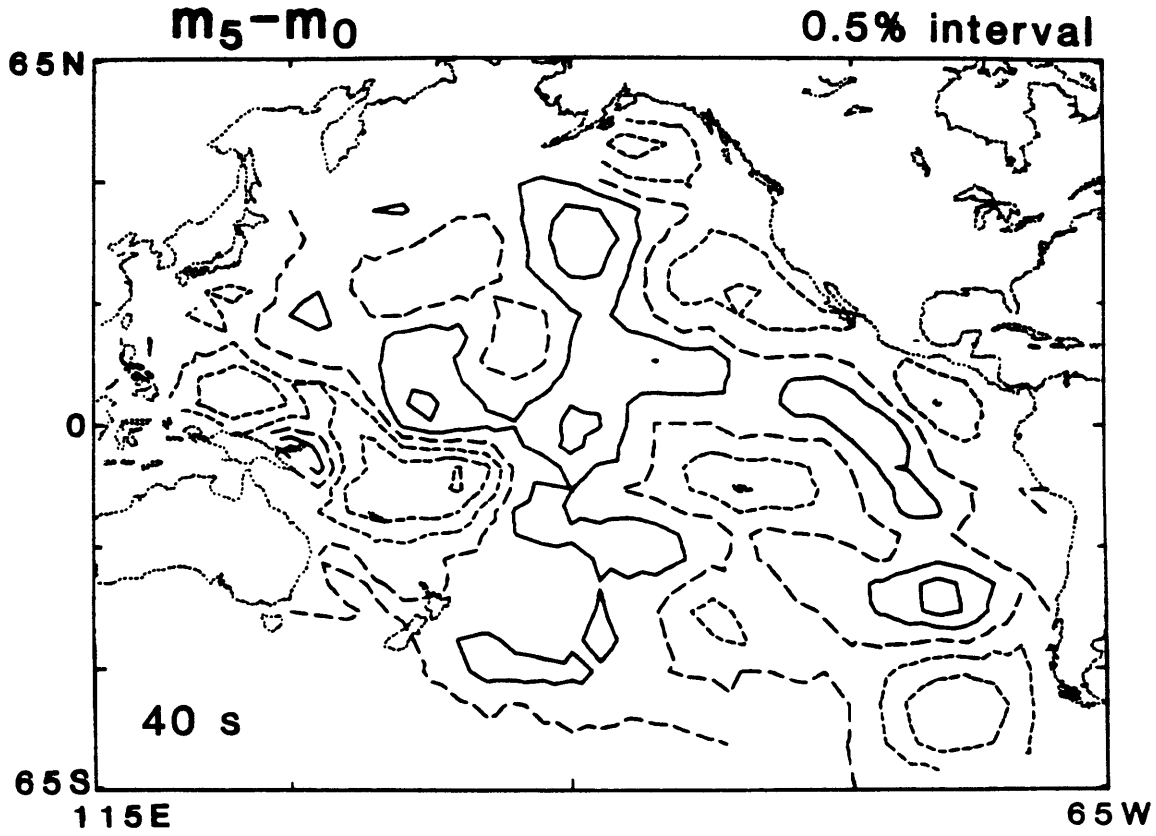

Figure 5.17 e).

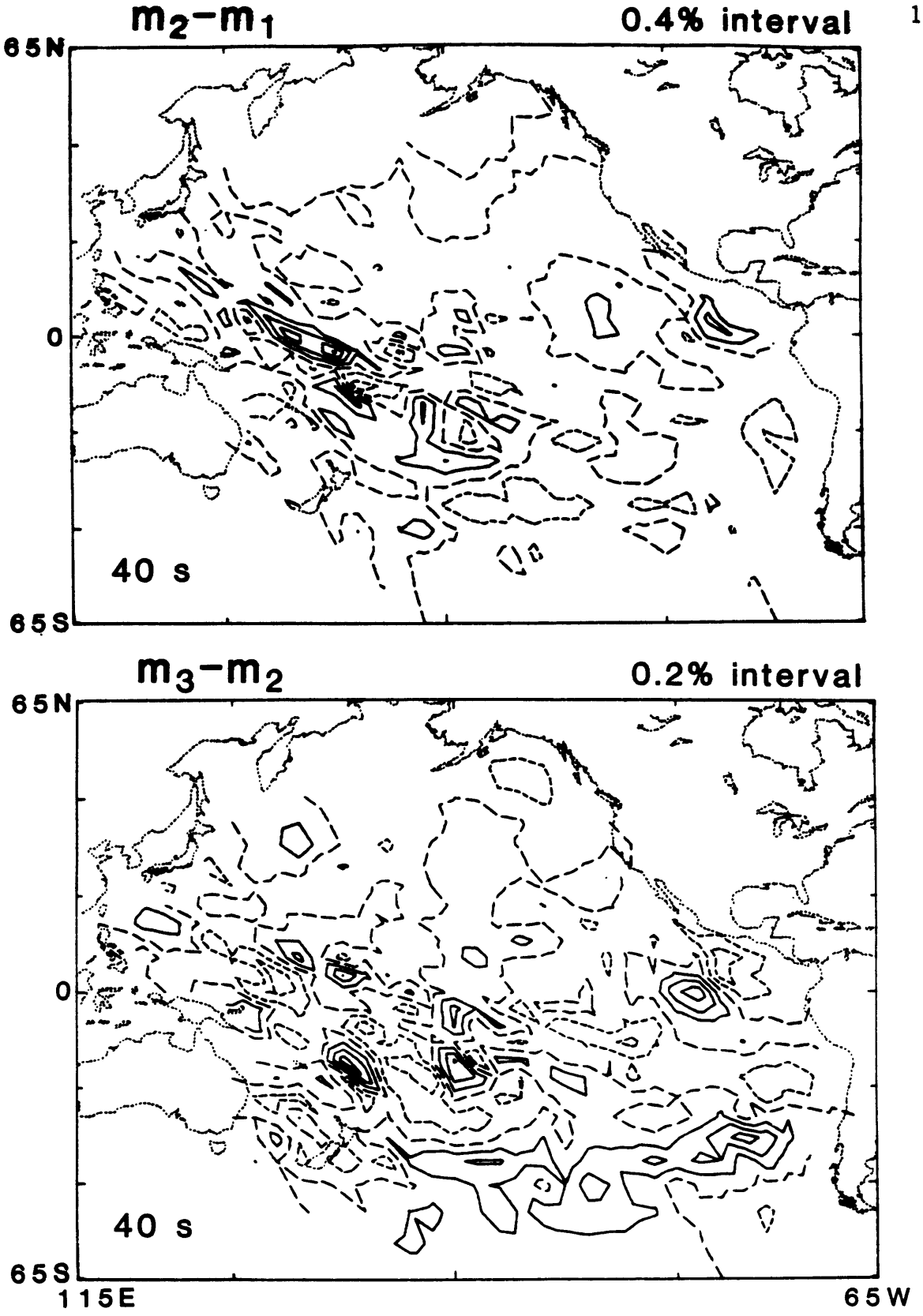

Figure 5.18. Perturbations from the previous iteration model for 40 s. a) Second, b) third, and c) fourth, and d) fifth iteration step.

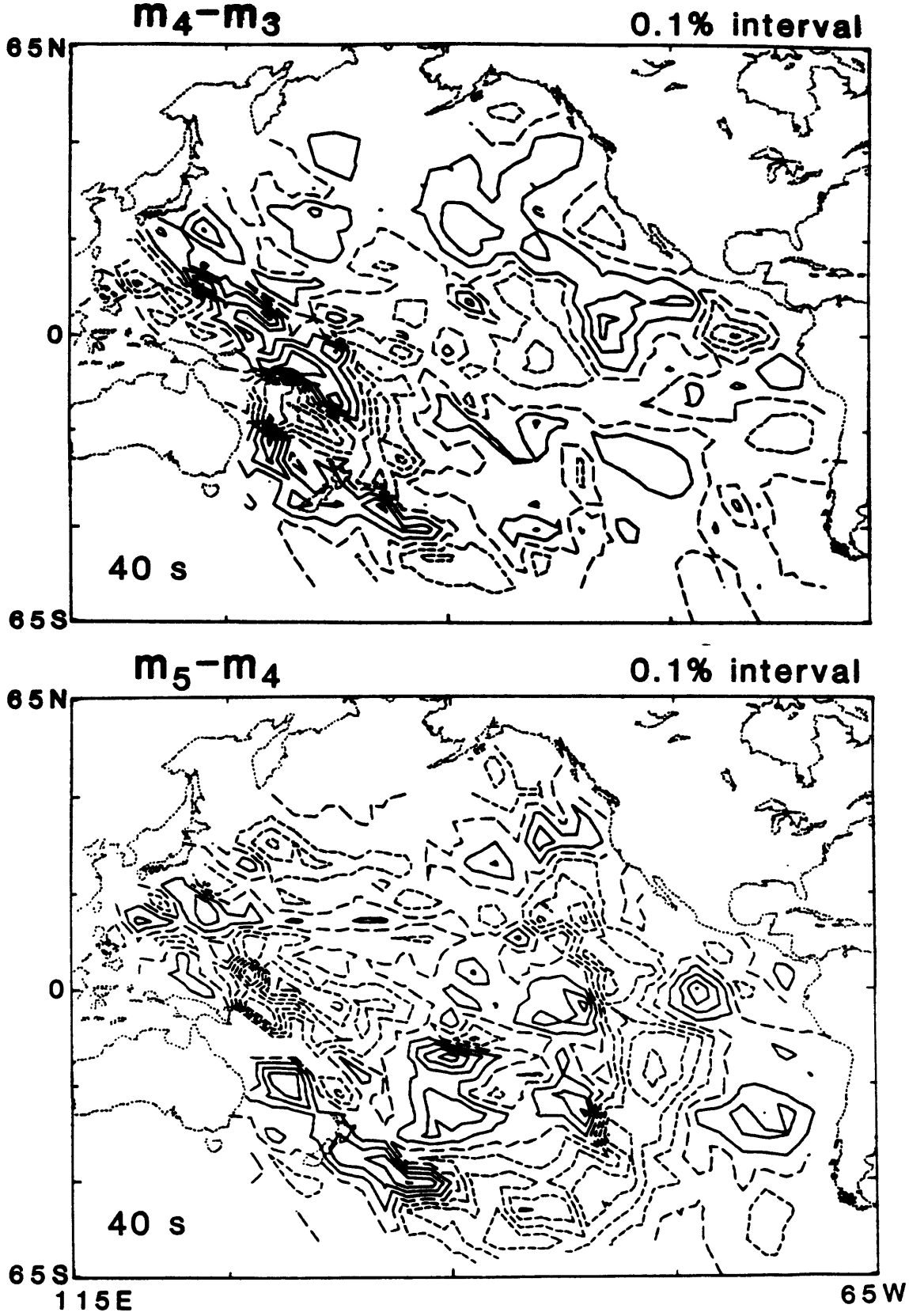

Figure 5.18 c) and d).

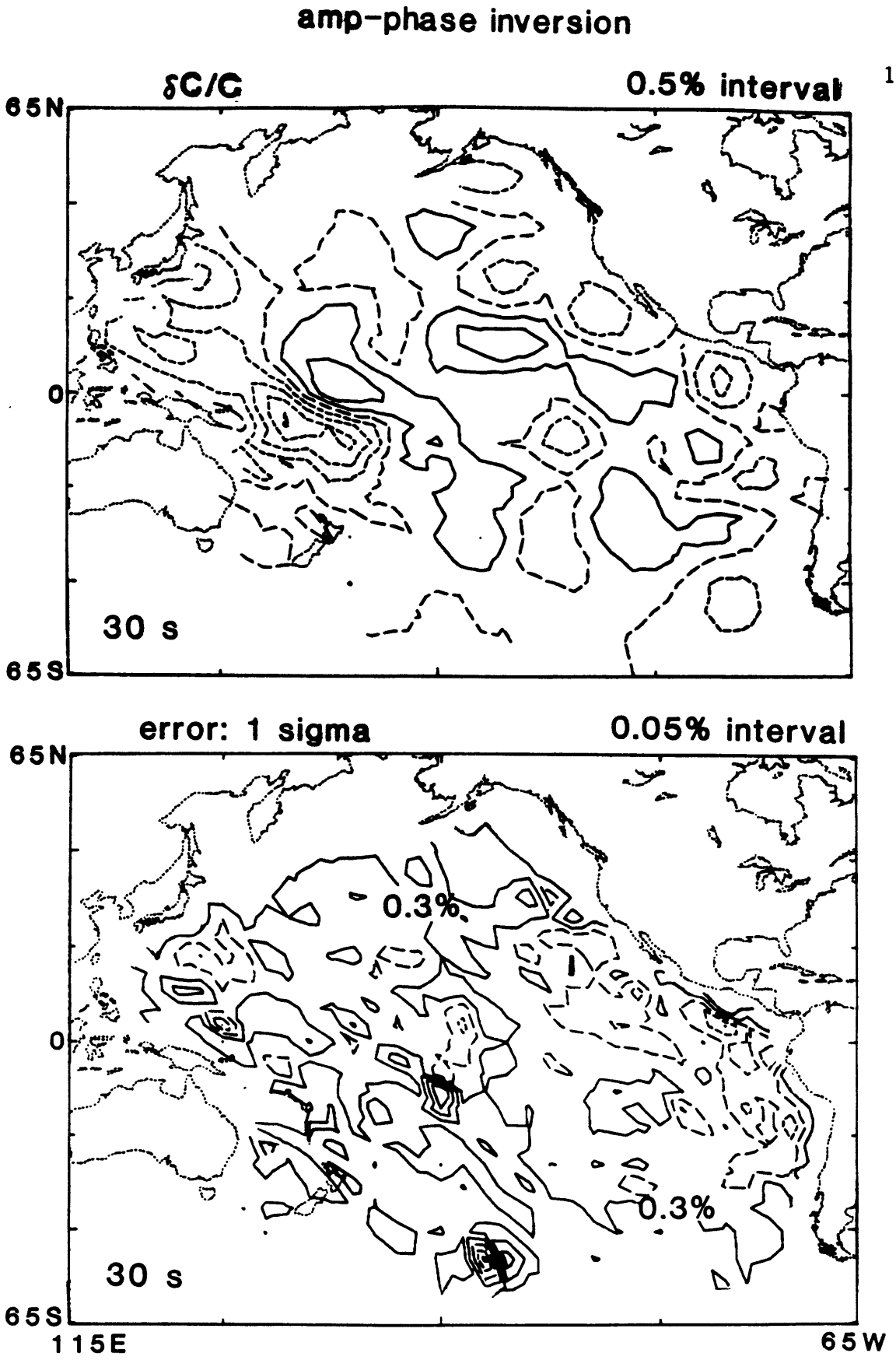

Figure 5.19. Final results of velocity perturbations after five iterations at a) 30, b) 40, c) 60, and d) 80 s. The bottom of each figure shows uncertainty level at each model point.

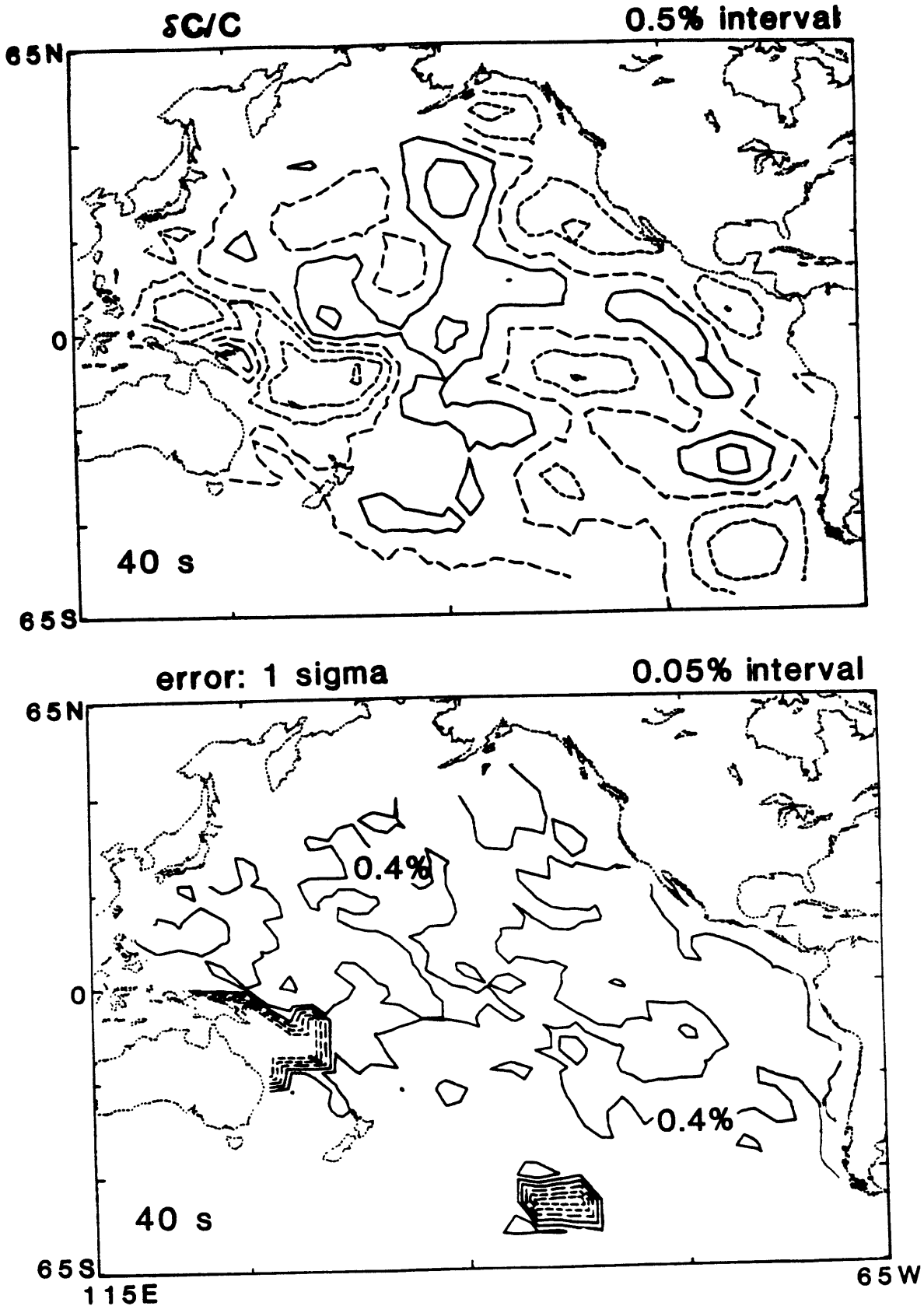
δC/C
0.5% interval
65N
0
65S
40 s
error: 1 sigma
0.05% interval
65N
0.4%
0.4%
0
40 s
65S
115E
65W

Figure 5.19 b).

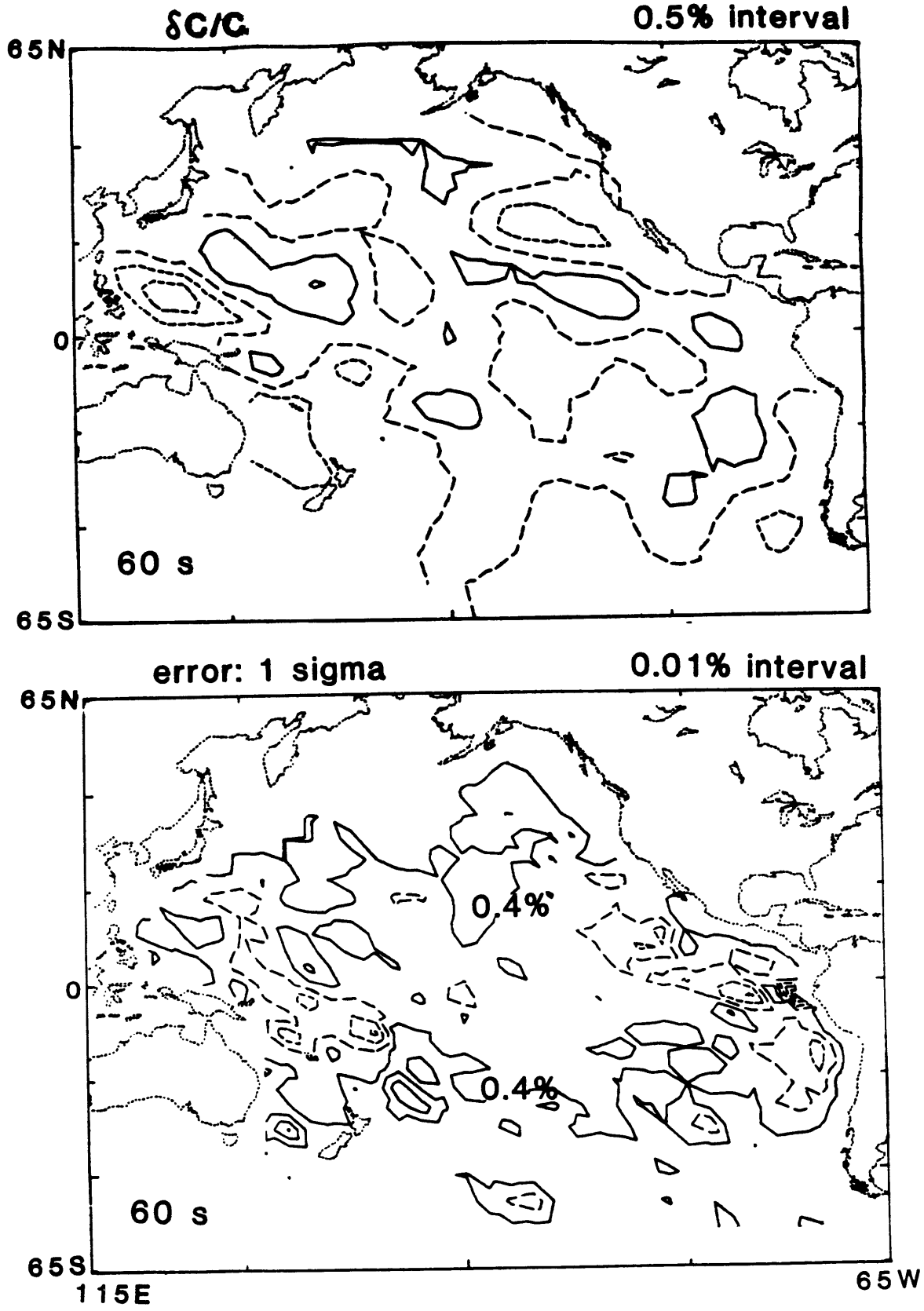
δC/C
0.5% interval
65N
0
65S
60 s
error: 1 sigma
0.01% interval
65N
0.4%
0.4%
0
60 s
65S
115E
65W

Figure 5.19 c).

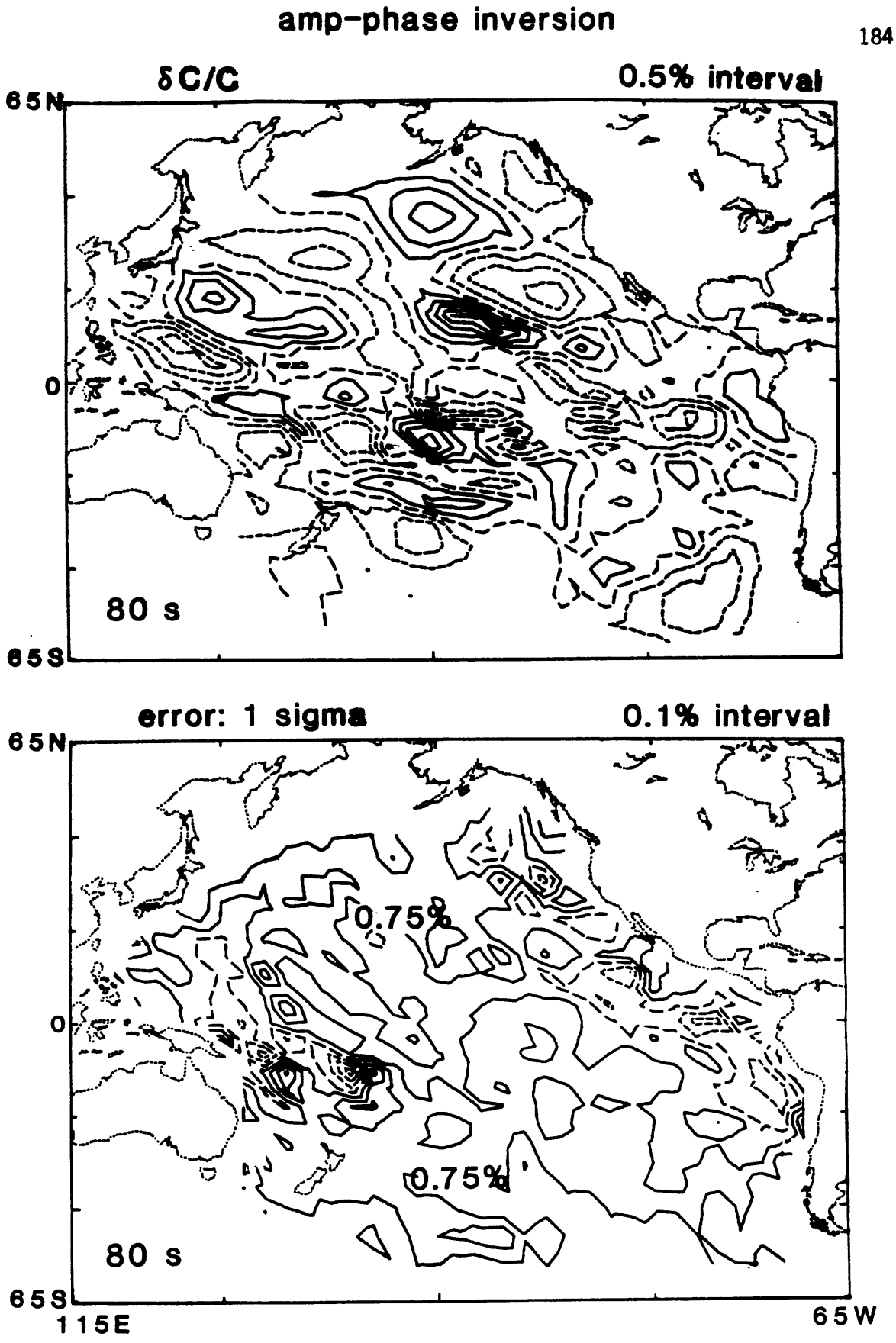
amp-phase inversion
δC/C
0.5% interval
65N
0
65S
80 s
error: 1 sigma
0.1% interval
65N
0.75%
0
0.75%
80 s
65S
115E
65W

Figure 5.19 d).

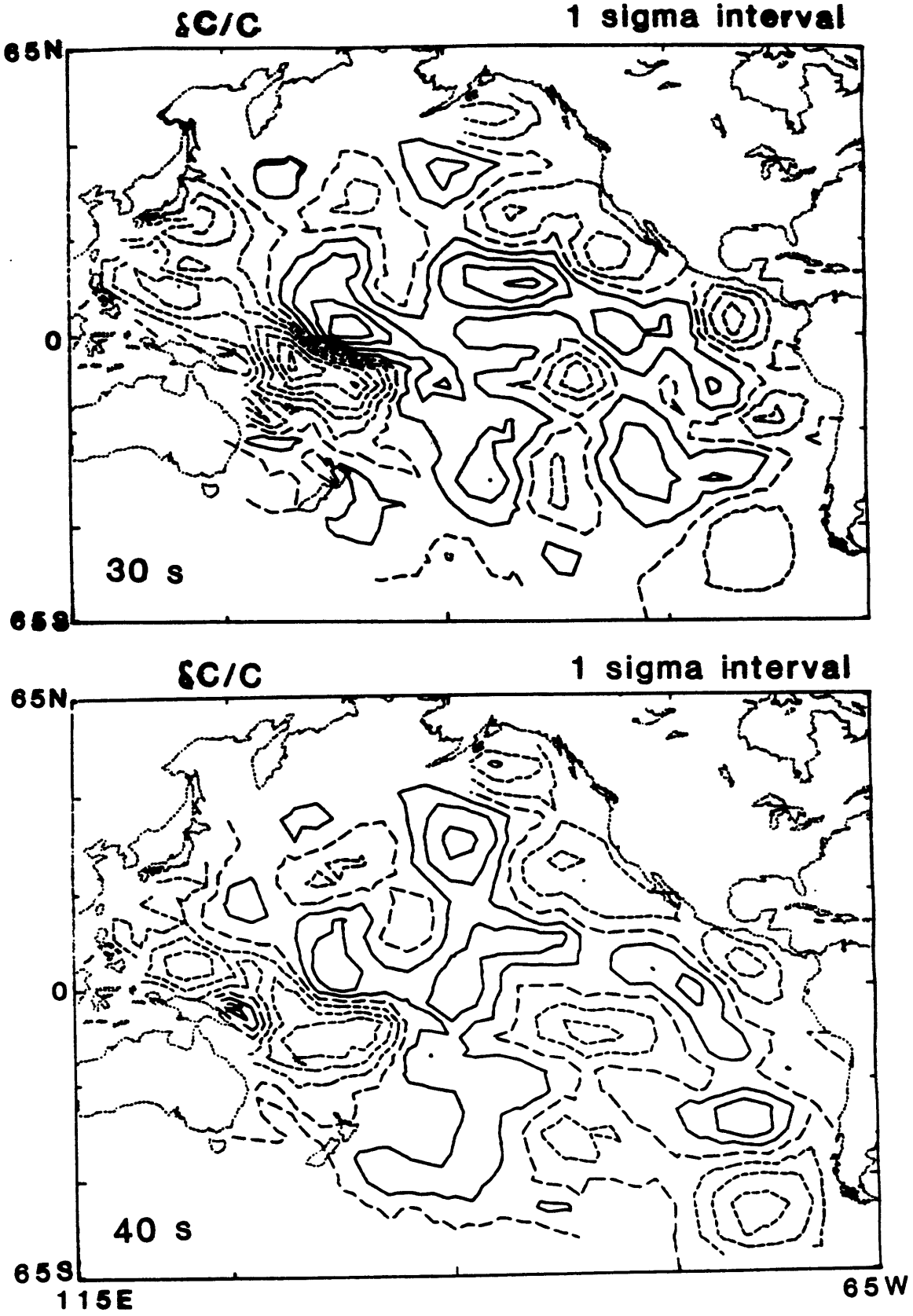

Figure 5.20. Velocity perturbations at a) 30 s, b) 40 s, c) 60 s and d) 80 s with a contour interval of one sigma velocity perturbations.

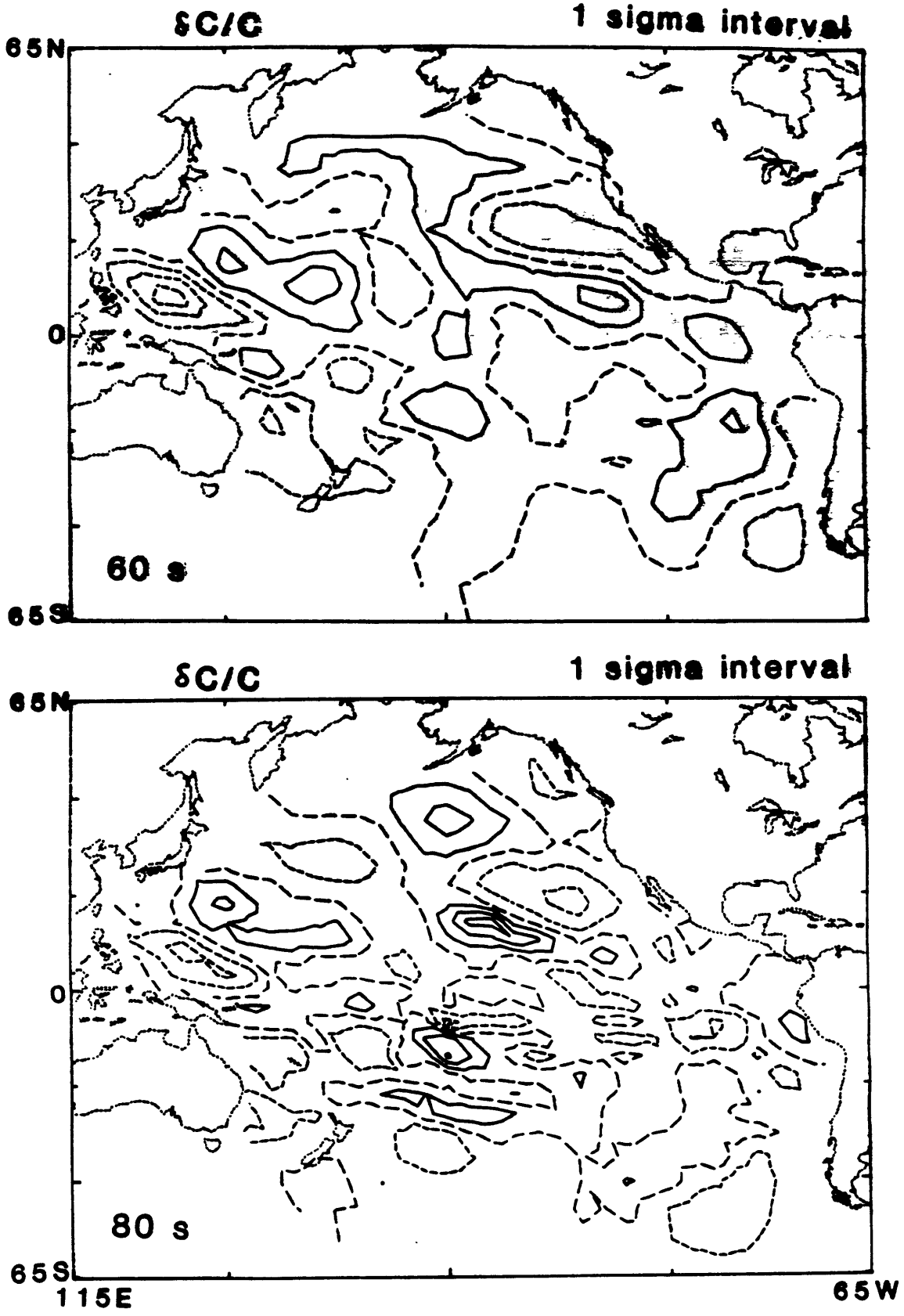

Figure 5.20 c) and d).

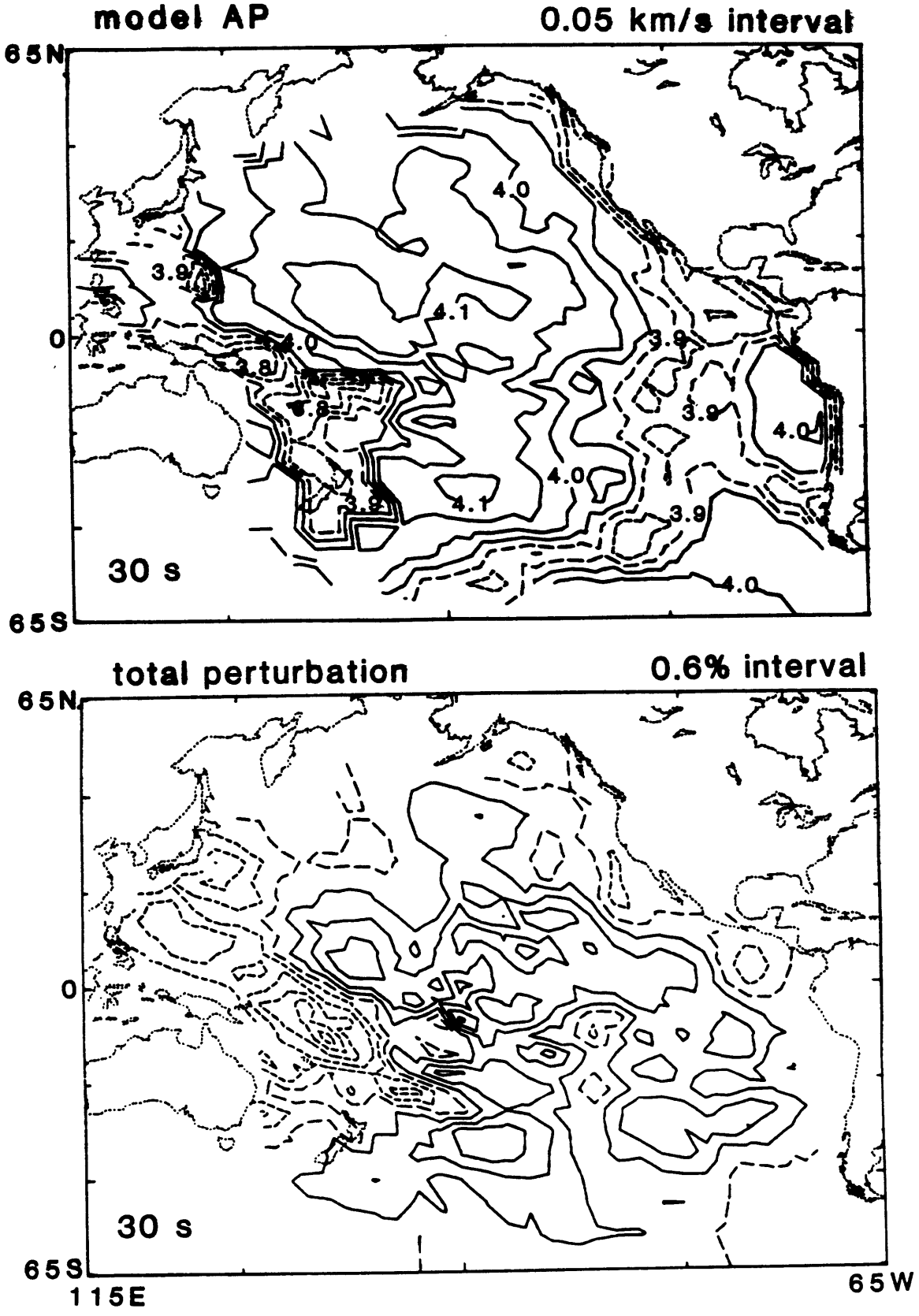

Figure 5.21. Final results of amplitude-phase inversions, "model AP" at a) 30 s, b) 40 s, c) 60 s, and d) 80 s. In each figure the bottom shows velocity anomalies as a reference of initial age-dependent model such as Figure 5.3.

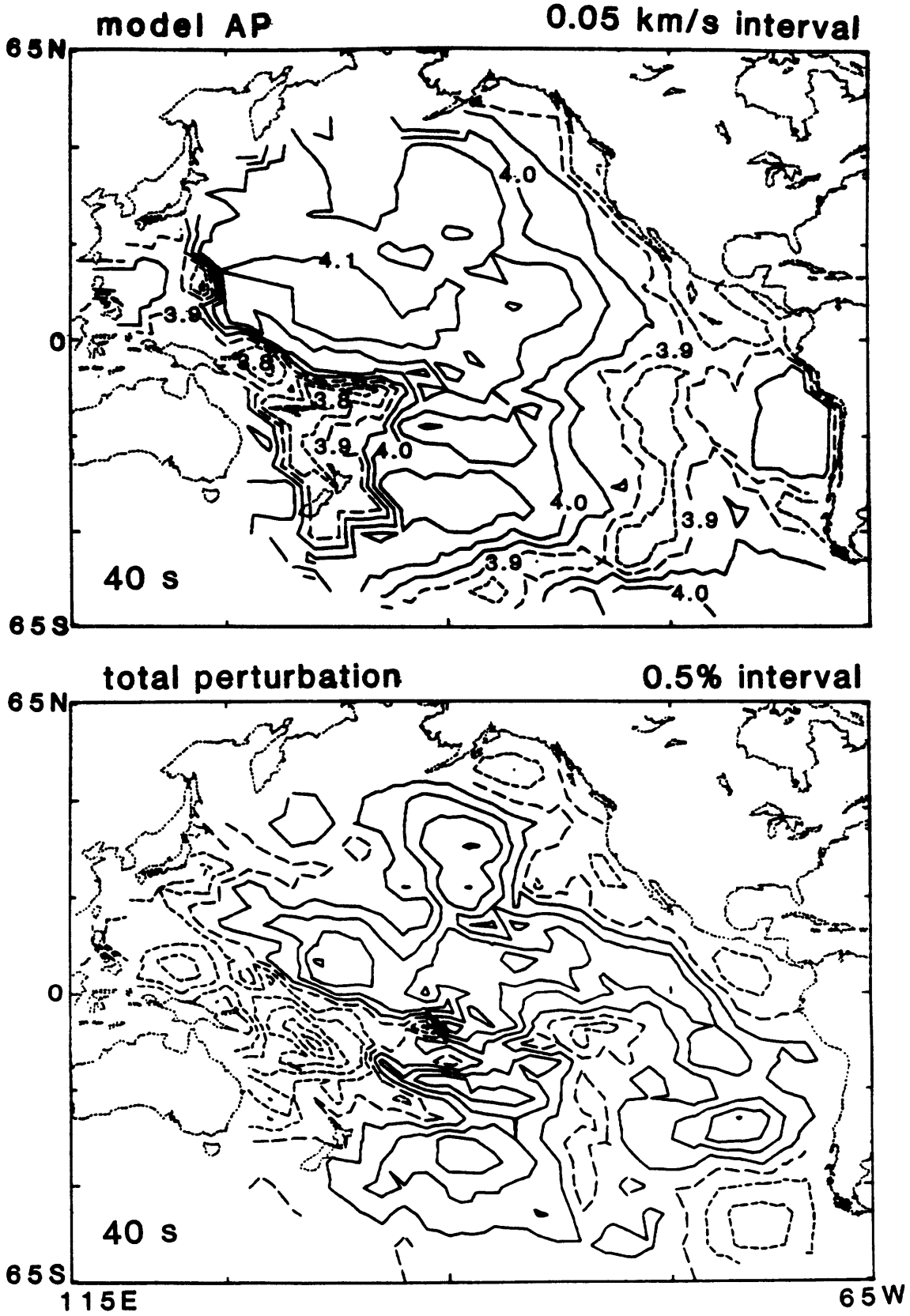
model AP
0.05 km/s interval
65N
0
65S
4.0
4.1
3.9
3.8
3.8
3.9
4.0
4.0
3.9
3.9
4.0
40 s
total perturbation
0.5% interval
65N
0
65S
40 s
115E
65W

Figure 5.21 b).

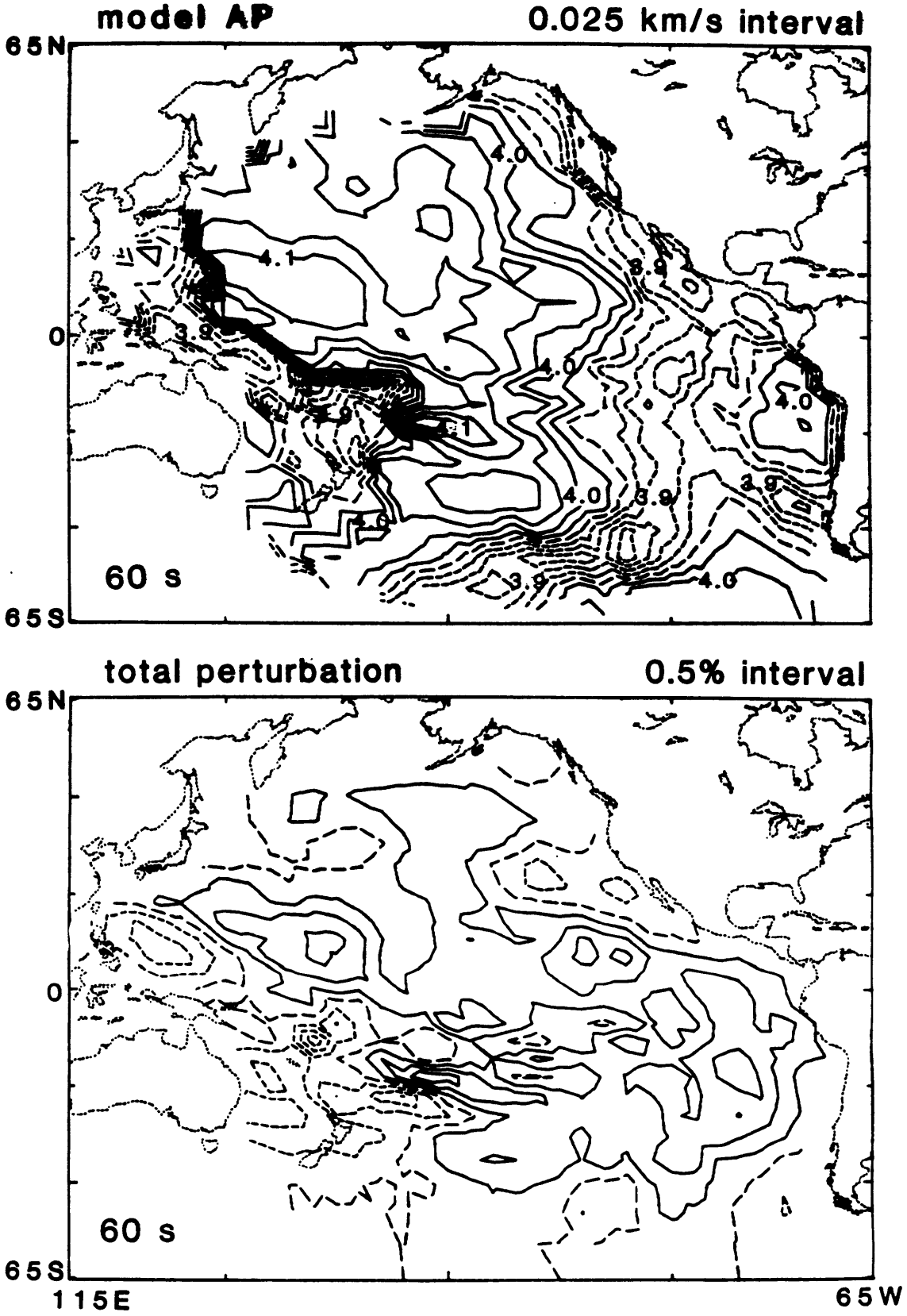
model AP
0.025 km/s interval
65N
0
65S
4.0
4.1
3.9
4.0
3.9
4.0
4.0
4.0
3.9
3.9
4.0
60 s
total perturbation
0.5% interval
65N
0
65S
60 s
115E
65W

Figure 5.21 c).

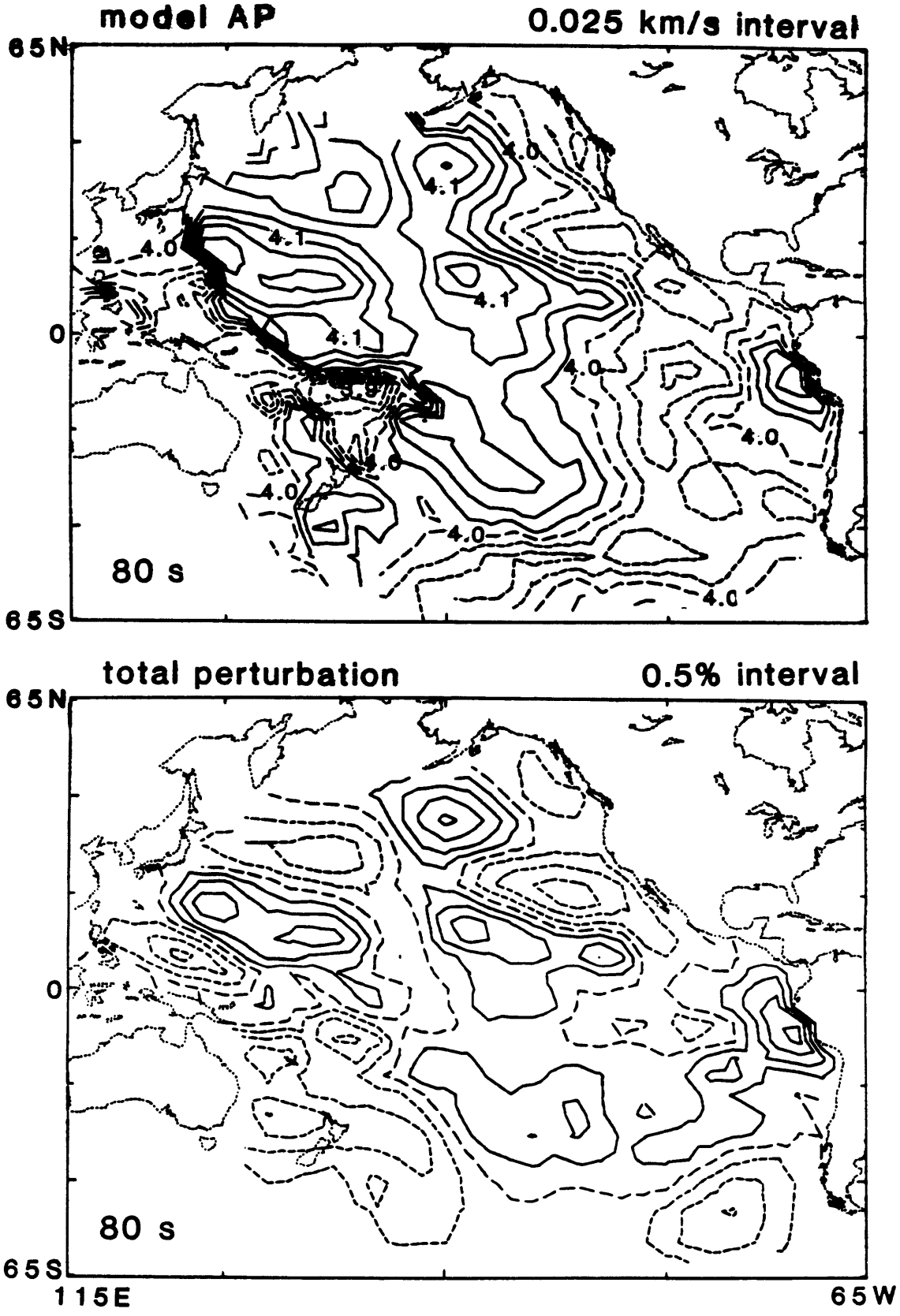
model AP
0.025 km/s interval
65N
0
65S
4.0
4.1
80 s
total perturbation
0.5% interval
65N
0
65S
80 s
115E
65W

Figure 5.21 d).

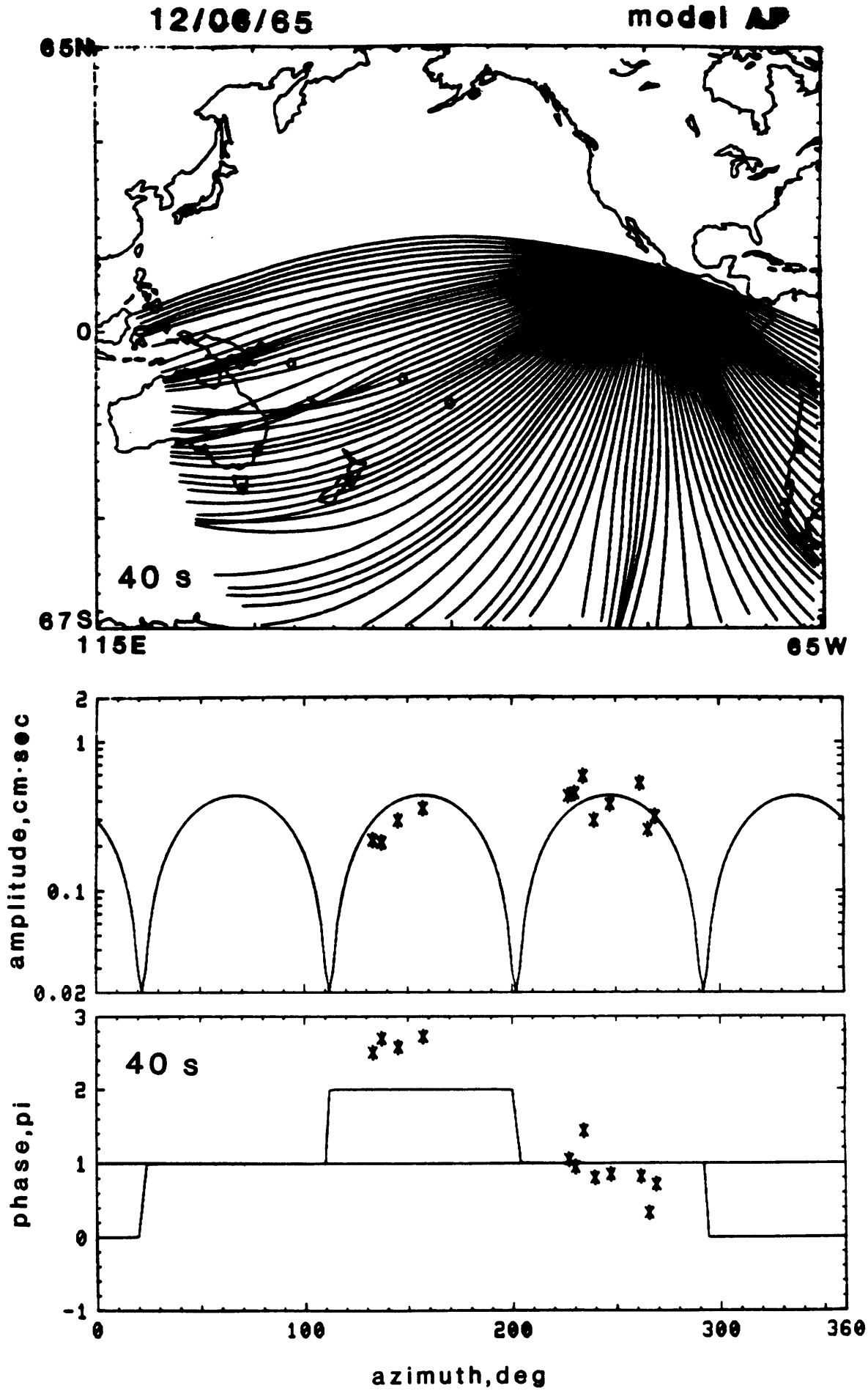

Figure 5.22. Example of a) ray traces and b) data fit to model AP at period 40 s for an event on December 6, 1965.

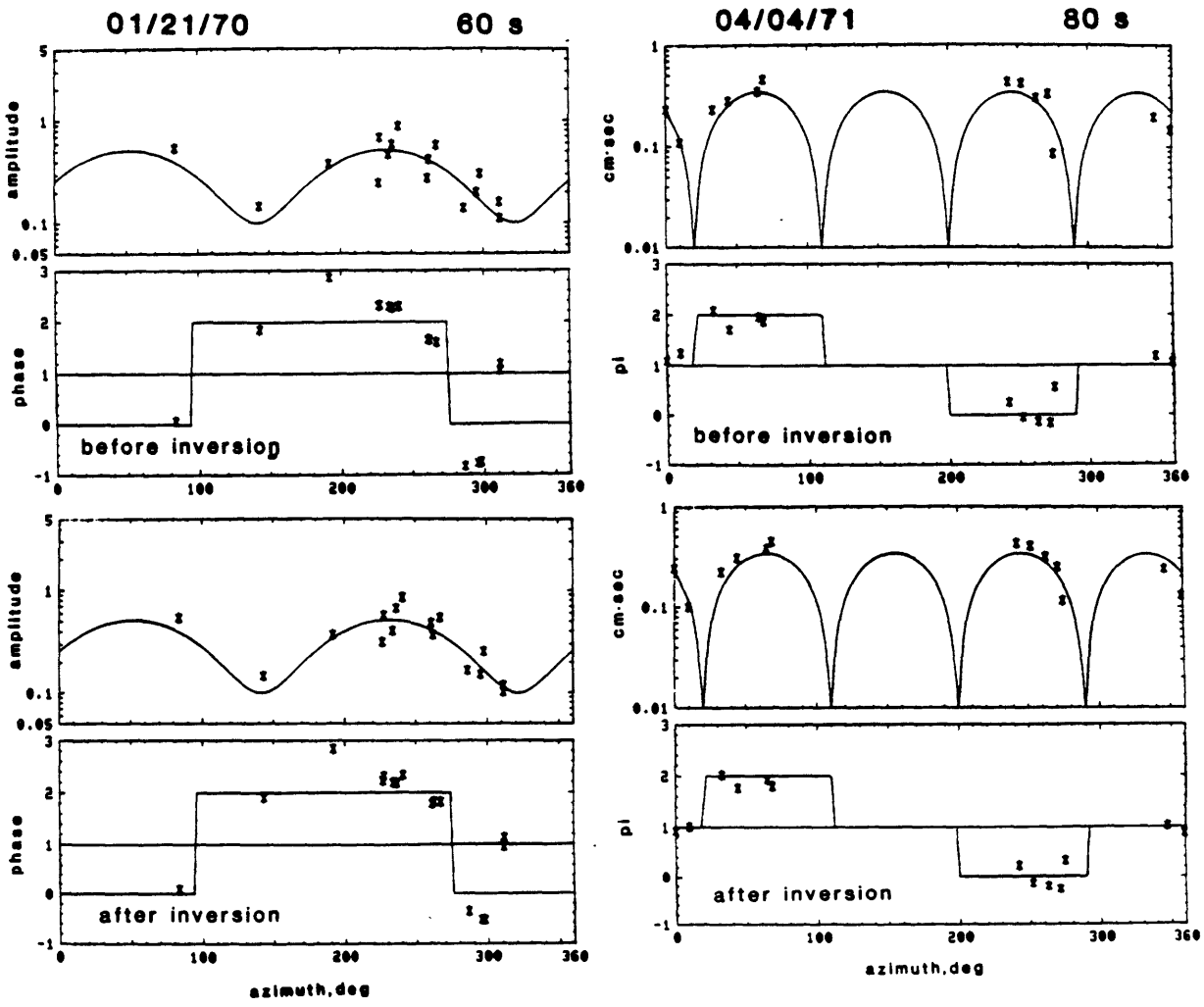

Figure 5.23. Four examples of data fit before and after inversions: a) January 21, 1970 at 60 s, b) April 4, 1971 at 80 s, c) September 27, 1972 at 80 s and d) December 6, 1965 at 30 s.

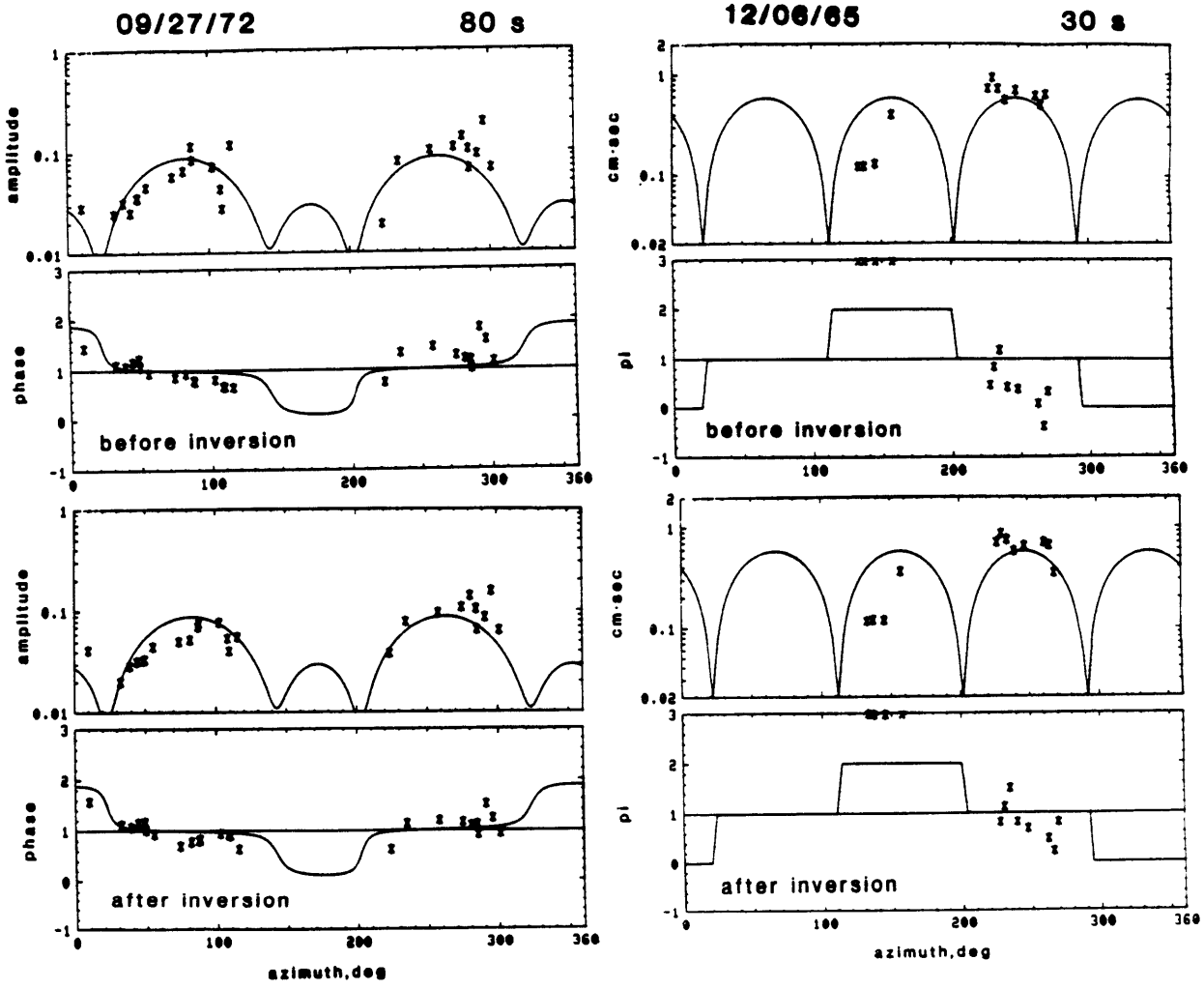

Figure 5.23 c) and d).

Chapter 6. Conclusions

We have developed formulations for modelling surface waveforms in a laterally heterogeneous Earth, tested their accuracy numerically by forward modelling, and finally applied the methods to real data with a non-linear iterative inversion scheme. The basic ideas are based on asymptotic ray theory, especially the Gaussian beam method, under the assumption of a medium with slowly-varying lateral heterogeneity. These methods were previously developed for acoustic or seismic body waves. In this study we showed that the main philosophy in these theory can be extended to the seismic surface wave problem by combining with normal mode theory for a laterally homogeneous medium: wavefields close to a ray can be expressed in terms of the paraxial ray approximation or a Gaussian beam whose basic element is an eigenfunction of the normal mode theory, (2.60) for Love waves and (2.66) for Rayleigh waves, respectively. For a single frequency, surface waves propagate horizontally like two-dimensional body waves, following the phase velocity distribution. Thus, the Gaussian beam approach developed for body waves can be directly applied to surface waves. Our formulations are fairly simple and give a clear understanding of the physics involved in the Gaussian beam approach to surface wave propagation.

To obtain synthetic seismograms we have only to superpose a number of Gaussian beams as for the case of two-dimensional acoustic waves [Cerveny et al., 1982] or seismic body waves [Cerveny and Psencik, 1983]. The following points should be noted because of the special characters of surface waves:

1. Compact ray tracing equations for surface waves are derived from the original canonical equations. In transversely isotropic media, wave

packets propagate at the local group velocity, while ray paths are determined by the local phase velocity.

2. Spherical Earth problems can be mapped into two-dimensional Cartesian coordinates by a Mercator projection which includes the effect of ellipticity.

3. Weighting factors are derived for superposing the Gaussian beams at each station. Complete formulae are given for both Love and Rayleigh waves for a point source specified by a moment-tensor.

4. The choice of a Gabor wavelet with large γ is proposed as a source time function, because the resulting synthetic seismograms can be compared directly to bandpass-filtered real data with similar frequency characteristics.

One of the greatest advantages of surface wave synthesis over body wave synthesis by Gaussian beams is that the problem is essentially two-dimensional for surface waves. Resolution of the depth of anomalies may be improved by using a range of periods. Numerical tests show that this waveform method may have the potential to detect small-scale velocity anomalies. In constructing synthetic seismograms, the phase velocity distribution is quite important while group velocity has only minor effects on the results.

Finally, we performed inversions for phase velocities in the Pacific Ocean at periods of 30-80 sec by employing both amplitude and phase information. First, the Born approximation was adopted to obtain the inverse formulations. We calculated Frechet derivatives by the methods developed in the early parts of this study. Since the initial model should be sufficiently close to the final model to avoid convergence of the solution to a local minima, we first performed conventional phase data

inversions. Then, with these results as an initial model, amplitude-phase inversions were conducted. Even though most of the residual variance reduction in phase was obtained in the phase data inversions, some improvement in the models, especially in matching amplitudes, was obtained by the amplitude-phase inversions. Also, with the formulation introduced by Tarantola and Valette [1982], we showed that the present non-linear iterative scheme gave a fairly reliable model.

In future work we should investigate several factors which were not carefully treated in this study. In this study we basically paid attention to lateral heterogeneity of the medium, but we should study both medium and source. For example, joint-inversions or alternative inversions for medium and source are one of our ultimate goals. Moreover, we may check the magnitude of lateral variations of attenuation factors Q and azimuthal anisotropy, which were totally neglected in this study. Especially, after corrections are applied for geometrical spreading in the laterally heterogeneous earth, measurements of Q are expected to be improved. Finally, we need to attack one difficult problem beyond the basic assumption of this study that the Earth is a laterally slowly-varying medium. In some areas such an assumption is not likely to be valid. An obvious example is an ocean-continent boundary, across which the structure varies rapidly. The asymptotic ray theory used in this study cannot deal with such regions. One way to study surface wave propagation through such boundaries is to obtain transmission and reflection coefficients with numerical procedures such as the finite-difference method. Then, we may combine the results of asymptotic ray theory with these coefficients to study areas with strongly heterogeneous media. For extremely complicated media the approaches used in this study cannot be applied. Even in

laterally homogeneous media, Chapman and Orcutt [1985] concluded that "No one method is ideal for all problems". Nevertheless, we cannot help feeling that the present approaches can deal with most of the surface wave propagation problems in the Earth and promote a better understanding of heterogeneity in the Earth and retrieval of more reliable source information.

REFERENCES

Aki, K., Scattering of P waves under the Montana Lasa, J. Geophys. Res., 78, 1334-1346, 1973.

Aki, K., 3-D inhomogeneities in lithosphere and asthenosphere: Evidence for decoupling in lithosphere and flow in asthenosphere, Rev. Geophys. Space Phys., 20, 161-170, 1981.

Aki, K., A. Christoffersson, and E.S. Husebye, Determination of the three dimensional seismic structure of the lithosphere, J. Geophys. Res., 82, 277-296, 1977.

Aki, K., and P.G. Richards, Quantitative Seismology, Theory and Methods, vols. 1 and 2, W.H. Freeman, San Francisco, Calif., 1980.

Babich, V.M. and N.J. Buldyrev, Asymptotic Methods in Problems of Diffraction of Short waves, Nauka, Moscow (in Russian), 1972.

Babich, V.M., B.A. Chikhachev, and T.B. Yanovskaya, Surface waves in a vertically inhomogeneous elastic half space with weak horizontal inhomogeneity, Izv. Earth Phys., 4, 24-31, 1976.

Babich, V.M. and N.J. Kirpichnikova, The Boundary Layer Method in Diffraction Problems, Leningrad University Press (in Russian, English translation by Springer-Verlag, 1980), 1974.

Backus, G.E., The propagation of short elastic surface waves on a slowly rotating Earth, Bull. Seismol. Soc. Am., 52, 823-846, 1962.

Backus, G. and F. Gilbert, Numerical applications of a formalism for geophysical inverse problems, Geophys. J. R. Astron. Soc., 13, 247-276, 1967.

Backus, G. and F. Gilbert, The resolving power of gross earth data, Geophys. J.R. Astron. Soc., 16, 169-205, 1968.

Backus, G. and F. Gilbert, Uniqueness in the inversion of inaccurate gross Earth data, Phil. Trans. R. Soc. London Ser. A266, 123-192, 1980.

Ben-Menahem, A., Observed attenuation and Q values of seismic surface waves in the upper mantle, J. Geophys. Res., 70, 4641-4651, 1965.

Bergman, E.A., Intraplate earthquakes and the state of stress in oceanic lithosphere, Ph.D. thesis, Mass. Inst. of Technol., Cambridge, 488 pp., 1984.

Bergman, E.A., and S.C. Solomon, Source mechanisms of earthquakes near mid-ocean ridges from body waveform inversion: implications for the early evolution of oceanic lithosphere, J. Geophys. Res., 89, 11415-11441, 1984.

Beydoun, W., and A. Ben-Menahem, Range of validity of seismic ray and beam methods in general inhomogeneous media, Part II, A canonical problem, Geophys. J.R. Astron. Soc., 82, 235-262, 1985.

Boore, D.M., Finite difference methods for seismic wave propagation in heterogeneous materials in seismology, in Surface Waves and Earth Oscillations (Methods in Computational Physics, vol. 11), Academic Press, New York, 1-37, 1972.

Boore, D.M., Love waves in nonuniform wave guides: Finite difference calculations, J. Geophys. Res., 75, 1512-1527, 1970.

Brune, J.N., J.E. Nafe, and L.E. Alsop, The polar phase shift of surface waves on a sphere, Bull. Seismol. Soc. Am., 51, 247-257, 1961.

Bullitt, J.W., and M.N. Toksöz, Three-dimensional ultrasonic modeling of Rayleigh wave propagation, Bull. Seismol. Soc. Am., 75, 1087-1104, 1985.

Bungum, H., and J. Capon, Coda pattern and multipath propagation of Rayleigh waves at NORSAR, Phys. Earth Planet. Inter., 9, 111-127, 1974.

Burridge, R. and H. Weinberg, Horizontal rays and vertical modes, in Wave Propagation and Underwater Acoustics, Lecture Notes in Physics, 70, 86-152, Springer-Verlag, Berlin, 1976.

Canas, J.A. and B.J. Mitchell, Lateral variation of surface-wave anelastic attenuation across the Pacific, Bull. Seismol. Soc. Am., 68, 1637-1650, 1978.

Canas, J.A. and B.J. Mitchell, Rayleigh wave attenuation and its variation across the Atlantic Ocean, Geophys. J.R. Astron. Soc., 67, 159-176, 1981.

Capon, J., Analysis of Rayleigh-wave multipath propagation at LASA, Bull. Seismol. Soc. Am., 60, 1701-1731, 1970.

Červený, V., Expansion of a plane wave into Gaussian beams, Studia Geophys. Geod., 26, 120-131, 1982.

Červený, V., Synthetic body wave seismograms for laterally varying layered structures by the Gaussian beam method, Geophys. J. R. Astron. Soc., 73, 389-426, 1983.

Červený, V. and F. Hron, The ray series method and dynamic ray tracing systems for 3-D inhomogeneous media, Bull. Seism. Soc. Am., 70, 47-77, 1980.

Červený V., and L. Klimeš, Synthetic body wave seismograms for three-dimensional laterally varying media, Geophys. J. R. Astron. Soc., 79, 119-133, 1984.

Červený, V., I.A. Molotkov, and I. Pšenčík, The Ray Method in Seismology, Karlova Univ., Praha, 1977.

Červený, V., M.M. Popov, and I. Pšenčík, Computation of wave fields in inhomogeneous media - Gaussian beam approach, Geophys. J. R. Astron. Soc, 70, 109-128, 1982.

Červený, V., and I. Pšenčík, Gaussian beams in two-dimensional elastic inhomogeneous media, Geophys. J. R. Astron. Soc., 72, 419-435, 1983.

Chapman, C.H., A new method for computing synthetic seismograms, Geophys. J. R. Astron. Soc., 54, 481-518, 1978.

Chapman, C., and R. Drummond, Body wave seismograms in inhomogeneous media using Maslov asymptotic theory, Bull. Seismol. Soc. Am., 72, S277-S317, 1982.

Chapman, C.H. and J.A. Orcutt, The computation of body-wave synthetic seismograms, Rev. Geophys., 23, 105-163, 1985.

Chen, T. and D.W. Forsyth, A detailed study of two earthquakes seaward of the Tonga Trench: Implications for mechanical behavior of the oceanic lithosphere, J. Geophys. Res., 83, 4995-5004, 1978.

Chernov, L.A., Wave Propagation in a Random Medium, McGraw-Hill, New York, 1960.

Chinn, D.S., and B.L. Isacks, Accurate source depths and focal mechanisms of shallow earthquakes in western South America and in the New Hebrides island arc, Tectonics, 2, 529-563, 1983.

Clayton, R.W. and Comer, R.P., A tomographic analysis of mantle heterogeneities for body wave travel times (abstract), EOS, Trans. AGU, 64, 776, 1983.

Cormier, V.F. and Spudich, P., Amplification of ground motion and waveform complexity in fault zones: Example from the San Andreas and Calaveras faults, Geophys. J. R. Astron. Soc., 79, 135-152, 1984.

Dorman, J., M. Ewing, and J. Oliver, Study of shear-velocity distribution in the upper mantle by mantle Rayleigh waves, Bull. Seismol. Soc. Am., 50, 87-115, 1960.

Dziewonski, A.M., Mapping the lower mantle: Determination of lateral heterogeneity in P velocity up to degree and order 6, J. Geophys. Res., 89, 5929-5952, 1984.

Evernden, J.F., Direction of approach of Rayleigh waves and related problems, Part I, Bull. Seismol. Soc. Am., 43, 225-274, 1953.

Evernden, J.F., Direction of approach of Rayleigh waves and related problems, Part II, Bull. Seismol. Soc. Am., 44, 159-184, 1954.

Ewing, M., W. Jardetzky, and F. Press, Elastic Waves in Layered Media, McGraw-Hill, New York, 1957.

Forsyth, D.W., The early structural evolution and anisotropy of the oceanic upper mantle, Geophys. J. R. Astron. Soc., 43, 103-162, 1975.

Forsyth, D.W., The evolution of the upper mantle beneath mid-ocean ridges, Tectonophysics, 38, 89-118, 1977.

Forsyth, D.W., Determinations of focal depths of earthquakes associated with the bending of oceanic plates at trenches, Phys. Earth Planet. Inter., 28, 141-160, 1982.

Gjevik, B., A variational method for Love waves in nonhorizontal layered structures, Bull. Seismol. Soc. Am., 63, 1013-1023, 1973.

Gregersen, S., and L.E. Alsop, Mode conversion of Love waves at a continental margin, Bull. Seismol. Soc. Am., 66, 1855-1872, 1976.

Haines, A.J., A phase-front method -I. Narrow frequency band SH waves, Geophys. J.R. Astron. Soc., 72, 783-808, 1983.

Hudson, J.A., A parabolic approximation for surface waves, Geophys. J.R. Astron. Soc., 67, 755-770, 1981.

Jobert, N., and G. Jobert, An application of ray theory to the propagation of waves along a laterally heterogeneous spherical surface, Geophys. Res. Lett., 10, 1148-1151, 1983.

Julian, B.R., Ray tracing in arbitrary heterogeneous media, in Tech. Note 1970-45, Lincoln Lab., M.I.T., Lexington, Mass., 1970.

Kirpichnikova, N.Y., Rayleigh waves concentrated near a ray on the surface of an inhomogeneous elastic body, in Mathematical problems in wave propagation theory, part II, Seminar in Mathematics, 15, 49-62, Steklov Mathematical Institute, Nauka, Leningrad (in Russian, English translation by Consultants Bureau, New York, 1971), 1969.

Klimeš, L., Hermite-Gaussian beams in inhomogeneous elastic media, Studia Geophys. Geod., 27, 354-365, 1983.

Knopoff, L., J.W. Schule, and F.A. Schwab, Phase veolcities of Rayleigh waves across the East Pacific Rise, Tectonophysics, 10, 321-334, 1970.

Koch, M., The determination of lateral velocity inhomogeneities by linear and non-linear inversion of teleseismic and local seismic travel times-application to the seismic zone Vrancea, Romania, Ph.D. thesis, University of Karlsruhe (in German), 1983.

Kravtsov, Y.A. and Y.I. Orlov, Limit of applicability of the method of geometric optics and related problems, Sov. Phys. Usp., 23, 750-762, 1980.

Landau, L.D., and E.M. Lifshitz, The Classical Theory of Fields, 4th Ed., Pergamon Press, Oxford, 1975.

Landau, L.D., and E.M. Lifshitz, Mechanics, 3rd. Ed., Pergamon Press, Oxford, 1976.

Langston, C.A., and D.V. Helmberger, A procedure for modelling shallow dislocation sources, Geophys. J.R. Astron. Soc., 42, 117-130, 1975.

Lawson, C.L., and R.J. Hanson, Solving Least Squares Problems, Prentice-Hall, Inc., Englewood Cliffs, 1974.

Lay, T., and H. Kanamori, Geometric effects of global lateral heterogeneity on long period surface wave propagation, J. Geophys. Res., 90, 605-621, 1985.

Leeds, A.R., Lithospheric thickness in the western Pacific, Phys. Earth Planet. Inter., 11, 61-64, 1975.

Lysmer, J. and L.A. Drake, A finite element method for seismology, in Seismology: Surface Waves and Earth Oscillations (Methods in Computational Physics, vol. 11), Academic Press, New York, 181-216, 1972.

Madariaga, R., Gaussian beam synthetic seismograms in a vertically varying medium, Geophys. J.R. Astron. Soc., 79, 589-612, 1984.

Madariaga, R., and P. Papadimitriou, Gaussian beam modelling of upper mantle phases, Annales Geophysicae, in press, 1985.

McGarr, A., Amplitude variations of Rayleigh waves - Propagation across a continental margin, Bull. Seismol. Soc. Am., 59, 1281-1305, 1969a.

McGarr, A., Amplitude variations of Rayleigh waves -horizontal refractions, Bull. Seismol. Soc. Am., 59, 1307-1334, 1969b.

Mendiguren, J.A., Inversion of surface wave data in source mechanism studies, J. Geophys. Res., 82, 889-894, 1977.

Miller, D., M. Oristaglio, and L. Dupal, Reservoir geometry from borehole seismics: VSP migration in theory and practice, Geophysics, in press, 1985.

Mitchell, B.J., and G.K. Yu, Surface wave dispersion, regionalized velocity models and anisotropy of the Pacific crust and upper mantle, Geophys. J.R. Astron. Soc., 63, 497-514, 1980.

Morgan, W.J., Convection plumes in the lower mantle, Nature, 230, 42-43, 1971.

Müller, G., Efficient calculation of Gaussian-beam seismograms for two-dimensional inhomogeneous media, Geophys. J. R. Astron. Soc., 79, 153-166, 1984.

Nakanishi, I., and D.L. Anderson, Measurements of mantle wave velocities and inversion for lateral heterogeneity and anisotropy 1. Analysis of great circle phase velocities, J. Geophys. Res., 88, 10267-10283, 1983.

Nakanishi, I. and D.L. Anderson, Measurements of mantle wave velocities and inversion for lateral heterogeneity and anisotropy, II, Analysis by the single-station method, Geophys. J.R. Astron. Soc., 78, 573-617, 1984.

Nataf, H.-C., I. Nakanishi, and D.L. Anderson, Anisotropy and shear-velocity heterogeneities in the upper mantle, Geophys. Res. Lett., 11, 109-112, 1982.

Nishimura, C.E., and D.W. Forsyth, Anomalous Love-wave phase velocities in the Pacific: Sequential pure-path and spherical harmonic inversion, Geophys. J.R. astr. Soc., 81, 389-407, 1985.

Nowack, R.L., and K. Aki, The 2-D Gaussian beam synthetic method: Testing and application, J. Geophys. Res., 89, 7797-7819, 1984a.

Nowack, R.L., and K. Aki, Iterative inversion for structure using complete waveforms (abstract), EOS Trans. AGU, 65, 237, 1984b.

Patton, H., A note on the source mechanism of the southeastern Missouri earthquake of October 21, 1965, J. Geophys. Res., 81, 1483-1486, 1976.

Patton, H., Crust and upper mantle structure of the Eurasian continent from phase velocity and Q of surface waves, Rev. Geophys. Space Phys., 18, 605-625, 1980.

Pierce, A.D., Extension of the method of normal modes to sound propagation in an almost stratified medium, J. Acoust. Soc. Am., 37, 19-27, 1965.

Pilant, W.L., and L. Knopoff, Observations of multiple seismic events, Bull. Seismol. Soc. Am., 54, 19-39, 1964.

Popov, M.M., A new method of computation of wave fields using Gaussian beams, Wave Motion, 4, 85-97, 1982.

Popov, M.M., and I. Pšenčík, Computation of ray amplitudes in inhomogeneous media rich curved interfaces, Studia Geophys. Geod., 22, 248-258, 1978.

Richardus, P., and R.K. Adler, Map projections for geodesists, cartographers and geographers, North-Holland Publishing Comp., Amsterdam, 1972.

Romanowicz, B., Depth resolution of earthquakes in central Asia by moment tensor inversion of long period Rayleigh waves: Effects of phase velocity variations across Eurasia and their calibration, J. Geophys. Res., 86, 5963-5984, 1981.

Saito, M., Excitation of free oscillations and surface waves by a point source in a vertically heterogeneous earth, J. Geophys. Res., 72, 3689-3699, 1967.

Saastamoinen, P.R., Ray asymptotic propagation of the spectra of elastic surface waves in a waveguide with laterally smooth inhomogeneities, Geophys. J. Roy. Astron. Soc., 79, 269-284, 1984.

Schwartz, S.Y., and T. Lay, Comparison of long-period surface wave amplitude and phase anomalies for two models of global lateral heterogeneity, Geophys. Res. Lett., 12, 231-234, 1985.

Sclater, J.G., B. Parsons, and C. Jaupart, Oceans and continents: Similarities and differences in the mechanism of heat loss, J. Geophys. Res., 86, 11535-11552, 1981.

Scott, P., and D.V. Helmberger, Applications of the Kirchhoff-Helmholtz integral to problems in seismology, Geophys. J.R. Astron. Soc., 72, 237-254, 1983.

Sobel, P.A., and D.H. von Seggern, Applications of surface-wave ray tracing, Bull. Seismol. Soc. Am., 68, 1359-1380, 1978.

Stewart, L.M., and E.A. Okal, Seismicity and aseismic slip along the Eltanin Fracture Zone, J. Geophys. Res., 88, 10495-10507, 1983.

Sykes, L.R., Mechanism of earthquakes and nature of faulting on the mid-oceanic ridges, J. Geophys. Res., 72, 2131-2153, 1967.

Takeuchi, H., and M. Saito, Seismic surface waves, in Surface Waves and Earth Oscillations (Methods in Computational Physics, Vol. 11), Academic Press, New York, 217-295, 1972.

Tanimoto, T., The Backus-Gilbert approach to the three-dimensional structure in the upper mantle: I. Lateral variation of surface wave phase velocity with its error and resolution, Geophys. J.R. Astron. Soc., 82, 105-123, 1985.

Tanimoto, T., and D.L. Anderson, Mapping convection in the mantle, Geophys. Res. Lett., 11, 287-290, 1984.

Tarantola, A., Nonlinear inverse problem for a heterogeneous acoustic medium, Geophysics, 49, 1259-1266, 1984a.

Tarantola, A., The principles of seismic imagery, preprint, 1984b.

Tarantola, A. and B. Valette, Generalized nonlinear inverse problems solved using the least-squares criterion, Rev. Geophys. Space Phys., 20, 219-232, 1982.

Thomson, C., Ray-theoretical amplitude inversion for laterally varying velocity structure below NORSAR, Geophys. J.R. Astron. Soc., 74, 525-558, 1983.

Tréhu, A.M., J.L. Nabelek, and S.C. Solomon, Source characterization of two Reykjanes Ridge earthquakes: Surface waves and moment tensors; P waveforms and nonorthogonal nodal planes, J. Geophys. Res., 86, 1701-1724, 1981.

Tsai, Y.-B. and K. Aki, Precise focal depth determination from amplitude spectra of surface waves, J. Geophys. Res., 75, 5729-5743, 1970.

Weinberg, H., and R. Burridge, Horizontal ray theory for ocean acoustics, J. Acoust. Soc. Am., 55, 63-79, 1974.

Weissel, J.K., Evolution of the Lau Basin by the growth of small plates, in Island Arcs, Deep Sea Trenches and Back-Arc Basins, Maurice Ewing Ser., Vol. 1, edited by M. Talwani and W.C. Pitman, III, pp. 429-436, AGU, Washington, D.C., 1977.

Wiggins, R.A., Interpolation of digitized waves, Bull. Seismol. Soc. Amer., 66, 2077-2081, 1976.

Wong, Y.K., and J.H. Woodhouse, Ray theory for surface waves on a sphere (abstract), EOS Trans. AGU, 64, 260, 1983.

Woodhouse, J.H., Surface waves in a laterally varying layered structure, Geophys. J. R. Astron. Soc., 37, 461-490, 1974.

Woodhouse, J.H., and A.M. Dziewonski, Mapping the upper mantle: Three-dimensional modeling of Earth structure by inversion of seismic waveforms, J. Geophys. Res., 84, 5953-5986, 1984.

Woodhouse, J.H., and T.P., Girnius, Surface waves and free oscillations in a regionalized earth model, Geophys. J.R. Astron. Soc., 68, 657-673, 1982.

Yomogida, K., Gaussian beams for surface waves in laterally slowly-varying media, Geophys. J.R. Astron. Soc., 82, 511-533, 1985.

Yomogida, K. and K. Aki, Waveform synthesis of surface waves in a laterally heterogeneous Earth by the Gaussian beam method, J. Geophys. Res., 90, 7665-7688, 1985.

APPENDIX: Data Sets for Inversions in Chapter 5

In this appendix, all of the data used in Chapter 5 are displayed. The basic data are vertical components of Rayleigh waves from the 18 events listed in Table 5.1 recorded at WWSSN stations (e.g., as given in Table 5.2 for 40s). In each figure the amplitudes and initial phases at 30s, 40s, 60s and 80s are exhibited. The azimuth is defined to be clockwise from north. The amplitudes are normalized to a distance of 90° by removing attenuation effects. Geometrical spreading is assumed to vary simply as $(\text{distance})^{-1/2}$. The phase corrections are performed with the pure-path approach and a simple age-dependent model (e.g., the model shown in Figure 5.3 for 40s). These plots thus exhibit the fit of the data to the initial models at each period. The source parameters used in this study are summarized in Table 5.1. Data off the scales of these figures are indicated by a cross ('X'); the bulk of the data are indicated by a star ('*').

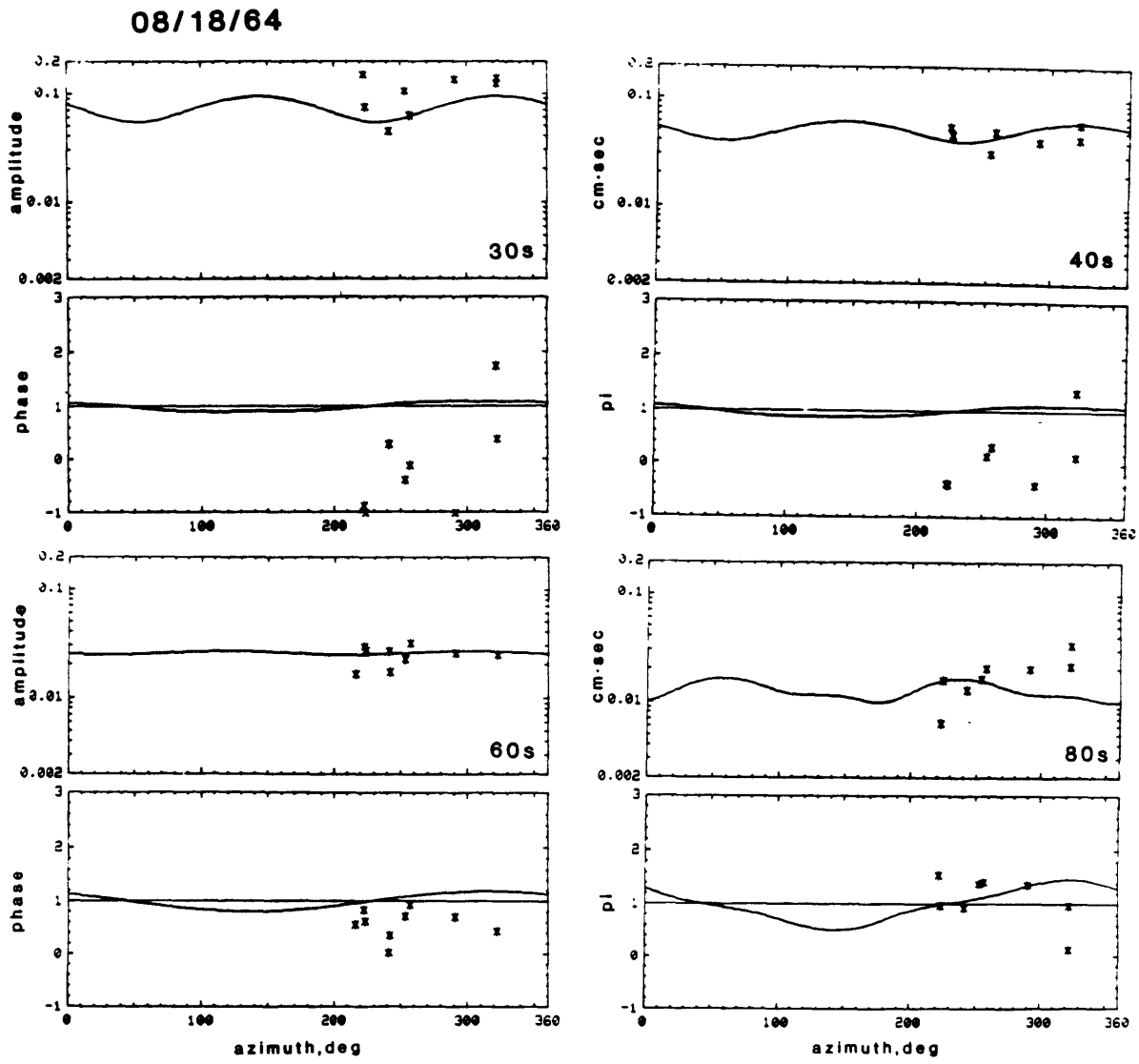

Figure A.1. Data for the event on August 18, 1964.

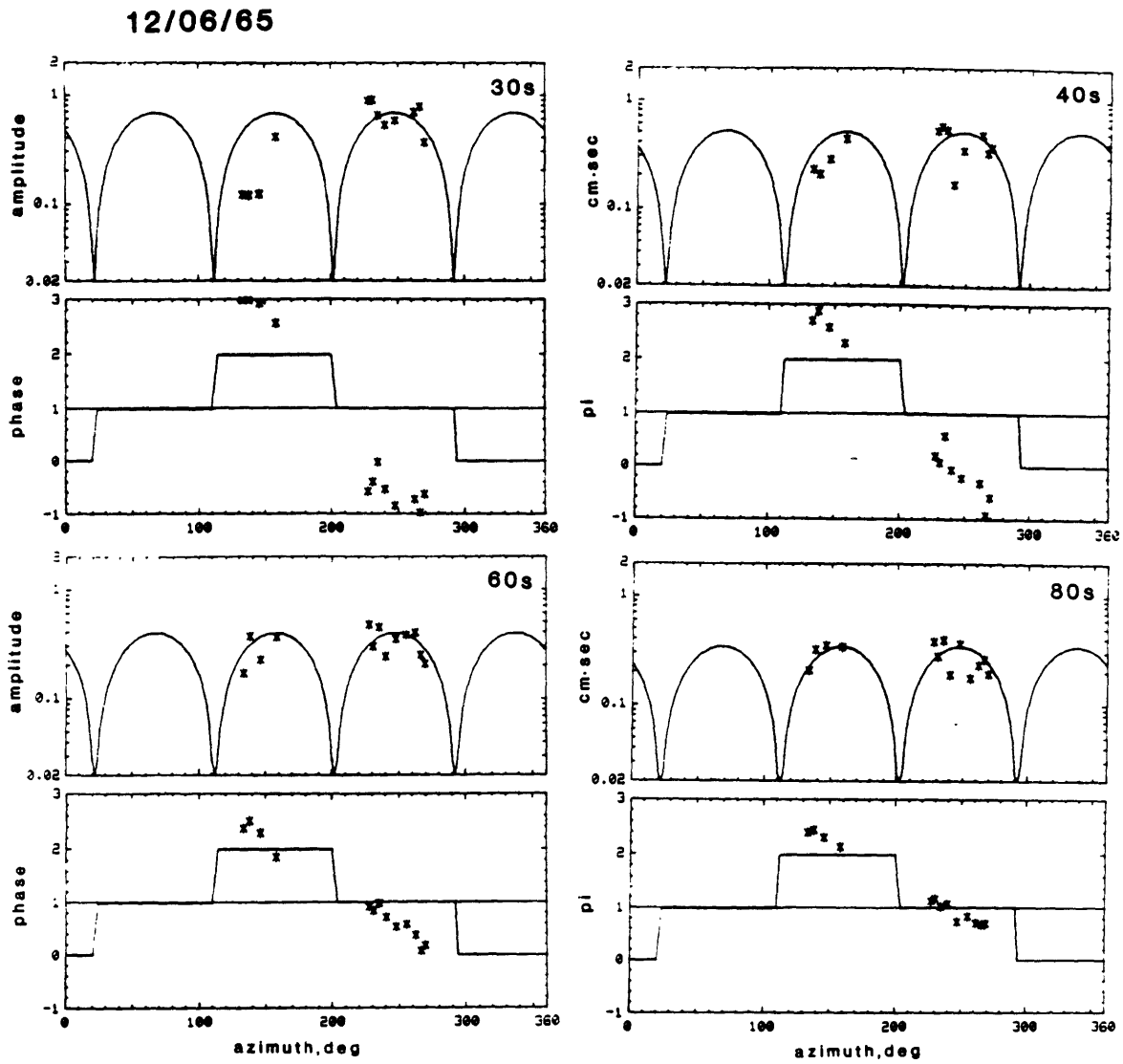

Figure A.2. Data for the event on December 6, 1965.

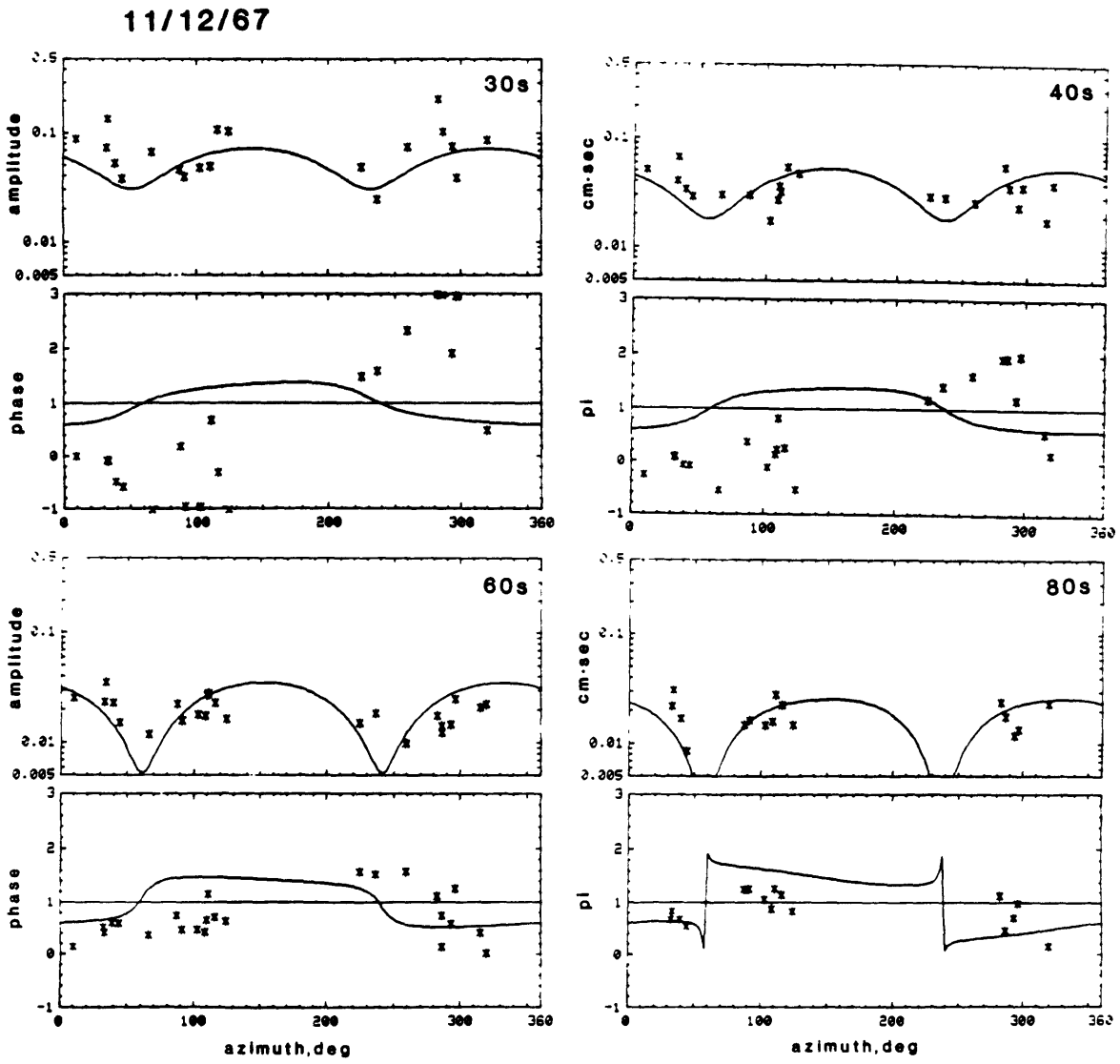

Figure A.3. Data for the event on November 12, 1967.

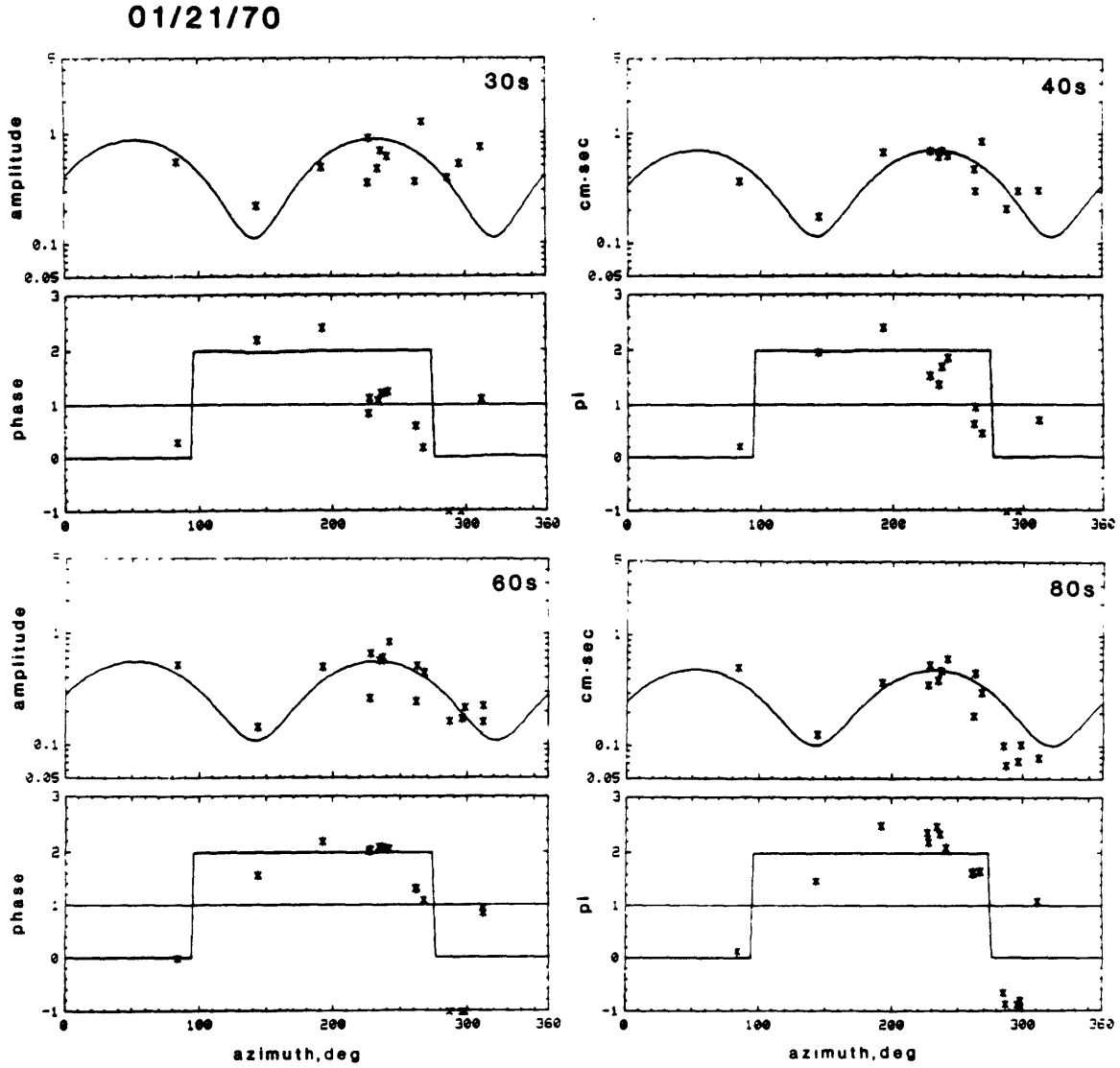

Figure A.4. Data for the event on January 21, 1970.

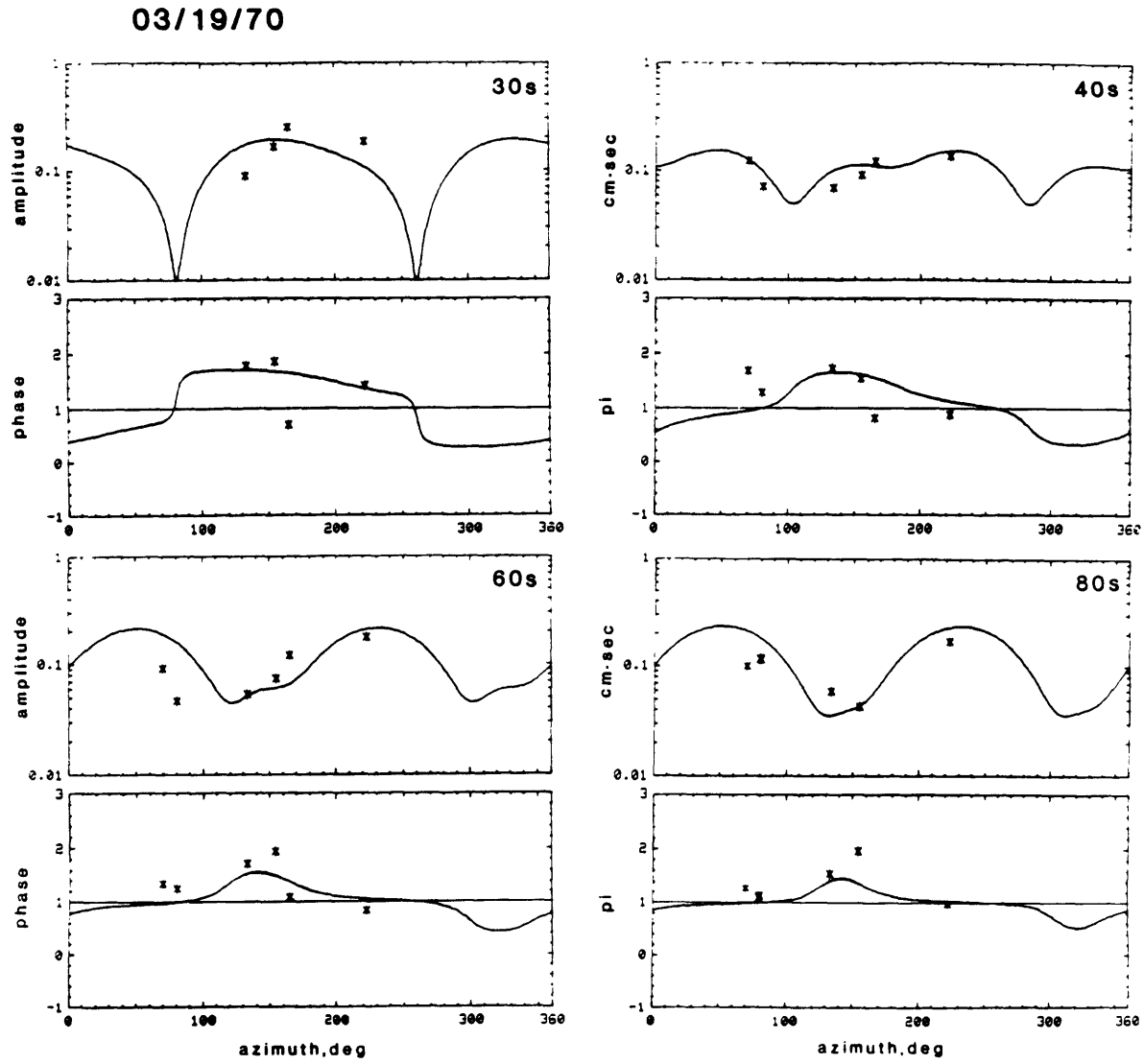

Figure A.5. Data for the event on March 19, 1970.

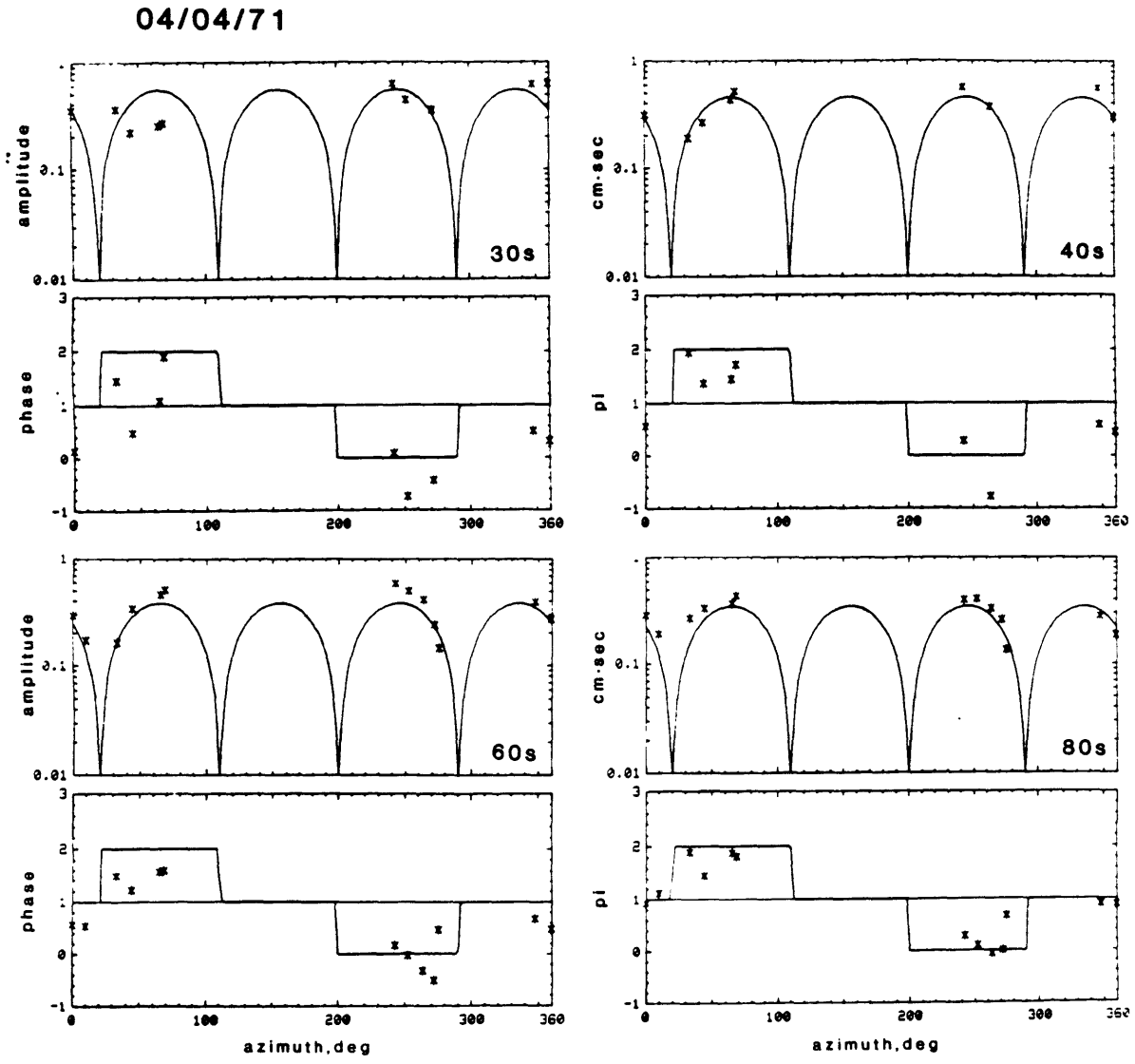

Figure A.6. Data for the event on April 4, 1971.

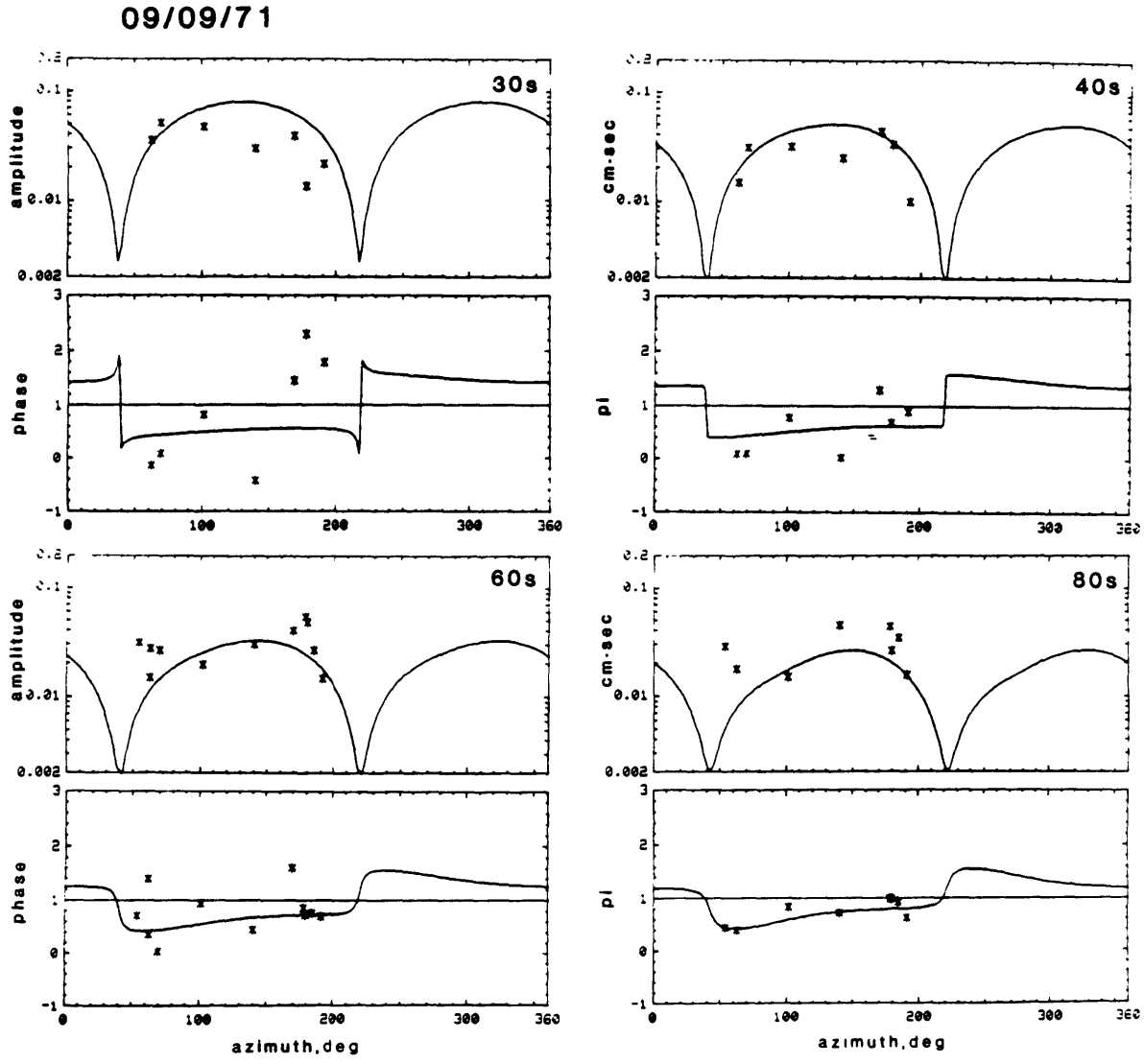

Figure A.7. Data for the event on September 9, 1971.

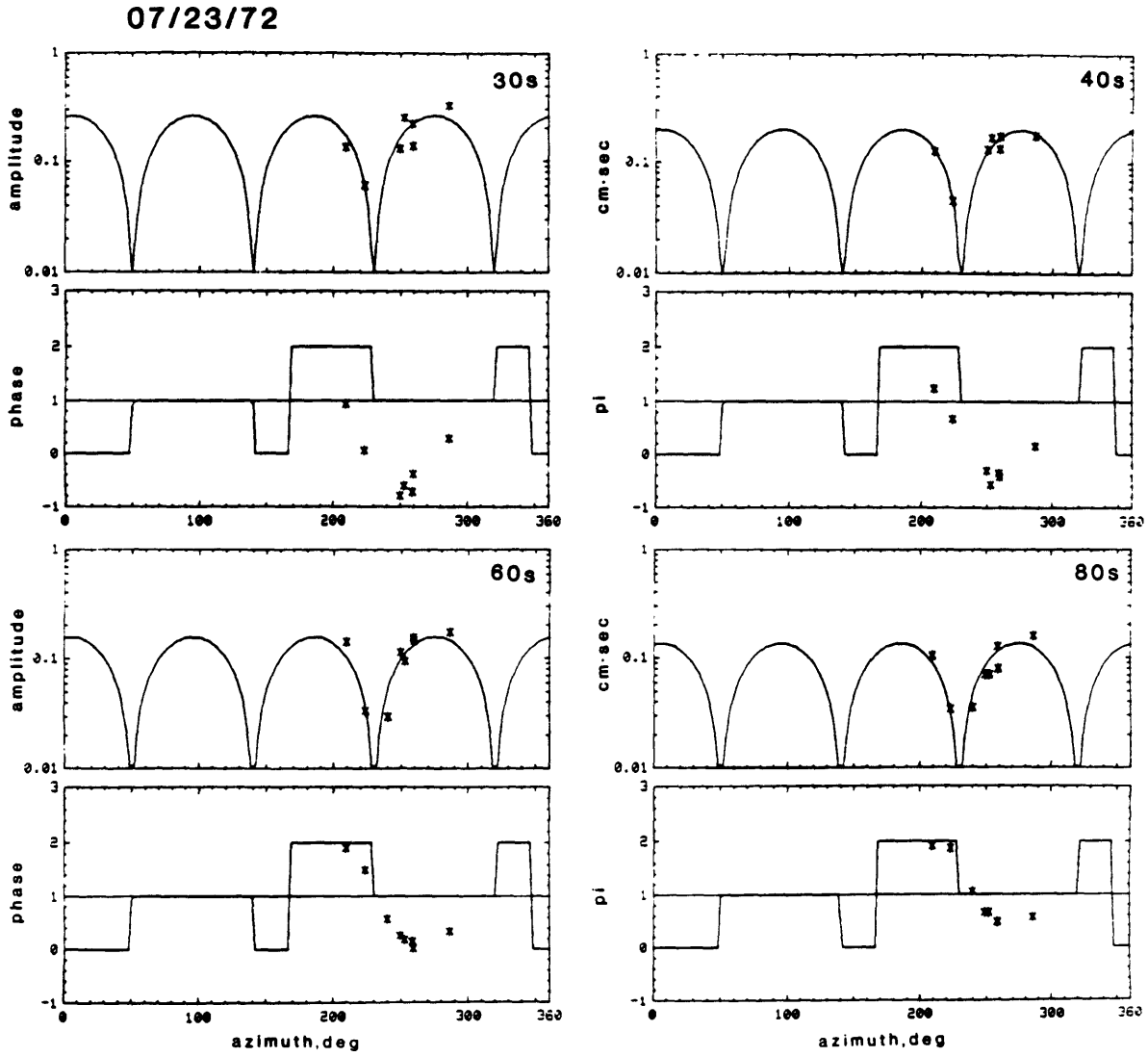

Figure A.8. Data for the event on July 23, 1972.

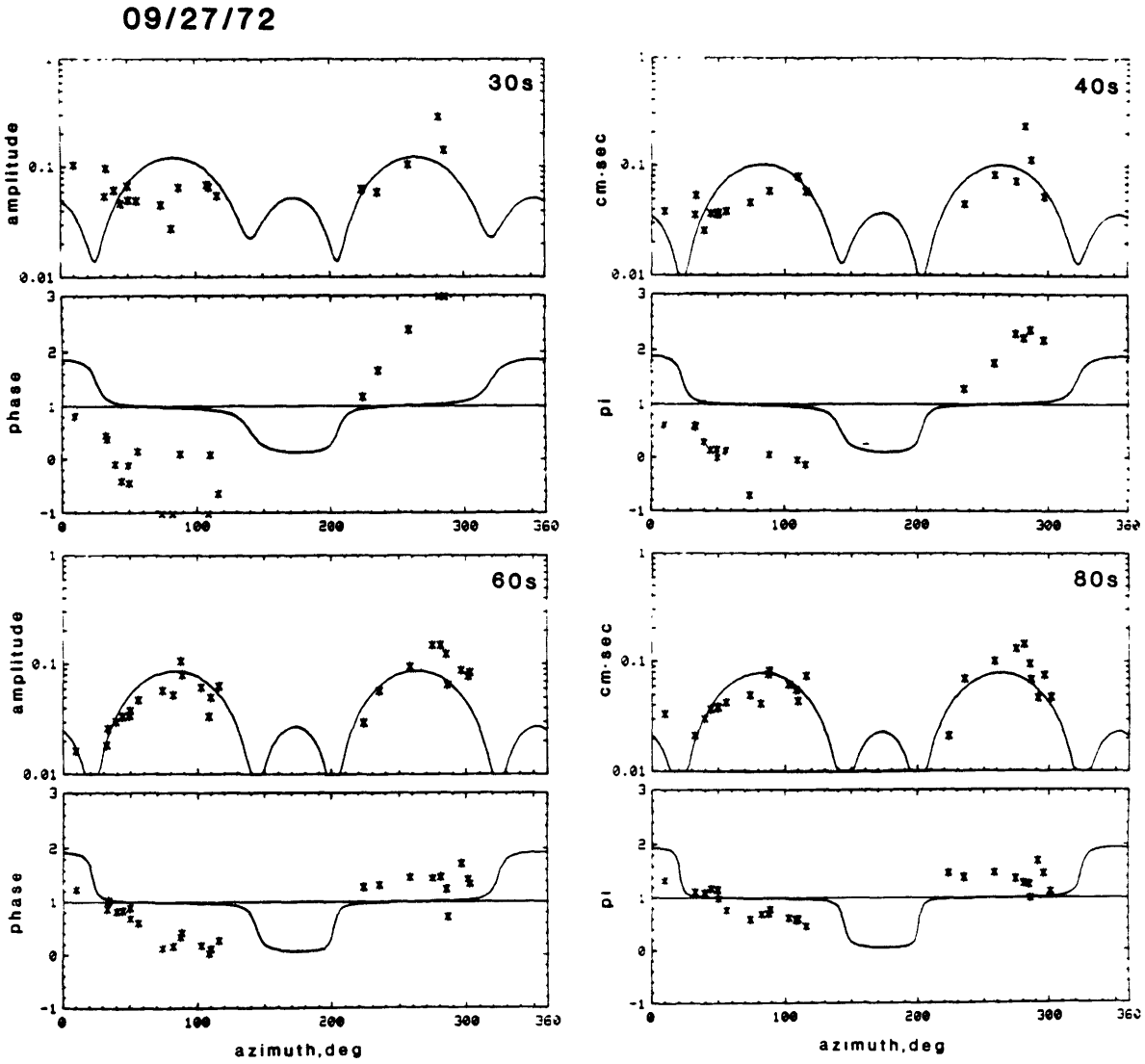

Figure A.9. Data for the event on September 27, 1972.

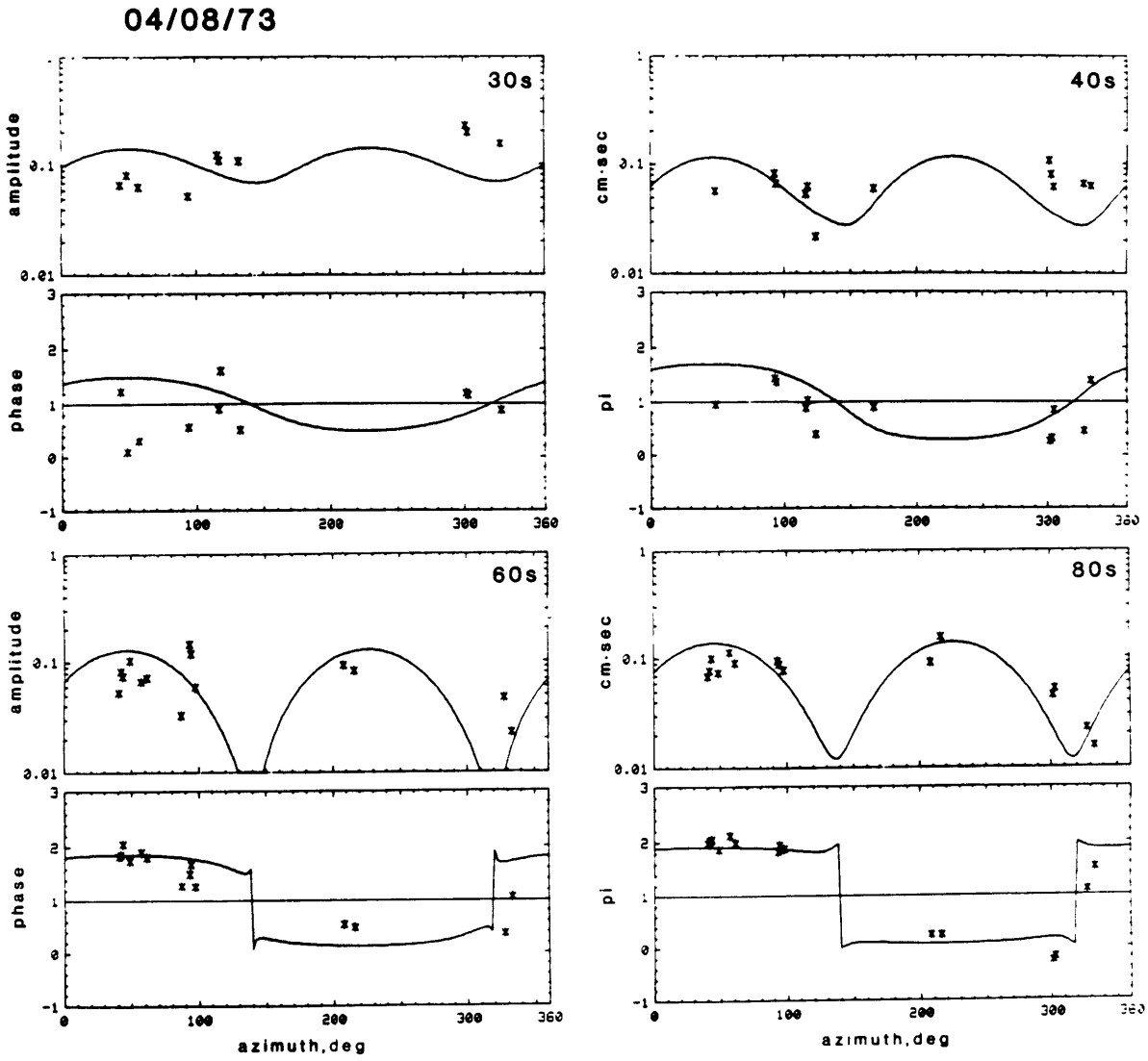

Figure A.10. Data for the event on April 8, 1973.

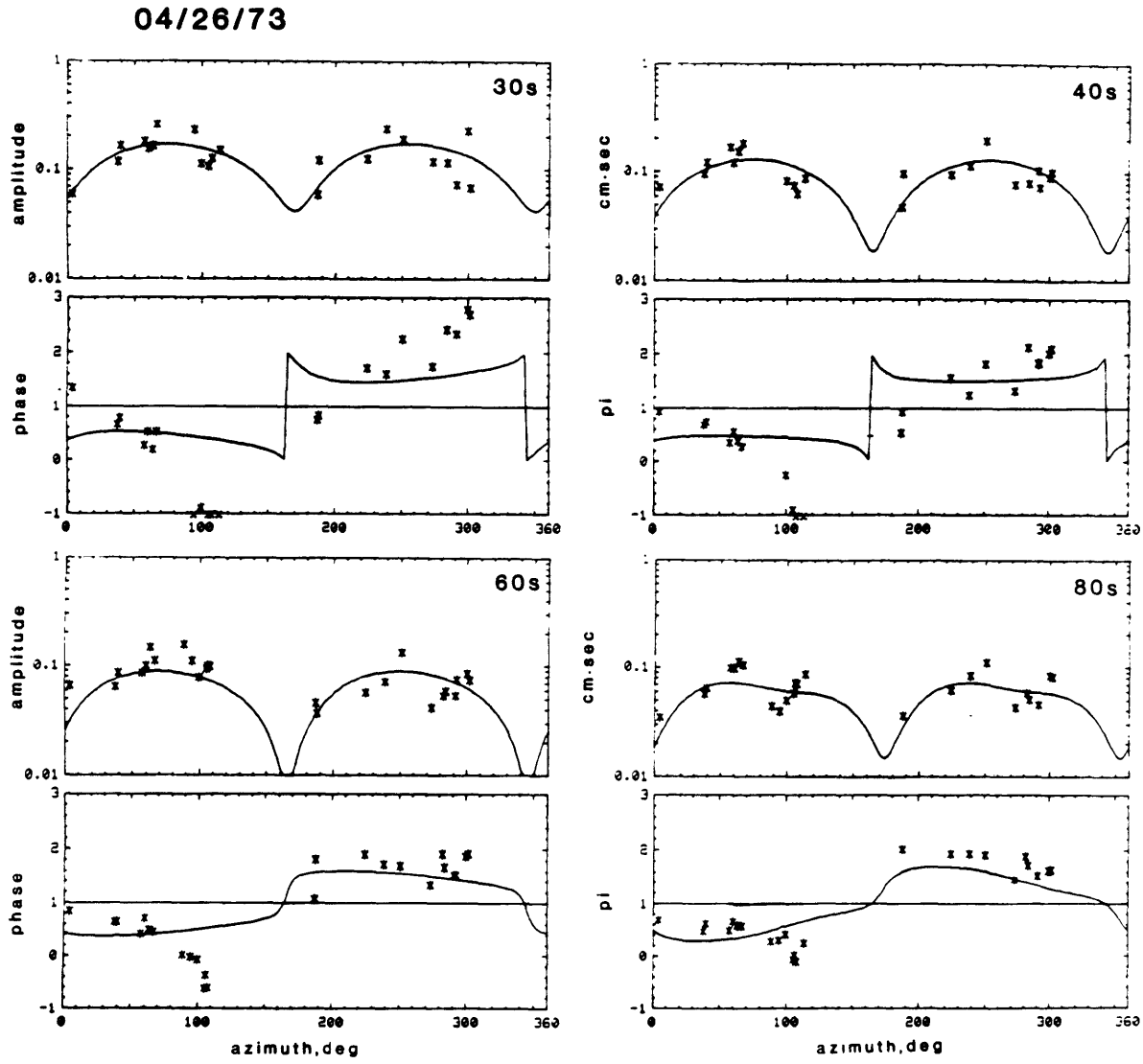

Figure A.11. Data for the event on April 26, 1973.

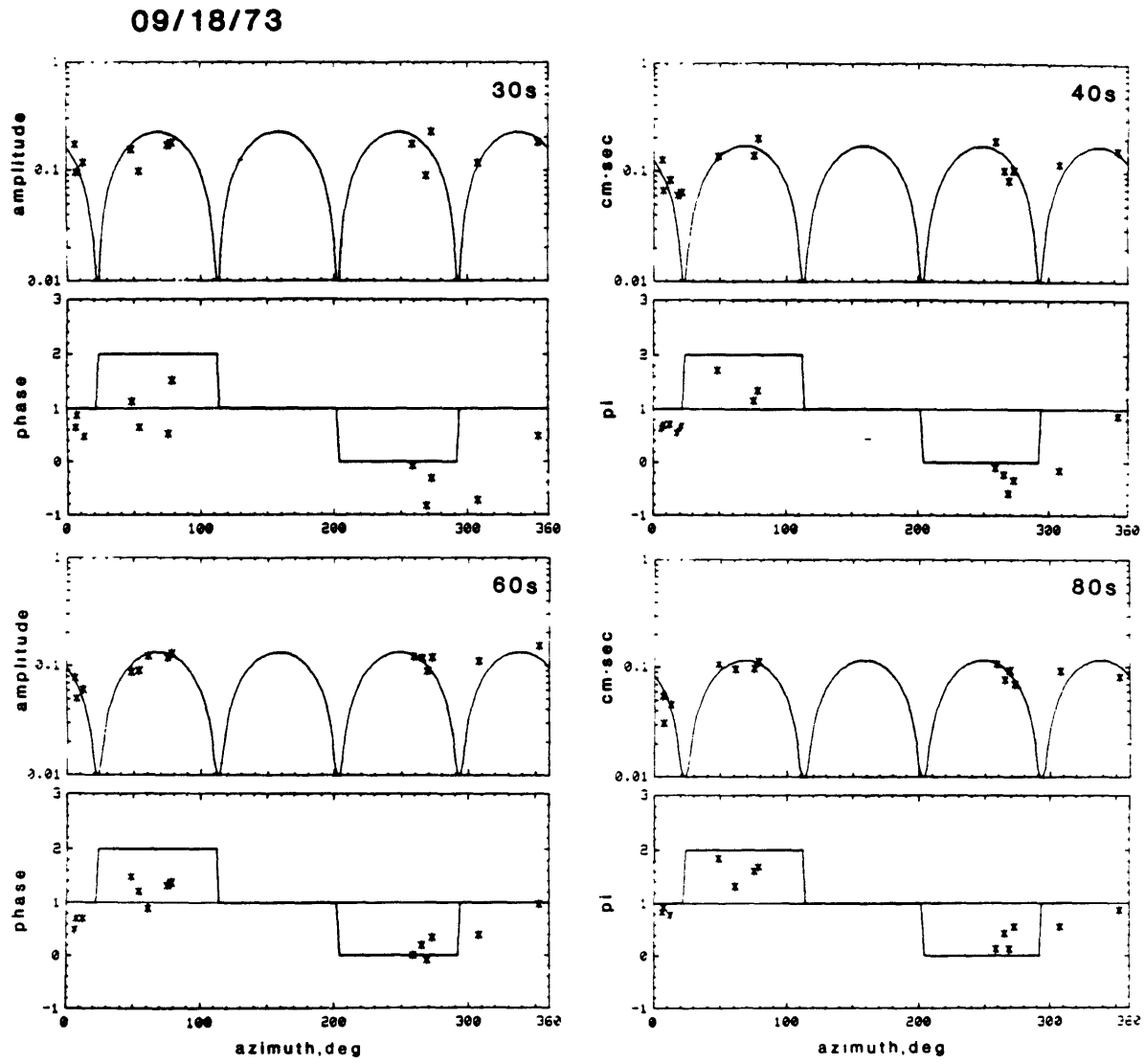

Figure A.12. Data for the event on September 18, 1973.

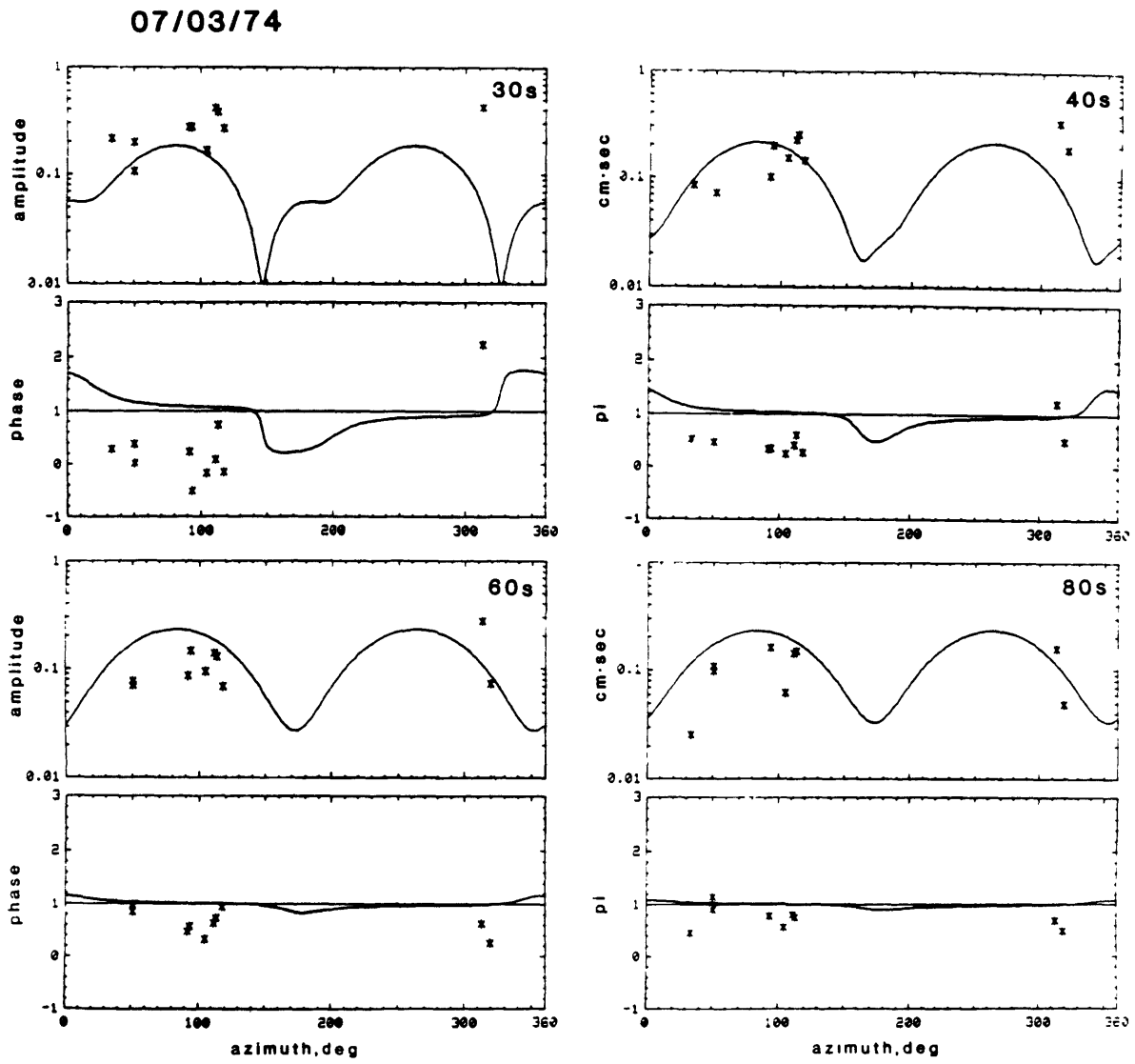

Figure A.13. Data for the event on July 3, 1974.

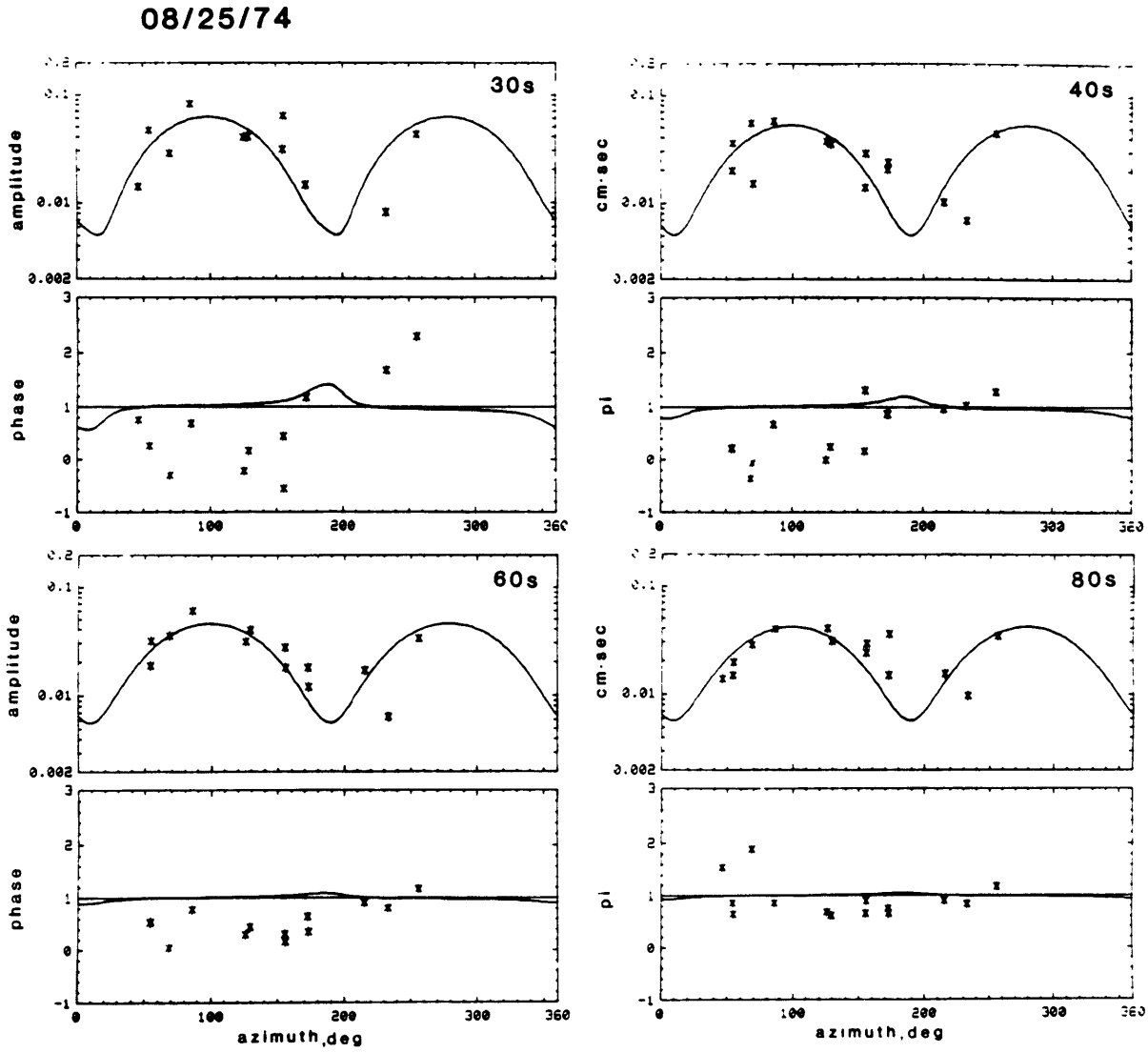

Figure A.14. Data for the event on August 25, 1974.

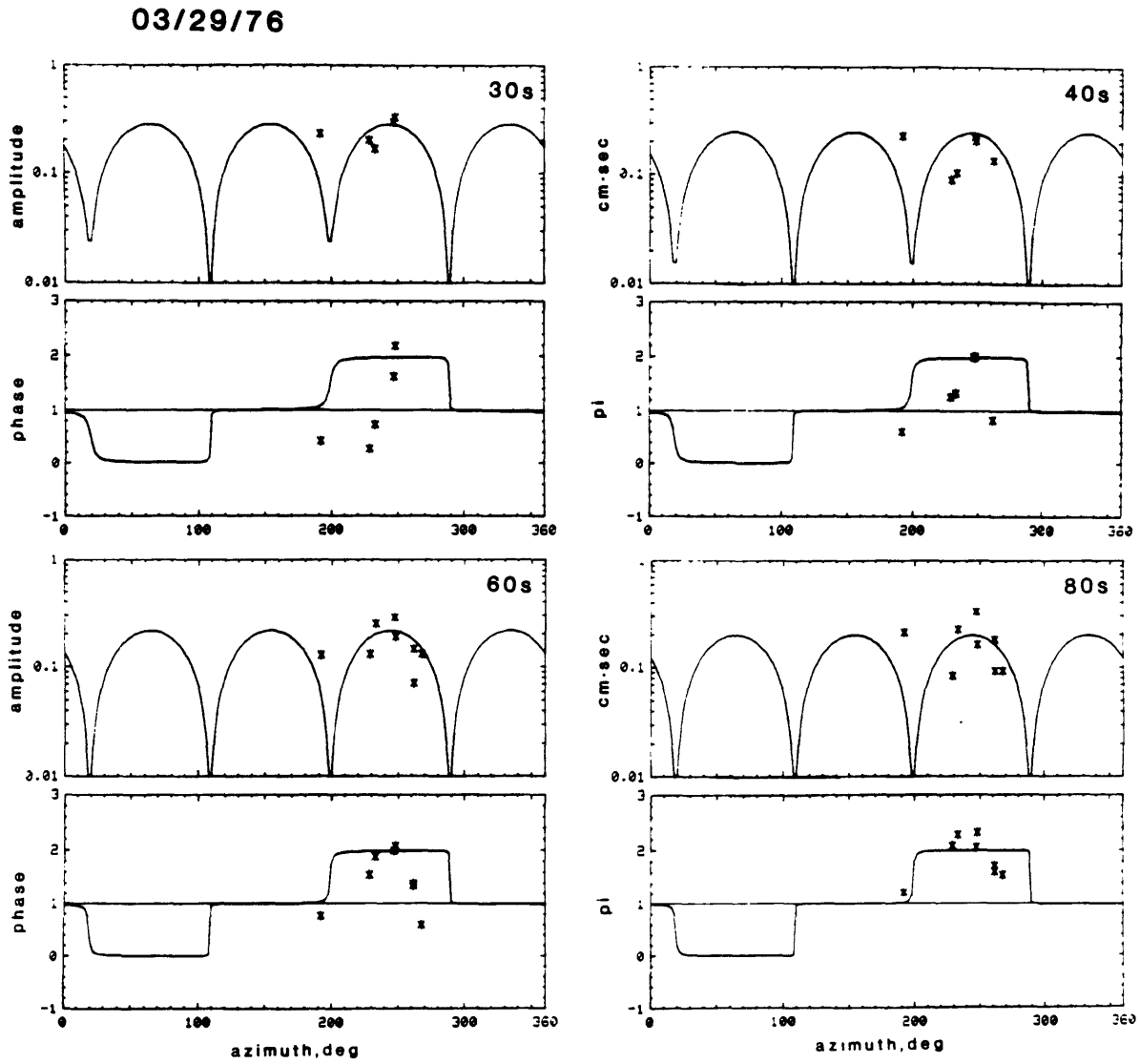

Figure A.15. Data for the event on March 29, 1976.

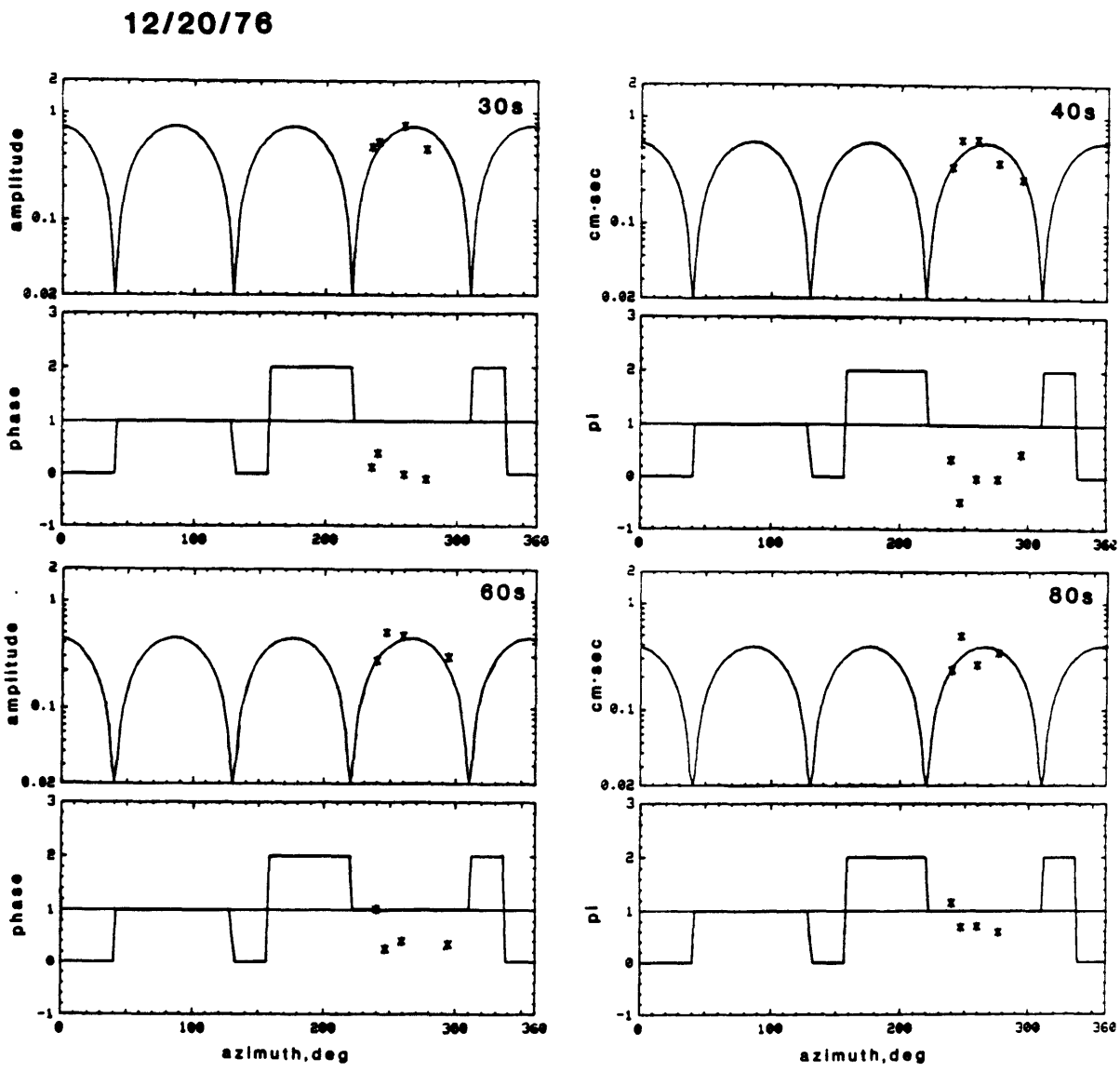

Figure A.16. Data for the event on December 20, 1976.

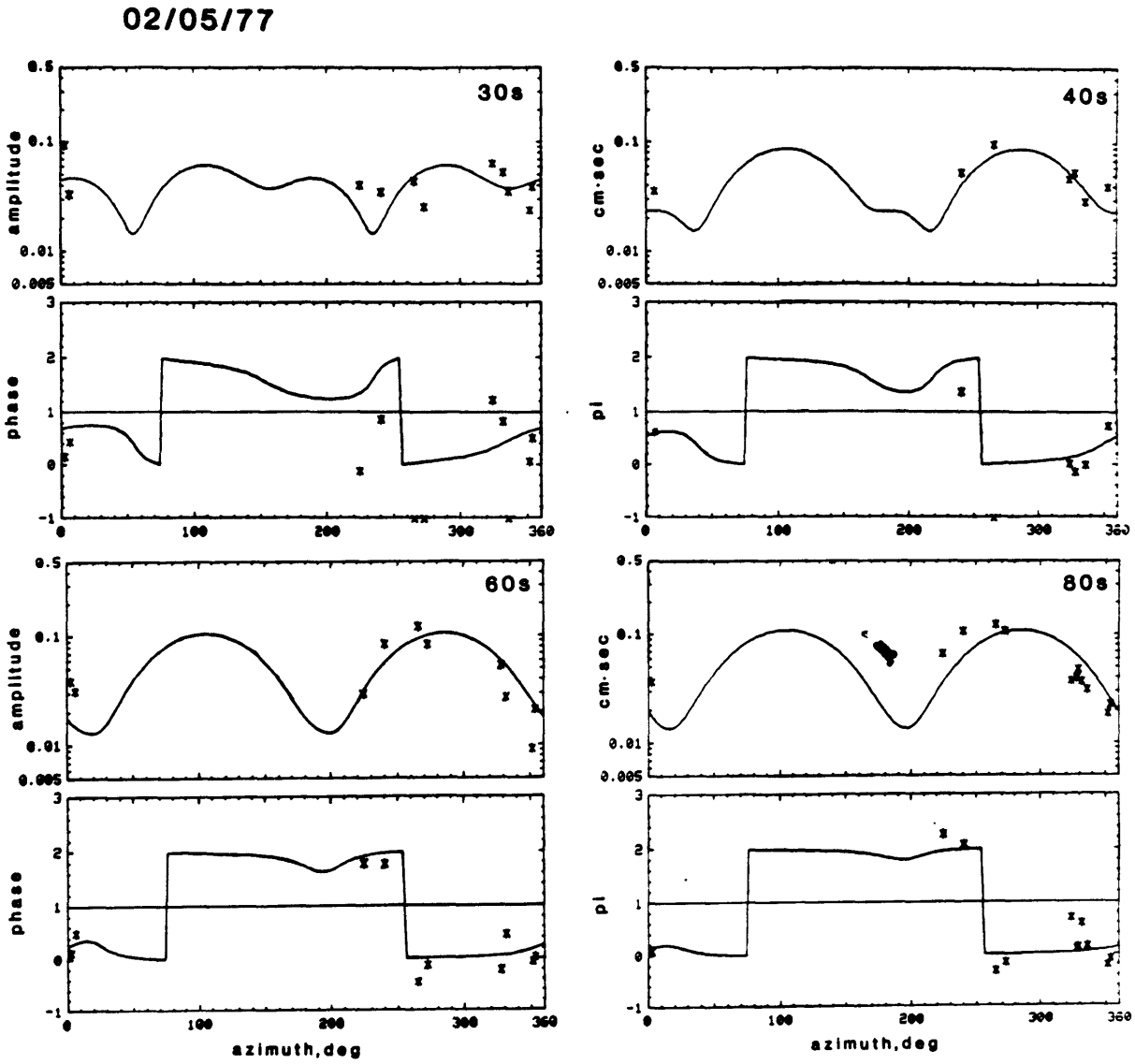

Figure A.17. Data for the event on February 5, 1977.

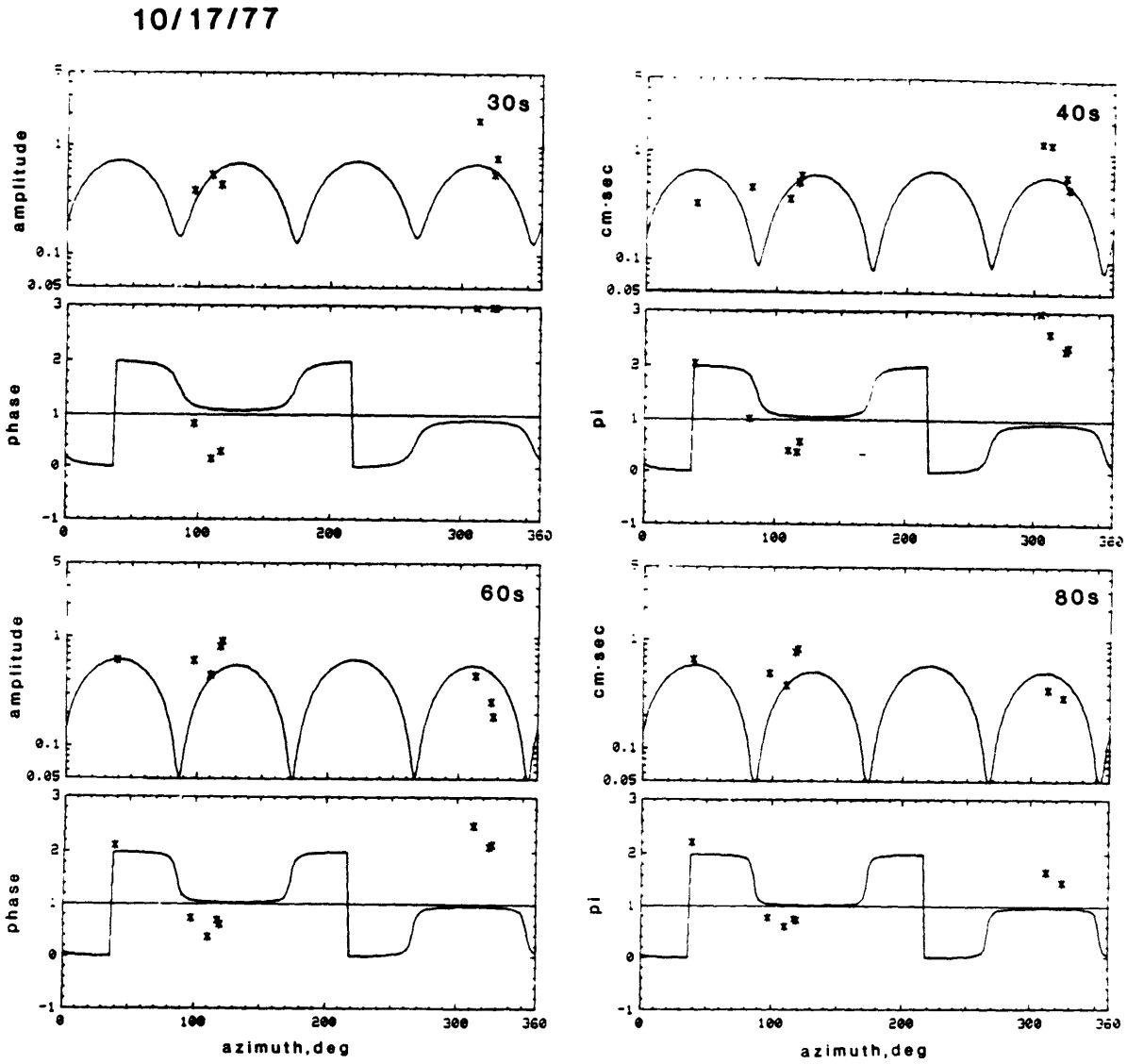

Figure A.18. Data for the event on October 17, 1977.